

| AD NUMBER | DATE | DTIC ACCESSION REQ# |
|---|------|------------------------|
| 20020320 056 | | |
| <p>1. REPORT IDENTIFYING INFORMATION</p> <p>A. ORIGINATING AGENCY <i>U.S. College Dublin, Ireland</i></p> <p>B. REPORT TITLE AND/OR NUMBER <i>Mechanism Under Composition Structures</i></p> <p>C. MONITOR REPORT NUMBER <i>R&D 9300-An-02</i></p> <p>D. PREPARED UNDER CONTRACT NUMBER <i>R&D 1700-M-5805</i></p> | | |
| <p>2. DISTRIBUTION STATEMENT</p> <p>APPROVED FOR PUBLIC DISTRIBUTION</p> <p>DISTRIBUTION UNLIMITED</p> <p>PROCEEDINGS</p> | | |
| <p>DTIC:</p> <ol style="list-style-type: none"> 1. Assign 2. Return <p>TONS ARE OBSOLETE</p> | | |

SOLID MECHANICS AND ITS APPLICATIONS

Volume 92

Series Editor: G.M.L. GLADWELL

*Department of Civil Engineering
University of Waterloo
Waterloo, Ontario, Canada N2L 3G1*

Aims and Scope of the Series

The fundamental questions arising in mechanics are: *Why?*, *How?*, and *How much?*

The aim of this series is to provide lucid accounts written by authoritative researchers giving vision and insight in answering these questions on the subject of mechanics as it relates to solids.

The scope of the series covers the entire spectrum of solid mechanics. Thus it includes the foundation of mechanics; variational formulations; computational mechanics; statics, kinematics and dynamics of rigid and elastic bodies; vibrations of solids and structures; dynamical systems and chaos; the theories of elasticity, plasticity and viscoelasticity; composite materials; rods, beams, shells and membranes; structural control and stability; soils, rocks and geomechanics; fracture; tribology; experimental mechanics; biomechanics and machine design.

The median level of presentation is the first year graduate student. Some texts are monographs defining the current state of the field; others are accessible to final year undergraduates; but essentially the emphasis is on readability and clarity.

For a list of related mechanics titles, see final pages.

IUTAM Symposium on Mechanical Waves for Composite Structures
Characterization

IUTAM Symposium on
**Mechanical Waves for
Composite Structures
Characterization**

Proceedings of the IUTAM Symposium
held in Chania, Crete, Greece,
June 14–17, 2000

Edited by

DIMITRIOS A. SOTIROPOULOS

*Southern Polytechnic State University,
Marietta, Georgia, U.S.A.*

DISTRIBUTION STATEMENT A
Approved for Public Release
Distribution Unlimited



KLUWER ACADEMIC PUBLISHERS
DORDRECHT / BOSTON / LONDON

20020320 056

A C.I.P. Catalogue record for this book is available from the Library of Congress.

ISBN 0-7923-7164-X

Published by Kluwer Academic Publishers,
P.O. Box 17, 3300 AA Dordrecht, The Netherlands.

Sold and distributed in North, Central and South America
by Kluwer Academic Publishers,
101 Philip Drive, Norwell, MA 02061, U.S.A.

In all other countries, sold and distributed
by Kluwer Academic Publishers,
P.O. Box 322, 3300 AH Dordrecht, The Netherlands.

Printed on acid-free paper

All Rights Reserved
© 2001 Kluwer Academic Publishers
No part of the material protected by this copyright notice may be reproduced or
utilized in any form or by any means, electronic or mechanical,
including photocopying, recording or by any information storage and
retrieval system, without written permission from the copyright owner.

Printed in the Netherlands.

Table of Contents

| | |
|---|-----|
| Preface | vii |
| Elastic waves from localized sources in composite laminates | |
| <i>A. Mal</i> | 1 |
| The method of generalized ray applied to plastic sources | |
| <i>F. Ziegler</i> | 25 |
| On the energy release rate from a moving dislocation and the equation of motion of a dislocation <i>X. Markenscoff</i> | |
| 37 | |
| Backscattering of bulk waves from a surface-breaking crack under a compressive load <i>C. Pecorari</i> | |
| 45 | |
| Asymptotic formulas for the stress field of a crack by nonlocal elasticity | |
| <i>H. H. Dai, K. Pan & Y. Fu</i> | 55 |
| Elastodynamic response of a cracked fiber-reinforced body to a non-uniform transient plane-strain loading <i>E. G. Velgaki, H. G. Georgiadis</i> | |
| 63 | |
| Effect of an imperfect interface on elastic P-wave scattering by a spherical inclusion <i>A. C. Wijeyewickrema, L. Mei-Chiang</i> | |
| 71 | |
| Recent advances of the use of Lamb waves for material characterization | |
| <i>T. Kundu</i> | 83 |
| On the role of material constitutive relations in long rod penetration mechanics <i>Z. Rosenberg, E. Dekel</i> | |
| 99 | |
| Wave propagation in planarly-stratified multilayers | |
| <i>A. Morro</i> | 107 |
| Ultrasonic Lamb waves in layered piezoelectric plates | |
| <i>J. M. Orellana, B. Collet</i> | 125 |
| Radiation mode model for multilayered structures | |
| <i>J. Vandepitte, G. Shkerdin, & O. Leroy</i> | 141 |
| Elastic wave scattering from a perturbed flat interface | |
| <i>S. Nair, D. A. Sotiropoulos</i> | 151 |
| The effect of stress on interfacial waves in elastic compressible interlayers <i>D. A. Sotiropoulos, C. G. Sifniotopoulos</i> | |
| 169 | |
| Author Index | |
| 187 | |

Preface

This book is a collection of selected reviewed papers that were presented at the *International Union of Theoretical and Applied Mechanics Symposium* "Mechanical waves for composite structures characterization". The Symposium took place June 14-17, 2000 in Chania, Crete, Greece. As is customary, IUTAM Symposia Proceedings are published in the series "Solid Mechanics and Its Applications" by Kluwer Academic Publishers. I am indebted to Professor G. M. L. Gladwell who is the series editor. I would also like to take this opportunity to express my sincere gratitude to Professor M. A. Hayes the Secretary General of the International Union of Theoretical and Applied Mechanics and a member of the Symposium's Scientific Committee. His constant encouragement and support made the Symposium not only possible but also successful. To the success also contributed all the members of the Symposium's Scientific Committee which I had the honor to chair. I express my appreciation to each one of them who are: Professor J. D. Achenbach (Northwestern University, Evanston, Illinois, USA), Professor M. A. Hayes (University College, Dublin, Ireland), Professor K. J. Langenberg (University of Kassel, Germany), Professor A. K. Mal (University of California, Los Angeles, USA), Professor X. Markenscoff (University of California, San Diego, USA), Professor S. Nair (Illinois Institute of Technology, Chicago, USA), Professor R. W. Ogden (University of Glasgow, UK), Professor G. J. Quentin (University of Paris, France), and Professor F. Ziegler (Technical University of Vienna, Austria). Finally, the financial support of Unesco, Iutam, and the US Army Research Laboratory-Europe Office is gratefully acknowledged.

The Symposium covered a wide variety of areas and subjects that fall under its title-theme. As the symposium theme is interdisciplinary in nature, participants were invited from diverse fields such as Applied Mathematics, Applied Physics, Biomedical Engineering, Civil Engineering, Electrical Engineering, Fluid and Solid Mechanics, Materials Engineering, Mechanical Engineering, and Seismology. The symposium covered analytical, computational, numerical, theoretical and experimental aspects from state-of-the-art fundamental research to applied research and applications in emerging technologies. The topics include body waves, elastic waves, guided waves, inhomogeneous waves, rays, surface waves, and ultrasound in composite materials which are fiber-reinforced, laminated, or homogeneous containing bonds, coatings, cracks, defects, or thin films. The symposium participants who represented four continents are here acknowledged. As mentioned above, however, only selected reviewed papers from the ones presented in the Symposium are included in this volume. These papers are placed in five thematic categories and presented in the volume sequentially: The first category includes two papers that deal with waves or rays from localized/plastic sources in layered media. In the second category five papers deal explicitly with discontinuities (e. g. dislocations, cracks). Two papers make up the third category in which experimental investigations are of primary interest. The fourth category includes three papers that concentrate on waves in multilayered structures. Finally, two papers are included in the fifth category dealing exclusively with elastic waves and interfaces. I cannot close without thanking each one of the authors that made this volume possible.

Dimitrios A. Sotiropoulos
Marietta, Georgia, USA

ELASTIC WAVES FROM LOCALIZED SOURCES IN COMPOSITE LAMINATES

AJIT MAL

Mechanical and Aerospace Engineering Department
University of California, Los Angeles
California 90095-1597, U.S.A.

1. Abstract

This paper is concerned with the analysis of elastic waves generated by localized dynamic sources in structural composites. The damage can be external, involving low-velocity foreign object impact on the surface of the structure, or internal, as in sudden crack initiation and its rapid growth from existing internal flaws. Both problems are of critical importance in the safe operation of composite structures, due to their vulnerability to hidden delaminations that can occur in composite materials when they are subjected to this type of loads. It is well known that both the dynamic surface loading associated with impact, and the sudden "opening" of an internal crack associated with the extension of a preexisting flaw, act as sources of elastic waves in the material of the structure. The research reported here consists of model-based analysis of the guided waves generated by localized low-velocity impact and microcrack initiation in graphite epoxy composite laminates commonly used in aircraft and aerospace structures. The objective of this study is to develop a mechanics based understanding of the causal relationship between the properties of the source and the characteristics of the waves generated by its initiation and propagation. The results of this research are expected to be useful in developing effective health monitoring systems for new as well as aging aircraft and aerospace structures.

2. Introduction

Fiber-reinforced composites are being used increasingly as primary structural components in aircraft and aerospace structures as well as in ground and marine transportation. These materials have highly desirable engineering properties, notably, relatively low weight accompanied by high strength and damage tolerance that can be exploited to design structures with high demands on their performance. They also offer a unique mix of formability and other processing advantages over conventional metals. However, composites are very sensitive to the presence of manufacturing flaws and service conditions that can lead to a serious degradation in their load carrying capacity. Another major concern is the growth of undetected hidden delaminations caused by low velocity foreign object impact. Both types of damage, if undetected, can grow to a critical size and lead to catastrophic failure of the structure. In order to insure the safety of the structure, it is often necessary to carry out expensive and extremely time consuming inspection procedures at regular intervals. The availability of a practical, on

board, damage monitoring system in aircraft and aerospace structures can be extremely helpful in improving their safety and reducing maintenance cost by a significant amount.

The sudden occurrence of small flaws initiated from damage sites in structural solids generates elastic waves that carry important information on the nature of the damage. Careful analysis of the waves can reveal the characteristics of the fracture process and the damage. A coordinated theoretical and experimental program of research is being carried out by the author and his associates in an effort to develop the knowledge base required for the design of a practical damage monitoring system in composite structures consisting of distributed surface mounted or embedded multiple sensors. One of the issues that has been studied carefully under this project is the relationship between the properties of the source and the characteristics of the guided elastic waves in composite laminates, and the major findings of these studies are summarized in this paper.

An extensive review of published research on low velocity as well as ballistic impact on laminated composites has been given by Abrate [1]. The focus of this research is wave propagation effects associated with impact. Research in this area has been very limited to date. Mal and Lih [2] and Lih and Mal [3-5] investigated the response of unidirectional as well as multidirectional composite laminates of infinite lateral dimensions to localized dynamic loads through theoretical modeling and laboratory tests. In contrast to the impact problem, studies on the waves generated by internal sources in structural composites, is rather sparse. Guo, Mal and Ono [6] carried out laboratory experiments and theoretical modeling to study the characteristic of the guided waves generated by crack initiation in thin composite laminates.

In this paper an overview of the theoretical and experimental studies carried out by the author's group to characterize the properties of the elastic waves generated by both types of sources, namely, localized surface loads and the initiation of embedded microcracks, is presented. The potential applications of this research in developing effective health monitoring systems for aerospace and aircraft structures are discussed.

3. Theory of Wave Propagation in Composite Laminates

The behavior of elastic waves propagating through a composite material is determined by its elastic properties. Since composites are highly heterogeneous and anisotropic materials, a number of assumptions need to be made in creating their models that can be treated under the framework of elastodynamic theories. For fiber reinforced graphite/epoxy materials, the homogeneous, and transversely isotropic medium with symmetry axis along the fibers, has been found to be quite reasonable in capturing the behavior of the waves in the frequency range of interest in low velocity impact and microcrack extension. This is due to the fact that the diameter of the graphite fibers (5 -10 μm) is significantly smaller than the wavelength (of about 100 μm) at frequencies up to 20 MHz, which is well above the frequency range of interest in the problems of interest here. Assuming that the symmetry is along the x_1 -axis the constitutive relation for the material can be expressed in the form (see, e.g., Mal and Singh, [7])

$$\begin{bmatrix} \sigma_{11} \\ \sigma_{22} \\ \sigma_{33} \\ \sigma_{23} \\ \sigma_{31} \\ \sigma_{12} \end{bmatrix} = \begin{bmatrix} C_{11} & C_{12} & C_{12} & 0 & 0 & 0 \\ C_{12} & C_{22} & C_{23} & 0 & 0 & 0 \\ C_{12} & C_{23} & C_{22} & 0 & 0 & 0 \\ 0 & 0 & 0 & C_{44} & 0 & 0 \\ 0 & 0 & 0 & 0 & C_{55} & 0 \\ 0 & 0 & 0 & 0 & 0 & C_{55} \end{bmatrix} \begin{bmatrix} u_{1,1} \\ u_{2,2} \\ u_{3,3} \\ u_{2,3} + u_{3,2} \\ u_{1,3} + u_{3,1} \\ u_{1,2} + u_{2,1} \end{bmatrix} \quad (1)$$

where σ_{ij} is the Cauchy's stress tensor, u_i is the displacement components, $C_{44} = (C_{22} - C_{23})/2$ and the five independent stiffness constants of the material are C_{11} , C_{12} , C_{22} , C_{23} and C_{55} .

Modeling the effective elastic moduli of composite materials has been the topic of many studies. For low frequencies and low fiber concentration, the theoretical prediction of the effective elastic constants is in good agreement with experimental results. On the other hand, for high frequencies the theoretical estimates are not satisfactory since the effect of wave scattering by the fibers becomes significant. For fiber-reinforced composite materials, dissipation of the waves is caused by the viscoelastic nature of the resin and by multiple scattering from the fibers as well as other inhomogeneities. Both of these effects can be modeled by assuming complex and frequency-dependent stiffness constants, C_{ij} , in the form Mal, Bar-Cohen and Lih, [8],

$$\begin{aligned} C_{11} &= \frac{c_{11}}{1 + ip\sqrt{c_{55}/c_{11}}}, & C_{22} &= \frac{c_{22}}{1 + ip\sqrt{c_{55}/c_{22}}}, \\ C_{12} + C_{55} &= \frac{c_{12} + c_{55}}{1 + ip\sqrt{c_{55}/(c_{12} + c_{55})}} & (2a) \\ C_{44} &= \frac{C_{22} - C_{23}}{2} = \frac{c_{44}}{1 + ip\sqrt{c_{55}/c_{44}}}, & C_{55} &= \frac{c_{55}}{1 + ip} \end{aligned}$$

where c_{ij} is the real, perfectly elastic, stiffness constant and p is the damping factor which can be expressed in the form,

$$p = p_0 [1 + a_0 (\frac{\omega}{\omega_0} - 1)^2 H(\frac{\omega}{\omega_0} - 1)] \quad (2b)$$

The parameter p_0 represents the effect of material dissipation, a_0 models the effect of scattering due to the fibers and other inhomogeneities, and ω_0 is a frequency below which the scattering effect is negligible.

For multilayered laminates, each layer is assumed to be transversely isotropic, with its own axis of symmetry along the fibers, and is bonded to its neighbors with a thin layer of the matrix material. In the present analysis these interfacial layers are ignored for the sake of simplicity, but if needed, they can be incorporated in the analysis without difficulty.

3.1. THE GLOBAL MATRIX METHOD FOR MULTILAYERED LAMINATES

Elastodynamic analysis of multilayered composite laminates is difficult due to the complex behavior of the waves caused by their multiple reflection and transmission at the interlaminar interfaces and the boundaries of the laminate. This is due to the fact that, each incident ray at an interface produces three reflected waves and three transmitted rays, as shown in Mal, Yin and Bar-Cohen, [9], in addition to diffracted waves and head waves. At the frequencies of interest here, the wavelengths are larger than the individual laminae, but can be smaller than the laminate thickness. Thus, the ray theoretical approach cannot be used to calculate the wavefield accurately. A wave theoretical treatment using a matrix method proposed by the author [10] has been found to be very effective in generating accurate numerical solutions to this class of problems. A brief description of this method is given here.

Three problems involving different types of sources that can be solved by this method are sketched in Figure 1. The first problem, shown in Figure 1A, models the so-called Leaky Lamb Wave (LLW) experiment in which the laminate is immersed in water and insonified by a beam of acoustic waves. The second problem, shown in Figure 1B, is the dynamic surface source problem typical of relatively low-frequency impact loading or high frequency ultrasonic testing. In the third problem, shown in Figure 1C, the source of the waves is the sudden occurrence or extension of a delamination at an interface. In all three cases, the interest is the determination of the elastodynamic field in the laminate, and in the second problem, the acoustic field in the fluid. All three problems can be formulated under the same general framework; they differ only in the specific forms of the boundary conditions.

Let us consider the general case of the multilayered laminate consisting of N laminae and total thickness H as shown in Fig. 1B. Each lamina is assumed to be transversely isotropic with fibers, or axis of symmetry on its plane. A global coordinate system, $\mathbf{X}(X_1, X_2, X_3)$, with origin on the top surface of the laminate and a local coordinate system, $\mathbf{x}(x_1, x_2, x_3)$, in each lamina, with the x_1 -axis along the fiber direction and x_3 -axis coincident with the global X_3 -axis, are introduced. The fiber direction in the m^{th} lamina makes an angle ϕ^m with the X_1 -axis, and the thickness of the m^{th} lamina is h^m .

The displacement and the stress components in the m^{th} lamina are denoted by U_i^m and Σ_{ij}^m in the global coordinate system and by u_i^m and σ_{ij}^m in the local coordinate system. Then the displacements and stresses in the local and global coordinate system are related by

$$\begin{aligned} \begin{bmatrix} u_1^m \\ u_2^m \\ u_3^m \end{bmatrix} &= [L^m] \begin{bmatrix} U_1^m \\ U_2^m \\ U_3^m \end{bmatrix}, & \begin{bmatrix} \sigma_{31}^m \\ \sigma_{32}^m \\ \sigma_{33}^m \end{bmatrix} &= [L^m] \begin{bmatrix} \Sigma_{31}^m \\ \Sigma_{32}^m \\ \Sigma_{33}^m \end{bmatrix} & \begin{bmatrix} \sigma_{11}^m \\ \sigma_{22}^m \\ \sigma_{12}^m \end{bmatrix} &= [M^m] \begin{bmatrix} \Sigma_{11}^m \\ \Sigma_{22}^m \\ \Sigma_{12}^m \end{bmatrix} \end{aligned} \quad (3a)$$

where

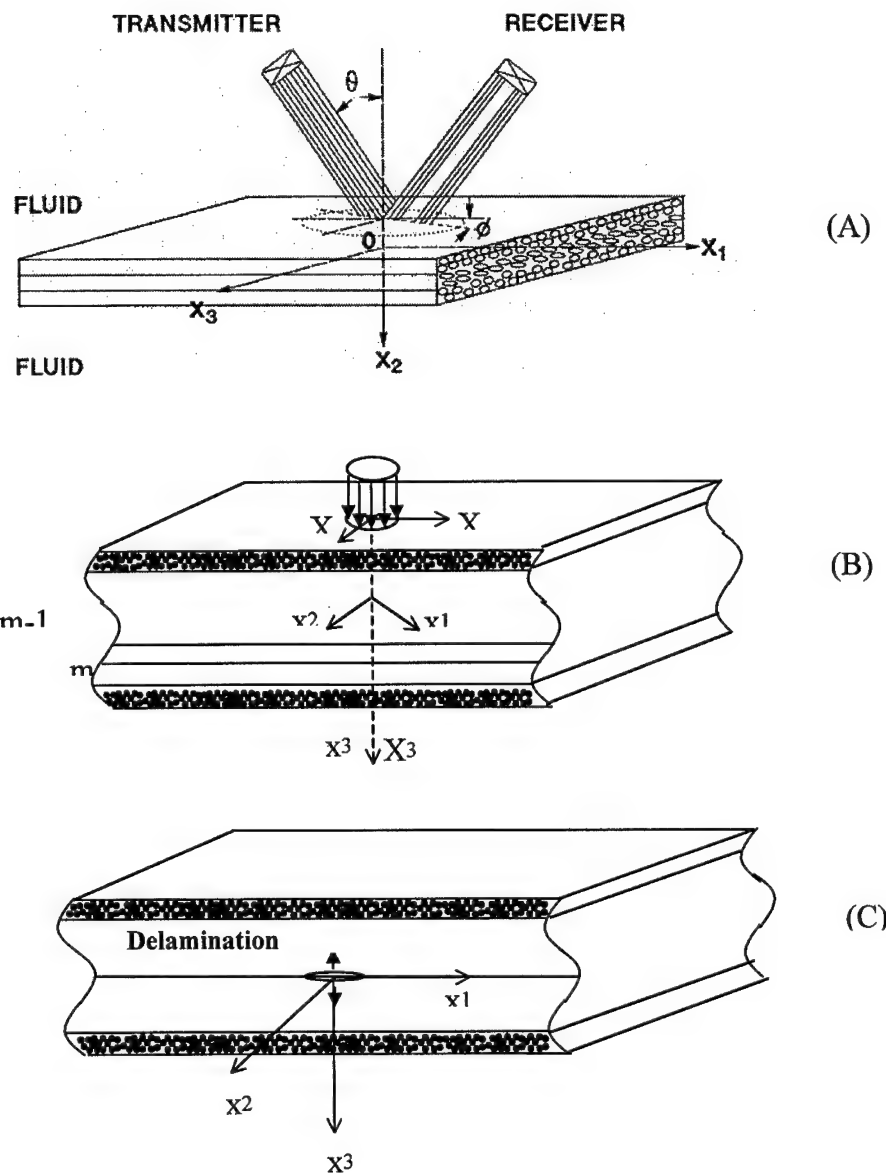


Figure 1. Geometry of the composite laminate with three types of loading:

- (A): Acoustic wave loading in the leaky Lamb wave experiment.
- (B): Surface loading in foreign object impact.
- (C): Microfracture initiation in a damage site.

$$\begin{bmatrix} L^m \\ M^m \end{bmatrix} = \begin{bmatrix} c^m & -s^m & 0 \\ s^m & c^m & 0 \\ 0 & 0 & 1 \end{bmatrix}, \quad \begin{bmatrix} (c^m)^2 & (s^m)^2 & -2c^m s^m \\ (s^m)^2 & (c^m)^2 & 2c^m s^m \\ c^m s^m & -c^m s^m & (c^m)^2 - (s^m)^2 \end{bmatrix} \quad (3b)$$

and $c^m = \cos(\phi^m)$, $s^m = \sin(\phi^m)$.

Let all field quantities be subject to the Fourier time transform so that the problem can be formulated in the frequency domain first. Time domain results will be obtained through FFT inversion of the frequency domain results. Denoting the Fourier time transform by an overbar, the Cauchy's equations of motion for the m^{th} lamina become,

$$\bar{\sigma}_{ij,j}^{(m)} + \rho^m \omega^2 \bar{u}_i^{(m)} = 0 \quad (4)$$

where ρ^m is the overall density of the material of the m^{th} lamina and the summation convention and comma notation apply. These equations must be supplemented by the constitutive equation (1) and the solution must satisfy the outgoing wave (or radiation) condition at large lateral distances from the load.

If there are no delaminations at the interfaces, the traction and displacement components must be continuous across the interfaces parallel to the $X_1 X_2$ -plane, i.e.,

$$\bar{u}_i^{(m-1)} = \bar{u}_i^{(m)}, \quad \bar{\sigma}_{i3}^{(m-1)} = \bar{\sigma}_{i3}^{(m)}, \quad X_3 = X_3^m \quad (5)$$

where X_3^m is the location of the interface between the layers m and $m-1$. The boundary conditions at the top and bottom faces of the laminate depend on the external loading and will be specified later.

The stress and displacement components are now subjected to a two dimensional Fourier transforms with respect to X_1 and X_2 , denoted by \hat{u}_i^m , $\hat{\sigma}_{ij}^m$ in the general form

$$\begin{aligned} \hat{\Phi}(K_1, K_2, X_3, \omega) &= \int_{-\infty}^{\infty} \int_{-\infty}^{\infty} \bar{\Phi}(X_1, X_2, X_3, \omega) e^{-i(K_1 X_1 + K_2 X_2)} dX_1 dX_2 \\ \bar{\Phi}(X_1, X_2, X_3, \omega) &= \frac{1}{4\pi^2} \int_{-\infty}^{\infty} \int_{-\infty}^{\infty} \hat{\Phi}(K_1, K_2, X_3, \omega) e^{i(K_1 X_1 + K_2 X_2)} dK_1 dK_2 \end{aligned} \quad (6)$$

where K_1 and K_2 are the global wave number in X_1 and X_2 directions, respectively.

In order to facilitate the application of the interface conditions, it is convenient to

introduce the six-dimensional "stress-displacement vector," $\{\hat{S}^m\}$, in the transformed domain through

$$\{\hat{S}^m(K_1, K_2, X_3, \omega)\} = \{\hat{u}_i^m \quad \hat{\sigma}_{i3}^m\} \quad (7)$$

The arguments, K_1 , K_2 and ω in $\{\hat{S}^m\}$ will be omitted for brevity. It should be noted that in absence of interfacial forces, $\{\hat{S}^m(X_3)\}$ is continuous in the domain, $0 < X_3 < H$ and that in the m^{th} lamina, $\{\hat{S}^m(X_3)\}$ can be expressed in a partitioned matrix product form

$$\{\hat{S}^m(X_3)\} = \begin{bmatrix} L^m & 0 \\ 0 & L^m \end{bmatrix} \begin{bmatrix} Q_{11}^m & Q_{12}^m \\ Q_{21}^m & Q_{22}^m \end{bmatrix} \begin{bmatrix} E_+^m(X_3) & 0 \\ 0 & E_-^m(X_3) \end{bmatrix} \begin{bmatrix} C_+^m \\ C_-^m \end{bmatrix} \quad (8)$$

where C_\pm^m are complex constants related to downgoing and upgoing waves within the m^{th} lamina, and $[E_\pm^m]$ are the "vertical" propagation vectors,

$$\begin{aligned} [E_+^m(X_3)] &= \text{Diag}\left[e^{i\zeta_1(X_3-X_3^{m-1})}, e^{i\zeta_2(X_3-X_3^{m-1})}, e^{i\zeta_3(X_3-X_3^{m-1})}\right] \\ [E_-^m(X_3)] &= \text{Diag}\left[e^{i\zeta_1(X_3^m-X_3)}, e^{i\zeta_2(X_3^m-X_3)}, e^{i\zeta_3(X_3^m-X_3)}\right] \end{aligned} \quad (9)$$

The matrices, Q_{ij}^m and the other symbols appearing in equation (8) are defined below, omitting the superscript m for brevity.

$$\begin{aligned} [Q_{11}] &= \begin{bmatrix} i\xi_1 q_{11} & i\xi_1 q_{12} & 0 \\ i\xi_2 q_{21} & i\xi_2 q_{22} & i\zeta_3 \\ i\zeta_1 q_{21} & i\zeta_2 q_{22} & -i\xi_2 \end{bmatrix}, [Q_{12}] = \begin{bmatrix} i\xi_1 q_{11} & i\xi_1 q_{12} & 0 \\ i\xi_2 q_{21} & i\xi_2 q_{22} & -i\zeta_3 \\ -i\zeta_1 q_{21} & -i\zeta_2 q_{22} & -i\xi_2 \end{bmatrix} \\ [Q_{21}] &= \begin{bmatrix} -\rho A_5 \xi_1 \zeta_1 (q_{11} + q_{21}) & -\rho A_5 \xi_1 \zeta_2 (q_{11} + q_{22}) & \rho A_5 \xi_1 \xi_2 \\ -2\rho A_4 \xi_1 \zeta_1 q_{21} & -2\rho A_4 \xi_2 \zeta_2 q_{22} & -\rho A_4 (\xi_2^2 - \zeta_3^2) \\ \Delta_1 & \Delta_2 & 2\rho A_4 \xi_2 \zeta_3 \end{bmatrix} \\ [Q_{22}] &= \begin{bmatrix} \rho A_5 \xi_1 \zeta_1 (q_{11} + q_{21}) & \rho A_5 \xi_1 \zeta_2 (q_{11} + q_{22}) & \rho A_5 \xi_1 \xi_2 \\ 2\rho A_4 \xi_1 \zeta_1 q_{21} & 2\rho A_4 \xi_2 \zeta_2 q_{22} & \rho A_4 (\xi_2^2 - \zeta_3^2) \\ \Delta_1 & \Delta_2 & -2\rho A_4 \xi_2 \zeta_3 \end{bmatrix} \end{aligned}$$

$$\Delta_1 = \rho \left[(A_5 - A_3) \xi_1^2 q_{11} - (A_1 - 2A_4) \xi_2^2 q_{21} - A_1 \zeta_1^2 q_{21} \right]$$

$$\Delta_2 = \rho \left[(A_5 - A_3) \xi_1^2 q_{12} - (A_1 - 2A_4) \xi_2^2 q_{22} - A_1 \zeta_2^2 q_{22} \right]$$

$$q_{11} = A_3 b_1, \quad q_{21} = \omega^2 - A_2 \xi_1^2 - A_5 b_1, \quad q_{12} = A_3 b_2$$

$$q_{22} = \omega^2 - A_2 \xi_2^2 - A_5 b_2$$

$$\alpha = A_1 b_5, \quad \beta = (A_1 A_2 + A_5^2 - A_3^2) \xi_1^2 - \omega^2 (A_1 + A_5),$$

$$\gamma = (A_2 \xi_1^2 - \omega^2)(A_5 \xi_1^2 - \omega^2)$$

$$\begin{aligned} b_1 &= -\left(\frac{\beta}{2\alpha}\right) - \sqrt{\left(\frac{\beta}{2\alpha}\right)^2 - \frac{\gamma}{\alpha}}, \quad b_2 = -\left(\frac{\beta}{2\alpha}\right) + \sqrt{\left(\frac{\beta}{2\alpha}\right)^2 - \frac{\gamma}{\alpha}} \\ \zeta_1^2 &= -\xi_2^2 + b_1, \quad \zeta_2^2 = -\xi_2^2 + b_2, \quad \zeta_3^2 = -\xi_2^2 + (\omega^2 - A_5 \xi_1^2)/A_4 \end{aligned} \quad (10)$$

$$A_1 = \frac{c_{22}}{\rho}, A_2 = \frac{c_{11}}{\rho}, A_3 = \frac{c_{12} + c_{55}}{\rho}, A_4 = \frac{c_{44}}{\rho}, A_5 = \frac{c_{55}}{\rho} \quad (11)$$

The "vertical" wavenumbers ξ_i are subject to the restriction, $\text{Im}(\xi_i) \geq 0$, to insure the outgoing wave condition at infinity and exponential decay of the evanescent waves in the layers at high frequencies. In each layer, the "horizontal" wave numbers, ξ_1 and ξ_2 , are related to the global wave numbers, K_1 and K_2 , through

$$\begin{bmatrix} \xi_1 \\ \xi_2 \end{bmatrix} = \begin{bmatrix} \cos(\phi^m) & \sin(\phi^m) \\ -\sin(\phi^m) & \cos(\phi^m) \end{bmatrix} \begin{bmatrix} K_1 \\ K_2 \end{bmatrix}$$

The interface continuity conditions (5) can be expressed as

$$[\mathcal{Q}^m]_- \{C^m\} = -[\mathcal{Q}^{m+1}]_+ \{C^{m+1}\} \quad (12a)$$

where

$$\{C^m\} = \begin{bmatrix} C_+^m & C_-^m \end{bmatrix} \quad (12b)$$

$$[\mathcal{Q}^m]_+ = \begin{bmatrix} -L^m Q_{11}^m & -L^m Q_{12}^m E^m \\ -L^m Q_{21}^m & -L^m Q_{22}^m E^m \end{bmatrix} \quad (13a)$$

$$[\mathcal{Q}^m]_- = \begin{bmatrix} L^m Q_{11}^m E^m & -L^m Q_{12}^m \\ L^m Q_{21}^m E^m & -L^m Q_{22}^m \end{bmatrix} \quad (13b)$$

$$[E^m] = \text{Diag} \left[e^{i\xi_1 h^m}, e^{i\xi_2 h^m}, e^{i\xi_3 h^m} \right]$$

The subscript "+" in $[\mathcal{Q}^m]_+$ represents the upper interface of m^{th} lamina and the subscript "-" indicates the lower interface.

The 6N constants C_{\pm}^m , must be determined from the interface conditions (11) and the appropriate boundary conditions on the top and bottom surfaces of the plate. In order to illustrate the solution procedure, we first consider the case where a time dependent and distributed normal force is applied to the top surface of the plate as shown in Figure 1.

Denoting the force by $f(X_1, X_2, t)$ and its triple Fourier transform by $\hat{f}(K_1, K_2, \omega)$, the boundary conditions can be expressed as

$$\left[\hat{\varrho}^I \right]_+ \left\{ C^I \right\}_+ = \{ \hat{F} \} \quad \left[\hat{\varrho}^N \right]_- \left\{ C^N \right\}_- = \{ 0 \} \quad (14)$$

where $\{ \hat{F} \} = \{ f \ 0 \ 0 \}$, and

$$\left[\hat{\varrho}^I \right]_+ = \begin{bmatrix} -L^I Q_{21}^I & -L^I Q_{22}^I E^I \end{bmatrix}, \quad \left[\hat{\varrho}^N \right]_- = \begin{bmatrix} L^N Q_{21}^N E^N & L^N Q_{22}^N \end{bmatrix} \quad (15)$$

One possible approach toward the solution of the system of equations given by (11) and (15) is to use the so called Thomson-Haskell approach [10] based on an recurrence relation between the constants $\{ C^m \}$ and $\{ C^{m+1} \}$. However, this approach introduces the so-called precision problem in the numerical calculation and the solution becomes unstable at high frequencies. An alternate global matrix method, which is free from the precision problem, is used here by assembling the linear algebraic equations into the $6N \times 6N$ banded system as follows.

$$\left[\begin{array}{cccccc} \left[\hat{\varrho}^1 \right]_+ & 0 & \dots & & & \\ \left[\hat{\varrho}^1 \right]_- & \left[\hat{\varrho}^2 \right]_+ & 0 & \dots & & \\ & \ddots & \ddots & & & \\ \dots & 0 & \left[\hat{\varrho}^{m-1} \right]_- & \left[\hat{\varrho}^m \right]_+ & 0 & \dots & \\ & \dots & 0 & \left[\hat{\varrho}^m \right]_- & \left[\hat{\varrho}^{m+1} \right]_+ & 0 & \dots & \\ & & & & \ddots & \ddots & & \\ & & & & \dots & 0 & \left[\hat{\varrho}^{N-1} \right]_- & \left[\hat{\varrho}^N \right]_+ & \vdots & \\ & & & & \dots & 0 & \left[\hat{\varrho}^N \right]_- & \left[\hat{\varrho}^N \right]_+ & \vdots & \\ & & & & & & \vdots & & \vdots & \\ & & & & & & & \vdots & & \\ & & & & & & & & \vdots & \\ & & & & & & & & & 0 \end{array} \right] \left\{ \begin{array}{c} C^1 \\ C^2 \\ \vdots \\ C^m \\ \vdots \\ C^N \end{array} \right\} = \left\{ \begin{array}{c} \hat{f} \\ 0 \\ \vdots \\ \vdots \\ \vdots \\ 0 \end{array} \right\} \quad (16)$$

In the problem shown in Figure 1A, the boundary conditions at the top and bottom surfaces of the plate can be expressed in the form

$$\begin{aligned} S(0) &= \{ U_0 \ V_0 \ i\eta_0(1-R) \ 0 \ 0 \ -\rho\omega^2(1+R) \} \\ S(H) &= \{ U_H \ V_H \ i\eta_0 T \ 0 \ 0 \ -\rho\omega^2 T \} \end{aligned} \quad (17)$$

where U_0, V_0 are the horizontal and vertical components of the displacement on the top surface of the laminate, U_H, V_H are those at the bottom surface, η_0 is the vertical wavenumber of the acoustic waves, R is the reflection coefficient of the acoustic waves above the plate and T is the transmission coefficient below the plate. Equations (17) can be used to modify the linear system (16) and the reflection and transmission coefficients can be determined through its solution [9]. The reflected and transmitted waves can then be calculated in the frequency domain or in the time domain. Another quantity that can be calculated from the theory is the dispersion equation for guided waves that can be transmitted along the laminate in the form

$$G(\omega, v, c_{ij}^m, \rho^m, h^m) = 0 \quad (18)$$

where v is the velocity of the guided waves at frequency ω . Equation (18) is a nonlinear relation between the velocity of the multimode guided waves and the material properties of the laminate. For given laminate properties the dispersion curves can be determined from the equation. The dispersion curves can be determined accurately from the LLW experiment, and for unidirectional composites the experimental dispersion data can be inverted to provide accurate estimates of the matrix dominated properties of the composite.

If there is an onset of delamination in a small area A at the p^{th} interface, as shown in Figure 1C, then the first of equation (5) must be modified to

$$\left[\bar{u}_i(X_1, X_2, X_3^p, \omega) \right]^+ = D_i(\omega), \quad (X_1, X_2) \in A \quad (19)$$

where $[u]^+$ implies jump discontinuity in u , and $D_i(\omega)$ is the Fourier time transform of the discontinuity. For assumed forms of the discontinuity, equations (16) after appropriate modifications can again be solved to determine the wavefield produced in the laminate by the initiation or propagation of internal delaminations. Accurate measurement of the wave signals by means of surface mounted transducers can be used to locate and characterize damage initiation and propagation in aircraft and other structures under service loads.

3.2. APPROXIMATE THEORY FOR THIN LAMINATES

If the thickness of the laminate, H , is much smaller than the wavelengths, then the problem can be solved by approximate methods. It is well known that the classical plate bending theory of the plate underestimates the deflections as well as the stresses and overestimates the phase velocity of the propagating waves. The classical theory becomes more and more inaccurate at higher frequencies. Refined higher order theories have been developed by many authors in an effort to improve the accuracy of the approximate results [4]. The first order shear deformation theory retaining transverse shear and rotary inertia of the plate elements is used here. Assuming that the xy -plane is the mid-plane of the laminate, the displacement components within the laminate are assumed to be of the form

$$\begin{aligned} u(x, y, z) &= u_0(x, y) + z\psi_x(x, y) \\ v(x, y, z) &= v_0(x, y) + z\psi_y(x, y) \\ w(x, y, z) &= w_0(x, y) \end{aligned} \quad (20)$$

where (u_0, v_0, w_0) are the displacement components at a point in the mid-plane, and ψ_x and ψ_y are the rotations of a line element, originally perpendicular to the longitudinal plane, about the y and x axes, respectively. Then from the first shear deformation theory, the governing equations can be expressed as

$$\{L\}\{\Delta\} = \{f\} \quad (21)$$

where $\{\Delta\} = \{u_0, u_0, u_0, \psi_x, \psi_y\}$, \mathbf{f} is the applied force, $[L]$ is a matrix of differential operator with components,

$$\begin{aligned} L_{11} &= -A_{55}d_{11} - 2A_{45}d_{12} - A_{44}d_{22} + I_1 d_u \\ L_{12} &= A_{55}d_1 - A_{45}d_2, \quad L_{13} = -A_{45}d_1 - A_{44}d_2 \\ L_{22} &= D_{11}d_{11} + 2D_{16}d_{12} + D_{66}d_{22} - A_{55}I_3 d_u \\ L_{23} &= (D_{12} + D_{66})d_{12} + D_{16}d_{11} + D_{26}d_{22} - A_{45} \\ L_{33} &= 2D_{26}d_{12} + D_{22}d_{22} + D_{66}d_{11} - A_{44}I_3 d_u \end{aligned} \quad (22)$$

and we have used the notations $d_u = \frac{\partial^2}{\partial t^2}$, $d_1 = \frac{\partial}{\partial x}$, $d_2 = \frac{\partial}{\partial y}$, $d_{12} = \frac{\partial^2}{\partial x \partial y}$ etc.

The constants D_{ij} , A_{ij} and I_i are defined by the integrals through the thickness as

$$A_{ij} = \int_{-H/2}^{H/2} \bar{Q}_{ij} dz, B_{ij} = \int_{-H/2}^{H/2} z \bar{Q}_{ij} dz, D_{ij} = \int_{-H/2}^{H/2} z^2 \bar{Q}_{ij} dz, I_i = \int_{-H/2}^{H/2} \rho z^{i-1} dz \quad (23)$$

The global constitutive equations can be written as

$$\begin{bmatrix} \sigma_{11} \\ \sigma_{22} \\ \sigma_{33} \\ \sigma_{23} \\ \sigma_{31} \\ \sigma_{12} \end{bmatrix} = \begin{bmatrix} \bar{Q}_{11} & \bar{Q}_{12} & \bar{Q}_{13} & & \bar{Q}_{16} \\ \bar{Q}_{12} & \bar{Q}_{22} & \bar{Q}_{23} & & \bar{Q}_{26} \\ \bar{Q}_{13} & \bar{Q}_{23} & \bar{Q}_{33} & & \bar{Q}_{36} \\ 0 & & \bar{Q}_{44} & \bar{Q}_{45} & \\ 0 & & \bar{Q}_{45} & \bar{Q}_{55} & \\ \bar{Q}_{16} & \bar{Q}_{26} & \bar{Q}_{36} & & \bar{Q}_{66} \end{bmatrix} \begin{bmatrix} u_{1,1} \\ u_{2,2} \\ u_{3,3} \\ u_{2,3} + u_{3,2} \\ u_{1,3} + u_{3,1} \\ u_{1,2} + u_{2,1} \end{bmatrix} \quad (24)$$

where the global material constants \bar{Q}_{ij} are related to the local material constants Q_{ij} through the equations

$$\begin{aligned} \bar{Q}_{11} &= Q_{11}c^4 + 2(Q_{12} + 2Q_{66})c^2s^2 + Q_{22}s^4 \\ \bar{Q}_{12} &= (Q_{11} + Q_{22} + 4Q_{66})c^2s^2 + Q_{12}(c^4 + s^4) \\ \bar{Q}_{13} &= Q_{13}c^2 + Q_{23}s^2 \\ \bar{Q}_{16} &= -cs^3Q_{22} + c^3sQ_{11} - cs(c^2 - s^2)(Q_{12} + 2Q_{66}) \\ \bar{Q}_{22} &= Q_{11}s^4 + 2(Q_{12} + 2Q_{66})c^2s^2 + Q_{22}c^4 \\ \bar{Q}_{23} &= Q_{13}s^2 + Q_{23}c^2, \quad \bar{Q}_{33} = Q_{33} \\ \bar{Q}_{26} &= c^3sQ_{22} + cs^3Q_{11} - cs(c^2 - s^2)(Q_{12} + 2Q_{66}) \\ \bar{Q}_{36} &= (Q_{13} - Q_{23})sc, \quad \bar{Q}_{44} = Q_{44}c^2 + Q_{55}s^2 \\ \bar{Q}_{45} &= (Q_{55} - Q_{44})cs, \quad \bar{Q}_{55} = Q_{55}c^2 + Q_{44}s^2 \\ \bar{Q}_{66} &= (Q_{11} + Q_{22} - 2Q_{12})c^2s^2 + Q_{66}(c^2 - s^2)^2 \end{aligned} \quad (25)$$

In the above, $c = \cos \phi$ and $s = \sin \phi$, ϕ is the angle between local and global systems and the superscript label for the layer, m , has been dropped for convenience. In the case of plane stress on the 12-plane,

$$Q_{ij} = C_{ij} - \frac{C_{i3}C_{j3}}{C_{33}} \quad (26)$$

where C_{ij} is the stiffness constant of the material of the layer. If, in addition, the laminate is symmetric about the xy-plane, then the equation for the out-of-plane motion reduces to

$$\begin{bmatrix} L_{11} & L_{12} & L_{13} \\ L_{21} & L_{22} & L_{23} \\ L_{31} & L_{32} & L_{33} \end{bmatrix} \begin{Bmatrix} w_0 \\ \psi_x \\ \psi_y \end{Bmatrix} = \begin{Bmatrix} f \\ 0 \\ 0 \end{Bmatrix} \quad (27)$$

The solution of this equation can be obtained by the transform technique in the form

$$\begin{aligned} \bar{\psi}_x(x, y, \omega) &= \frac{1}{4\pi^2} \int_{-\infty}^{\infty} \int_{-\infty}^{\infty} \hat{\psi}_x(\xi_1, \xi_2, \omega) e^{i(\xi_1 x + \xi_2 y)} d\xi_1 d\xi_2 \\ \bar{\psi}_y(x, y, \omega) &= \frac{1}{4\pi^2} \int_{-\infty}^{\infty} \int_{-\infty}^{\infty} \hat{\psi}_y(\xi_1, \xi_2, \omega) e^{i(\xi_1 x + \xi_2 y)} d\xi_1 d\xi_2 \\ \bar{w}_0(x, y, \omega) &= \frac{1}{4\pi^2} \int_{-\infty}^{\infty} \int_{-\infty}^{\infty} \hat{w}_0(\xi_1, \xi_2, \omega) e^{i(\xi_1 x + \xi_2 y)} d\xi_1 d\xi_2 \end{aligned} \quad (28)$$

where $\bar{\psi}_x(x, y, \omega), \bar{\psi}_y(x, y, \omega), \bar{w}_0(x, y, \omega)$ are the Fourier time transforms of $\psi_x(x, y, \omega), \psi_y(x, y, \omega), w_0(x, y, \omega)$ respectively. Substitution from (27) into (20) results in a system of linear algebraic equations for the unknowns $\hat{\psi}_x, \hat{\psi}_y, \hat{w}_0$. The inversion into the frequency and time domains can be carried out as in the previous section. In the classical plate bending theory, $\psi_x = \psi_y = 0$, and the out-of-plane deflection of the plate due to a normal concentrated force $f(t)$ at the origin is given by the simple closed form expression,

$$\bar{w}_0(x, y, \omega) = \frac{F(\omega)}{4\pi^2} \int_{-\infty}^{\infty} \int_{-\infty}^{\infty} \frac{1}{D_{11}\xi_1^2 + 2(D_{12} + 2D_{55})\xi_1\xi_2 + D_{22}\xi_2^2} e^{i(\xi_1 x + \xi_2 y)} d\xi_1 d\xi_2 \quad (29)$$

where $F(\omega)$ is the Fourier transform of the forcing function $f(t)$. This integral can be evaluated to give the spectrum and its inversion by FFT gives the time history of the deflection.

4. Numerical Results

Equations (8) and (16) provide the formal solution for the displacement and stress components of the surface load problem in the triple transform domain. The inversion of the transformed quantities needs to be carried out for most problems of practical interest.

After C_{\pm}^m is determined from (16) for the impact loads and its modified form for the

LLW problem or the delamination problem the displacement and stress components in each lamina can be obtained from equation (8). Their frequency spectra are derived through evaluation of the wavenumber integrals and the time histories are determined through inversion of the spectra by means of FFT. The evaluation of the wavenumber integrals is complicated by the presence of the Rayleigh-Lamb poles and sharp spikes in the vicinity of the poles on the path of integration. The FFT inversion requires evaluation of the integrals at a large number of frequencies. An efficient and adaptive integration algorithm has been developed by the author's group - the details of the method can be found in Lih and Mal [4] and will not be repeated here. Numerical results are presented for a number of typical problems involving the three types of loading discussed in the previous section.

4.1. MATERIAL CHARACTERIZATION USING LEAKY LAMB WAVE DATA

A major objective of the LLW experiment, shown in Figure 1A, is to determine the elastic constants of the bulk composite material. The dispersion curves measured by this experiment can be inverted to yield accurate estimates of the matrix dominated elastic constants, c_{22} , c_{23} and c_{55} of the bulk composite material. The details of the experiment and the data inversion procedure can be found in Bar-Cohen, Mal and Lih [11]. The theoretical and experimental dispersion curves for Lamb waves for a unidirectional composite plate are shown in Figure 2. The dissipative properties of the material have negligible influence on the dispersion curves in the frequency range considered and were ignored in the theoretical model. The real elastic constants, determined through inversion of the LLW data using equation (18), are: $c_{11} = 161.31$ GPa, $c_{12} = 6.10$ GPa, $c_{22} = 13.90$ GPa, $c_{23} = 6.53$ GPa, $c_{55} = 7.26$ GPa. These values are substantially different from those calculated homogenization theories using the constituent properties of graphite and epoxy.

It should be noted that the dispersion curves in the frequency range used in the experiment are not very sensitive to the elastic constants, c_{11} , c_{12} , and the dissipation constants, p_0 , a_0 and ω_0 . Thus, the values of these parameters cannot be determined accurately from the measured dispersion curves. They require the use of time-of-flight or other data as discussed in Mal, Bar-Cohen and Lih [8] and in Bar-Cohen, Mal and Lih [11]. The waveforms recorded in a typical LLW experiment with incident angle 20° and three different fiber orientations on a 25 mm thick unidirectional graphite/epoxy laminate are shown in Figure 3 together with calculated results using the exact theory. The elastic constants and the damping parameters that gave the best visual fit between the theoretical and experimental signals are given by: $\rho = 1.59$ g/cc, $C_{11} = 160.7$ GPa, $C_{12} = 6.4$ GPa, $C_{22} = 13.9$ GPa, $C_{23} = 6.9$ GPa, $C_{55} = 7.1$ GPa, $p_0 = 0.01$, $a_0 = 0.3$, $\omega_0 = 0.6\pi$.

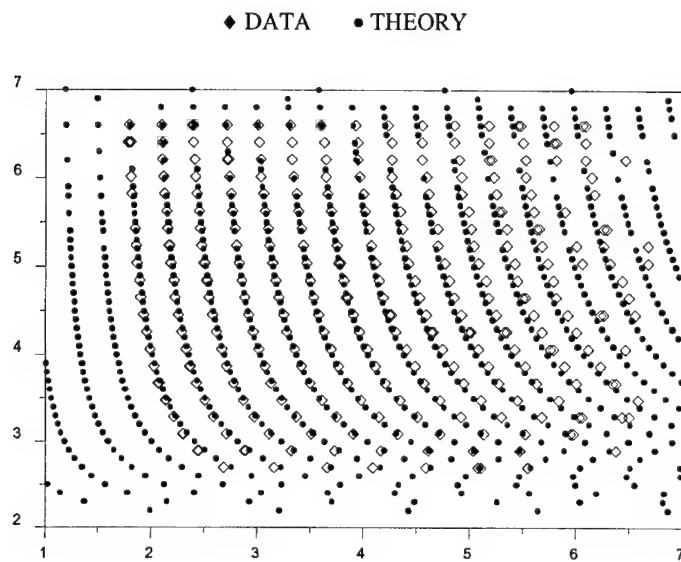


Figure 2. Dispersion data for a defect-free 16-ply unidirectional Gr/Ep laminate of thickness 2.8 mm and density 1.59 g/cc.

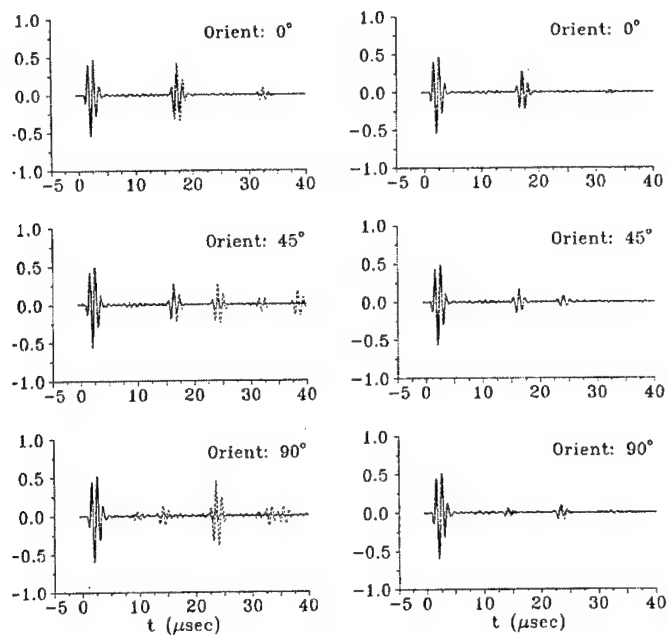


Figure 3. Reflected acoustic waves from a 25 mm thick unidirectional graphite/epoxy plate recorded in the LLW experiment are compared with those calculated from the theoretical model using perfectly elastic material in the left column) and dissipative material (right column).

4.2. DYNAMIC SURFACE LOAD ON A MULTILAYERED LAMINATE

The response of multilayered graphite/epoxy laminates with different ply configurations to a variety of dynamic surface loads has been calculated based on the exact and approximate theories described in Section 3 [4, 5]. The normal surface displacement produced in a 1 mm thick [0, 90]_s cross-ply laminate by a concentrated unit (1 kN) normal force on its surface is shown in Figure 4. The material properties of each lamina are assumed to be: $\rho = 1.58 \text{ g/cc}$, $c_{11} = 160.7 \text{ GPa}$, $c_{12} = 6.4 \text{ GPa}$, $c_{22} = 13.9 \text{ GPa}$, $c_{23} = 6.9 \text{ GPa}$, $c_{55} = 7.1 \text{ GPa}$, $p_0 = 0.005$, $a_0 = 0.1$, and $\omega_0 = 0.6\pi$. The time dependence of the force and its Fourier transforms are given by

$$f(t) = \sin \frac{2\pi t}{\tau}, \quad 0 < t < \tau \quad (30)$$

$$\begin{aligned} F(\omega) &= \frac{i\tau \sin(\omega\tau/2)}{\pi(1-\omega\tau/2\pi)} e^{-i\omega\tau/2}, \quad \omega \neq 2\pi/\tau \\ &= \frac{i\pi}{\omega} e^{-i\omega\tau/2}, \quad \omega = 2\pi/\tau \end{aligned} \quad (31)$$

where τ is the duration of the source.

The calculated results using the exact theory and the approximate laminate theory are compared in Figure 4 for different distances of propagation on a line oriented at 45° to the fibers. The duration of the source, τ , is assumed to take on the values 5 μsec and 0.5 μsec in the two cases shown in Figures 4A and 4B. It can be seen that for $\tau = 0.5 \mu\text{sec}$, (Figure 4B), that the high frequency oscillations in the exact solution are absent in the approximate solution. The oscillations are caused by the reflection of the waves at the interfaces and these are smeared out in the laminate theory. The agreement between the exact and approximate results is improved significantly at $\tau = 5 \mu\text{sec}$. The main pulse in the time domain solution is caused by the plate guided flexural waves and these are reproduced well in the approximate solution, but their speed is overestimated, resulting in their earlier arrival at larger distances. Interface delamination is a common problem in composite structures when they are subjected to foreign object impact.

Since delamination damage is often caused by the transverse stresses, σ_{13} , at the interfaces, their determination is of great interest in developing strategies for predicting this critical damage in the structure. The theory described in Section 3 can be used to determine the transverse interfacial stresses in multilayered laminates subject to distributed surface loads. An example of this is given in Figure 5, where the stress component, σ_{33} , at the topmost interface in a 1 mm thick [0, 45, -45, 90]_s quasi-isotropic graphite/epoxy laminate produced by a distributed normal load in a circular area on its surface is calculated. The spatial dependence of the load is assumed to be a Gaussian and its time dependence is the same as in equation (30), i.e.,

$$f(x_1, x_2, t) = e^{-(x_1^2 + x_2^2)} \sin(2\pi t/\tau), \quad (x_1^2 + x_2^2) < 1, \quad 0 < t < \tau \quad (32)$$

It can be seen that σ_{33} has the general shape of the sign reversed force with superposed high frequency oscillations, that are less prominent for propagation near 45° to the fibers in the top lamina.

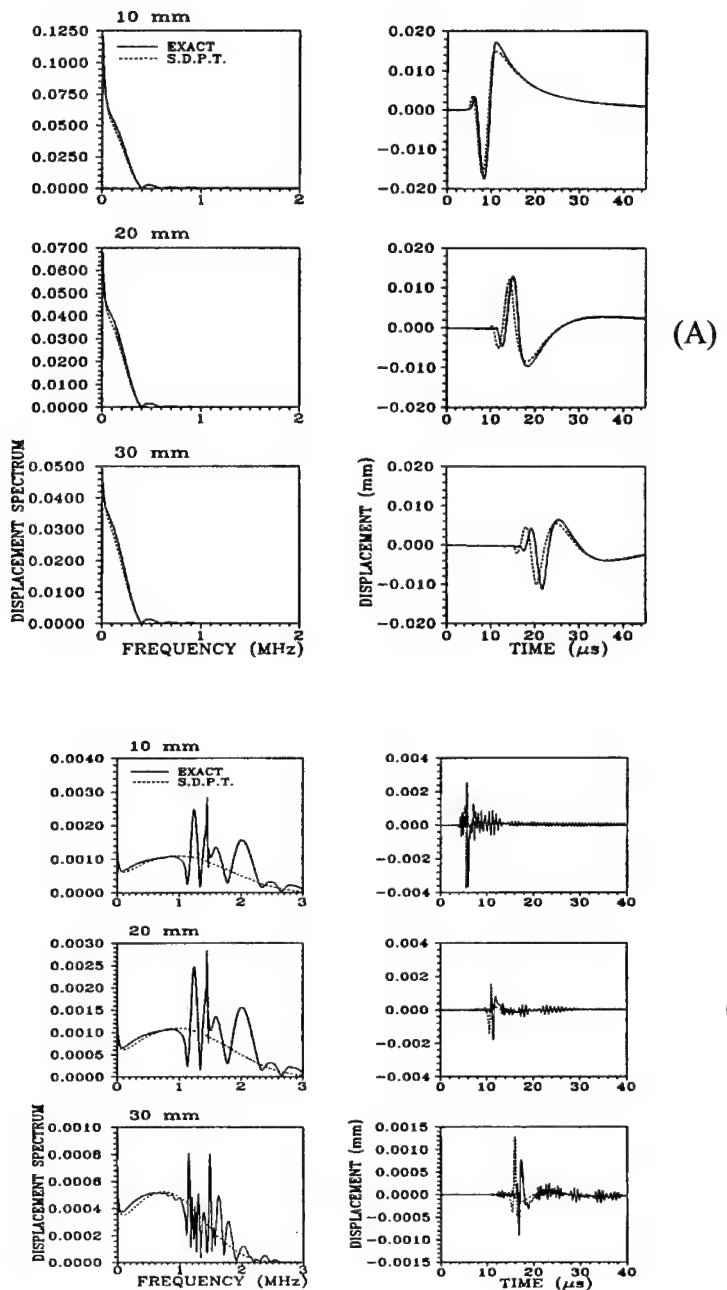


Figure 4. source Exact and approximate (SDPT) spectra and time histories of the normal surface displacement on a 1 mm thick $[0, 90^\circ]_s$ cross ply laminate due to a unit concentrated force normal to the surface. The displacements are at points along a line through the source at 45° to the top fibers at different distance form the source, a single cycle of sine wave of duration $5 \mu\text{sec}$ in (A) and $0.5 \mu\text{sec}$ in (B).

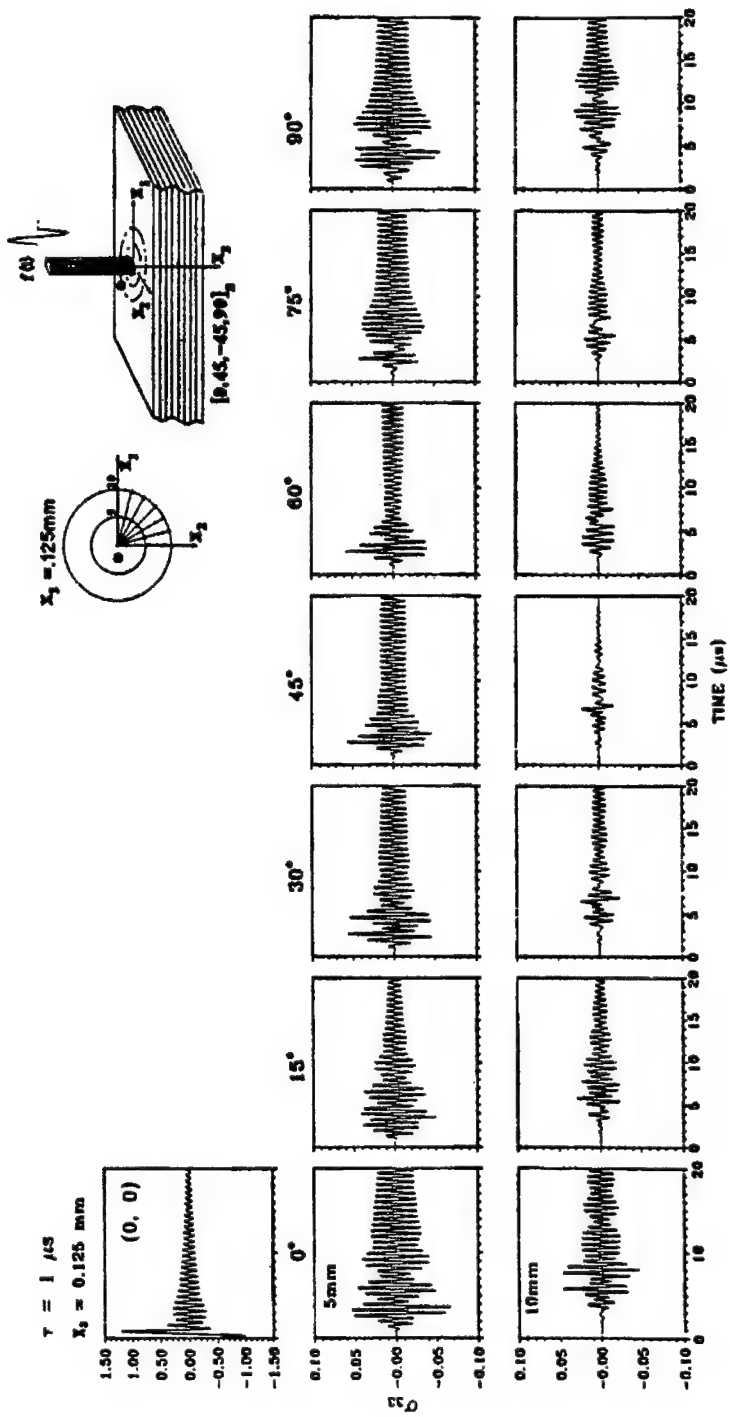


Figure 5. Time histories of the stress component, σ_{33} , at the first interface in a 1 mm thick $[0, 45, -45, 90]_4 s$ laminate subject to a distributed normal surface force given in equation (32) on a circle of radius 1 mm. The angles indicate the polar angle of the field point relative to the fibers in the top lamina.

4.3. RADIATION FROM INITIATION OF MICROFRACTURE

Composite materials are very sensitive to the presence of hidden flaws that may develop during their manufacturing, due to fatigue loading, and from foreign object impact during service. These defects, if undetected can grow to critical sizes, resulting in a serious degradation in the performance of composite structures and can compromise their safety. Thus, composite structures require careful monitoring of the initiation and growth of these flaws through nondestructive methods in order to insure their safety and integrity. At the present time periodic inspection and maintenance procedures are carried out on many aircraft and aerospace structures. These procedures are expensive and often unnecessary for a variety of reasons [see, e.g., 12]. Implementation of on-board continuous monitoring systems in defects critical structures can be very effective in dealing with this issue in aging as well as new structures. Recording and analysis of the elastic waves generated by crack initiation can be used to detect and characterize flaw initiation and growth in aircraft and aerospace structures. The basic idea behind such a system for a thin composite laminate used in aircraft components is described in this subsection.

A typical crack monitoring system is sketched in Figure 6. It consists of a number of broadband sensors attached to the surface of the laminate. The waves generated by initiation of a new crack or the extension of an existing crack is simultaneously recorded by the sensors and stored in a computer. The theory developed in Section 3 can be used to locate the initiation site and to characterize some of the properties of the crack in the laminate. It can be shown that if the distance of the field point is more than twice the laminate thickness, then the motion at the field point is dominated by the plate-guided, multimode Lamb waves, and the surface displacement can be expressed as a sum of these modes [6]. The number of modes depends on the dominant frequency of the source (i.e., its rise time) and the relative contributions from the modes depend on the detailed nature of the source including its location within the laminate.

In order to verify the accuracy of the approximate calculations, a pencil lead break source was used to generate and record the response on a unidirectional graphite epoxy plate of 1 mm thickness. The source can be represented by a vertical force, but its time dependence is not known a priori. The response of the measurement system is also unknown, as is the case with most such systems. The source time history modified by the system response was determined by measuring the surface Rayleigh wave response produced by the same source in a large aluminum block. The modified source time history is shown in Figure 6(a). The normal displacement generated by the source was then calculated using the theory. The measured and calculated results are compared in Figure 6 for three directions of propagation relative to the fibers. It can be seen that the agreement between the theoretical and experimental results are excellent in all three cases.

The radiation from the three major types of microfracture in thin multilayered composite laminates is considered next. A number of [0, 90]_s cross-ply graphite/epoxy laminate coupon specimens of thickness 0.125 mm and lateral dimensions 100 mm × 150 mm with embedded defects were prepared in an autoclave, and subjected to fatigue loading in a servohydraulic test frame [INSTRON 8501]. The waves generated by crack

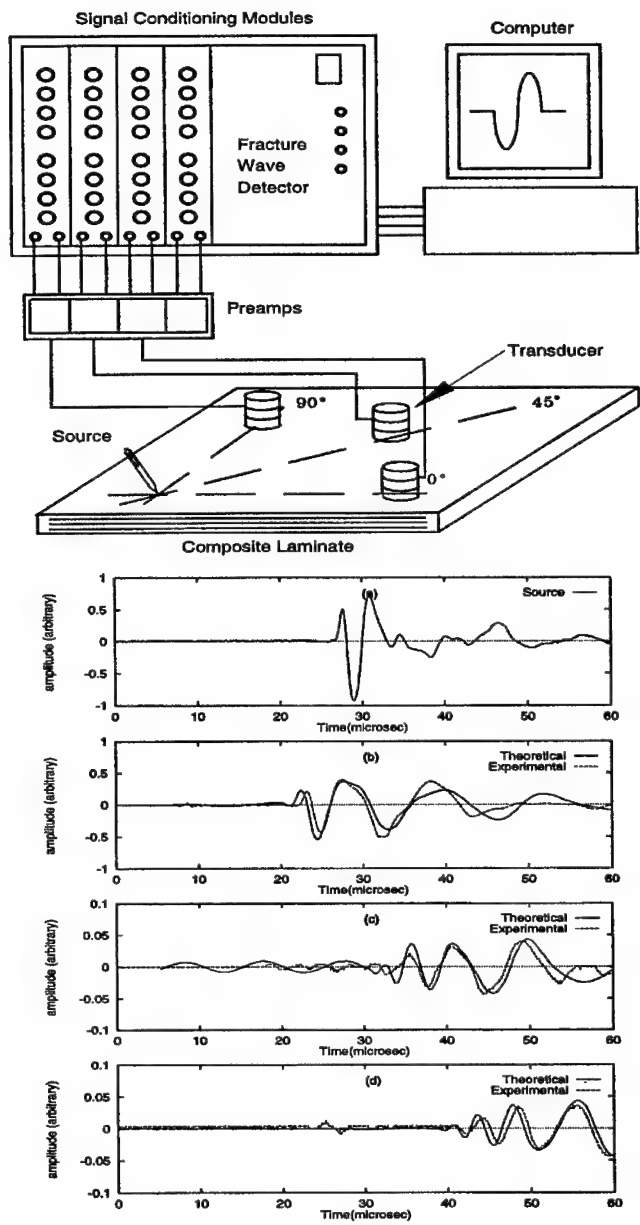


Figure 6. Top: the ultrasonic experimental setup. Bottom: (a) modified source function for the pencil lead break including the response of the recording system, the surface response at (b) 0°, (c) 45°, and (d) 90° to the fibers in a 1 mm thick unidirectional graphite/epoxy plate. Calculated results are based on the approximate thin plate theory.

initiation due to fiber break, matrix cracking and delamination, the three most common types of damage in composite materials, were recorded by four broadband sensors attached to the sample during the tests. The details of the sample preparation and testing procedure can be found in [6]. Theoretical calculations of the Lamb waves from the sources were carried out using the laminate theory outlined in Section 3.2. The source time function was assumed to be of the form

$$f(t) = \sin^2(\pi t / 2\tau) H(t - \tau) \quad (33)$$

where τ is the rise time of the source and $H(t)$ is the Heaviside step function.

The experimental and theoretical results are compared in Figure 7 for each type of damage initiation. The values of the rise time, τ , that produced the best visual fit to the data were 0.5 μ sec, 1.0 μ sec and 2 μ sec for fiber break, matrix cracking and delamination, respectively. It should be noted that there is very agreement between the calculated and measured displacements during the arrival of the main pulses from the source. The later arrivals in the experimental data are due to multiple reflections at the edges of the specimens and are not included in the theoretical model. Another noteworthy feature of the results is the differences in the nature of the signals due to the three source types. The wave motion due to fiber break and matrix cracking are primarily the symmetric or extensional modes while that due to delamination contains both symmetric and antisymmetric (or flexural) modes. The difference in the properties of the signals generated by the three types of damage can be used to identify the onset or growth of delaminations during service in composite structures. The time histories and the spectral amplitude of the signals generated by the initiation of fiber break, matrix cracking and shear delamination in the middle layer of a $[0, 90]_s$ laminate are shown in Figure 8. The differences in the properties of the signals are obvious - the first two types of damage generate mostly extensional waves of higher frequency, while the motion due to the delamination is dominated by flexural waves of lower frequency.

5. Concluding Remarks

The elastic waves generated by three classes of sources in composite laminates are investigated through laboratory experiments and theoretical models. The first source is a beam of acoustic waves incident on the laminate immersed in water, and is the basic feature in the so called Leaky Lamb Wave experiment. The dispersion curves of the plate-guided Lamb waves and the reflected acoustic waves were studied to determine the effective elastic constants and damping parameters of the material nondestructively. The second source is impact loading on the surface of the laminate, for which the surface displacement and internal transverse stress components were calculated by means of an exact and an approximate (laminate) theories. The accuracy of the approximate method was evaluated through comparison between the results obtained by the two methods. The third source is the initiation of three common types of damage, namely, fiber break, matrix cracking and delamination within the laminate. The signals produced by each type of damage were determined through laboratory experiments and theoretical modeling. The agreement between the two sets of results was found to be very good in all three cases. The differences in the signals generated by the three types of damage were

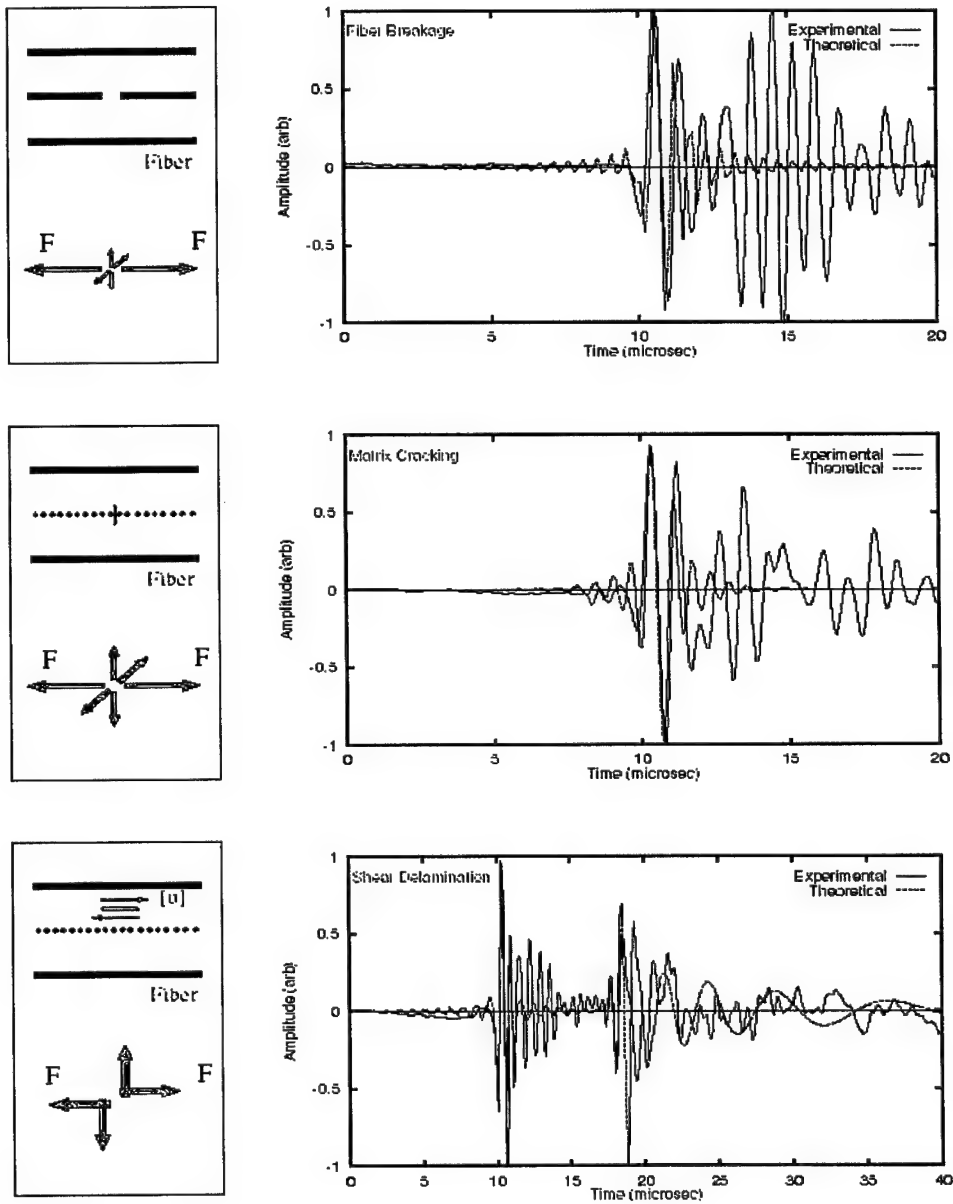


Figure 7. Theoretical and experimental waveforms on the surface of a $[0, 90]_s$ cross-ply composite due to three types of microfracture sources. The calculations are based on thin plate theory.

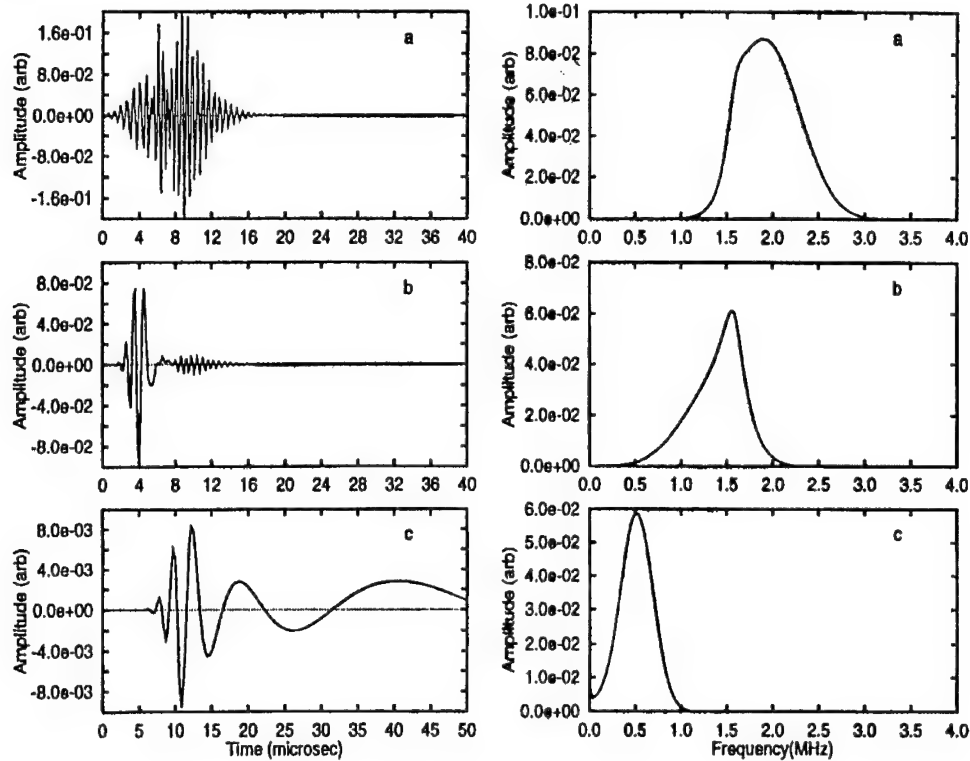


Figure 8. Predicted differences in the signals and their spectra generated by (a) fiber break, (b) matrix cracking, and (c) shear delamination, in a $[0, 90]_s$ cross-ply composite.

6. References

1. Abrate, S. (1998) *Impact on Composite Structures*, Cambridge University Press, New York.
2. Mal, A.K. and Lih, S.-S. (1992) Elastodynamic response of a unidirectional composite laminate to concentrated surface loads: Part I, *J. Appl. Mech.*, **59**, 878-886.
3. Lih, S.-S. and Mal, A.K. (1992) Elastodynamic response of a unidirectional composite laminate to concentrated surface loads: Part II, *J. Appl. Mech.*, **59**, 887-892.
4. Lih, S.-S. and Mal, A.K. (1995) On the Accuracy of approximate plate theories for wave field calculations in composite laminates, *Wave Motion*, **21**, 17-34.
5. Lih, S.-S. and Mal, A.K. (1996) Response of multilayered composite laminates to dynamic surface loads, *Composites B*, **29B**, 633-641.
6. Guo, D., Mal, A.K. and Ono, K (1996) Wave theory of acoustic emission in composite laminates, *J. Acoust. Emission*, **14**, S19-S46.
7. Mal, A.K. and Singh, S.(1991) *Deformation of elastic solids*, Prentice Hall, New Jersey.

8. Mal, A.K., Bar-Cohen, Y. and Lih, S.-S. (1992) Wave attenuation in fiber-reinforced composites, *Proceedings of International Conference on Mechanics and Mechanisms of Material Damping*, ASTM STP, **1169**, 245-261.
9. Mal, A.K., Yin, C.-C. and Bar-Cohen, Y. (1992) Analysis of acoustic pulses reflected from fiber-reinforced composites, *J. Appl. Mech.*, **59**, 136-144.
10. Mal, A.K. (1988) Wave propagation in layered composite laminates under periodic surface loads, *Wave Motion*, **10**, 257-266.
11. Bar-Cohen, Y., Mal A.K., and Lih, S.-S. (1993) NDE of composite materials using ultrasonic oblique insonification, *Materials Eval.*, **51**, 1285-1296.
12. Mal, A.K. (2000) The role of NDE in structural health monitoring of aircraft and aerospace structures, *SPIE Conf. on NDE of Aging Aircraft, Airports & Aerospace Hardware*, Newport Beach, California, **3994**, ix-xiii.
13. Haugse, E., Leeks, T.J., Ikegami, R., Johnson, P.E., Ziola, S.M., Doroghi, J.F., May, S. and Phelps, N. (1999) Crack growth detection and monitoring using broadband acoustic emission technique, *Nondestructive Evaluation of Aging Aircraft, Airports, and Aerospace hardware III*, Proceedings of SPIE Conference, Ajit Mal (ed), **3586**, 32 - 40.

THE METHOD OF GENERALIZED RAY APPLIED TO PLASTIC SOURCES*)

F. ZIEGLER

Department of Civil Engineering, Technical University of Vienna

Wiedner Hauptstr. 8-10/E201, A-1040 Vienna, Austria

Email: franz.ziegler@tuwien.ac.at

*) Dedicated in memoriam to Professor Dr. Dr.h.c. Ekkehart Kröner

Abstract. The expansion into plane waves of cylindrical or spherical waves propagating in a layered elastic half-space proves to be quite efficient for short observation times at a fixed receiver. Even the divergence effects of dipping interfaces of wedge-type layers are perfectly included by proper coordinate rotations and the exact "seismograms" are observed at a point receiver from any source located at the hypocenter. These nontrivial technique relies on invariance of the phase function and of the infinitesimal amplitude of the plane waves in the ray expansion. Recently, the concept of the elastic background was explored for the elastic-viscoplastic waves propagating in thin rods and extended to the 3-D problem of spherical waves with point symmetry. In that context and in an incremental formulation, the notion of plastic sources was used, which emit elastic waves in the background. Further, the dynamic generalization of Maysel's formula of thermo-elasticity to include all kinds of eigenstrains connected the dynamic stress Green's function of the background with the eigenstrain distribution by a convolution and the domain integral. The novel contribution of that paper to acoustic emission and monitoring of (layered) structures is the formulation of the full 3-D problems and the introduction of the generalized rays in the background considering an instantaneous oblique force point source.

Taking into account the progress in symbolic manipulation with integrated numeric such a formulation seems timely and may be competitive to the entirely computational Finite Element Method of analysis of signals received from plastic sources.

1. Introduction

Elastic-viscoplastic uniaxial waves in thin rods are considered by means of the elastic background with additional plastic sources acting in the transient, progressing plastic zone in [1] and [2]. A localized plastic source emits elastic waves in both directions of the rod if an increment of plastic strain (kept constant within a single cell of sufficiently small length) is caused within the time step. Causal superposition of the elastic wave pattern produced in the background by the external load and of the elastic waves

emitted from the plastic sources produces the fully nonlinear solution eventually including plastic shock fronts. The basic equations are in consecutive order, generalized Hooke's law, and the resulting nonhomogeneous wave equation of the axial displacement u

$$\dot{\sigma} = E(\dot{\varepsilon} - \bar{\varepsilon}) , \quad u_{,xx} - c^{-2}u_{,tt} = \bar{\varepsilon}_{,x}, \quad c^2 = E/\rho \quad (1)$$

Boundary conditions and the material law of the rod are understood to be given in the course of the full solution. The waves emitted from a concentrated unit plastic source,

$$\bar{\varepsilon}_{,x} = \delta_{,x}(x - \xi) \delta(t - \tau) \quad (2)$$

are, however, given by the stress influence function of the infinite rod. The force Green's function is a D'Alembert box-type wave of amplitude $c/2E$, hence, the stress takes on the form of two Dirac pulses propagating in opposite directions

$$\tilde{\sigma}(x, \xi; t, \tau) = \frac{c}{2} \left\{ \delta[x - \xi - c(t - \tau)] - \delta[x - \xi + c(t - \tau)] \right\} H(t - \tau) \quad (3)$$

Distributions of plastic sources render, the particular solution of the nonhomogeneous Eq. (1) takes on the integral form (of the dynamic and generalized Maysel's formula), homogeneous boundary conditions (b.c.) apply, - for convenience, the unit force is now applied at x , -note the displacement Green's function of a unit plastic source,

$$u^*(x, t) = \int_0^t d\tau \int_0^l \tilde{\sigma}(\xi, x; t, \tau) \bar{\varepsilon}(\xi, \tau) A d\xi , \quad \tilde{\sigma}(\xi, x; t) = \tilde{u}(x, \xi; t) . \quad (4)$$

The nonhomogeneous boundary conditions render the D'Alembert wave $u_0(x, t)$ that is a solution of the homogeneous wave equation, and thus, the total displacement becomes incrementally,

$$u = u_0(x, t) + u^*(x, t) \quad (5)$$

Figure 1 shows the Mach plane of the action of a single plastic source with a stress wave reflection at one finite boundary indicated, i.e. the stress Green's function of the infinite rod was used in Eq. (4) in that simple case. Thus, when monitoring the rod, development of plastic deformations can be identified by analysis of the observed signals (taking the time or spectral correlation), see Figure 2.

The three-dimensional wave propagation problem with point symmetry resulting from an explosion in a cavity of a viscoplastic material is analyzed by means of the background concept in [3] and [4], including the unloading phases. The spherical waves

when using the displacement potential, $u(R, t) = \phi_{,R}$, are the solution of the nonhomogeneous D'Alembert wave equation for $f(R, t) = (R \phi)$,

$$f_{,RR} - c_L^{-2} f_{,tt} = R \int P(R, t) dR ,$$

$$P = P_1 + P_2 , P_1 = \frac{2}{\kappa^2} \left(\bar{\varepsilon}_{R,R} + \frac{3}{R} \bar{\varepsilon}_R \right) , P_2 = \left(1 - \frac{2}{\kappa^2} \right) \bar{\varepsilon}_{,R} - \frac{2}{\kappa^2} \frac{\bar{e}}{R} , \kappa = c_L / c_S \quad (6)$$

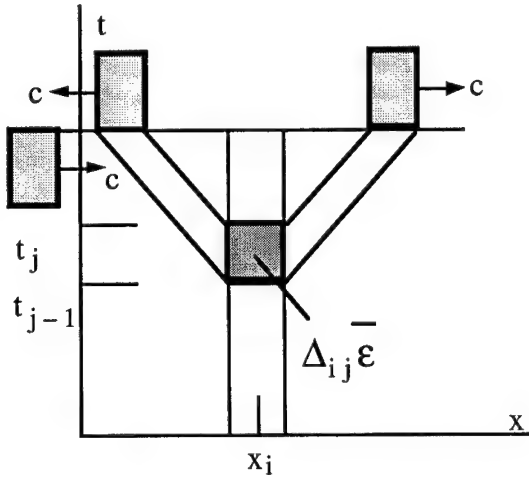


Figure 1. Acoustic emission from a local plastic source in a semi-infinite rod, stress wave shown.
Transducer in receiving mode during monitoring of the rod.

however, at the price of nonlocal plastic sources due to the integral of the forcing function. $P_2 = 0$, in case of classical incompressible plasticity dilatation $e = 0$. Considering such a discretized plastic source (distributed over a shell of thickness ΔR) of some proper time signature assigned, $\bar{\varepsilon}_R^{(k)} = \dot{F}(t) \delta(R - R_k)$, yields, after integrating P_1 ,

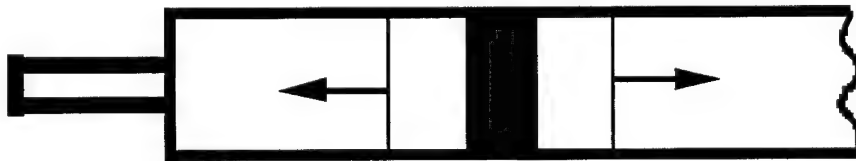


Figure 2: Monitoring an elastic-plastic rod with a transducer in receiving mode attached.

$$R \int P_1(R, t) dR = \frac{2 \dot{F}(t)}{\kappa^2} \left[\delta(R - R_k) + \frac{3R}{R_k} H(R - R_k) \right] \quad (7)$$

Updating of the plastic sources in space and time is done in a time stepping procedure by substituting the current state in the constitutive relations. For viscoplastic materials with a first order time evolution law of the plastic strain even a one-step Euler increment sufficiently well approximates the strength of the plastic sources (with no iterations necessary), see e.g. [5]. Ductile damage with growth of voids in the plastic zone is taken into account by means of Kachanov's damage parameter proportional to porosity (below the critical value), [6], without additional computational costs. A micromechanical foundation of the plastic source concept is given in [7]. Equation (7) provides the forcing terms of acoustic emission of a single plastic event for further processing the wave pattern analytically.

In the present paper the three dimensional localized plastic source is considered with respect to acoustic emission and, by domain integration, the extension to a plastic zone. The displacements of P- and S-body waves in the elastic background continuum, according to the Helmholtz decomposition and the definitions by the gradient and the curl of the potentials are associated to the wave-operators, and are produced by the given dynamic load and by the plastic sources. They are solutions of the nonhomogeneous p.d.e.,

$$\square_1 u_i^{(1)} = g_{,i}, \quad \square_2 u_i^{(2)} = e_{ijk} h_{kj}, \quad \square_{1,2} = c_{L,S}^2 \Delta - \frac{\partial^2}{\partial t^2}. \quad (8)$$

where

$$g c_S^{-2} = 2(\kappa^2 - 1) G_{i,i} - (\kappa^2 - 2) H_{ii,jj}, \quad \kappa = c_L / c_S, \quad h_i c_S^{-2} = -e_{ijk} G_{kj} \quad (9)$$

$$G_i = (U_{ik} + e_{irs} V_{sk,r})_{,k}, \quad H_{ij} = H_{ji} = -e_{jkl} V_{ik,l}, \quad (10)$$

with two (related) potentials, see e.g. Kröner [8] for details of that dislocation based analysis,

$$U_{ij,kk} = \overline{\epsilon}_{ij}, \quad V_{ij,kk} = e_{imn} U_{mj,n}, \quad \overline{G}_i = (U_{ik} - e_{irs} V_{sk,r})_{,k} \rightarrow \overline{G}_{i,j} = \overline{G}_{j,i} \quad (11)$$

In that connection in [9] the combined displacement influence function $\tilde{u}_{i(\alpha\beta)} = \tilde{u}_{i\alpha\beta}^{(1)} + \tilde{u}_{i\alpha\beta}^{(2)}$ are reported by considering a singular point source in the infinite background with body forces. The integral representation of the particular solution consequently results, valid in incremental form in the infinite background,

$$u_i^*(x, t) = \int_0^t d\tau \int_V \tilde{u}_{i(\alpha\beta)}(x, x_0; t - \tau) \overline{\epsilon_{\alpha\beta}}(x_0, \tau) dV(x_0). \quad (12)$$

Equation (12) is the basis of analysis of acoustic emission from phase transformations, see e.g. [10]. Analogous, Pao [11] used the Green's displacement dyadic to derive solutions for dynamic nuclei of strains (see the list of papers in acoustic emission there).

In [12], however, is the generalized dynamic Maysel's formula of thermoelasticity derived, see again Eq. (4) for the uniaxial case, that exhibits a more promising characteristic. It contains time convolution too, but it is complementary to Eq. (12) in the sense that it applies the dynamic force in the background at the point of observation and it holds good for finite bodies. In the incremental form, nonhomogeneous initial conditions are to be considered as well. In the time Laplace domain, a slightly different notation is introduced, part of the surface is free of traction, the remaining part has prescribed displacements, the contribution of the surface integral vanishes if the b.c. of the original and the auxiliary problem (of instantaneous single force loading) are identical,

$$\begin{aligned} u_i^*(\mathbf{x}_0; s) &= \int_V \overline{\varepsilon_{\alpha\beta}}(\mathbf{x}; s) \tilde{\sigma}_{\alpha\beta(i)}(\mathbf{x}, \mathbf{x}_0; s) dV(\mathbf{x}) \\ &+ \rho \int_V \left[\overline{u_{\alpha 0}}(\mathbf{x}) \dot{\tilde{u}}_{\alpha(i)}(\mathbf{x}, \mathbf{x}_0; s) + \overline{v_{\alpha 0}}(\mathbf{x}) \tilde{u}_{\alpha(i)}(\mathbf{x}, \mathbf{x}_0; s) \right] dV(\mathbf{x}) \end{aligned} \quad (13)$$

Acoustic emission of a single plastic event is merely given by the convolution contained in the first line of Eq. (13). Note the reciprocity of the influence functions of stress and displacement in Eqs. (12) and (13),

$$\tilde{\sigma}_{\alpha\beta(i)}(\mathbf{x}, \mathbf{x}_0; s) = \tilde{u}_{i(\alpha\beta)}(\mathbf{x}_0, \mathbf{x}; s) \quad (14)$$

2. The 3-D dynamic Green functions expanded in plane waves

Consequently, acoustic emission from a concentrated plastic source (in a single cell) should be observed primarily in Eq. (13) taking into account Eq. (14). However, the influence functions must be presented in a suitable form for inversion of the Laplace transform and for taking into account reflections on the traction-free surface of a half space, at the interface of a surface layer, at the surfaces of a plate or wedge wave guide, etc. The expansion into plane waves, i.e. the resulting generalized ray theory seems appropriate for short observation times. Subsequently, we suppress the tilde.

2.1 BASIC EQUATIONS

The Helmholtz decomposition of the displacements in a homogeneous and isotropic solid yields the set of wave equations for P- and S-waves, in absence of body forces,

$$\mathbf{u} = \text{grad } \phi + \text{curl } \boldsymbol{\psi}, \quad \Delta \phi = c^{-2} \ddot{\phi}, \quad \Delta \boldsymbol{\psi} = C^{-2} \ddot{\boldsymbol{\psi}}, \quad \text{div } \boldsymbol{\psi} = 0 \quad (15)$$

Furthermore the three components of stresses, given by Hooke's law enter the "internal" boundary value problems of vertical and horizontal single forces to be considered below

$$\begin{aligned}\sigma_{zz} &= \lambda c^{-2} \ddot{\phi} + 2\mu \left(\frac{\partial^2 \phi}{\partial z^2} + \frac{\partial^2 \psi_y}{\partial x \partial z} - \frac{\partial^2 \psi_x}{\partial y \partial z} \right), \\ \sigma_{zx} &= \mu \left[-C^{-2} \ddot{\psi}_y + 2 \left(\frac{\partial^2 \phi}{\partial x \partial z} - \frac{\partial^2 \psi_x}{\partial x \partial y} + \frac{\partial^2 \psi_y}{\partial x^2} \right) \right], \quad \sigma_{zy} = \mu \left[-C^{-2} \ddot{\psi}_x + 2 \left(\frac{\partial^2 \phi}{\partial y \partial z} - \frac{\partial^2 \psi_z}{\partial x \partial z} + \frac{\partial^2 \psi_x}{\partial z^2} \right) \right]. \quad (16)\end{aligned}$$

2.2 VERTICAL INSTANT SINGLE FORCE

Laplace-transformation in time, Fourier transformations with respect to the horizontal (x, y) coordinates, render the solution via the three conditions provided by the internal b. v. problem

$$z=0: \tilde{\sigma}_{zz}(\xi, \kappa, s) = -\frac{1}{2} \epsilon_z Q_z \bar{f}(s), \quad u_x = u_y = 0 \quad (17)$$

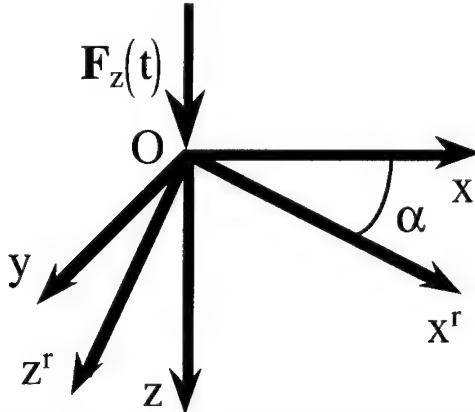


Figure 3. Vertical force in infinite space. Rotation of coordinates about the y -axis

in terms of the P- and S-wave potentials, expanded into plane waves and in the form of the Weyl-Sommerfeld integrals, the phase - time relationship has been indicated, note the simple form of the emittance functions, see also [13], [14] and [15],

$$\begin{aligned}\bar{\phi}^z(x, y, z, s) &= s^2 Q_z \bar{F}(s) \int_{-\infty}^{\infty} \int_{-\infty}^{\infty} S_P^z \exp(s g_P) d\xi d\kappa, \\ -t = g_P &= i\xi x + i\kappa y - \eta |z - z_0|, \quad \eta = \sqrt{c^{-2} + \xi^2 + \kappa^2}, \\ \bar{\psi}_j^z(x, y, z, s) &= s^2 Q_z \bar{F}(s) \int_{-\infty}^{\infty} \int_{-\infty}^{\infty} S_{Sj}^z \exp(s g_S) d\xi d\kappa, \\ -t = g_S &= i\xi x + i\kappa y - \zeta |z - z_0|, \quad \zeta = \sqrt{C^{-2} + \xi^2 + \kappa^2}, \quad j = x, y\end{aligned}$$

$$\bar{F}(s) = \bar{f}(s) / 8\pi^2 s^2 \rho, \quad S_P^z = -\epsilon_z, \quad S_{Sx}^z = -\frac{i\kappa}{\zeta}, \quad S_{Sy}^z = \frac{i\xi}{\zeta}, \quad \bar{\psi}_z^z(x, y, z, s) = 0 \quad (18)$$

The potentials, e.g. of Eq. (18), are easily referred to rotated coordinates, see Figure 3, by enforcing the following invariance conditions for the plane wave amplitudes and phases, P or S waves are understood,

$$\begin{aligned} S d\xi d\kappa &= S^r d\xi^r d\kappa, \quad -t = g = g^r = i\xi x + i\kappa y - (\eta, \zeta)|z| = i\xi^r x^r + i\kappa^r y^r - (\eta, \zeta)^r |z^r| \\ i\xi^r &= i\xi \cos \alpha - (\eta, \zeta) \sin \alpha, \quad i\kappa^r = i\kappa \end{aligned} \quad (19)$$

However, the transformed 3-dimensional solution cannot be interpreted to represent the potentials of the counter-rotated (horizontal) force by putting $\alpha = \pi/2$. Violation of the condition of axisymmetry is the major reason,- the interpretation holds true only for the 2-dimensional case of line loads, see again [13].

2.3 HORIZONTAL INSTANT SINGLE FORCES

The instantaneous forces are considered in the x - and y -directions and the internal b. v. problems yield alternated emittance functions, listed in Table 1,

$$\begin{aligned} z = 0: \tilde{\sigma}_{zx}(\xi, \kappa, s) &= -\frac{1}{2} \epsilon_z Q_x \bar{f}(s), \quad u_z = u_y = 0 \\ z = 0: \tilde{\sigma}_{zy}(\xi, \kappa, s) &= -\frac{1}{2} \epsilon_z Q_y \bar{f}(s), \quad u_z = u_x = 0 \end{aligned} \quad (20)$$

Table 1 Emittance functions of horizontal forces

| | | |
|--|---|-------------------------|
| $S_P^x = C^{-2} \frac{i\xi}{\eta} \frac{\eta}{\Delta_x}$ | $S_{Sx}^x = \epsilon_z \xi \kappa \frac{\eta - \zeta}{\Delta_x}$ | $S_{Sy}^x = \epsilon_z$ |
| $S_{Sz}^x = i \kappa \frac{\eta \zeta - \xi^2 - \kappa^2}{\Delta_x}$ | $\Delta_x = \eta (\zeta^2 - \xi^2) - \zeta \kappa^2$ | |
| $S_P^y = C^{-2} \frac{i\kappa}{\eta} \frac{\eta}{\Delta_y}$ | $S_{Sx}^y = -\epsilon_z, \quad S_{Sy}^y = -\epsilon_z \xi \kappa \frac{\eta - \zeta}{\Delta_y}$ | |
| $S_{Sz}^y = -i \xi \frac{\eta \zeta - \xi^2 - \kappa^2}{\Delta_y}$ | $\Delta_y = \eta (\zeta^2 - \kappa^2) - \zeta \xi^2$ | |

Putting alternatively $j = x, y$ in the displacement potentials, note the coupling by the characteristic determinants of the Eqs. (20),

$$\bar{\phi}^j(x, y, z, s) = s^2 Q_j \bar{F}(s) \int_{-\infty}^{\infty} \int_{-\infty}^{\infty} S_P^j \exp(s g_P) d\xi d\kappa \quad (21)$$

$$\begin{aligned} \bar{\psi}_x^j(x, y, z, s) &= s^2 Q_x \bar{F}(s) \int_{-\infty}^{\infty} \int_{-\infty}^{\infty} S_{Sx}^j \exp(s g_S) d\xi d\kappa \\ \bar{\psi}_y^j(x, y, z, s) &= s^2 Q_y \bar{F}(s) \int_{-\infty}^{\infty} \int_{-\infty}^{\infty} S_{Sy}^j \exp(s g_S) d\xi d\kappa \\ \bar{\psi}_z^j(x, y, z, s) &= s^2 Q_z \bar{F}(s) \int_{-\infty}^{\infty} \int_{-\infty}^{\infty} S_{Sz}^j \exp(s g_S) d\xi d\kappa \end{aligned} \quad (22)$$

and considering Table 1 renders the desired solutions. Note the vector potentials, now with all three components present.

2.4 THE OBLIQUE FORCE

Since a common time source function is understood in the above given solutions, Table 1, the potentials are summed to render the so called source ray. We note the emitted P- and S-waves, for a unit force just the direction cosines are substituted,

$$\begin{aligned} \bar{\phi}(x, y, z, s) &= s^2 \bar{F}(s) \int_{-\infty}^{\infty} \int_{-\infty}^{\infty} S_P \exp(s g_P) d\xi d\kappa, \quad S_P = Q_x \frac{i\xi}{C^2 \Delta_x} - Q_y \frac{i\kappa}{C^2 \Delta_y} - Q_z \epsilon_z, \\ \bar{\psi}_x &= s^2 \bar{F}(s) \int_{-\infty}^{\infty} \int_{-\infty}^{\infty} S_{Sx} \exp(s g_S) d\xi d\kappa, \quad S_{Sx} = Q_x \frac{\epsilon_z \xi \kappa (\eta - \zeta)}{\Delta_x} - Q_y \epsilon_z - Q_z \frac{i\kappa}{\zeta}, \\ \bar{\psi}_y &= s^2 \bar{F}(s) \int_{-\infty}^{\infty} \int_{-\infty}^{\infty} S_{Sy} \exp(s g_S) d\xi d\kappa, \quad S_{Sy} = Q_x \epsilon_z - Q_y \frac{\epsilon_z \xi \kappa (\eta - \zeta)}{\Delta_y} + Q_z \frac{i\xi}{\zeta}, \\ \bar{\psi}_z &= s^2 \bar{F}(s) \int_{-\infty}^{\infty} \int_{-\infty}^{\infty} S_{Sz} \exp(s g_S) d\xi d\kappa, \quad S_{Sz} = [\eta \zeta - (\xi^2 + \kappa^2)] \left[Q_x \frac{i\kappa}{\Delta_x} - Q_y \frac{i\xi}{\Delta_y} \right]. \end{aligned} \quad (23)$$

2.5 THE OBLIQUE SURFACE FORCE

Considering a transducer in the receiving mode at the traction free surface. Hence, buried source and receiver, where $z - z_0 > 0$, in the half-space are taken into account i.e. the direction factor is positive in the source ray, Eq. (23), and secondly, the reflected rays, (first segment pointing upwards) Pp and Ps, are superposed. In that solution, the limit of the source depth to zero is performed to render the proper emittance functions of the surface force, the reflection coefficients for potentials are derived in [16], see Fig. 4 for the P-source ray (further reflections are illustrated),

$$\overline{\varphi_p} = \overline{\phi}_0 + \lim_{z_0 \rightarrow 0} \left(\overline{\varphi_{Pp}} + \sum_k \overline{\varphi_{Skp}} \right), \quad S_p = S_{0p} + S_P R^{PP} + \sum_k S_{Sk} R^{SkP}, \quad k = x, y, z,$$

$$\bar{\psi}_{s,j} = \bar{\psi}_{0,j} + \lim_{z_0 \rightarrow 0} \left(\bar{\psi}_{P,s,j} + \sum_k \bar{\psi}_{S,k,s,j} \right), S_{s,j} = S_{0,s,j} + S_P R^{P,S,j} + \sum_k S_{S,k} R^{S,k,S,j} \quad (24)$$

$j = x, y, z$

Similarly, the force in a point source located in the interface between a surface layer and an underlying dissimilar half space is considered, however, the direction factor is negative. Since the acoustic signals emitted from any buried plastic source are received in an ultrasonic transducer at the surface, Eq. (24) represents the proper Green's functions. The Green's stress tensor at the location of the plastic source, i.e. at an interior point, is derived from Hooke's law which renders what is commonly called the stress receiver functions, note also the factors s in Table 2 and use $\operatorname{div} \psi = 0$. For completeness sake also the receiver functions of displacements are listed, derived from Eq. (15). Velocity and acceleration are received by multiplication with s or s^2 , respectively.

Table 2 Receiver functions at interior (plastic source) point, $\mu = \rho C^2$

| 3D-Displacements | D_j^P / s | D_j^{Sx} / s | D_j^{Sy} / s | D_j^{Sz} / s |
|---------------------|--|-------------------------------|---------------------------------|---------------------------------|
| u_x | $i\xi$ | 0 | $\varepsilon\zeta$ | $i\kappa$ |
| u_y | $i\kappa$ | $-\varepsilon\zeta$ | 0 | $-i\xi$ |
| u_z | $-\varepsilon\eta$ | $-i\kappa$ | $i\xi$ | 0 |
| 3D-stresses | Σ_{jk}^P / s^2 | Σ_{jk}^{Sx} / s^2 | Σ_{jk}^{Sy} / s^2 | Σ_{jk}^{Sz} / s^2 |
| σ_{xx} / μ | $\xi^2 - \zeta^2 + \kappa^2 - 2\eta^2$ | 0 | $2\varepsilon(i\xi)\zeta$ | $-2\xi\kappa$ |
| σ_{yy} / μ | $\xi^2 + \zeta^2 - \kappa^2 - 2\eta^2$ | $-2\varepsilon(i\kappa)\zeta$ | 0 | $2\xi\kappa$ |
| σ_{zz} / μ | $\xi^2 + \zeta^2 + \kappa^2$ | $2\varepsilon(i\kappa)\zeta$ | $-2\varepsilon(i\xi)\zeta$ | 0 |
| σ_{xy} / μ | $-2\xi\kappa$ | 0 | $2\varepsilon(i\kappa)\zeta$ | $-(\xi^2 - \zeta^2 + \kappa^2)$ |
| σ_{yz} / μ | $-2\varepsilon(i\kappa)\eta$ | $\xi^2 + \zeta^2 + \kappa^2$ | 0 | $2\varepsilon(i\xi)\zeta$ |
| σ_{zx} / μ | $-2\varepsilon(i\xi)\eta$ | $2\xi\kappa$ | $-(\xi^2 + \zeta^2 - \kappa^2)$ | 0 |

2.6 THE OBLIQUE INTERFACE FORCE

Buried source and receiver in a source layer, where $z - z_0 < 0$, are considered first, i.e. the direction factor is negative in the source ray, Eq. (23), and secondly, the reflected rays, (first segment pointing downwards) pP and pS, are superposed (the resulting rays of interest are propagating upwards). Three dimensional reflection coefficients of plane waves at the interface of two dissimilar half spaces are taken into account and the limit $z_0 \rightarrow h$ is understood. The phase functions are set up according to the two wave modes and the absolute vertical segment becomes $(h - z)$. In all these cases we end up with a fully coupled problem. Potentials of the reflected waves are

$$\overline{\varphi_{pP}} = s^2 \bar{F}(s) \int_{-\infty}^{\infty} \int_{-\infty}^{\infty} S_P R_{PP} \exp(s g_{pP}) d\xi d\kappa, \quad (25)$$

$$\overline{\psi_{pS,j}} = s^2 \bar{F}(s) \int_{-\infty}^{\infty} \int_{-\infty}^{\infty} S_P R_{PS,j} \exp(s g_{pS}) d\xi d\kappa,$$

$$\overline{\varphi_{s,kP}} = s^2 \bar{F}(s) \int_{-\infty}^{\infty} \int_{-\infty}^{\infty} S_{s,k} R_{s,kP} \exp(s g_{sP}) d\xi d\kappa,$$

$$\overline{\psi_{s,kS,j}} = s^2 \bar{F}(s) \int_{-\infty}^{\infty} \int_{-\infty}^{\infty} S_{s,k} R_{s,kS,j} \exp(s g_{sS}) d\xi d\kappa \quad (26)$$

Superposition yields

$$\begin{aligned} \overline{\varphi_p} &= \overline{\varphi_{0P}} + \lim_{z_0 \rightarrow h} \left(\overline{\varphi_{pP}} + \sum_k \overline{\varphi_{s,kP}} \right), \quad S_P = S_{0P} + S_p R_{PP} + \sum_k S_{s,k} R_{s,kP}, \\ \overline{\psi_{S,j}} &= \overline{\psi_{0S,j}} + \lim_{z_0 \rightarrow h} \left(\overline{\psi_{pS,j}} + \sum_k \overline{\psi_{s,kS,j}} \right), \quad S_{S,j} = S_{0S,j} + S_p R_{PS,j} + \sum_k S_{s,k} R_{s,kS,j} \quad (27) \end{aligned}$$

Using rotated coordinates according to a dipping layer in Eqs. (25) to (27) the oblique force acts on a dipping fault. The slowness are given by enforcing the invariance conditions (19).

The phases of the upward propagating reflected rays are considered in unrotated coordinates and their slowness is derived by another forward rotation according to Eq. (19). Rays received are grouped according to their last ray segment, P or S and according to their arrival times. A fast bottom produces refracted rays.

2.7 GREEN'S STRESS DYADIC RECEIVED IN AN INTERLAYER POINT

When considering a localized interlayer slip as a plastic source, it becomes necessary to substitute the Green's stress dyadic received at this point into Eq. (13). A transducer in the receiving mode is commonly situated at the traction free surface, i.e. the solution of section 2.5 applies, with a "receiver" situated within the surface layer, see again Fig. 4 for the P-source ray. The source ray, Eq. (24), with a positive direction factor, and the rays reflected at the interface, Eq. (25), are superposed. The result is similar to Eq. (27), however, the limit $z \rightarrow h$ of the depth of the buried receiver to the layer thickness is

performed. Again, a dipping interface requires rotated coordinates for the consideration of classical reflection.

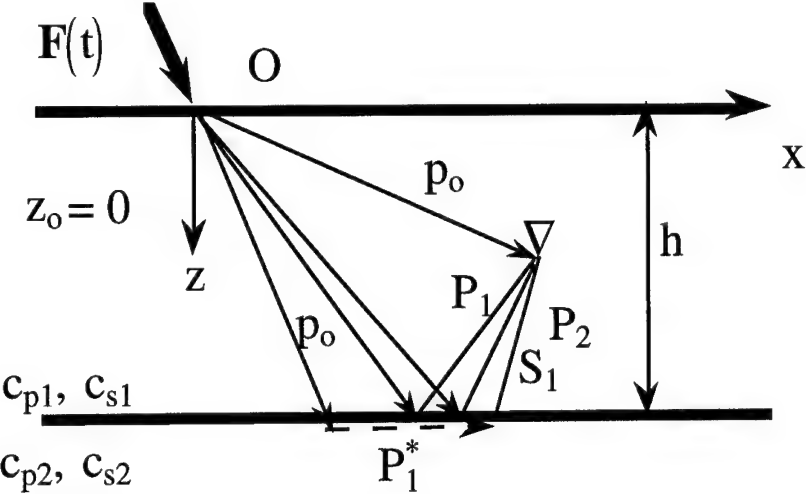


Figure 4: P-waves emitted from a surface force and received at a buried receiver (at a local plastic source). A plastic interlayer slip requires the limit of receiver depth taken to the layer thickness, Section 2.7.

3. Conclusions

Since the influence functions of displacements and stresses enter the generalized dynamic Mayssel's formula, receiver functions become the additional factors in the ray integrals together with higher powers of the Laplace transform variable s , see Eq. (16). For cylindrical waves, these functions are tabulated in [17], for spherical waves see Table 2. All necessary transformations of the Cagniard-de Hoop inversion technique are performed symbolically. Thus, the response of a single plastic source is fully accounted for by varying the receiver coordinates. To locate the plastic source emitting the acoustic signal by triangulation needs at least three separately placed transducers. The matrix notation introduced in the IUTAM selected landmark paper [13] is a starting point for such an enterprise. Identification of waves from plastic sources is of great importance in monitoring the safety of ductile structures eventually under the action of dynamic overload. The plastic interlayer slip, section 2.7, provides a special case of Eq. (13). Superiority of Eq. (13) over Eq. (12) or other classical convolution integrals, like the Mura-Willis integral, should be emphasized.

References

1. Irschik, H. and Ziegler, F.: Uniaxial Dissipative Elastic Waves Due to High Velocity Impact, in J.D. Achenbach, S.K. Datta, Y.S. Rajapakse (eds.), *Proc. IUTAM-Symp. on Elastic Wave Propagation and Ultrasonic Nondestructive Evaluation*, pp. 333-338, North-Holland, Amsterdam 1990.
2. Irschik, H. and Ziegler, F.: Dynamic processes in structural thermo-viscoplasticity, *AMR* **48** (1995), 301 - 316.
3. Ziegler, F., Irschik, H. and Holl, H.: Spherical Elastic-Plastic Waves. *J. Vibration and Control* **1** (1995), 345-360.
4. Fotiu, P.A. and Ziegler, F.: The Propagation of Spherical Waves in Rate-Sensitive Elastic-Plastic Materials, *Int. J. Solids and Structures* **33** (1996), 811 - 833.
5. Perzyna, P.: The constitutive equations for rate sensitive plastic materials, *Quart. Appl. Math.* **20** (1963), 321 - 332.
6. Lemaitre, J.: *A Course on Damage Mechanics*, Springer, Berlin, 1992.
7. Fotiu, P.A., Irschik, H. and Ziegler, F.: Micromechanical foundations of dynamic plasticity with applications to damaging structures, in O. Brüller et al (eds.), *Advances in Continuum Mechanics*, pp. 338 - 349, Springer , Berlin 1991.
8. Kröner, E.: Kontinuumstheorie der Versetzungen und Eigenspannungen, *Erg. Angew. Math.* **5**, Springer, Berlin, 1958.
9. Eringen, A.C.; Suhubi, E.S.: *Elastodynamics*. II, Academic Press, New York, 1975.
10. Simmons, J.A. and Wadley, H.N.G.: Theory of acoustic emission from inhomogeneous inclusions, in G.C. Johnson, (ed.), *Wave Propagation in Homogeneous Media and Ultrasonic Nondestructive Evaluation*, pp. 51-59, ASME, AMD-Vol. 62, New York 1984.
11. Pao, Y.-H.: Theory of acoustic emission, in Y.-H. Pao (ed.), *Elastic Waves and Non-Destructive Testing of Materials*, pp.107-128, ASME, AMD-Vol. 29, New York 1978.
12. Irschik, H., Fotiu, P.A. and Ziegler, F.: Extension of Maysel's Formula to the Dynamic Eigenstrain Problem, *J. Mech. Behavior of Materials* **5** (1993), 59-66.
13. Pao, Y.-H. and Gajewski, R. R.: The generalized ray theory and transient responses of layered elastic solids, in Mason, W. P. and Thurston, R. N. (eds.) *Physical Acoustics* **13**, Ch. 6, pp. 183-265, Academic Press, New York 1977.

Note: Reference [13], in the year 2000, was selected by IUTAM as a landmark paper.

14. Borejko, P. and Ziegler, F.: Pulsed asymmetric point force loading of a layered half-space, in Guran, A., Boström, A.A., Leroy, O. and Maze, G. (eds.), *Acoustic Interactions with Submerged Elastic Structures*, Part 4, Ch. 11. World Scientific, Singapore (in press)
15. Borejko, P. and Ziegler, F.: Influence of the dipping angle on seismic response spectra, in *Proc. Big Cities World Conference on Natural Disaster Mitigation*, pp. 73-92, Cairo University Publishing and Printing Center (1997/2229), Cairo 1998.
16. Borejko, P.: Reflection and transmission coefficients for three-dimensional plane waves. *Wave Motion* **24** (1996), pp. 371-393
17. Ziegler, F. and Irschik, H.: Elastic-plastic waves by superposition in the elastic background, *ZAMM* **80** (2000), Suppl. 1, pp. S109-S112.

On the Energy Release Rate from a Moving Dislocation and the Equation of Motion of a Dislocation

Xanthippi Markenscoff
Department of Mechanical and Aerospace Engineering
University of California, San Diego
La Jolla, CA 92093-0411
xmarkens@mae.ucsd.edu

Abstract

It is shown that the energy release rate for a moving dislocation may be obtained by using the energy flux through the slip-plane. This facilitates the calculation for the case of a general motion of the dislocation, since it requires only the $O(1)$ term in the near-field expansion of the resolved shear stress radiated by the dislocation, which is already obtained. This energy release rate is equated to the externally supplied energy-rate to give the equation of motion for a dislocation.

I. Introduction

The energy release rate of a moving dislocation may be calculated in a similar way as a moving crack. However, the dislocation is more singular than the crack with essential differences between the two. The energy release rate is very important in the sense that it is intimately related to the equation of motion of a dislocation. Here is calculated the energy release rate for a screw and edge dislocation jumping from rest to a speed v_d by

using a rectangular contour surrounding the dislocation and moving with it. The result is the same if the whole slip-plane is used for the calculation of the energy flux. Using the whole slip-plane, the energy release rate is calculated for moving dislocations (screw and edge) in general motion $x = \lambda(t)$. The energy rate that is required for this motion needs to be externally supplied, and this provides the equation of motion of the dislocation. Eshelby (1953) wrote a key paper on the equation of motion of a dislocation, but the question is too difficult and it has remained unanswered since then.

II. Energy – release rate from a dislocation jumping from rest to a constant velocity

In order to compute the energy radiated during the transient motion of the dislocation, we compute the rate at which energy passes through the surface S_d towards the core of the dislocation, which is (Freund 1972)

$$\mathbf{E} = \int_{S_d} \left\{ \sigma_{ij} n_j v_i + \left(\frac{1}{2} \sigma_{ij} u_{i,j} + \frac{1}{2} \rho v_i v_i \right) v_n \right\} dS \quad (1)$$

where σ_{ij} , u_i and v_i are the stress, displacement and particle velocity fields, respectively; n_j are the components of the unit outside normal n to S_d ; v_n is the component of the dislocation velocity in the direction of the normal n , and ρ is the density of the solid.

It has been shown in Clifton & Markenscoff (1981) that for a dislocation jumping from rest to a constant speed the integral (1) is independent of the shape of the contour. In Clifton & Markenscoff (1981) a circular contour was chosen. We will show here that the half-plane may be used as a contour, and this will facilitate the derivation of the energy release rate for a general motion of the dislocation. But first we will use a rectangle contour, so that the transition to the half-plane becomes apparent.

II.1 EDGE DISLOCATION

Let us choose a rectangular contour bounded by the lines: $x = \lambda - \delta$, $x = \lambda + \delta$ and

$$z = -\varepsilon, \quad z = \varepsilon, \text{ where } \lambda = \frac{t}{d}. \quad \text{Let}$$

$$x = \lambda + r \cos \theta, \quad z = r \sin \theta \quad (2)$$

Then we need to compute:

$$\mathbf{E} = \lim_{\varepsilon \rightarrow 0} \int_{\lambda - \delta}^{\lambda + \delta} [\sigma_{i3} \dot{u}_i(x, \varepsilon, t) - \sigma_{i3} \dot{u}_i(x, -\varepsilon, t)] dx \quad i=1,2,3 \quad (3)$$

The terms of interest are: $\frac{\partial u_x}{\partial t}, \frac{\partial u_z}{\partial t}, \sigma_{xz}, \sigma_{zz}$

and they are found by expansion of the expressions given in Markenscoff & Clifton (1981) around the current position of the dislocation. These near field expansions are along $z = \pm \varepsilon$, i.e. for ($d z = 0 = dr \sin \theta + r \cos \theta d\theta$) and for small ε :

$$\begin{aligned}
\frac{\partial u_x}{\partial t}(x, \pm \varepsilon, t) &= \frac{\Delta u}{\pi b^2} \left\{ -\frac{d \sqrt{1-\alpha^2} \sin \theta}{(1-\alpha^2 \sin^2 \theta)r} + \frac{d(2-\beta^2)\sqrt{1-\beta^2} \sin \theta}{2(1-\beta^2 \sin^2 \theta)r} + \dots \right\} \\
\frac{\partial u_z}{\partial t}(x, \pm \varepsilon, t) &= \frac{\Delta u}{\pi b^2} \left\{ \frac{-d^2(2-\alpha^2)}{\sqrt{1-\alpha^2}t} - \frac{d^2(4-6\beta^2+\beta^4)}{2\beta^2(1-\beta^2)^{3/2}t} + \dots \right\} \\
\sigma_{xz}(x, \pm \varepsilon, t) &= \frac{\Delta u}{\pi b^2} \mu \left\{ -\frac{2d^3(3-2\alpha^2)}{\sqrt{1-\alpha^2}t} + \frac{d^3(12-20\beta^2+7\beta^4)}{\beta^2\sqrt{(1-\beta^2)^3}t} + \dots \right\} \quad (4) \\
\sigma_{zz}(x, \pm \varepsilon, t) &= \frac{\Delta u}{\pi b^2} \mu \left\{ \frac{\lambda}{\mu} \frac{\alpha^2 \sin \theta}{\beta^2 \sqrt{(1-\alpha^2)^3}} - \frac{2d^2 \sqrt{(1-\alpha^2)^3} \sin \theta}{(1-\alpha^2 \sin^2 \theta)r} \right. \\
&\quad \left. + \frac{d^2(2-\beta^2)\sqrt{1-\beta^2} \sin \theta}{(1-\beta^2 \sin^2 \theta)r} + \dots \right\}
\end{aligned}$$

where α and b are the longitudinal and shear wave slownesses respectively,

$$\alpha = \frac{v_d}{c_1} = \frac{a}{d}, \quad \beta = \frac{v_d}{c_2} = \frac{b}{d}$$

The products $\sigma_{zz} \frac{\partial u_x}{\partial t}$, and $\sigma_{zz} \frac{\partial u_z}{\partial t}$ are odd functions of θ ; thus the two terms in

(3) corresponding to $z = \pm \varepsilon$ can be combined. Substituting (4) into (3) yields:

$$\begin{aligned}
&\left(\frac{\pi b^2}{\Delta u} \right)^2 \frac{1}{\mu} \text{E} = \lim_{\varepsilon \rightarrow 0} \frac{-2}{t} \int_{\tan^{-1}\frac{\varepsilon}{\delta}}^{\tan^{-1}\frac{\varepsilon}{\delta}} \left\{ -\frac{d^4 2(3-2\alpha^2)}{(1-\alpha^2 \sin^2 \theta)} \right. \\
&\quad \left. + \frac{d^4 (2-\beta^2)(3-2\alpha^2)\sqrt{1-\beta^2}}{2\sqrt{1-\alpha^2}(1-\beta^2 \sin^2 \theta)} + \frac{d^4 (12-20\beta^2+7\beta^4)\sqrt{1-\alpha^2}}{2(1-\alpha^2 \sin^2 \theta)\sqrt{(1-\beta^2)^3}} \right. \\
&\quad \left. - \frac{d^4 (2-\beta^2)(12-20\beta^2+7\beta^4)}{4(1-\beta^2)(1-\beta^2 \sin^2 \theta)} \right\} \\
&- \frac{\lambda}{\mu} \frac{a^2 d^2 (2-\alpha^2)}{(1-\alpha^2 \sin^2 \theta)} + \frac{\lambda}{2\mu} \frac{a^2 d^2 \sqrt{1-\alpha^2} (4-6\beta^2+\beta^4)}{(1-\alpha^2 \sin^2 \theta)\sqrt{(1-\beta^2)^3}}
\end{aligned}$$

$$\begin{aligned}
& + \frac{2d^4(2-\alpha^2)(1-\alpha^2)}{(1-\alpha^2 \sin^2 \theta)} - \frac{d^4(4-6\beta^2+\beta^4)\sqrt{1-\alpha^2}(1-\alpha^2)}{(1-\alpha^2 \sin^2 \theta)\sqrt{(1-\beta^2)^3}} \\
& \left. - \frac{d^4(2-\alpha^2)(2-\beta^2)\sqrt{1-\beta^2}}{\sqrt{1-\alpha^2}(1-\beta^2 \sin^2 \theta)} + \frac{d^4(4-6\beta^2+\beta^4)(2-\beta^2)}{2(1-\beta^2)\sqrt{1-\beta^2 \sin^2 \theta}} \right\} d\theta \tag{5}
\end{aligned}$$

$$\text{where } \frac{\mu}{\lambda+2\mu} = \frac{c_2^2}{c_1^2} = \frac{a^2}{b^2} \text{ and } \frac{\lambda}{\mu} = \frac{1}{\alpha^2}(\beta^2 - 2\alpha^2)$$

During the calculation of (3) it is observed that due to symmetry the $O\left(\frac{1}{r}\right)$ terms in the expansion near the dislocation do not contribute to the integral. This is expected considering that the coefficients of the $\frac{1}{r}$ terms is the steady-state solution with velocity the current velocity of the dislocation, and for steady-state motion no energy is required if the material is purely elastic.

Collecting terms and performing the integration in (5) yields:

$$E = \frac{\mu(\Delta u)^2}{2\pi \beta^2 t} \left\{ \frac{12-8\alpha^2}{(1-\alpha^2)^2} - \frac{(12-20\beta^2+7\beta^4)}{(1-\beta^2)^3} \right\} \tag{6}$$

This expression coincides with the one for circular contour obtained by Clifton and Markenscoff (1981).

II.2 SCREW DISLOCATION

We compute the energy release rate for a screw dislocation jumping from rest to a velocity \mathbf{v}_α based on a rectangular contour surrounding the dislocation. Let us choose a contour of sides 2ϵ in the z -direction and 2δ in the x direction centered at the current position of the dislocation. (See figure.)

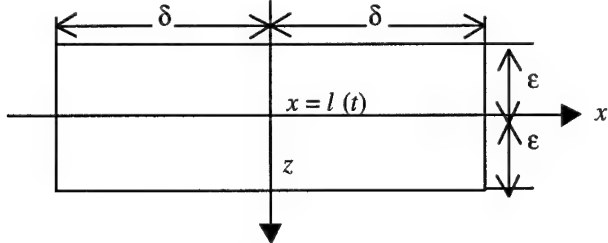


Figure 1

For a screw dislocation integral (1) becomes:

$$\mathbf{E} = \lim_{\delta \rightarrow 0} \lim_{\epsilon \rightarrow 0} \int_{\tan^{-1}\epsilon/\delta}^{\tan^{-1}\epsilon/\delta} \frac{\partial u_y}{\partial z} \frac{\partial u_y}{\partial t} d\theta \quad (7)$$

where $\frac{\partial u_y}{\partial z}$, $\frac{\partial u_y}{\partial t}$ are the expansions near the current position of the dislocation obtained by Clifton and Markenscoff (1981).

$$\frac{\partial u_y}{\partial z} = \left(\frac{\Delta u}{2\pi} \right) \left\{ \frac{-\cos\theta \sqrt{1-\beta^2}}{(1-\beta^2 \sin^2\theta)r} + \frac{d}{\sqrt{1-\beta^2 t}} - \frac{d}{t} \right\} \quad (8)$$

$$\frac{\partial u_y}{\partial t} = -\frac{\Delta u}{2\pi} \frac{\sin\theta \sqrt{1-\beta^2}}{d(1-\beta^2 \sin^2\theta)r}$$

Substituting (8) into (7) yields;

$$\begin{aligned} \mathbf{E} &= \mu \left(\frac{\Delta u}{2\pi} \right)^2 \left(\frac{\sqrt{1-\beta^2} - 1}{t} \right) \lim_{\delta \rightarrow 0} \lim_{\epsilon \rightarrow 0} \int_{\tan^{-1}\epsilon/\delta}^{\tan^{-1}\epsilon/\delta} \frac{d\theta}{1-\beta^2 \sin^2\theta} \\ &= \frac{\mu(\Delta u)^2}{2\pi t} \frac{\left(\sqrt{1-\beta^2} - 1 \right)}{\sqrt{1-\beta^2}} \end{aligned} \quad (9)$$

It may be observed that the limit $\delta \rightarrow 0$ is never taken, i.e. \mathbf{E} is independent of δ as long as $\epsilon/\delta \rightarrow 0$. This is important in allowing δ to extend from $-\infty, +\infty$ in x . It is also observed in both calculations for screw and edge, that only the $O(1)$ terms in the near field expansion contribute.

The above calculation of the integral in (5) for an edge dislocation is lengthy and tedious. It may be avoided by choosing a rectangular contour C with $\delta = \epsilon^{-n}$, $n < 1$, so that from

$$\begin{aligned} \mathbf{E} &= \lim_{\epsilon \rightarrow 0} \int_C \sigma_{ij} n_j d\gamma dx = \lim_{\epsilon \rightarrow 0} \frac{1}{\epsilon^n} \int_{\frac{1}{\epsilon^n}} \sigma_{ij}(x, \epsilon, t) n_j \delta_i(x, \epsilon, t) dx \\ &= \frac{\Delta u}{d} \int_{-\infty}^{\infty} \sigma_{xz}(x, 0, t) \delta(x - \lambda(t)) dx = \frac{\Delta u}{d} \sigma_{xz}(\lambda(t), 0, t) \end{aligned} \quad (10)$$

where it was taken into account that $\sigma_{nn} = 0$ at the upper and lower faces, and that the displacement is a step function discontinuity on the slip-plane.

Substituting $\sigma_{xz}(\lambda(t), 0, t)$ from (4) into (10) we obtain:

$$\mathbf{E} = \frac{\mu(\Delta u)^2}{2\pi t \beta^2} \left[\frac{12 - 8\alpha^2}{\sqrt{1 - \alpha^2}} - \frac{12 - 20\beta^2 + 7\beta^4}{\sqrt{(1 - \beta^2)^3}} \right] \quad (11)$$

which coincides with the circular and rectangular contours.

III. Energy release rate for a nonuniformly moving dislocation in general motion

When a dislocation is moving nonuniformly, i.e. with acceleration, then, unlike cracks, a logarithmic singularity appears that has as coefficient the current value of the acceleration of the dislocation. In case of a dislocation loop (Markenscoff & Ni, 1990) the coefficient also depends on the current value of the loop curvature.

This logarithmic singularity does not cancel by integration around the contour the way the $\frac{1}{\epsilon}$ singularity does. Actually the λn terms give rise to divergence of the integral, which is due to the strong step-function discontinuity of the core in the Volterra dislocation model.

However, in an approximation effort, one may cut-off the radius of the core at a distance r_o , and then the logarithmic term is treated as a constant term in the near field. This is consistent with other dislocation core models, such as the Peierls-Nabarro one (Hirth & Lothe, 1982). This constant term will be added to the $O(1)$ term that has to be computed by singular expansion of the integral that gives the radiated field from the moving dislocation as an integral over the history of the motion.

$$\begin{aligned} \frac{\partial u_y}{\partial z}(x, z, t) = & -\frac{\Delta u}{2\pi} \int_0^\infty \frac{(t-\eta(\xi))(x-\xi)^2 H(t-\eta(\xi)-rb)}{r^4 [(t-\eta(\xi))^2 - r^2 b^2]^{1/2}} d\xi \\ & + \frac{\Delta u}{2\pi} z^2 \frac{\partial}{\partial t} \int_0^\infty \frac{(t-\eta(\xi))^2 H(t-\eta(\xi)-rb)}{r^4 [(t-\eta(\xi))^2 - r^2 b^2]^{1/2}} d\xi - \frac{\Delta u}{2\pi} \frac{x}{x^2 + z^2} \end{aligned} \quad (12)$$

where $r^2 = (x-\xi)^2 + z^2$, and where $\eta(x)$ is the inverse of $l(t)$ and $t = \eta(x)$ describes the motion equivalently to $x = l(t)$.

The $O(1)$ term in the asymptotic expansion of (12) has been computed by Markenscoff (2000). For the equation of motion of a dislocation the energy rate given by \dot{E} in (3) must be provided by an external agent. Finding the motion $\lambda(t)$ from this can be done only numerically.

Acknowledgement

This research was supported by the National Science Foundation, Grant Number CMS-9734939.

References

- Clifton, R.J., and X. Markenscoff, Elastic Precursor Decay and Radiation From Nonuniformly Moving Dislocation, *Journal of the Mechanics and Physics of Solids*, Vol.29, No.3, pp.227-251. (1981)
- Eshelby, J.D., Uniformly Moving Dislocations, *Proc. Phys. Soc. Lond.* 62A, pp. 307-314. (1949)
- Freund, L.B., Energy Flux into the Tip of an Extending Crack in an Elastic Solid. *J.Elasticity* 2, 341-349 (1972)
- Hirth, J.P. and J. Lothe, *Theory of Dislocations* (2nd Ed.), Wiley Interscience (1982)
- Markenscoff, X., The Equation of Motion and the Near-Field of a Nonuniformly Moving Dislocation, *J. Elast.*, (under revision) (2000).

Markenscoff, X. and R.J. Clifton, The Nonuniformly Moving edge Dislocation, *Journal of the Mechanics and Physics of Solids*, Vol.29, No.3, pp.253-262 (1981).

Ni., L. and Markenscoff, X., The Singular Nature of the Stress Field Near an Arbitrarily Moving Dislocation Loop, *Journal of the Mechanics & Physics of Solids*, vol 38, pp. 481-490 (1990).

BACKSCATTERING OF BULK WAVES FROM A SURFACE-BREAKING CRACK UNDER A COMPRESSIVE STRESS

CLAUDIO PECORARI

Institute for Advanced Materials
European Commission
PO BOX 2, 1755 ZG Petten
The Netherlands

Abstract

A recent investigation into the scattering of a Rayleigh wave from a one-dimensional surface-breaking crack under a compressive stress field has shown the occurrence of a surprising phenomenon. When the crack depth is of the order of a wavelength or larger, and the compressive stress is lower than a characteristic value, a significant increase of the reflected signal is predicted theoretically and observed experimentally. The purpose of this work is to extend the previous investigation to the case when the incident field is either a longitudinal or a shear wave.

The effect of the compressive stress on the scattering event is modeled by using the quasi-static approximation for two rough surfaces in contact. The spring elastic constants K_N and K_T , which simulate the macroscopic elastic behavior of the contacting crack faces, may vary along the crack faces. This additional degree of freedom allows the model to consider situations where the crack is either uniformly partially closed along its whole extent, or partially closed at its tip, or at its mouth only. The scattered field is evaluated in its far-field zone. The dependence of the backscattered signal on i) the intensity and spatial dependence of the compressive stress, ii) the direction of incidence of the inspecting ultrasonic wave, and iii) the normalized crack depth is investigated, and possible implications for the detection and characterization of the partial closure of a surface-breaking crack is discussed.

1. Introduction

During the last twenty years, the scattering of elastodynamic waves by cracks has been investigated extensively by many authors both theoretically and experimentally. In particular, considerable attention has been given to the description of elastodynamic wave scattering by surface-breaking cracks. Datta (1979) presented a model of the diffraction of an antiplane shear wave by an edge crack, which is valid in the low frequency limit. Stone, Gosh, and Mal (1980) extended Datta's work on scattering of shear horizontal (SH) waves to moderate and high frequencies by solving an integral

equation for the crack opening displacement (COD) first, and, then, providing expressions for the scattered wave in the far-field region.

To the best of this author's knowledge, Achenbach, Keer, and Mendelsohn (1980) and Mendelsohn, Achenbach and Keer (1980) were the first to describe the scattering of surface (Rayleigh) and bulk waves from an open, surface-breaking crack. They formulated the problem in terms of two uncoupled integral equations for the COD's gradients, also known as dislocation densities. A ray analysis of the same problem was presented by Achenbach, Gautesen, and Mendelsohn (1980). The latter work, however, neglected the radiation of bulk waves from the crack tip. Kundu and Mal (1981) considered the problem of an open crack, insonified by both surface and bulk waves, breaking the surface of a plate. They provided high-frequency solutions to these problems following the same approach adopted by Achenbach, Gautesen, and Mendelsohn (1980), except that the analysis by Kundu and Mal (1981) accounted also for the bulk waves radiated by the crack tip. The validity of these theoretical models was tested experimentally by Vu and Kinra (1985), and Tittmann, Ahlberg, and Mal (1986). Vu and Kinra (1985) considered a surface-breaking crack insonified by an incident Rayleigh wave at normal incidence. They measured the scattered field at low, intermediate, and high frequencies along the surface containing the scatterer. The experimental measurements were found to agree well with the theoretical predictions. Tittmann, Ahlberg, and Mal (1986) focused their work on the high frequency results, and, in particular, they measured the amplitude of the bulk waves radiated by the tip of a crack insonified by an incident Rayleigh wave. The experimental results supported the theoretical prediction of Kundu and Mal's analysis. Angel and Achenbach (1984) extended the modeling of scattering of Rayleigh waves by open, surface-breaking cracks to include the case of oblique incidence. The model was validated by Achenbach, Komsky *et al.* (1992) by employing a self-calibrating ultrasonic technique to measure the ratio between the transmission and reflection coefficients as a function of the normalized crack depth at several values of the angle of incidence. Finally, Zhang and Achenbach (1988) considered the scattering of a Rayleigh wave by a surface-breaking crack which is inclined with respect to the surface that contains it. A boundary element method was used to solve the integral equations for the COD, and values for the reflection and transmission coefficient of the incident Rayleigh wave were given as functions of the angle between the crack and the normal to the surface, and of the normalized frequency.

The effect of the partial closure of a crack on the wave scattering properties of a crack has been investigated to a lesser extent. A literature review on this subject was recently presented by Pecorari (2000), who also extended the work by Achenbach, Keer, and Mendelsohn (1980) and Mendelsohn, Achenbach and Keer (1980) to the case of Rayleigh wave scattering by a surface-breaking crack which is partially closed by a compressive stress field. The partial closure of the crack faces was modeled by invoking a quasi-static approximation (QSA) according to which the macroscopic elastic response of the crack to an incident wave can be described by means of a continuous distribution of normal and tangential springs. Within the framework of the QSA, the components of the total stress applied to the crack faces produce a discontinuity of the displacement components according to the well-known boundary conditions,

$$\sigma_{xx}(x = 0^+, z) = \sigma_{xx}(x = 0^-, z) = K_N [u(x = 0^+, z) - u(x = 0^-, z)], \quad (1)$$

$$\sigma_{xz}(x = 0^+, z) = \sigma_{xz}(x = 0^-, z) = K_T [v(x = 0^+, z) - v(x = 0^-, z)]. \quad (2)$$

In Eq. (1) and Eq. (2), the first equality enforces the continuity of the total stress components, σ_{xx} and σ_{xz} , across the crack faces placed at $x = 0$ and extending into the material to a depth $z = h$. The second equality in both equations relates the applied stress to the displacement discontinuity across the crack faces via a quantity, K_N or K_T , that represents the stiffness of the distributed springs. Following the results of several investigations by Buck, Rehbein, Thompson (1987 and references therein), provision was made for the spring stiffness constants K_N and K_T to vary along the crack faces. An essential component of the model was the choice of the ratio K_T/K_N , which experimental evidence shows being of the order of 0.5 (Nagy (1992)), slowly increasing with increasing strength of the applied stress. Alternatively, a ratio close to unity can be expected between two rough surfaces showing a high degree of conformity, as may be the case of the faces of fatigue cracks. For values of the ratio K_T/K_N of the order of 0.5, and for surface-breaking cracks with depth larger than half a wavelength of the incident Rayleigh wave, a surprising and considerable increase up to 40 percent of the reflection coefficient was predicted (see Fig. 1). These results were obtained for a surface-breaking crack in an aluminum half-space characterized by the following properties: longitudinal wave velocity, $C_L = 6286 \text{ ms}^{-1}$, shear velocity, $C_T = 3195 \text{ ms}^{-1}$, mass density $\rho = 2.7 \cdot 10^3 \text{ kg m}^{-3}$. Experimental results supporting the model predictions were also presented.

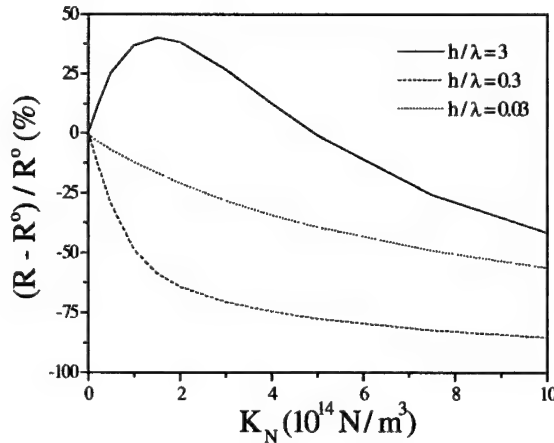


Figure 1. Relative variation of the reflection coefficient of an incident Rayleigh wave vs. K_N for a crack that is partially and uniformly closed. Three values of the normalized crack depth, h/λ_R , are considered: 0.03, 0.3, and 3.0. The frequency of the incident and scattered wave is equal to 4 MHz.

In this work, elastodynamic scattering by a surface breaking crack with faces in partial contact is extended to the case of longitudinal and shear incidence. The dependence of the backscattered signal on systems parameters such as the intensity and spatial dependence of the compressive stress, the direction of incidence of the inspecting ultrasonic wave and the normalized crack depth is investigated. Possible implications for the detection and characterization of a surface-breaking crack are also discussed.

2. Theory

Following the approach presented by Achenbach, Keer, and Mendelsohn (1980) and Mendelsohn, Achenbach and Keer (1980), the mathematical formulation of the problem of interest is expressed via two uncoupled integral equations of the first kind for the gradients of the COD caused by the incident wave. To this end, the same equation of motion and the same boundary conditions discussed in Pecorari (2000) are utilized. In this work, the stress carried by the incident field comprises the contributions of the primary field, i.e., the bulk plane wave propagating from infinity towards the cracks, and of the plane waves reflected by the stress-released surface containing the crack (see Neerhoff (1980)).

Once the COD of the crack faces is calculated, the far-field amplitude of the scattered bulk waves can be evaluated by using the asymptotic expansion of the integral representation of the scattered field (Neerhoff (1980)). Expressions for the cylindrical longitudinal and shear components of the scattered field are found in this way. Adhering to Neerhoof's notation as far as possible, the field radiated from the crack into the bulk of the host material can be written as follows,

$$u_{\alpha}^{rad}(r, \hat{e}) \equiv \frac{1}{4} \sqrt{\frac{2}{\pi k_p r}} \exp\left(ik_p r - \frac{1}{4}i\pi\right) P_p(\hat{e}) \hat{e}_{\alpha} + \frac{1}{4} i \sqrt{\frac{2}{\pi k_s r}} \exp\left(ik_s r - \frac{1}{4}i\pi\right) P_s(\hat{e}) \varepsilon_{\alpha\gamma 2} \hat{e}_{\alpha}, \quad (3)$$

where, r is the distance between the mouth of the crack and the observation point located in the far-field, \hat{e} is the unit vector pointing along the position vector of the observer, k_p and k_s are the wavenumbers of the longitudinal and shear waves, respectively, and, finally, $P_{P,S}(\cdot)$ are the characteristic functions for the longitudinal (P) and shear (S) waves, respectively. These quantities can be calculated using the following integral,

$$P_{P,S}(\hat{e}) = \int_0^h \Delta u_{\alpha} \partial_{\alpha\beta} B_{\beta}^{P,S}(z, \hat{e}) dz. \quad (4)$$

In eq. (4), $\partial_{\alpha\beta} B_{\beta}$ represent the far-field components of the Green's stress tensor, and Δu_{α} is the α -th component of the COD. Thus, through Δu_{α} the characteristic functions depend on the angle of incident of the exciting wave, and on the interfacial conditions between the crack faces. The integration is performed along the crack depth. Thus, the

characteristic functions contain the dependence of the scattered amplitude on all the system parameters except for the distance of the observation point from the scatterer, r . In this work, numerical results are presented for the characteristic function of the scattered bulk waves having the polarization and wave (propagation) vectors parallel to the analogous quantities of the incident wave. For the sake of simplicity, in the following the characteristic function is referred to as backscattered amplitude. The mechanical properties of the host material are those used in Pecorari (2000) and reported above.

Numerical Results

Figure 2 illustrates the dependence of the longitudinal backscattered amplitude on the angle of incidence at an ultrasonic frequency of 2.25 MHz. Figure 2a refers to a crack having a normalized depth $h/\lambda_T = 0.3$, while Figure 2b refers to a crack with $h/\lambda_T = 3.0$. The symbol λ_T is the wavelength of a shear wave at the frequency of 2.25 MHz. Three values of the interfacial spring constant, K_N , are considered: $K_N = 0$ (open crack), $2.0 \cdot 10^{14} \text{ Nm}^{-3}$, and $4.0 \cdot 10^{14} \text{ Nm}^{-3}$. In this and the following figures, the partial closure of the crack is uniform along the crack extension, unless otherwise specified. Worth noting in Fig. 2 is the tendency of the characteristic interference oscillations of the backscattered amplitude to disappear with increasing values of the crack depth. In other words, the angular dependence of the amplitude backscattered by the crack increasingly resembles that of a longitudinal wave impinging on an imperfect interface of infinite extent as the normalized crack depth increases.

Figure 3 shows the angular behavior of the amplitude of the backscattered shear wave for the same set of system parameters considered in Fig. 2. Note the large peak of the backscattered wave around the critical value for the longitudinal wave reflected by the stress-released surface, that is, $\theta_L = 30.5$ degrees.

Figure 4 illustrates the behavior of the normalized backscattered amplitude for cracks with normalized depth, h/λ_T , equal to 0.3, and 3.0, at a frequency of 2.25 MHz, as the spring stiffness, K_N , increases. The amplitude of the wave backscattered by an open crack under the same conditions is used as normalization constant. Figure 4a refers to a longitudinal wave incident at 45 degrees from the normal to the stress-released surface, while Fig. 4b shows the data relative to a shear wave impinging on the stress-free surface at an angle of incidence of 30 degrees. In both cases, the decrease of the scattered amplitude with increasing values of the interfacial spring constant follows the expectations based upon the behavior of the reflection coefficient of a bulk wave insonifying an imperfect interface at normal incidence.

The dependence of the backscattered amplitude on the crack depth was also investigated and Fig. 5 reports sample results obtained for an open crack, and a crack the faces of which are partially closed ($K_N = 2.0 \cdot 10^{14} \text{ Nm}^{-3}$). The longitudinal backscattered amplitude (Fig. 5a) shows pronounced variations caused by interference, especially around $h/\lambda_T = 1.0$, while the shear backscattered amplitude (Fig. 5b) increases in a smoother fashion. In both cases, the absolute magnitude of the oscillation is reduced by the partial crack closure.

Cracks may be partially closed only along a confined region of their extent. For instance, crack closure may occur only at the crack tip due to the action of a compressive residual stress field present within the plastically deformed region around the crack tip. This situation may be modeled by letting the normal stiffness of the distributed spring vary in the following way,

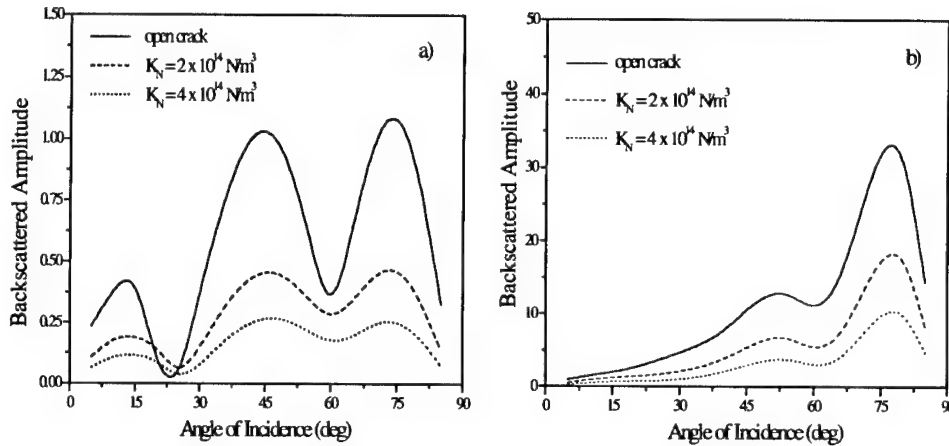


Figure 2. Longitudinal backscattered amplitude vs. angle of incidence for two values of the normalized crack depth, $h/\lambda_T = 0.3$ (a), and 3.0 (b), and three values of the normal spring stiffness, $K_N = 0$ (open crack), $2. 10^{14} \text{ Nm}^{-3}$, and $4. 10^{14} \text{ Nm}^{-3}$. The ultrasonic frequency is $f = 2.25 \text{ MHz}$.

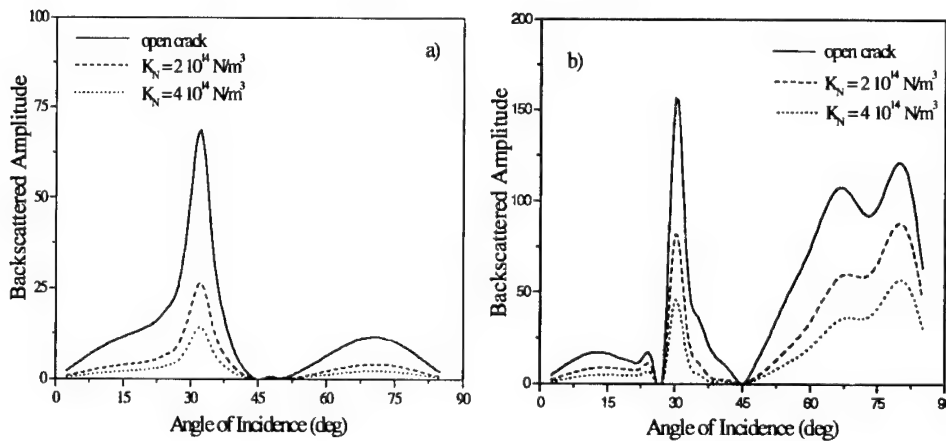


Figure 3. Shear backscattered amplitude vs. angle of incidence for two values of the normalized crack depth, $h/\lambda_T = 0.3$ (a), and 3.0 (b), and three values of the normal spring stiffness, $K_N = 0$ (open crack), $2. 10^{14} \text{ Nm}^{-3}$, and $4. 10^{14} \text{ Nm}^{-3}$. The ultrasonic frequency is $f = 2.25 \text{ MHz}$.

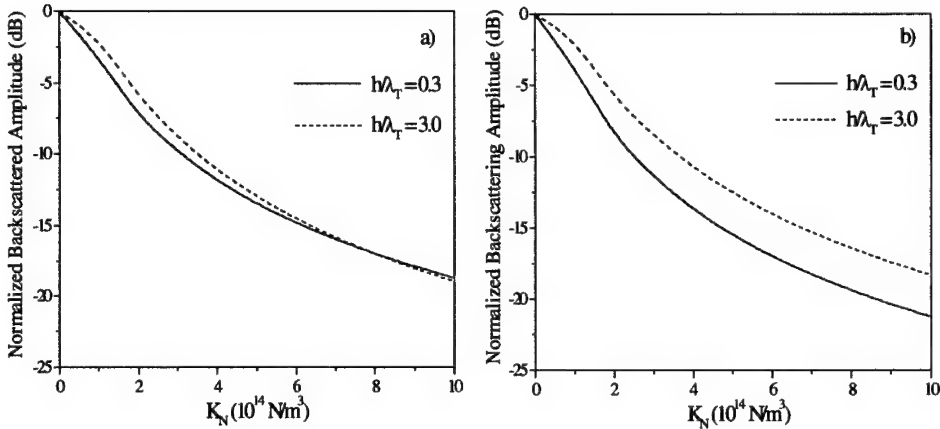


Figure 4. Normalized backscattered amplitude vs. K_N for a) longitudinal, and b) shear incidence at 45 degrees and 30 degrees, respectively. As before, the ultrasonic frequency is 2.25 MHz.

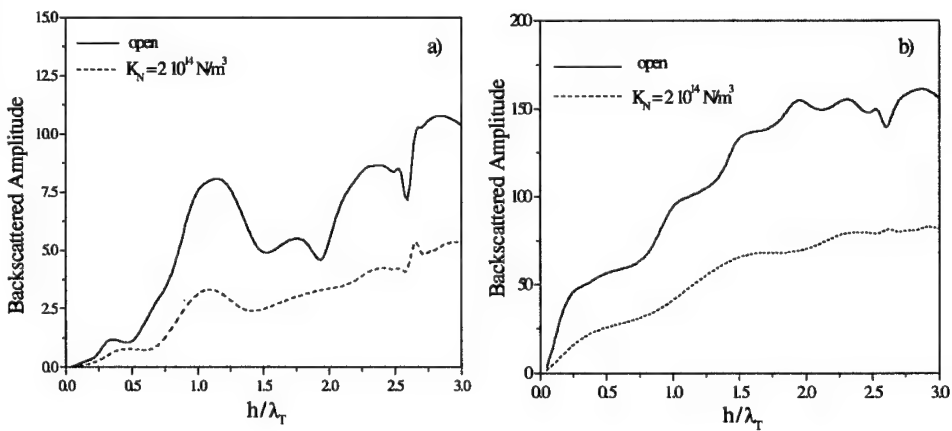


Figure 5. Backscattered amplitude vs. normalized crack depth for an open crack and for a crack partially closed with a spring constant $K_N = 2.0 \cdot 10^{14} \text{ Nm}^{-3}$. a) longitudinal incidence at 45 degrees, b) shear incidence at 30 degrees. The ultrasonic frequency is equal to 2.25 MHz.

$$K_N = \begin{cases} K_N^o \cos^2 \left(\frac{\pi}{2} \frac{h-z}{0.4h} \right) & \text{for } h < z < 0.6h \\ 0 & \text{for } 0.6h < z < 0 \end{cases}. \quad (5)$$

In Eq. (5), the quantity K_N^o is the maximum value of the normal spring stiffness. The latter decreases to zero, that is, the crack is open at depths smaller than $0.6h$. Figure 6 illustrates the variation of the backscattered amplitude with increasing values of K_N^o for two cracks having a normalized depth equal to 0.3 and 3.0, respectively. Although hardly of any practical relevance because of its magnitude, the variation of the amplitude of both longitudinal and shear waves which are backscattered by the deeper crack is seen to increase with the interfacial stiffness, as previously reported for the case of Rayleigh wave reflection.

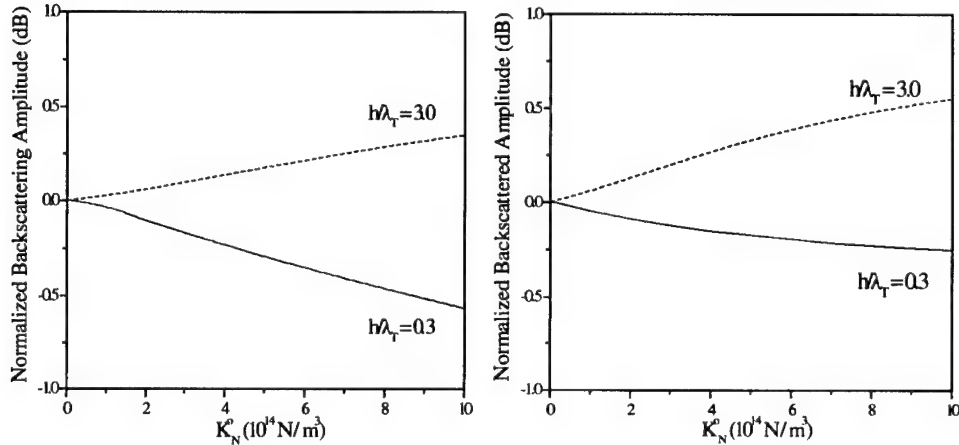


Figure 6. Variation of the longitudinal (a) and shear (b) backscattered amplitude vs. K_N^o . Cracks considered here are partially closed within their tip region, and have a normalized depth equal to 0.3 and 3.0. The ultrasonic frequency is equal to 2.25 MHz.

Finally, a legitimate question may be asked as to whether any ratio between amplitudes of scattered waves may be used to characterize the state of partial closure of a surface-breaking crack. Figure 7 reports the ratio between the amplitude of the longitudinal and shear waves backscattered at 45 degrees and 30 degrees, respectively, by an open and a partially closed crack ($K_N = 2.0 \cdot 10^{14} \text{ Nm}^{-3}$) versus the normalized frequency, $f/(C_p/h)$. The crack depth chosen equaled 3.195 mm, so that the normalization constant would be equal to 1 MHz. For values of the normalized frequency up to 3.0, the behavior of the ratio does not show any clear feature that may be considered characteristic of the partially closed state versus the open state.

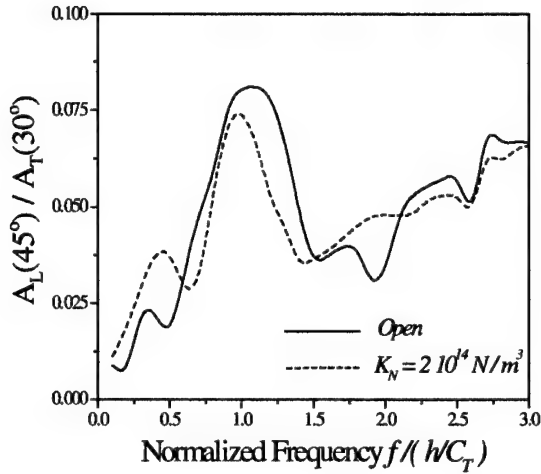


Figure 7. Ratio between the longitudinal and shear waves that are backscattered at 45 degrees and 30 degrees, respectively, vs. the normalized frequency, for an open crack and a crack that is partially closed. The crack depth, h , is equal to 3.195 mm.

3. Concluding Remarks

A model that describes the scattering of elastodynamic waves by a surface-breaking crack with faces in partial contact is now available. For the case of Rayleigh wave incidence, the model predicts a surprising and considerable increase of the reflection coefficient for crack depths larger than half a wavelength of the incident wave, and a normal spring stiffness, K_N , smaller than a characteristic value. Such a prediction is supported by experimental results, and may lend itself to practical applications. For the cases of both longitudinal and shear incidence, the model yields a description of the backscattering phenomenon that qualitatively resembles the reflection of a bulk wave impinging on an imperfect interface of infinite extent: the amplitude of the backscattered wave decreases continuously with increasing spring stiffness.

The model relies on the introduction of the stiffness constants of the macroscopic distributed springs to incorporate the effects of the microscopic contacts on wave scattering. Unfortunately, the QSA does not provide a direct link between the spring constants, K_N and K_T , and the compressive stress causing the partial closure. Thus, additional modeling accounting for the topographical and mechanical properties of the two partially contacting surfaces is required to fill the gap. To the best of this author's knowledge, no model explaining the contact problem in all its aspects is available to this date. However, even if such a program were brought to a successful conclusion, the lack of a characteristic acoustic signature of the partial crack closure on the scattered field seems to hinder the possibility of characterizing the compressive field partially closing the crack by ultrasonic methods based on linear phenomena. Nonlinear scattering of elastodynamic waves might enhance the chance of solving this problem.

In fact, the generation of higher harmonic components of the scattered field is a phenomenon that occurs only when the faces of the crack interact with each other. Therefore, it may provide a clear and unique signature of a compressive stress acting on the crack faces.

Acknowledgments

This work was performed as part of the institutional program carried out within the European Network for Inspection Qualification (ENIQ) supported by the Commission of the European Communities.

References

Achenbach, J.D., Gautesen, A.K., Mendelsohn D.A. (1980), Ray analysis of surface-wave interaction with an edge crack, *IEEE Trans. Sonics and Ultrasonics* **27**, 125-129.

Achenbach, J.D., Keer, L.M., Mendelsohn, D.A., (1980), Elastodynamic Analysis of an edge crack, *J. Appl. Mech.* **47**, 551-556.

Achenbach, J.D., Komsky, I.N., Lee, Y.C., Angel, Y.C. (1992), Self-calibrating ultrasonic technique for crack depth measurement, *J. Non-Destruct. Eval.* **11**, 103-108.

Angel, Y.C., Achenbach, J.D. (1984), Reflection and transmission of obliquely incident Rayleigh waves by a surface-breaking crack, *J. Acoust. Soc. Am.* **75**, 313-319.

Buck, O., Rehbein, D.K., Thompson, R.B. (1987), Crack tip shielding by asperity contact as determined by acoustic measurements, *Engineering Fracture Mechanics* **28**, 413-424 and references therein.

Datta, S.K. (1979), Diffraction of SH waves by an edge crack, *J. Appl. Mech.* **46**, 101-106.

Kundu, T., Mal, A.K. (1981), Diffraction of elastic waves by a surface crack on a plate, *J. Appl. Mech.* **48**, 570-576.

Mendelsohn, D.A., Achenbach, J.D., Keer, L.M. (1980) Scattering of elastic waves by a surface-breaking crack, *Wave Motion* **2**, 277-292.

Nagy, P. B. (1992), Ultrasonic classification of imperfect interfaces, *J. Non-Destruct. Eval.* **11**, 127-140 and references therein.

Neerhoff, F.L. (1980), Reciprocity and Power-flow theorems for scattering of plane elastic waves in a half-space, *Wave Motion* **2**, 99-113.

Pecorari, C. (2000), Scattering of a Rayleigh wave by a surface-breaking crack with faces in partial contact, to appear in Wave Motion.

Stone, S.F., Gosh, M.L., Mal A.K. (1980), Diffraction of antiplane shear waves by an edge crack, *J. Appl. Mech.* **47**, 359-362.

Tittmann, B.R., Ahlberg, L.A., Mal, A.K. (1986), Rayleigh wave diffraction from surface-breaking discontinuities, *Appl. Phys. Lett.* **49**, 1333-1335.

Vu, B., Kinra, V.K., (1985)"Diffraction of Rayleigh waves in a half-space. I. Normal edge crack, *J. Acoust. Soc. Am.* **77**, 1425-1430.

Zhang, C., Achenbach, J.D. (1988), Numerical analysis of surface-wave scattering by the boundary element method, *Wave Motion* **10**, 365-374.

ASYMPTOTIC FORMULAS FOR THE STRESS FIELD OF A CRACK BY NONLOCAL ELASTICITY

HUI-HUI DAI*, KELIN PAN** and YIBIN FU***

*City University of Hong Kong, Kowloon, HK

** Tongji University, Shanghai, China (present ***)

*** Keele University, Staffordshire ST5 5BG, UK

Abstract- A new mathematical approach is adopted to deal with the crack tip stress field. By considering the parameter α , which is proportional to the reciprocal of the distance between atoms, being large, we construct two asymptotic expansions for the stress field, which are uniformly valid for $r\alpha$ (r is the distance to the crack tip) being bounded and unbounded respectively. The results show that the classical singularity is eliminated and a finite value at the crack tip is found. We define this value as Nonlocal Boundary Residual (NBR) which is microscopic mechanics quantity and disappears in macroscopic mechanics theory. It is also found that to small angle stress there is a maximum stress near to the crack tip.

1 INTRODUCTION

The concept of nonlocal elasticity has been developed in 60s and 70s. The basic idea of nonlocal elasticity is that microstructures of materials are considered in constitutive equations. The Nonlocal Residuals exist in nonlocal theory. They are not only mathematical quantities but also physical quantities (Pan and Ji, 1997, Pan and Takeda, 1998).

In this paper, we calculate the stress field by uniform asymptotic analysis (UAA) (Dai and Wong 1994, Dai 1997). In our mathematical treatment, we find that it is necessary to consider the cases of $r\alpha$ being bounded and unbounded respectively. We leave unbounded case to other paper because of limited pages. For bounded $r\alpha$, by using the series representation of the classical stress field and the Taylor expansion for the exponential function in the polar coordinates, we first take term by term integration to obtain the first N terms in the expansion. To establish the asymptotic nature of that expansion with mathematical rigor, the remainder has to be estimated, which is done in the appendix. The remarkable features of nonlocal solutions are that the solution eliminates the singularity and has a

finite value at the crack tip. The existence of the finite value has been proved by Actinson (1980) and Ari and Eringen (1983). We gave the value by UAA and explained it as NBR. The maximum of the stress near the crack tip changes its position and the value with different angles. The changes are revealed only by nonlocal theory.

2 NONLOCAL THEORY

The character of nonlocal theory is that the constitutive relation considers the microstructures of the material by introducing a kernel function $\gamma(|\mathbf{x}' - \mathbf{x}|, \alpha)$, where α reflects the microstructure of the material. In this way, the only difference between nonlocal and classical theory is the constitutive relation. The other displacement or geometric quantities are same for both. The nonlocal stress field for linear, isotropic, homogeneous, elastic solid with vanishing body force and in a static case can be expressed as (Pan and Takeda, 1998):

$$t_{ij}(\mathbf{x}) = \int_v \gamma(|\mathbf{x}' - \mathbf{x}|) \sigma_{ij}(\mathbf{x}') dv(\mathbf{x}'), \quad (1)$$

where t_{ij} and σ_{ij} are the nonlocal and classical stresses respectively, $\gamma = \gamma_0 \exp[-\alpha^2 (|\mathbf{x}' - \mathbf{x}|)^2]$ and $\gamma_0 = \pi^{-3/2} \alpha^3$, $\alpha = k/a$, $k = 1.65$ are constants, a is a distance between atoms. The equilibrium equation can be satisfied in nonlocal case

$$t_{ij,j} = 0 \quad (2)$$

which is easy to be proved using identities $\gamma_{,j} \sigma'_{ij} = -(\gamma \sigma'_{ij})_{,j} + \gamma \sigma'_{ij,j}$, and considering Green-Gauss theorem and classical stress equilibrium. In fact, we have

$$t_{ij,j} = \int_v \gamma_{,j} \sigma'_{ij} dv' = - \oint_{\partial v} (\gamma \sigma'_{ij}) n_j dS + \int_v \gamma \sigma'_{ij,j'} dv' = 0$$

where ∂v denotes the surface of the body enclosing v , and \mathbf{n} is direction vector of the surface.

3 ASYMPTOTIC FORMULAS FOR NONLOCAL STRESS FIELD OF CRACK

The classical stress field near to the crack tip can be found in any book of fracture mechanics, which can be expressed by

$$\begin{aligned} \sigma_r(r, \theta) &= r^{-1/2} \sum_{i=0}^{\infty} r^{i/2} f_r^i(\theta), \\ \sigma_\theta(r, \theta) &= r^{-1/2} \sum_{i=0}^{\infty} r^{i/2} f_\theta^i(\theta), \end{aligned}$$

$$\tau_{r\theta}(r, \theta) = r^{-1/2} \sum_{i=0}^{\infty} r^{i/2} f_{r\theta}^i(\theta), \quad (3)$$

where

$$\begin{aligned} f_r^i &= \frac{1}{4\sqrt{r}} \sum_{i=0}^{\infty} (i+1) r^{\frac{i}{2}} \{ \{(5-i)\cos(\frac{i-1}{2}\theta) + [i+1-2(-1)^i]\cos(\frac{i+3}{2}\theta)\} \alpha_{i+1} \\ &\quad + \{(5-i)\sin(\frac{i-1}{2}\theta) + [i+1+2(-1)^i]\sin(\frac{i+3}{2}\theta)\} \beta_{i+1} \}, \\ f_\theta^i &= \frac{1}{4\sqrt{r}} \sum_{i=0}^{\infty} (i+1) r^{\frac{i}{2}} \{ \{(i+3)\cos(\frac{i-1}{2}\theta) - [i+1-2(-1)^i]\cos(\frac{i+3}{2}\theta)\} \alpha_{i+1} \\ &\quad + \{(i+3)\sin(\frac{i-1}{2}\theta) - [i+1+2(-1)^i]\sin(\frac{i+3}{2}\theta)\} \beta_{i+1} \}, \\ f_{r\theta}^i &= \frac{1}{4\sqrt{r}} \sum_{i=0}^{\infty} (i+1) r^{\frac{i}{2}} \{ \{(i-1)\sin(\frac{i-1}{2}\theta) - [i+1-2(-1)^i]\sin(\frac{i+3}{2}\theta)\} \alpha_{i+1} \\ &\quad + \{(1-i)\cos(\frac{i-1}{2}\theta) + [i+1+2(-1)^i]\cos(\frac{i+3}{2}\theta)\} \beta_{i+1} \}. \end{aligned}$$

where α_i , and β_i are constants. It is obvious that the classical stresses are not valid when $r \rightarrow 0$ due to the infinite values. Then we can write

$$\begin{aligned} \sigma_{11} &= r^{-1/2} \sum_{i=0}^{\infty} r^{i/2} f_{11}^i, \\ \sigma_{22} &= r^{-1/2} \sum_{i=0}^{\infty} r^{i/2} f_{22}^i, \\ \tau_{12} &= r^{-1/2} \sum_{i=0}^{\infty} r^{i/2} f_{12}^i, \end{aligned} \quad (4)$$

where

$$\begin{aligned} f_{11}^i &= f_r^i \cos^2 \theta + f_\theta^i \sin^2 \theta - f_{r\theta}^i \sin 2\theta, \\ f_{22}^i &= f_r^i \sin^2 \theta + f_\theta^i \cos^2 \theta + f_{r\theta}^i \sin 2\theta, \\ f_{12}^i &= \frac{1}{2} (f_r^i - f_\theta^i) \sin^2 \theta + f_{r\theta}^i \cos 2\theta. \end{aligned}$$

Since the distance a between two atoms is very small, $\alpha = k/a$ is very large. Next, we shall regard α being the large parameter to deduce the asymptotic formulas for t_{ij} from its integral by substituting (4) into (1). We write (4) as

$$\sigma_{nm}(r, \theta) = r^{-1/2} \sum_{i=0}^N r^{i/2} f_{nm}^i(\theta) + F_{nm}(r, \theta), \quad (5)$$

where N is an arbitrary integer, and

$$F_{nm}(r, \theta) = r^{-1/2} \sum_{i=N+1}^{\infty} r^{i/2} f_{nm}^i(\theta). \quad (6)$$

Obviously, as $r \rightarrow 0$,

$$F_{nm}(r, \theta) = O((r)^{N/2}) \quad (7)$$

uniformly valid in θ . Substituting (5) into (1), we obtain

$$t_{nm} = R_1 + R_2, \quad (8)$$

where

$$R_1 = \gamma_0 \exp(-\alpha^2 r^2) \sum_{i=0}^N \int_0^\infty (r')^{(1+i)/2} \exp(-\alpha^2 r'^2) \int_{-\pi}^{\pi} \exp[2\alpha^2 rr' \cos(\theta - \theta')] f_{nm}^i(\theta') d\theta' dr' \quad (9)$$

and the remainder is

$$R_2 = \gamma_0 \exp(-\alpha^2 r^2) \int_0^\infty \exp(-\alpha^2 r'^2) \int_{-\pi}^{\pi} \exp[2\alpha^2 rr' \cos(\theta - \theta')] F_{nm}(r', \theta') d\theta' dr'. \quad (10)$$

We shall deal with R_1 first. According to the Taylor series for an exponential function, we have

$$\exp[2\alpha^2 rr' \cos(\theta - \theta')] = \sum_{j=0}^{\infty} [2\alpha^2 rr' \cos(\theta - \theta')]^j / j! \quad (11)$$

It should be noted that the series in (11) is convergent for any r' and θ' . Substituting (11) into (9) and interchanging summation and integration (this is permissible because of the previous point), we obtain

$$R_1 = \gamma_0 \exp(-\alpha^2 r^2) \sum_{i=0}^N \sum_{j=0}^{\infty} \frac{(2\alpha^2 r)^j}{j!} \int_0^\infty \exp(-\alpha^2 r'^2) r'^{\frac{i+1}{2}+j} dr' g_{nm}^{ij}(\theta), \quad (12)$$

where

$$g_{nm}^{ij}(\theta) \equiv \int_{-\pi}^{\pi} \cos^j(\theta - \theta') f_{nm}^i(\theta') d\theta'. \quad (13)$$

The integral in (12) can be easily evaluated by using the Gamma function $\Gamma(r)$, and as a result we obtain

$$R_1 = \frac{1}{2} \gamma_0 \exp(-\alpha^2 r^2) \sum_{i=0}^N \left[\sum_{j=0}^{\infty} \frac{2^j (r\alpha)^j}{j!} \Gamma\left(\frac{i+2j+3}{4}\right) g_{nm}^{ij}(\theta) \right] \alpha^{-\frac{i+3}{2}}. \quad (14)$$

To establish an asymptotic formula for t_{nm} , one needs to prove that the remainder R_2 is smaller than the last term in the second summation in the right-hand side of (14). In the

appendix, we have provided a detailed proof that when $r\alpha$ is bounded, it is indeed such a case. Thus, we have established that

$$t_{nm}(r, \theta) \sim \frac{1}{2} \gamma_0 \exp(-\alpha^2 r^2) \sum_{i=0}^N \left[\sum_{j=0}^{\infty} \frac{2^j (r\alpha)^j}{j!} \Gamma\left(\frac{i+2j+3}{4}\right) g_{nm}^{ij}(\theta) \right] \alpha^{-\frac{i+3}{2}} \quad (15)$$

as $\alpha \rightarrow \infty$ uniformly valid for $r\alpha$ being bounded. The radial stress can be obtained by

$$t_r = t_{11} \cos^2 \theta + t_{22} \sin^2 \theta + t_{12} \sin 2\theta. \quad (16)$$

Setting $\rho = \alpha r$ in Equation (16), the curve of t_r versus ρ is given in Fig.2 for an opening crack.

4 DISCUSSIONS AND REMARKS

In (16), if only the first term is taken (the error is $O(\alpha^{-2})$), we have

$$t_r(r, \theta) \sim \frac{\pi}{2} \exp(-\alpha^2 r^2) \left[\sum_{j=0}^{\infty} \frac{2^j (r\alpha)^j}{j!} \Gamma\left(\frac{2j+3}{4}\right) g_r^{0j}(\theta) \right] \alpha^{\frac{1}{2}} \quad (17)$$

as $\alpha \rightarrow \infty$ uniformly valid for $r\alpha$ being bounded, where $g_r = g_{11} \cos^2 \theta + g_{22} \sin^2 \theta + g_{12} \sin 2\theta$. The curves of the nondimensional stress $T = t_r \alpha^{-1/2} / K_I$ versus the nondimensional distance $\rho = \alpha r$ with different θ according to the above formula are shown in Figure 2. From the results of Fig.2, we find that there is a maximum of the stress near to the crack tip. The value of the maximum increases with the decreasing θ . In the figure, the value changes from 3.75 to 3.78 when the angle θ changes from $\pi/3, \pi/4, \pi/6$ to 0. When the distance from the crack tip increases, the effect of the angle disappears gradually. The result returns to the classical one. We can prove that for unbounded (large) $\rho = r\alpha$, the solution is also convergent by the asymptotic approach (we will publish this part in other paper). So, for any bounded value of $\rho = r\alpha$, as long as a sufficient number of terms in the series is taken, an accurate result can be obtained. If in particular $r = 0$, and noting that

$$g_{00} = \frac{16}{3} \alpha_1,$$

from (17) we have

$$t_r(0, 0) = \frac{8}{3} \left(\frac{2}{\pi}\right)^{1/2} \alpha^{1/2} \Gamma\left(\frac{3}{4}\right) K_I. \quad (18)$$

Here a commonly used constant K_I in fracture mechanics is introduced in the above equation instead of the original constant α_1 for a crack of type I. The stress at crack tip

was also calculated by some authors numerically. For example, Eringen (1978) showed that the stress at the crack tip is zero in nonlocal case. Atkinson (1980) revealed that the value at the crack tip is not zero. Later, Ari and Eringen (1983) calculated the stress field close to the crack tip and gave a value of the maximum of the stress near to the crack tip which is

$$t_{yy\max}/t_0 = 0.643395\alpha^{1/2}.$$

By our result (18), we have

$$t_0/K_I = 2.607\alpha^{1/2}.$$

In our approach we show that a large value is existent and can be given accurately at the crack tip. The value is reasonable in physics. The value produced is due to the effect of microstructures. The value reveals the existence of nonlocal boundary residual. This is because that to match the value at the crack tip the surface of the crack should have stresses (NBR). When a (the distance between two atoms) is neglected (tends to 0), the value of $t_r(0, 0)$ is infinity, which gives the classical result. Now in nonlocal consideration $t_r(0, 0)$ is connected with microstructure of the material, which means that the value of crack tip stress is micromechanics quantity. For other stress components we can obtain the same conclusion.

ACKNOWLEDGEMENT

This work was supported partly by a CERG Grant from Hong Kong Government and a Strategic Grant from City University of Hong Kong. The work is sponsored by Royal Society K.C.Wong Fellowship when K.Pan was visiting Keele University.

REFERENCES

- Abromowitz, M. and Stegun, I.A. (1965) *Handbook of Mathematical Functions*. Dover, New York.
- Ari, N. and Eringen, A.C. (1983) *Cryst. Latt. Def. and Amorph. Mat.*, **10** 33.
- Atkinson, A. (1980) *Arch. Mech.* **32** 317 and 597.
- Dai, H.-H. and Wong, R. (1994) *Wave Motion* **19** 293.
- Dai, H.-H. (1997) *IMA J. Applied Mathematics* **59** 245.
- Eringen, A.C. (1978) *Arch. Mech.* **30** 55.
- Pan, K.L. and Ji, X. (1997) *Mech. Res. Commu.* **24** 325.
- Pan, K.L. and Takeda, N. (1998) *Archive of Applied Mechanics* **68** 179.

APPENDIX

Estimate of R_2

From the fact that $F(r, \theta)$ is bounded and of order $(r)^{N/2}$ as $r \rightarrow 0$ (see (7)), we know that there exists a positive constant K_1 such that

$$|F(r', \theta')| < K_1(r')^{N/2}. \quad (19)$$

Using the above equation in (10), we have

$$\begin{aligned} |R_2| &< K_1 \gamma_0 \exp(-\alpha^2 r^2) \int_0^\infty (r')^{N/2} \exp(-\alpha^2 r'^2) \int_{-\pi}^\pi \exp[2\alpha^2 rr' \cos(\theta - \theta')] d\theta' dr' \\ &= K_1 \gamma_0 \exp(-\alpha^2 r^2) \int_0^\infty I_0(2\alpha^2 rr')(r')^{N/2} \exp(-\alpha^2 r'^2) dr' \\ &= \frac{1}{2} K_1 \gamma_0 \alpha^{-N/2-1} \exp(-\alpha^2 r^2) \int_0^\infty I_0(2\alpha r \tau^{1/2}) \tau^{\frac{N-2}{4}} \exp(-\tau) d\tau. \end{aligned} \quad (20)$$

In deriving (20), an integral representation for the modified Bessel function $I_0(\cdot)$ has been used (see formula 9.6.16, Abramowitz and Stegun 1965). Since

$$I_0(2\alpha r \tau^{1/2}) = \sum_{k=0}^{\infty} \frac{(\alpha^2 r^2 \tau)^k}{k! \Gamma(k+1)} \quad (21)$$

(formula 9.6.10, Abramowitz and Stegun 1965), which is convergent for any α , r and τ , we have

$$\begin{aligned} \int_0^\infty I_0(2\alpha r \tau^{1/2}) \tau^{\frac{N-2}{4}} \exp(-\tau) d\tau &= \sum_{k=0}^{\infty} \frac{(\alpha r)^{2k}}{k! \Gamma(k+1)} \int_0^\infty \tau^{k+\frac{N-2}{4}} \exp(-\tau) d\tau \\ &= \sum_{k=0}^{\infty} \frac{(\alpha r)^{2k}}{k! \Gamma(k+1)} \Gamma(k + \frac{N-2}{4}) = O(1) \end{aligned} \quad (22)$$

for αr being bounded.

From (20), (21) and (22), we conclude that

$$R_2 = O(\gamma_0 \alpha^{-N/2-1} \exp(-\alpha^2 r^2)), \quad (23)$$

which is smaller than the last term in the right-hand side of the summation in (14) as $\alpha \rightarrow \infty$.

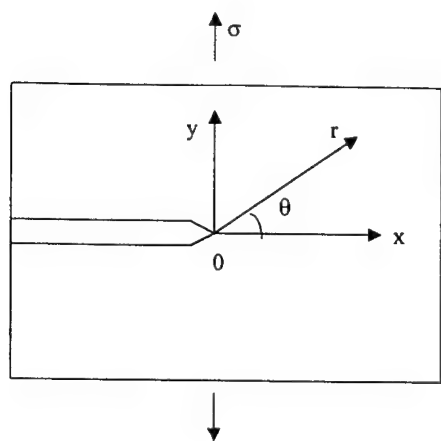


Fig. 1 An infinite crack with tensile

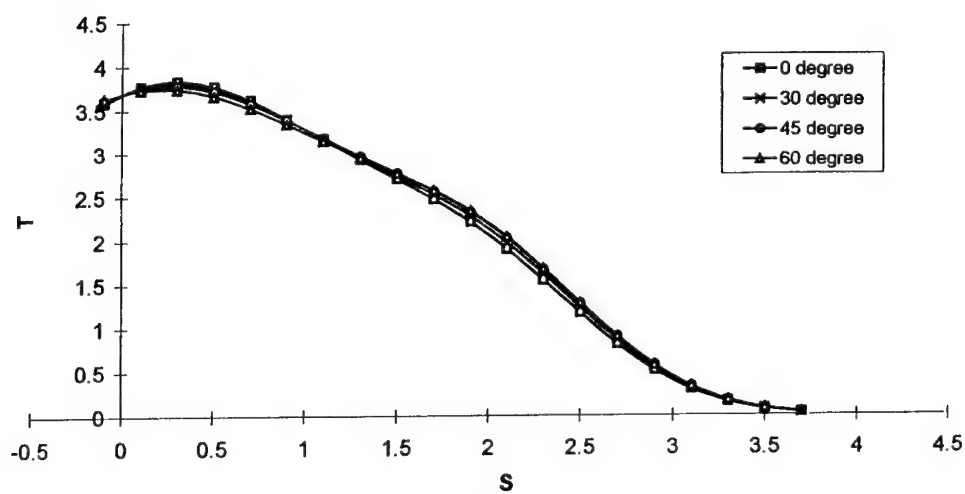


Fig. 2 Stress distribution near an infinite crack tip ($s=\rho$)

ELASTODYNAMIC RESPONSE OF A CRACKED FIBER-REINFORCED BODY TO A NON-UNIFORM TRANSIENT PLANE-STRAIN LOADING

E.G. VELGAKI and H.G. GEORGIADIS *

*Mechanics Division, National Technical University of Athens,
5 Heroes of Polytechnion Avenue, Zographou GR-15773, Greece
(* Corresponding author. E-mail: georgiad@central.ntua.gr)*

1. Summary

A near-tip, transient, elastodynamic solution is presented for the plane-strain problem of a crack in a *fiber-reinforced* composite body subjected to a non-uniform loading, which is suddenly and symmetrically applied to the crack faces. Interest is focused on the stress field in the immediate vicinity of the crack edge during a small time-interval right after the application of loading and, therefore, the cracked body is considered of infinite extent and the crack itself of semi-infinite length. The loading consists of a pair of equal, but opposite, line concentrated normal forces which have a step-function time dependence. In this way, the present solution provides the Green's function for more general cases of spatially/temporally non-uniform loading. The fiber-reinforced composite is modeled as elastic *orthotropic* with four different material constants. The mathematical diffraction problem is solved in an exact manner through integral transforms, an analytic-function decoupling technique, asymptotics and convolutions. Our results provide the time variation of the crack-tip stress intensity factor. These results may serve to quantify the fracture resistance of fiber-reinforced composite materials.

2. Problem Statement

As Fig. 1 depicts, we consider a *fiber-reinforced* body occupying the region $(-\infty < x < \infty, -\infty < y < \infty)$ and containing a stationary semi-infinite crack situated along the plane $(-\infty < x < 0, y = 0)$, with respect to an (x,y) Cartesian coordinate system. The body is modeled as elastic and orthotropic, with either the x or y axis being the axis of material symmetry. The cracked body is stress-free and at rest for time $t < 0$ but at $t = 0$ the crack faces are suddenly acted upon by a pair of concentrated line normal forces F , which tend to open the crack under *plane-strain* conditions. Because of symmetry with respect to the plane $y = 0$, the problem can be viewed as a half-plane problem with the body occupying the domain $(-\infty < x < \infty, 0 < y < \infty)$.

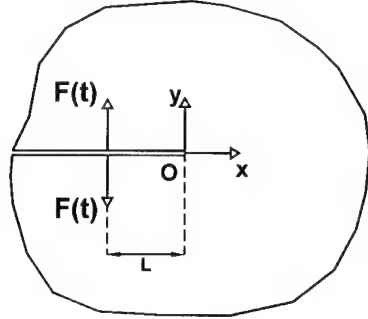


Figure 1. Cracked body under concentrated impact loading.

The governing equations for the problem described above are written as (see e.g. Lekhnitskii, 1963)

$$c_{11} \frac{\partial^2 u_x}{\partial x^2} + c_{66} \frac{\partial^2 u_x}{\partial y^2} + (c_{12} + c_{66}) \frac{\partial^2 u_y}{\partial x \partial y} = \rho \frac{\partial^2 u_x}{\partial t^2} \quad (1a)$$

$$c_{66} \frac{\partial^2 u_y}{\partial x^2} + c_{22} \frac{\partial^2 u_y}{\partial y^2} + (c_{12} + c_{66}) \frac{\partial^2 u_x}{\partial y \partial x} = \rho \frac{\partial^2 u_y}{\partial t^2} \quad (1b)$$

$$\sigma_{xx} = c_{11} \frac{\partial u_x}{\partial x} + c_{12} \frac{\partial u_y}{\partial y}, \quad \sigma_{yy} = c_{12} \frac{\partial u_x}{\partial x} + c_{22} \frac{\partial u_y}{\partial y}, \quad \sigma_{xy} = c_{66} \left(\frac{\partial u_x}{\partial y} + \frac{\partial u_y}{\partial x} \right) \quad (2a,b,c)$$

where (u_x, u_y) are the components of displacement vector, $(\sigma_{xx}, \sigma_{yy}, \sigma_{xy})$ are the components of the stress tensor, ρ is the mass density, t is the time, and $(c_{11}, c_{12}, c_{22}, c_{66})$ are the four (independent) elastic constants.

The initial and boundary conditions of the problem are as follows (for the upper half of the domain)

$$u_k(x, y, t=0) = \partial u_k(x, y, t=0) / \partial t = 0, \quad (k = x, y) \quad (3)$$

$$\sigma_{yy}(x, y=0, t) = -F \cdot \delta(x+L) \cdot H(t) \quad \text{for } -\infty < x < 0 \quad (4a)$$

$$\sigma_{xy}(x, y=0, t) = 0 \quad \text{for } -\infty < x < \infty \quad (4b)$$

$$u_y(x, y=0, t) = 0 \quad \text{for } 0 < x < \infty \quad (4c)$$

where $\delta(\cdot)$ is the Dirac delta distribution, $H(\cdot)$ is the Heaviside step function, and F is expressed in dimensions of force per unit length. To render the initial/boundary value problem a well-posed one, eqns (1)-(4) should be supplied with the *edge* conditions at the crack tip (i.e. restrictions on the singular behavior of the fields) and the *finiteness*

conditions at remote regions (which are direct consequence of the asymptotic behavior of the pertinent Green's function). The former of these conditions are necessary for solution uniqueness in elastic crack problems (Knowles and Pucik, 1973), whereas the latter guarantee that the field at infinity consists of outgoing waves only. Both conditions are properly utilized at certain steps in the solution procedure (see e.g. Georgiadis and Rigatos, 1996).

The objective of the present analysis is to exactly determine the stress field at the vicinity of the crack tip for the problem described above.

3. Basic Integral-Transform Analysis

The one- and two-sided Laplace transforms (LTs) are utilized to suppress the t and x dependence, respectively, in the governing equations and the boundary conditions. The transforms and their corresponding inversion operations are defined as

$$G(x,y,s) = \int_0^\infty g(x,y,t) \cdot e^{-st} dt , \quad g(x,y,t) = \frac{1}{2\pi i} \int_{\Gamma_1} G(x,y,s) \cdot e^{st} ds \quad (5a,b)$$

$$G^*(q,y,s) = \int_{-\infty}^\infty G(x,y,s) \cdot e^{-sqx} dx , \quad G(x,y,s) = \frac{s}{2\pi i} \int_{\Gamma_2} G^*(q,y,s) \cdot e^{sqx} dq \quad (6a,b)$$

with the convention followed whereby a function which is to be transformed is denoted by a small letter, its one-sided LT by the corresponding capital letter, and its two-sided LT by an asterisk. The inversion paths (Γ_1, Γ_2) are the pertinent Bromwich paths in the associated complex planes.

It can be shown now that successive application of the above transforms along with use of some elements from the theory of linear ODEs leads to the following general solution (bounded as $y \rightarrow +\infty$) in the double transform domain (provided that pertinent branch cuts are introduced in the complex q -plane so that $\operatorname{Re}(\kappa_1, \kappa_2) > 0$)

$$U_x^*(q,y,s) = A_1(q,s) \cdot \exp(-s\kappa_1 y) + A_2(q,s) \cdot \exp(-s\kappa_2 y) \quad (7a)$$

$$\begin{aligned} U_y^*(q,y,s) = & \frac{\kappa_1^2 + \beta q^2 - a_1^2}{mq\kappa_1} A_1(q,s) \cdot \exp(-s\kappa_1 y) + \\ & + \frac{\kappa_2^2 + \beta q^2 - a_2^2}{mq\kappa_2} A_2(q,s) \cdot \exp(-s\kappa_2 y) \end{aligned} \quad (7b)$$

where (A_1, A_2) are unknown functions which will be determined in each specific problem through enforcement of the boundary conditions, the new constants $(\alpha, \beta, \gamma, m, n)$ are related to the material parameters as

$$\begin{aligned}\alpha &= \frac{c_{22}}{c_{66}}, \quad \beta = \frac{c_{11}}{c_{66}}, \quad \gamma = 1 + \alpha\beta - \left(\frac{c_{12}}{c_{66}} + 1\right)^2, \quad m = \frac{c_{12}}{c_{66}} + 1 \equiv (1 + \alpha\beta - \gamma)^{1/2}, \\ n &= \frac{c_{66}}{\rho}\end{aligned}\quad (8a-e)$$

and

$$\kappa_1 = (2\alpha)^{-1/2} \left[(\alpha+1)a_2^2 - \gamma q^2 + [\phi(q)]^{1/2} \right]^{1/2}, \quad \kappa_2 = (2\alpha)^{-1/2} \left[(\alpha+1)a_2^2 - \gamma q^2 - [\phi(q)]^{1/2} \right]^{1/2} \quad (9a,b)$$

with the following definitions being employed

$$\phi(q) = [(\alpha+1)a_2^2 - \gamma q^2]^2 - 4\alpha\beta(a_1^2 - q^2)(a_2^2 - q^2) \quad (10)$$

$$a_1 = (\beta n)^{-1/2}, \quad a_2 = n^{-1/2} \quad (11a,b)$$

Further, we notice that for a wide class of anisotropic materials (both natural and composite materials like, e.g., Magnesium, Titanium, Boron Epoxy and Graphite Epoxy) the following inequalities hold for the material constants (Payton, 1983): $1 < \beta < \alpha$ or $1 < \alpha < \beta$ or $1 < \beta = \alpha$. In that case, when q takes pure imaginary values, the functions (κ_1, κ_2) are real. Generally, the axis $i\text{Im}(q)$ is free from branch points, some of which are complex and the remaining are real at the locations $\pm a_1$ and $\pm a_2$. In what follows, we confine attention to this class of anisotropic materials stressing that this is the most common case of material anisotropy.

4. Transformed Problem and Decoupling

In order to create a functional equation in the double transform domain connecting the two yet-unknown quantities of interest, i.e. the cleavage stress $\sigma_{yy}(0 < x < \infty, y=0, t)$ and the crack-face displacement $u_y(-\infty < x < 0, y=0, t)$, the following *half-line* transforms are defined

$$\Sigma_{yy+}^*(q, s) = \int_0^\infty \Sigma_{yy}(x, 0, s) \cdot e^{-sqx} dx, \quad U_{y-}^*(q, s) = \int_{-\infty}^0 U_y(x, 0, s) \cdot e^{-sqx} dx \quad (12a,b)$$

where the first function has a region of analyticity in the right (subscript '+') half-plane and the second function in the left (subscript '-') half-plane of the complex variable q . Transforming now the boundary conditions (eqns (4)) and considering the general solution (7) along with the definitions in (12) leads to the following equation involving the unknown functions Σ_{yy+}^* and U_{y-}^*

$$\Sigma_{yy+}^* - \frac{Fe^{sqL}}{s} = c_{66}s \frac{Q}{(a_1^2 - q^2)^{1/2}} U_{y-}^* \quad (13)$$

where the kernel function Q is given by

$$Q(q) = (a_2^2 - q^2)^{1/2} [H_1(q) \cdot V_2(q) - H_2(q) \cdot V_1(q)] \left[m(\alpha\beta)^{1/2} (\kappa_1^2(q) - \kappa_2^2(q)) \right]^{-1} \quad (14)$$

$$H_j(q) = [(1-m) \cdot \kappa_j^2(q) - \beta(a_1^2 - q^2)] [\kappa_j(q)]^{-1} \quad (15a)$$

$$V_j(q) = m(m-1)q^2 - \alpha\kappa_j^2(q) + \alpha\beta(a_1^2 - q^2) \quad (15b)$$

with $j = (1,2)$ in eqns (15). Notice also that (13) holds only along a *strip* of analyticity along the $i\text{Im}(q)$ axis.

Further, eqn (13) will be solved (i.e. the yet-unknown functions will be decoupled) through the technique advanced in the works by Georgiadis and Brock (1993), and Georgiadis and Rigatos (1996). As explained in the latter paper, this technique is more general than the conventional Wiener-Hopf technique (see e.g. Noble, 1958) in problems involving *characteristic lengths* (like the length L here) in the forcing function. In fact, the Wiener-Hopf technique is not applicable at all in such a case where, in addition, the strip of analyticity degenerates into a line. The technique employed here is based on contour integration, kernel factorization, Cauchy's theorem and integral formula, and Jordan's lemma. Also, use of the asymptotic Abel-Tauber theorems (see e.g. Noble, 1958) will permit the determination of the exact stress field in the immediate vicinity of the crack tip. Below, a brief description of the procedure will be given along with representative numerical results.

As a necessary step of the decoupling procedure, a factorization (Noble, 1958) of the kernel should be accomplished. A direct factorization looks difficult, however, due to the complexity of the functions H_j and V_j . Instead, the analysis of Norris and Achenbach (1984) (who dealt with the simpler problem of the time-harmonic *steady-state* response of a crack to a *uniform* loading) is adopted according to which pertinent auxiliary functions are used with the kernel taking the form

$$Q(q) = \frac{\Phi_0(q) \cdot \Phi_1(q) \cdot (q^2 - a_R^2)}{\Psi} \quad (16)$$

where

$$\Phi_0(q) = \frac{(4q^2 + N_1)(a_1^2 - q^2)^{1/2}(a_2^2 - q^2)^{1/2} + (a_2^2 - 2q^2)^2 + N_1 q^2 + N_2}{2(a_1^2 - a_2^2)(q^2 - a_R^2)} \quad (17)$$

$$\Phi_1(q) = \Psi \frac{[\gamma - 2(m-1)](a_1^2 - q^2)^{1/2} + (a_2^2 - q^2)^{1/2}}{2(\alpha\beta)^{1/2} a_2^2} \frac{\kappa_1(q) + \kappa_2(q)}{\kappa_1(q) + \kappa_2(q)} \quad (18)$$

$$\Psi = \frac{\beta a_2^2}{(2\alpha)^{1/2}} \frac{[\gamma - (\gamma^2 - 4\alpha\beta)^{1/2}]^{1/2} + [\gamma + (\gamma^2 - 4\alpha\beta)^{1/2}]^{1/2}}{[\alpha\beta - (m-1)^2]} \quad (19)$$

$$N_1 = 4a_2^2 \frac{(\alpha\beta)^{1/2} - \alpha}{\gamma - 2(m-1)}, \quad N_2 = a_2^4 \frac{(\alpha\beta)^{1/2} [2(1-m) - \gamma + 4\alpha] - 4\alpha}{[\gamma - 2(m-1)](\alpha\beta)^{1/2}} \quad (20a,b)$$

with $\pm\alpha_R$ being the roots of the equation $Q(q)=0$. These roots correspond to anisotropic Rayleigh wavefronts in the physical space/time domain (Norris and Achenbach, 1984). The new functions Φ_0 and Φ_1 possess the asymptotic behavior at infinity needed for a factorization (Noble, 1958), i.e. that $\Phi_0 \rightarrow 1$ and $\Phi_1 \rightarrow 1$ when $|q| \rightarrow \infty$. Then, application of Cauchy's theorem provides

$$\Phi_0 = \Phi_{0+} \cdot \Phi_{0-}, \quad \Phi_1 = \Phi_{1+} \cdot \Phi_{1-} \quad (21a,b)$$

where

$$\Phi_{0\pm}(q) = \exp\left(-\frac{1}{\pi} \int_{\alpha_1}^{\alpha_2} \tan^{-1}\left[\frac{(4p^2 + N_1)(a_2^2 - p^2)^{1/2}(p^2 - a_1^2)^{1/2}}{(a_2^2 - 2p^2)^2 + N_1 p^2 + N_2}\right] \cdot \frac{1}{p \pm q} dp\right) \quad (22)$$

$$\Phi_{1\pm}(q) = \exp\left(-\frac{1}{\pi} \int_{\alpha_1}^{\alpha_2} \tan^{-1}\left[\frac{|a_1^2 - p^2|^{1/2} |\kappa_1(p)| - |a_2^2 - p^2|^{1/2} |\kappa_2(p)|}{|a_2^2 - p^2|^{1/2} |\kappa_1(p)| + |a_1^2 - p^2|^{1/2} |\kappa_2(p)|}\right] \cdot \frac{1}{p \pm q} dp\right) \quad (23)$$

Now, eqns (21) allow writing eqn (13) as

$$\left[\Sigma_{yy^+}^* - \frac{Fe^{sqL}}{s} \right] \frac{(a_1 + q)^{1/2}}{(q + a_R) \cdot \Phi_{0+} \cdot \Phi_{1+}} = c_{66}s \frac{(q - a_R) \cdot \Phi_{0-} \cdot \Phi_{1-}}{(a_1 - q)^{1/2} \Psi} U_{y^-}^* \quad (24)$$

Further, according to the decoupling technique (Georgiadis and Brock, 1993; Georgiadis and Rigatos, 1996), we obtain

$$\frac{\Sigma_{yy+}^*(q,s) \cdot (a_1 + q)^{1/2}}{(q + a_R) \cdot \Phi_{0+}(q) \cdot \Phi_{1+}(q)} = \frac{1}{2\pi i} \frac{F}{s} \left\{ i \int_{a_1}^{a_2} \frac{e^{-sL\omega} |a_1 - \omega|^{1/2} \Phi_{0+}(\omega) \cdot \Phi_{1+}(\omega) \cdot \hat{\Phi}(\omega)}{(\omega - a_R)(\omega + q)} d\omega + \right. \\ \left. + i 2 \int_{a_2}^{\infty} \frac{e^{-sL\omega} (\omega - a_1)^{1/2}}{(\omega - a_R)(\omega + q) \cdot \Phi_{0-}(\omega) \cdot \Phi_{1-}(\omega)} d\omega \right\} \quad (25)$$

where

$$\hat{\Phi}(\omega) = \frac{4(\omega^2 - a_R^2)}{X \left[T^2 + |a_1^2 - \omega^2| |a_2^2 - \omega^2| (4\omega^2 + N_1)^2 \right]} \left\{ |\kappa_1| |a_2^2 - \omega^2|^{1/2} [|a_1^2 - \omega^2| (4\omega^2 + N_1) - T] - \right. \\ \left. - |\kappa_2| |a_1^2 - \omega^2|^{1/2} [|a_2^2 - \omega^2| (4\omega^2 + N_1) + T] \right\} \quad (26)$$

$$X = \Psi \frac{\alpha\beta - (m-1)^2}{2(a\beta)^{1/2} a_2^2}, \quad T = (a_2^2 - 2\omega^2)^2 + N_1\omega^2 + N_2 \quad (27a,b)$$

5. Results

Equation (25) may provide the cleavage stress in the physical space/time domain by two successive LT inversions according to (6b) and (5b). The former inversion is accomplished asymptotically by invoking the Abel-Tauber theorem. The latter is obtained through properties of convolution of one-sided LTs. The time Laplace transformed stress is found as

$$\lim_{x \rightarrow +0} \Sigma_{yy}(x, y=0, s) = \frac{F}{2\pi(\pi x s)^{1/2}} \left\{ \int_{a_1}^{a_2} \frac{e^{-sL\omega} (\omega - a_1)^{1/2} \Phi_{0+} \Phi_{1+} \hat{\Phi}}{(\omega - a_R)} d\omega + \right. \\ \left. + 2 \int_{a_2}^{\infty} \frac{e^{-sL\omega} (\omega - a_1)^{1/2}}{(\omega - a_R) \cdot \Phi_{0-} \Phi_{1-}} d\omega \right\} \quad (28)$$

whereas the stress intensity factor (SIF), $k_I(t) \equiv \lim_{x \rightarrow +0} [(2\pi x)^{1/2} \cdot \sigma_{yy}(x, y=0, t)]$, has the following *exact* form

$$k_I(t) = \frac{(2/\pi L)^{1/2} F}{\pi} \cdot \int_0^t \left(\frac{(\tau - La_1)^{1/2}}{(\tau - La_R)(t - \tau)^{1/2}} \left[\frac{H(\tau - La_2)}{\Phi_{0-}(\tau) \cdot \Phi_{1-}(\tau)} + \right. \right. \\ \left. \left. + \frac{1}{2} [H(\tau - La_1) - H(\tau - La_2)] \cdot \Phi_{0+}(\tau) \cdot \Phi_{1+}(\tau) \cdot \hat{\Phi}(\tau) \right] \right) d\tau \quad (29)$$

The graph in Fig. 2 shows the variation of the normalized SIF $k_l [(2/\pi L)^{1/2} F]^{-1}$ with the normalized time $t/(La_2)$ for Boron Epoxy. This composite has the following material constants: $\alpha = 35.47$, $\beta = 11.47$, $\gamma = 402.5$, $n^{1/2} = 1407.12$ m/sec and $\rho = 2.44$ gr/cm³. It is noticeable here that the SIF takes on positive values only after the arrival of the anisotropic Rayleigh wave at the crack tip.

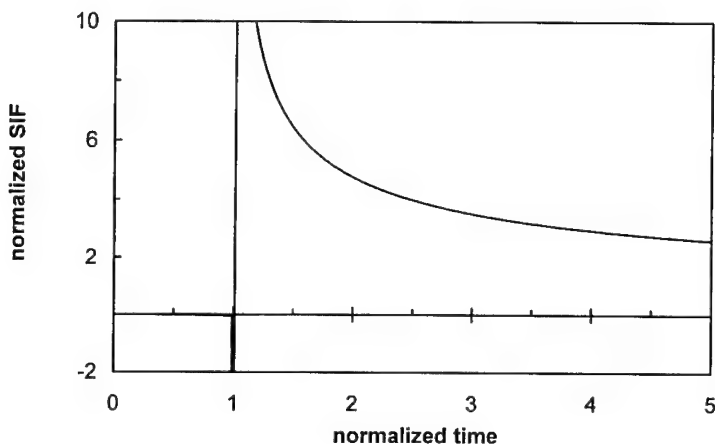


Figure 2. Normalized SIF versus normalized time for Boron Epoxy.

Acknowledgment: The authors acknowledge with thanks support of this research by the Greek General Secretariat for Research and Technology under the program PENED 99 ED 642. Also, HGG is thankful to Prof. G.A. Kardomateas (Georgia Tech) for discussions on subjects related to the present work.

References

- Georgiadis, H.G. and Brock, L.M. (1993) An exact method for cracked elastic strips under concentrated loads - Time-harmonic response, *International Journal of Fracture* **63**, 201-214.
- Georgiadis, H.G. and Rigatos, A.P. (1996) Transient SIF results for a cracked viscoelastic strip under concentrated impact loading - An integral-transform/function-theoretic approach, *Wave Motion* **24**, 41-57.
- Knowles, J.K. and Pucik, T.A. (1973) Uniqueness for plane crack problems in linear elastostatics, *Journal of Elasticity* **3**, 155-160.
- Lekhnitskii, S.G. (1963) *Theory of Elasticity of an Anisotropic Elastic Body*, Holden-Day, San Francisco.
- Noble, B. (1958) *Methods Based on the Wiener-Hopf Technique*, Pergamon Press, New York.
- Norris, A.N. and Achenbach, J.D. (1984) Elastic wave diffraction by a semi-infinite crack in a transversely isotropic material, *Quarterly Journal of Mechanics and Applied Mathematics* **37**, 565-580.
- Payton, R.G. (1983) *Elastic Wave Propagation in Transversely Isotropic Media*, Martinus Nijhoff, The Hague.

EFFECT OF AN IMPERFECT INTERFACE ON ELASTIC P-WAVE SCATTERING BY A SPHERICAL INCLUSION

ANIL C. WIJEYEWICKREMA

*Department of Civil Engineering, Tokyo Institute of Technology
Ookayama, Meguro-ku, Tokyo 152-8552, Japan*

LAI MEI-CHIANG

*Department of Rapid Transit Systems, Taipei City Government
Taipei, Taiwan, R.O.C.*

1. Abstract

The wave function expansion method is utilized in the present study to investigate a spherical inclusion excited by an incident plane P-wave. The spherical obstacle is considered rigid while the exterior infinite medium is considered to be a homogenous, isotropic, elastic material. The imperfect interface is simulated by a spring type resistance model which can also accommodate the extreme cases of a perfect bond or a sliding interface. Results are presented for normalized rigid body displacements of the spherical inclusion and dynamic stress concentration factors. It is found that the effect of the flexibility of spring is more significant for reducing the dynamic stress concentration factor in tangential stress rather than in radial stress.

2. Introduction

The earliest study about spherical obstacles in an elastic medium, was the work of Ying and Truell (1956). They considered scattering by three types of fixed spherical obstacles, i.e. an isotropically elastic sphere, a rigid sphere and a spherical cavity due to an incident plane, longitudinal wave. A perfectly rigid sphere excited by a plane P-wave was investigated by Knopoff (1959) where the range of size of obstacles varied from very small to comparable to the wavelength. Pao and Mow (1963) also considered the same geometric problem as Ying and Truell (1956) for the case of incident plane compressional waves, but assumed that the displacement due to the combined incident and reflected waves must be associated with the rigid body translation. Iwashimizu (1972) treated the scattering of P and S waves by a movable rigid sphere embedded in an infinite elastic material, and compared the scattering cross section with that obtained by others, especially in the Rayleigh limit.

The scattering behavior for an incident transverse wave is totally different from the case of an incident longitudinal wave. A spherical obstacle scattering an incident plane transverse wave, is no longer an axially symmetric problem, like the behavior under a longitudinal plane wave. Einspruch et al. (1960) investigated the scattering of a shear wave by a spherical discontinuity where the scattering is due to a cavity, a rigid sphere, a fluid-filled cavity and an elastic inclusion with properties different from those of the surrounding material. Kraft and Franzblau (1971) investigated the scattering of transverse waves from an empty spherical cavity in a solid and the relative contributions of the various components of longitudinal and transverse scattering cross sections were

isolated from each other. Jain and Kanwal (1978) studied the scattering of low frequency plane harmonic elastic P and S waves when they impinged on a movable or an immovable rigid spherical inclusion or a spherical cavity by an integral equation perturbation technique. Hinders (1991) and Bogan et al. (1992) investigated the scattering of elastic waves from an elastic spherical inclusion of arbitrary size in an infinite elastic medium. The scatterer and exterior medium are isotropic, homogeneous and linear elastic. They assumed arbitrarily differing material parameters with compressional and shear waves in both media. Exact expressions for the scattered and transmitted field, caused by an incident plane compressional or shear waves of unit amplitude, were calculated analytically, and general expressions for extinction cross sections and scattering cross sections were derived.

Mow (1965) investigated the transient response of a rigid spherical inclusion of arbitrary density, embedded in an elastic medium, due to an incident P-wave. He used the Fourier-integral method and obtained an exact solution of this response. The same geometric problem was considered by Wijeyewickrema and Keer (1989) who calculated the response of the inclusion and the interfacial stresses by the Fourier synthesis technique. This method of solution yields an exact solution for the inclusion response. They also found that the interfacial stresses were suitably expressed by an infinite series in the long-time response. In the early time analysis, the problem was reformulated in the Laplace transform domain and the results in the shadow region were obtained by utilizing the Watson's transformation.

The boundary element method has been used to study P-wave scattering by a spherical cavity and a spherical inclusion with a perfect interface and an imperfect interface by Kitahara et al. (1989a, 1989b, 1990).

In order to characterize defects Gubernatis et al. (1979), Kohn and Rice (1979) and Sotiropoulos et al. (1987) have investigated elastic wave scattering from spherical and ellipsoidal flaws.

In the present study a rigid sphere embedded in a linear-elastic full space with an imperfect interface, subjected to an incident plane P-wave is considered using the procedures adopted by Pao and Mow (1963, 1973).

3. An imperfectly Bonded Rigid Spherical Inclusion Excited by a Plane P-Wave

When a spherical inclusion is much more rigid than the surrounding material, it may be treated as a perfectly rigid sphere. A rigid spherical inclusion and an incident wave is shown in Fig. 1. Ying and Truell (1956) solved the problem of a sphere fixed in a certain position by external forces or other constraints. Since this is not very realistic considering that the sphere is embedded in an infinite elastic solid, it is assumed that the sphere will translate as a rigid body under the impact of incident waves. Since a rigid spherical inclusion is considered in this study, there are no refracted waves inside the sphere. A spring type resistant model is introduced, to simulate the imperfectly bonded interface.

3.1 BASIC EQUATIONS

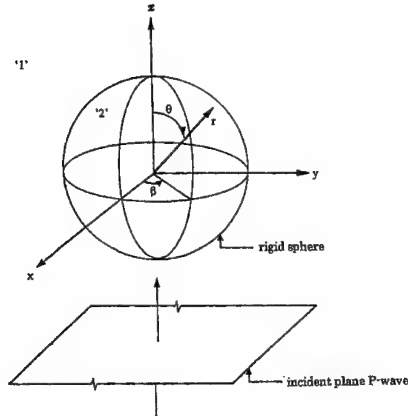


Figure 1. A rigid spherical inclusion excited by a plane P-wave.

The spherical coordinate system (r, θ, β) used is shown in Fig. 1, where the elastic infinite medium is denoted '1' and the rigid sphere of radius a is denoted '2'. The superscripts (in), (sc), and (t) represent incident, scattered and total waves respectively. In medium 1, the total wave is the sum of the incident wave and the scattered wave. The displacement potential due to the incident wave propagating in the positive z-direction can be expressed as,

$$\phi^{(in)}(r, \theta, t) = \varphi_0 e^{i(k_{p1}z - \omega t)}, \quad (3.1)$$

where k_{p1} is the wave number of the P-wave in medium 1, ω is the circular frequency and φ_0 is the amplitude of the incident wave. Equation (3.1) can be rewritten as

$$\phi^{(sc)}(r, \theta, t) = \varphi_0 e^{-i\omega t} \sum_{n=0}^{\infty} (2n+1) i^n j_n(k_{p1} r) P_n(\cos \theta), \quad (3.2)$$

where j_n is the spherical Bessel function of the first kind of order n and P_n is the Legendre polynomial.

The two outward propagating reflected waves can be represented by

$$\phi^{(sc)}(r, \theta, t) = e^{-i\omega t} \sum_{n=0}^{\infty} A_n h_n^{(1)}(k_{s1} r) P_n(\cos \theta), \quad (3.3)$$

$$\psi^{(sc)}(r, \theta, t) = e^{-i\omega t} \sum_{n=0}^{\infty} B_n h_n^{(0)}(k_{s1} r) P_n(\cos \theta), \quad (3.4)$$

where $h_n^{(1)}$ is the spherical Hankel function of the first kind of order n , k_{s1} is the wave number of the S-wave in medium 1 and A_n, B_n are unknown expansion coefficients.

For the axisymmetric case under consideration, the relevant non-zero displacements and stresses in the medium 1 are,

$$u_{r1}^{(i)}(r, \theta, t) = \frac{1}{r} e^{-i\omega t} \sum_{n=0}^{\infty} [-\varphi_0 \xi_{10} + A_n \xi_{11} + B_n \xi_{12}] P_n(\cos \theta), \quad (3.5)$$

$$u_{\theta 1}^{(i)}(r, \theta, t) = \frac{1}{r} e^{-i\omega t} \sum_{n=0}^{\infty} [-\varphi_0 \xi_{20} + A_n \xi_{21} + B_n \xi_{22}] \frac{d}{d\theta} P_n(\cos \theta), \quad (3.6)$$

$$\sigma_{r1}^{(i)}(r, \theta, t) = \frac{2\mu_1}{r^2} e^{-i\omega t} \sum_{n=0}^{\infty} [-\varphi_0 \xi_{30} + A_n \xi_{31} + B_n \xi_{32}] P_n(\cos \theta), \quad (3.7)$$

$$\sigma_{\theta 1}^{(i)}(r, \theta, t) = \frac{2\mu_1}{r^2} e^{-i\omega t} \sum_{n=0}^{\infty} [-\varphi_0 \xi_{40} + A_n \xi_{41} + B_n \xi_{42}] \frac{d}{d\theta} P_n(\cos \theta), \quad (3.8)$$

where the coefficients ξ_i , ($i = 1 - 4, j = 0, 1, 2$) are given in the Appendix, μ_1 is the shear modulus of medium 1 and the expansion coefficients A_n, B_n are to be determined by appropriate boundary conditions.

3.2 DETERMINATION OF THE EXPANSION COEFFICIENTS FOR AN IMPERFECTLY BONDED RIGID SPHERE

Due to the axisymmetric situation, the rigid body displacement of the sphere $U_z(t)$ is in the direction of the incident P-wave. It is assumed that a displacement jump is allowed in the θ -direction and that the displacement must be continuous in the radial direction, i.e., slip is allowed but a gap is not permitted between the sphere and the elastic medium. The displacement jump between the elastic medium and the inclusion in the tangential direction is considered to be proportional to the shear stress at the interface. Hence, the boundary conditions at $r = a$ are,

$$[u_{r1}^{(m)}(a, \theta) + u_{r1}^{(sc)}(a, \theta)] = u_{r2}(a, \theta), \quad (3.9)$$

$$[u_{\theta 1}^{(m)}(a, \theta) + u_{\theta 1}^{(sc)}(a, \theta)] - u_{\theta 2}(a, \theta) = \Lambda \sigma_{\theta 1}^{(i)}(a, \theta), \quad (3.10)$$

where $u_{r2}(a, \theta) = U_z \cos \theta$, $u_{\theta 2}(a, \theta) = -U_z \sin \theta$ and Λ is an interfacial sliding flexibility parameter where $\Lambda = 0$ represents a perfectly bonded interface and $\Lambda \rightarrow \infty$ represents a sliding interface. The displacement U_z is determined by the equation of motion,

$$m \ddot{U}_z = \int_0^{2\pi} \int_0^\pi (\sigma_{r1}^{(i)}(a, \theta) \cos \theta - \sigma_{\theta 1}^{(i)}(a, \theta) \sin \theta) a^2 \sin \theta d\theta d\beta, \quad (3.11)$$

where $m = \frac{4}{3} \pi a^3 \rho_2$ is the mass, and ρ_2 is the mass density of the sphere and the integral over the spherical surface represents the force components acting on the sphere. By introducing eqns (3.7) and (3.8) into eqn (3.11), the displacement caused by rigid body motion can be expressed as,

$$U_z = \frac{\bar{\rho}}{a} [3i\varphi_0 j_1(k_{p1}a) + A_1 h_1^{(1)}(k_{p1}a) - 2B_1 h_1^{(1)}(k_{p1}a)] e^{-i\omega t}, \quad (3.12)$$

where $\bar{\rho} = \rho_1/\rho_2$ is the density ratio of the medium to the inclusion and ρ_1 is the mass density of the elastic medium.

The expansion coefficients A_1, B_1 and $A_n, B_n, (n = 0, 2, 3, \dots)$ can be determined after substituting for the displacements and the stress $\sigma_{r\theta}^{(1)}$ from eqns (3.5), (3.6) and (3.8) into the boundary conditions eqns (3.9) and (3.10), and are given in the Appendix.

3.3 RIGID BODY MOTION OF THE SPHERICAL INCLUSION

Substituting for A_1 and B_1 from eqns (A.13) and (A.14) into eqn (3.12), the rigid body displacement of the sphere is

$$U_z = \Delta e^{-i\omega t}, \quad (3.13)$$

where

$$\Delta = \frac{-3\varphi_0 \bar{\rho}}{|D_1|} \kappa \left[\left(1 + 2 \frac{\mu_1 \Lambda}{a} \right) h_2^{(1)}(k_{s1}a) - k_{s1}a \frac{\mu_1 \Lambda}{a} h_1^{(1)}(k_{s1}a) \right], \quad (3.14)$$

$|D_1|$ is given by eqn (A.17) and

$$\kappa^2 = \left(\frac{k_{s1}}{k_{p1}} \right)^2 = \frac{2(1 - \nu_1)}{1 - 2\nu_1}, \quad (3.15)$$

where ν_1 is the Poisson's ratio of medium 1.

From the incident displacement potential defined by eqn (3.1), the displacement and stress in the incident direction can be expressed as,

$$u_z^{(in)} = \varphi_0 i k_{p1} e^{i(k_{p1}z - \omega t)}, \quad (3.16)$$

$$\sigma_{zz}^{(in)} = \sigma_0 e^{i(k_{p1}z - \omega t)}, \quad (3.17)$$

where $\sigma_0 = -(\lambda_1 + 2\mu_1)k_{p1}^2\varphi_0 = -\mu_1 k_{s1}^2 \varphi_0$ and λ_1 is the Lamé's elastic constant of medium 1. It is noted that σ_0 is the stress amplitude of the incident wave, in the direction of propagation. The rigid body motion of the sphere, normalized by the amplitude of eqn (3.16) can be expressed as

$$\bar{U}_z\left(\bar{\rho}, \kappa, \frac{\mu_1 \Lambda}{a}, k_{p1} a\right) = \frac{3i\bar{\rho}}{k_{p1} a |D_1|} \kappa e^{-i\omega t} \left[\left(1 + 2\frac{\mu_1 \Lambda}{a}\right) h_2^{(1)}(k_{s1} a) - k_{s1} a \frac{\mu_1 \Lambda}{a} h_1^{(1)}(k_{s1} a) \right]. \quad (3.18)$$

For the perfectly bonded interface, i.e., when $\Lambda = 0$, eqn (3.18) yields

$$\begin{aligned} \bar{U}_z\left(\bar{\rho}, \kappa, 0.0, k_{p1} a\right) &= \frac{3i\bar{\rho}\kappa h_2^{(1)}(k_{s1} a)e^{-i\omega t}}{\left[k_{p1} a(1 - \bar{\rho})h_1^{(1)}(k_{p1} a)h_2^{(1)}(k_{s1} a) + 2(1 - \bar{\rho})h_2^{(1)}(k_{p1} a)h_1^{(1)}(k_{s1} a)\right.} \\ &\quad \left.\left.- k_{s1} a h_2^{(1)}(k_{p1} a)h_1^{(1)}(k_{s1} a)\right]\right] \end{aligned} \quad (3.19)$$

which agrees with Pao and Mow (1973, p. 649, eqn 4.3).

For the rigid body motion, two special cases are of interest. The first case is when $\bar{\rho} = 0$, i.e. when the obstacle is much heavier than the surrounding medium. From eqn (3.18), it can be easily seen that the normalized displacement $\bar{U}_z\left(0.0, \kappa, \frac{\mu_1 \Lambda}{a}, k_{p1} a\right)$ is zero, i.e., the spherical inclusion does not move. The second case is when the density of inclusion and medium are the same, i.e., $\bar{\rho} = 1$, and here the normalized displacement is reduced to

$$\bar{U}_z\left(1.0, \kappa, \frac{\mu_1 \Lambda}{a}, k_{p1} a\right) = -\frac{3ie^{-i\omega t}}{k_{p1}^3 a^3 h_2^{(1)}(k_{p1} a)}. \quad (3.20)$$

From eqn (3.20) it is seen that when $\bar{\rho} = 1$, the normalized rigid body motion of the sphere is independent of the material properties of the surrounding medium and the interfacial sliding flexibility parameter and is only dependent on the incident wave number. An analogous result was obtained for the perfect bond case by Pao and Mow (1973, p. 649).

The normalized rigid body displacement of the spherical inclusion for different values of $\frac{\mu_1 \Lambda}{a}$ are shown in Fig. 2.

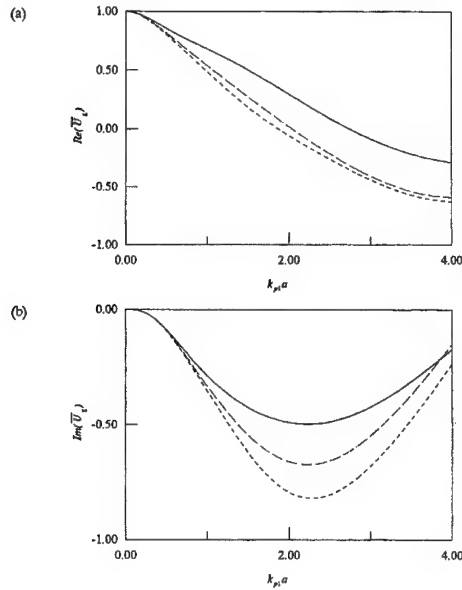


Figure 2. Normalized rigid body displacement of spherical inclusion for various $\frac{\mu_1\Lambda}{a}$
when $\bar{\rho} = 10.0$ and $\kappa = \sqrt{3}$, (a) $\text{Re}(\bar{U}_z)$ and (b) $\text{Im}(\bar{U}_z)$;
—— : $\frac{\mu_1\Lambda}{a} = 0.0$; - - - : $\frac{\mu_1\Lambda}{a} = 0.5$; - · - : $\frac{\mu_1\Lambda}{a} = 1.0$.

3.4 DYNAMIC STRESS CONCENTRATION FACTORS

Expressions for the stresses can be obtained from eqns (3.7) and (3.8) and are normalized by σ_0 , the stress amplitude of the incident wave (see eqn 3.17), to obtain,

$$\bar{\sigma}_{rrl}(a, \theta) = \frac{-e^{-i\omega t}}{k_{p1}a} \left[F_{31} P_1(\cos \theta) + \sum_{\substack{n=0 \\ n \neq 1}}^{\infty} G_{3n} P_n(\cos \theta) \right], \quad (3.21)$$

$$\bar{\sigma}_{r\theta l}(a, \theta) = \frac{e^{-i\omega t}}{k_{p1}a} \left[F_{41} \frac{d}{d\theta} P_1(\cos \theta) + \sum_{\substack{n=0 \\ n \neq 1}}^{\infty} G_{4n} \frac{d}{d\theta} P_n(\cos \theta) \right]. \quad (3.22)$$

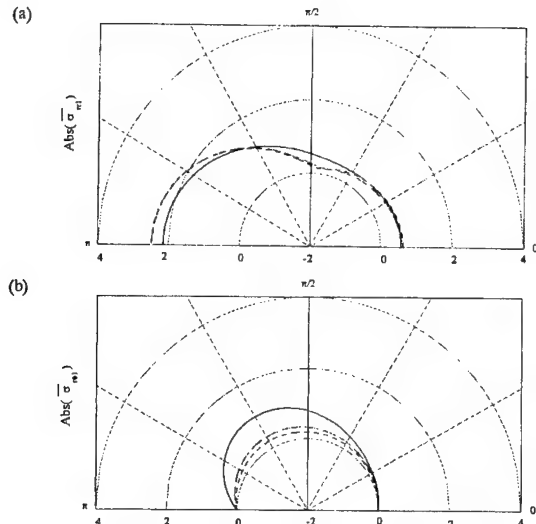


Figure 3. Dynamic stress concentration factors vs. θ , when $\bar{\rho} = 0.1$, $\kappa = \sqrt{3}$ and $k_{p1}a = 1.0$, (a) $\text{Abs}(\bar{\sigma}_{\tau n_1})$ and (b) $\text{Abs}(\bar{\sigma}_{r01})$;

$$\text{———} : \frac{\mu \Lambda}{a} = 0.0; \text{-----} : \frac{\mu \Lambda}{a} = 0.5; \text{.....} : \frac{\mu \Lambda}{a} = 1.0.$$

The normalized stresses given by eqn (3.21) and (3.22) are the *dynamic stress concentration factors* and the coefficients F_{31} , F_{41} , and G_{3n}, G_{4n} , ($n = 0, 2, 3, \dots$) are given in the Appendix.

In Figs. 3 and 4, the effect of the imperfect interface is shown for $k_{p1}a = 1.0$ and 0.1, respectively; where it can be observed that the effect of the sliding flexibility parameter is more significant in reducing the dynamic stress concentration factors in tangential stress rather than in the radial stress. From Fig. 3 it can be seen that the dynamic stress concentration factors are higher on the incident side ($\pi/2 < \theta < \pi$) and lower on the shadow side ($0 < \theta < \pi/2$). Figure 4 indicates that when $k_{p1}a = 0.1$, the dynamic stress concentration factors are symmetric about the plane $\theta = \pi/2$, i.e. for low values of $k_{p1}a$ the solution tends to the static solution of Goodier (1933).

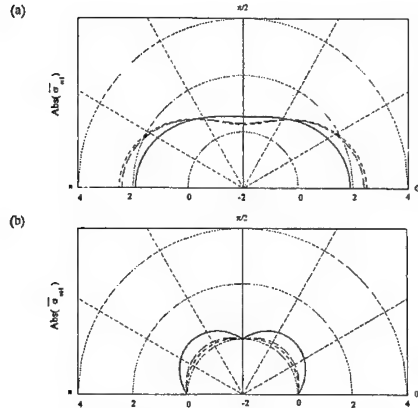


Figure 4. Dynamic stress concentration factors vs θ , when $\bar{\rho} = 0.1$, $\kappa = \sqrt{3}$ and $k_p a = 0.1$, (a) $\text{Abs}(\bar{\sigma}_{r1})$ and (b) $\text{Abs}(\bar{\sigma}_{r01})$;
 $\text{———} : \frac{\mu\Lambda}{a} = 0.0$; $\text{-----} : \frac{\mu\Lambda}{a} = 0.5$; $\text{.....} : \frac{\mu\Lambda}{a} = 1.0$.

Acknowledgements

The second author gratefully acknowledges a partial scholarship from the Asian Institute of Technology, Thailand, which enabled her to complete her graduate studies. The research reported in this article was carried out at the School of Civil Engineering, AIT.

References

- Bogart, S. D., Fang, T. M. and Hinders, M. K., (1992), "Spherical-Wave Scattering from an Elastic Sphere", *Il Nuovo Cimento*, Vol. 107B, No. 10, pp. 1215-1217.
- Einspruch, N. G., Witterholt, E. J. and Truell, R., (1960), "Scattering of a Plane Transverse Wave by a Spherical Obstacle in an Elastic Medium", *Journal of Applied Physics*, Vol. 31, No. 5, pp. 806-818.
- Goodier, J. N., (1933), "Concentration of Stress Around Spherical and Cylindrical Inclusions and Flaws", *Journal of Applied Mechanics, Transactions of the ASME*, Vol. 1, pp. 39-44.
- Gubernatis, J. E., Krumhansl, J. A. and Thomson, R. M., (1979), "Interpretation of Elastic-Wave Scattering Theory for Analysis and Design of Flaw-Characterization Experiments: The Long-wavelength Limit", *Journal of Applied Physics*, Vol. 50, pp. 3338-3345.
- Hinders, M. K., (1991), "Plane-Elastic-Wave Scattering from an Elastic Sphere", *Il Nuovo Cimento*, Vol. 106B, No. 7, pp. 799-818.
- Iwashimizu, Y., (1972), "Scattering of Elastic Waves by a Movable Rigid Sphere Embedded in an Infinite Elastic Solid", *Journal of Sound and Vibration*, Vol. 21, No. 4, pp. 463-469.
- Jain, D. L. and Kanwal, R. P., (1978), "Scattering of P and S Waves by Spherical Inclusions and Cavities", *Journal of Sound and Vibration*, Vol. 57, No. 2, pp. 171-202.
- Kitahara, M., Nakagawa, K. and Achenbach, J. D., (1989a), "Boundary-Integral Equation Method for Elastodynamic Scattering by a Compact Inhomogeneity", *Computational Mechanics*, Vol. 5, pp. 129-144.
- Kitahara, M., Nakagawa, K. and Achenbach, J. D., (1989b), "Backscatter from a Spherical Inclusion with Compliant Interphase Characteristics", *Review of Progress in Quantitative Nondestructive Evaluation*, Vol. 8A, Edited by D. O. Thompson and D. E. Chimenti, Plenum Press, pp. 47-54.

Kitahara, M., Nakagawa, K. and Achenbach, J. D., (1990), "Scattering Characteristics of a Partially Debonded Compliant Inclusion-Matrix Interphase", *Review of Progress in Quantitative Nondestructive Evaluation*, Vol. 9, Edited by D. O. Thompson and D. E. Chimenti, Plenum Press, pp. 69-76.

Knopoff, L., (1959), "Scattering of Compression Waves by Spherical Obstacles", *Geophysics*, Vol. 24, No. 1, pp. 30-39.

Kohn, W. and Rice, J. R., (1979), "Scattering of Long-Wavelength Elastic Waves from Localized Defects in Solids", *Journal of Applied Physics*, Vol. 50, pp. 3346-3353.

Kraft, D. W. and Franzblau, M. C., (1971), "Scattering of Elastic Waves from a Spherical Cavity in a Solid Medium", *Journal of Applied Physics*, Vol. 42, No. 8, pp. 3019-3024.

Mow, C. C., (1965), "Transient Response of a Rigid Spherical Inclusion in an Elastic Medium", *Journal of Applied Mechanics, Transactions of the ASME*, Vol. 32, pp. 637-642.

Pao, Y. H. and Mow, C. C., (1963), "Scattering of Plane Compressional Waves by a Spherical Obstacle", *Journal of Applied Physics*, Vol. 34, No. 3, pp. 493-499.

Pao, Y. H. and Mow, C. C., (1973), *Diffraction of Elastic Waves and Dynamic Stress Concentrations*, Crane Russak, New York.

Sotiropoulos, D. A., Achenbach, J. D. and Zhu, H., (1987), "An Inverse Scattering Method to Characterize Inhomogeneities in Elastic Solids", *Journal of Applied Physics*, Vol. 62, pp. 2771-2777.

Wijeyewickrema, A. C. and Keer, L. M., (1989), "Transient Elastic Wave Scattering by a Rigid Spherical Inclusion", *Journal of Acoustical Society America*, Vol. 86, No. 2, pp. 802-809.

Ying, C. F. and Truell, R., (1956), "Scattering of a Plane Longitudinal Wave by a Spherical Obstacle in an Isotropically Elastic Solid", *Journal of Applied Physics*, Vol. 27, No. 9, pp. 1086-1097.

Appendix A

The functions ξ_{ij} , ($i = 1 - 4, j = 0, 1, 2$) appearing in eqns (3.5)-(3.8) are given by

$$\xi_{10} = -i^r(2n+1)[nj_n(k_{p1}r) - k_{p1}rj_{n+1}(k_{p1}r)], \quad (\text{A.1})$$

$$\xi_{20} = -i^r(2n+1)j_n(k_{p1}r), \quad (\text{A.2})$$

$$\xi_{30} = -i^r(2n+1)\left[\left(n^2 - n - \frac{1}{2}k_{s1}^2r^2\right)j_n(k_{p1}r) + 2k_{p1}rj_{n+1}(k_{p1}r)\right], \quad (\text{A.3})$$

$$\xi_{40} = -i^r(2n+1)[(n-1)j_n(k_{p1}r) - k_{p1}rj_{n+1}(k_{p1}r)], \quad (\text{A.4})$$

$$\xi_{11} = nh_n^{(1)}(k_{p1}r) - k_{p1}rh_{n+1}^{(1)}(k_{p1}r), \quad (\text{A.5})$$

$$\xi_{21} = h_n^{(1)}(k_{p1}r), \quad (\text{A.6})$$

$$\xi_{31} = \left(n^2 - n - \frac{1}{2}k_{s1}^2r^2\right)h_n^{(1)}(k_{p1}r) + 2k_{p1}rh_{n+1}^{(1)}(k_{p1}r), \quad (\text{A.7})$$

$$\xi_{41} = (n-1)h_n^{(1)}(k_{p1}r) - k_{p1}rh_{n+1}^{(1)}(k_{p1}r), \quad (\text{A.8})$$

$$\xi_{12} = -n(n+1)h_n^{(1)}(k_{s1}r), \quad (\text{A.9})$$

$$\xi_{22} = -(n+1)h_n^{(1)}(k_{s1}r) + k_{s1}rh_{n+1}^{(1)}(k_{s1}r), \quad (\text{A.10})$$

$$\xi_{32} = -n(n+1)[(n-1)h_n^{(1)}(k_{s1}r) - k_{s1}rh_{n+1}^{(1)}(k_{s1}r)], \quad (\text{A.11})$$

$$\xi_{42} = -\left(n^2 - 1 - \frac{1}{2}k_{s1}^2r^2\right)h_n^{(1)}(k_{s1}r) - k_{s1}rh_{n+1}^{(1)}(k_{s1}r) \quad (\text{A.12})$$

The expansion coefficients A_1, B_1 and $A_n, B_n, (n = 0, 2, 3, \dots)$ are given by,

$$A_1 = \frac{3i\varphi_0}{|D_1|} \left\{ k_{s1}^2 a^2 \frac{\mu_1 \Lambda}{a} (1 - \bar{\rho}) j_1(k_{p1} a) h_1^{(1)}(k_{s1} a) + k_{s1} a \left(1 + 2 \frac{\mu_1 \Lambda}{a} \right) (\bar{\rho} - 1) j_1(k_{p1} a) h_2^{(1)}(k_{s1} a) - k_{p1} a \left[k_{s1}^2 a^2 \frac{\mu_1 \Lambda}{a} + 2(1 - \bar{\rho}) - 4 \frac{\mu_1 \Lambda}{a} (\bar{\rho} - 1) \right] j_2(k_{p1} a) h_1^{(1)}(k_{s1} a) + k_{p1} k_{s1} a^2 \left(1 + 2 \frac{\mu_1 \Lambda}{a} \right) j_2(k_{p1} a) h_2^{(1)}(k_{s1} a) \right\} \quad (A.13)$$

$$B_1 = \frac{3\varphi_0}{k_{p1} a |D_1|} (1 - \bar{\rho}) \left(1 + 2 \frac{\mu_1 \Lambda}{a} \right), \quad (A.14)$$

$$A_n = \frac{(2n+1)i^n \varphi_0}{|D_n|} \left\{ k_{s1}^2 a^2 \frac{\mu_1 \Lambda}{a} j_n(k_{p1} a) h_n^{(1)}(k_{s1} a) - nk_{s1} a \left(1 + 2 \frac{\mu_1 \Lambda}{a} \right) j_n(k_{p1} a) h_{n+1}^{(1)}(k_{s1} a) - k_{p1} a \left[k_{s1}^2 a^2 \frac{\mu_1 \Lambda}{a} + (n+1) + 2 \frac{\mu_1 \Lambda}{a} (n+1) \right] j_{n+1}(k_{p1} a) h_n^{(1)}(k_{s1} a) + k_{p1} k_{s1} a^2 \left(1 + 2 \frac{\mu_1 \Lambda}{a} \right) j_{n+1}(k_{p1} a) h_{n+1}^{(1)}(k_{s1} a) \right\} \quad (n = 0, 2, 3, \dots), \quad (A.15)$$

$$B_n = -\frac{(2n+1)i^{n+1} \varphi_0}{k_{p1} a |D_n|} \left(1 + 2 \frac{\mu_1 \Lambda}{a} \right), \quad (n = 0, 2, 3, \dots), \quad (A.16)$$

where

$$|D_1| = \left\{ k_{s1}^2 a^2 \frac{\mu_1 \Lambda}{a} (\bar{\rho} - 1) h_1^{(1)}(k_{p1} a) h_1^{(1)}(k_{s1} a) + k_{s1} a \left(1 + 2 \frac{\mu_1 \Lambda}{a} \right) (1 - \bar{\rho}) h_1^{(1)}(k_{p1} a) h_2^{(1)}(k_{s1} a) + k_{p1} a \left[k_{s1}^2 a^2 \frac{\mu_1 \Lambda}{a} + 2(1 - \bar{\rho}) + 4 \frac{\mu_1 \Lambda}{a} (1 - \bar{\rho}) \right] h_2^{(1)}(k_{p1} a) h_1^{(1)}(k_{s1} a) - k_{p1} k_{s1} a^2 \left(1 + 2 \frac{\mu_1 \Lambda}{a} \right) h_2^{(1)}(k_{p1} a) h_2^{(1)}(k_{s1} a) \right\} \quad (A.17)$$

and

$$\begin{aligned}
|D_n| = & \left\{ nk_{s1}^2 a^2 \frac{\mu_1 \Lambda}{a} h_n^{(1)}(k_{p1} a) h_n^{(1)}(k_{s1} a) \right. \\
& + nk_{s1} a \left(1 + 2 \frac{\mu_1 \Lambda}{a} \right) h_n^{(1)}(k_{p1} a) h_{n+1}^{(1)}(k_{s1} a) \\
& + k_{p1} a \left[k_{s1}^2 a^2 \frac{\mu_1 \Lambda}{a} + (n+1) + 2(n+1) \frac{\mu_1 \Lambda}{a} \right] h_{n+1}^{(1)}(k_{p1} a) h_n^{(1)}(k_{s1} a) \\
& \left. - k_{p1} k_{s1} a^2 \left(1 + 2 \frac{\mu_1 \Lambda}{a} \right) h_{n+1}^{(1)}(k_{p1} a) h_{n+1}^{(1)}(k_{s1} a) \right\} \quad (n=0, 2, 3\dots).
\end{aligned} \tag{A.18}$$

The functions F_{31}, F_{41} and G_{3n}, G_{4n} , ($n = 0, 2, 3, \dots$) appearing in eqns (3.21) and (3.22) are given by,

$$F_{31} = \frac{3}{|D_1|} \left\{ k_{s1} a \left(1 + 2 \frac{\mu_1 \Lambda}{a} \right) h_2^{(1)}(k_{s1} a) - \left[k_{s1}^2 a^2 \frac{\mu_1 \Lambda}{a} - 2(\bar{\rho} - 1) \right] h_1^{(1)}(k_{s1} a) \right\}, \tag{A.19}$$

$$F_{41} = \frac{3}{|D_1|} (\bar{\rho} - 1) h_1^{(1)}(k_{s1} a), \tag{A.20}$$

$$\begin{aligned}
G_{3n} = & \frac{(2n+1)i^{n+1}}{|D_n|} \left\{ k_{s1}^2 a^2 \frac{\mu_1 \Lambda}{a} + (n+1) + 2(1-n^2) \frac{\mu_1 \Lambda}{a} \right\} h_n^{(1)}(k_{s1} a) \\
& - k_{s1} a \left(1 + 2 \frac{\mu_1 \Lambda}{a} \right) h_{n+1}^{(1)}(k_{s1} a) \quad (n=0, 2, 3, \dots),
\end{aligned} \tag{A.21}$$

$$G_{4n} = \frac{(2n+1)i^{n+1}}{|D_n|} h_n^{(1)}(k_{s1} a), \quad (n=0, 2, 3, \dots). \tag{A.22}$$

RECENT ADVANCES OF THE USE OF LAMB WAVES FOR MATERIAL CHARACTERIZATION

T. KUNDU

Department of Civil Engineering and Engineering Mechanics

University of Arizona, Tucson, AZ 85721, USA

e-mail: tkundu@u.arizona.edu, fax: 520-621-2550

Abstract

In recent years Lamb waves have been successfully used for detecting defects in homogeneous metal plates, coated plates, and multi-layered composite plates. Different Lamb modes generate various stress and displacement profiles in the plate. These stress and displacement components are altered by the internal defects, and thus the defects are detected. All Lamb modes are not equally sensitive to a particular defect. A number of studies have been carried out to identify which Lamb mode is most effective for detecting a defect at a specific location of the plate. Superiority of the Lamb wave inspection technique compared to the conventional ultrasonic technique using P-waves has been established. The overwhelming success of the Lamb wave inspection technique for metal and composite plate inspection has encouraged Kundu and his coworkers to investigate its applicability for some new problems. The new applications include internal defect detection in metal pipes, concrete beams, as well as some new applications in composite plate inspection. One such new application is to generate the "Near-Lamb Mode Image" of a multi-layered composite plate, instead of the "Lamb Mode Image". Advantage of the "Near-Lamb Mode Image" is that it can distinguish between the layers of mirror symmetry in a composite plate. The pipe inspection has been carried out by the higher-order non-axisymmetric flexural modes instead of the commonly used longitudinal and torsional modes. A brief review of these recent advances of the Lamb wave inspection technique is presented in this paper.

1. Introduction

Lamb waves, also known as *guided waves*, are elastic stress waves that are observed in plates and pipes. These waves are guided by the traction free boundary surfaces of a plate and by the traction-free outer and inner surfaces of a hollow cylinder. The plate or pipe structure that helps the guided wave to propagate is called a *wave-guide*. The Lamb wave observed in a plate is also known as the *plate wave*; the Lamb wave in a cylinder is more commonly known as the *cylindrical guided wave*. When the plate or pipe is immersed in a liquid then the boundary surfaces are not traction free and the energy of

the propagating wave leaks into the surrounding liquid and the propagating wave is called the *leaky Lamb wave*.

Lamb waves have an infinite number of modes that a plate can vibrate with. Different Lamb modes can be generated by changing the signal frequency and the incidence angle of the transmitter. In a homogeneous plate these modes can be classified into two groups, symmetrical and anti-symmetrical modes, according to the direction of the particle displacement.

Lamb waves propagate dispersively, that is the wave speed is a function of frequency. It excites the entire plate thickness unlike Rayleigh waves where the particle displacement is observed only in the region close to the surface.

1.1. ADVANTAGES OF USING LAMB WAVES FOR ULTRASONIC INSPECTION

With conventional ultrasonic methods, the area under interrogation at any instant is limited to the region covered by the transducer. As a result, the conventional methods are time consuming because transducer needs to inspect each point of the structure. However, the Lamb wave can be excited at one point of the structure and received at another point after propagating a considerable distance along the structure. This path length depends on the wavelength. With the pitch-catch arrangement, a receiving transducer, kept at a distance, picks up the propagating signals that contain information about the integrity of the region between the two transducers. Therefore, the Lamb wave inspection technique monitors a comparatively large region and requires less time.

The entire thickness of the plate can be inspected by different modes exciting different depths of the plate. This makes it possible to detect defects near the surfaces as well as those inside the plate because each mode has its own sensitivity to each defect along the depth.

Detection of defects by conventional ultrasonic methods is based on the principle of ultrasound being reflected or scattered by the defects. Therefore, the wavelength determines the smallest size defect that can be detected by certain signal. Small defects cannot be detected by signals of low frequencies. On the other hand the high frequency signals have high attenuation. That is why there is always a compromise between the smallest defect that can be detected and the maximum distance of the defect from the transducers for successfully detecting the defect. The Lamb wave inspection technique is very promising for detecting small defects because the defect detection capability does not simply depend on the reflection of the waves from defects, but on how the waves interact with them. This important interaction affects the $V(f)$ (Voltage amplitude versus frequency) curves in two ways. The peak amplitude corresponding to a particular Lamb mode may change because of the presence of a defect, or there may be a frequency shift of the peak amplitude.

In summary, Lamb waves are used because they offer an improved inspection potential due to their multi-mode characteristics, sensitivity to different types of flaws, propagation over long distances, guiding character that enables them to follow curvature and reach hidden and/or buried parts, and the capability of in-situ testing.

The theory of Lamb wave propagation in multi-layered plates (Karim, Mal and Bar-Cohen, 1990; Mal, Yin and Bar-Cohen, 1991; Taylor and Nayfeh, 1992; Potel and de Belleval, 1993a,b; Castaings and Hosten, 1994; Nayfeh, 1995; Yang and Kundu, 1998)

and pipes (Gazis, 1959) are available in the literature. Those theories are not repeated here. Different applications of the Lamb wave inspection technique are described below.

2. Pipe Inspection

Pipeline operators use a variety of methods to give their pipes periodic checkups, but all these methods use a "smart pig," a robotic device that crawls through the pipe carrying sensors. Smart pigs are expensive to run, several thousand US Dollars per mile (Kiefner, 1986) and the results sometimes are not reliable. Under the best circumstances, smart pigs only provide data for infrequent periodic integrity assessment (once every two to ten years), yet crack and corrosion type defects may develop and grow between inspections. Furthermore, to use pigs, pipelines must allow free passage and must have pig launch and retrieval facilities that are not always available.

Because of the shortcomings of the current "smart pig" technique it is necessary to develop a technology to assess the integrity of the pipeline in non-intrusive manner without disrupting its operation. One way of doing it is by launching Lamb waves or cylindrical guided waves in the pipe. Lamb waves can be launched in the pipeline by ultrasonic excitors placed either at the outside wall or inside wall. Alleyne and Cawley (1995) have inspected pipe defects using Lamb waves. In their effort the time histories recorded by the receiver have been carefully analyzed for detecting any small signal reflected by the defect. Although this has been useful for detecting some defects, sometimes such small "defect signals" may remain undetected. Guo and Kundu (1998, 2000a,b) detected the pipe defect from the change in the $V(f)$ curve. $V(f)$ curve is the plot of the variation of the received signal voltage as a function of the signal frequency. Ideally, the strike angle and the signal frequency should be adjusted to launch the Lamb mode that is most sensitive to the pipe damage and least prone to attenuation and can propagate a long distance along the pipeline before losing its strength. Lamb wave frequency should be set at such a level that it is not affected by the noise generated by the fluid flowing through the pipe so that the pipes can be inspected under normal operating conditions. Guo and Kundu (1998, 2000a,b) have developed a new coupling mechanism for efficiently generating non-axisymmetric cylindrical Lamb waves in pipes. This new design is briefly described in the following; experimental results generated by the new coupling mechanism are also presented.

2.1. DESCRIPTION OF THE TRANSDUCER-PIPE COUPLING MECHANISM

Kundu et.al.(1996), Ghosh and Kundu (1999) selectively generated different Lamb modes in a plate by rotating the transducer in the coupling fluid, thus changing the incident angle of the striking beam and fine tuning the frequency of excitation. Following the same principle two small open-ended water containers were placed directly over the pipe wall as shown in Figure 1 to have similar capability (free rotation of transducers) for the pipe inspection. The water container shape was made conical to block the diverging signals from the transducer from reaching the pipe wall.

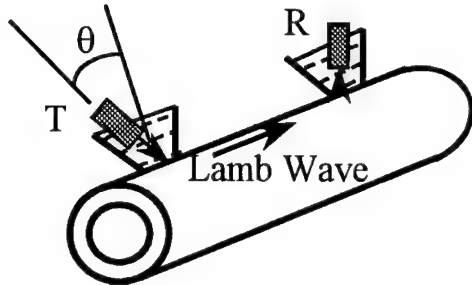


Figure 1. Relative Positions of the Transmitter (T), Receiver (R), Conical Containers and the Pipe Specimen

2.2. SPECIMENS

Five aluminum pipes of same dimensions, 22.2 mm (0.875 inch) outside diameter and 20.6 mm inside diameter have been inspected. The receiver was placed at a distance of 0.5 m from the transmitter. Received signals were first generated with a damage-free pipe. Then these signals were again recorded after replacing the defect-free pipe by four other pipes containing three types of defects – removed metal, dent, and gouge as shown in Figure 2. Most mechanical damage defects are combinations of these three primary components (Davis and T. A. Bubenik, 1996).

Figure 2 shows the defect free pipe (top geometry) and four defective pipes – one gouge, one dent and two removed metal type defects. Two different dimensions of removed metal type defects were fabricated and denoted by the terms ‘removed metal (less)’ and ‘removed metal (more)’. The gouge defect was fabricated by pressing the outer wall of the pipe while keeping the inner diameter unchanged by placing a rigid rod inside the pipe. The same size outer groove was made in another pipe by machining and removing the metal. Although dimensions (depth = 0.022 inch, width = 0.165 inch, see Figure 2) of the two defects [gouge and removed metal (less)] are identical they are different in many respects. The groove in the gouge was formed by removing no metal but pressing the pipe wall while the removed metal type defect was fabricated by removing metal from the pipe wall. The amount of cold working and residual stress is much more in the gouge defect than the removed metal type defect.

The bottom geometry of Figure 2 shows a dent type defect. It is formed by pressing the pipe wall at that location. During the formation of this defect the inner wall was free to move. As a result, both outer and inner diameters of the pipe were changed. For this defect the wall thickness did not change significantly in the defect position although the pipe diameter changed. This defect has the largest groove size (depth = 0.03 inch, width = 0.181 inch). The second from the bottom geometry shows another removed metal type defect with a different groove size (depth = 0.0245 inch, width = 0.173 inch), it is marked as removed metal (more).

2.3. EXPERIMENTAL RESULTS ON PIPE SPECIMENS

Receiving signal voltage versus frequency or $V(f)$ curves generated by the five aluminum pipe specimens of Figure 2 are shown in Figure 3.

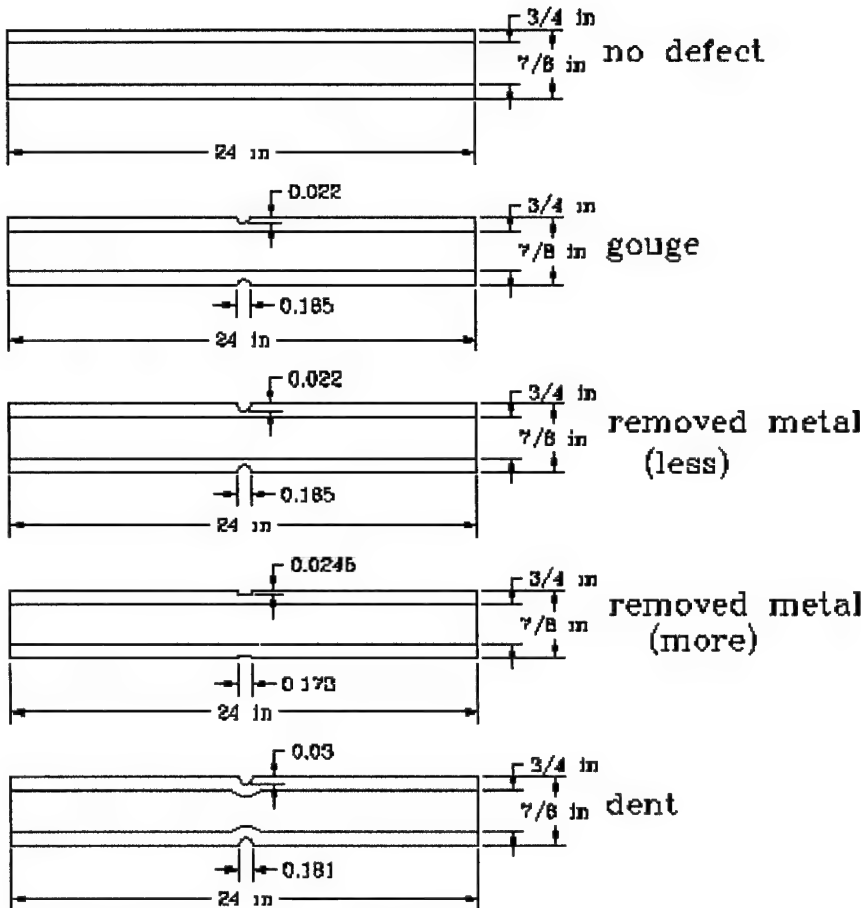


Figure 2. Aluminum pipe specimens – defect free (top) and four defective pipes containing gouge, dent and two removed metal type defects. All dimensions are in inch (1 inch = 25.4 mm) (after Guo and Kundu, 2000).

For generating these curves the transducers are inclined at 18° relative to the plane that is perpendicular to the pipe axis. This inclination is needed to generate strong Lamb modes in the pipe. The transmitter is excited in the tone-burst mode with the signal frequency continuously changing from 500 to 1400 kHz. The received signal amplitude is plotted (along the vertical axis) against the signal frequency to generate the V(f) curve. The curve with the cross markers is generated by the defect-free specimen. Two peaks, one near 700 kHz and the second one near 900 kHz correspond to two Lamb modes. V(f) curves for all defective specimens are smaller than the non-defective specimen. Percentage change of the peak amplitude due to the presence of the defect is more (almost 50% reduction) for the lower frequency mode than the higher frequency mode. However, the higher frequency mode is more sensitive to the type of defect. V(f) curves for the two removed metal type defects are shown by solid and open square markers. As expected, removal of more metal gives rise to smaller V(f) curves (line with open

squares). $V(f)$ curve generated by the gouge is shown by open circles. It is interesting to note that although gouge and one removed metal type defect have same groove dimensions [depth = 0.022 inch (0.56 mm), width = 0.165 inch (4.19 mm)], $V(f)$ curves corresponding to these two defects (curves with open square and open circle markers, respectively) are quite different. From these experimental results it can be concluded that the non-axisymmetric Lamb waves generated by the new transducer holder mechanism can detect and distinguish between different types of mechanical defects in pipes.

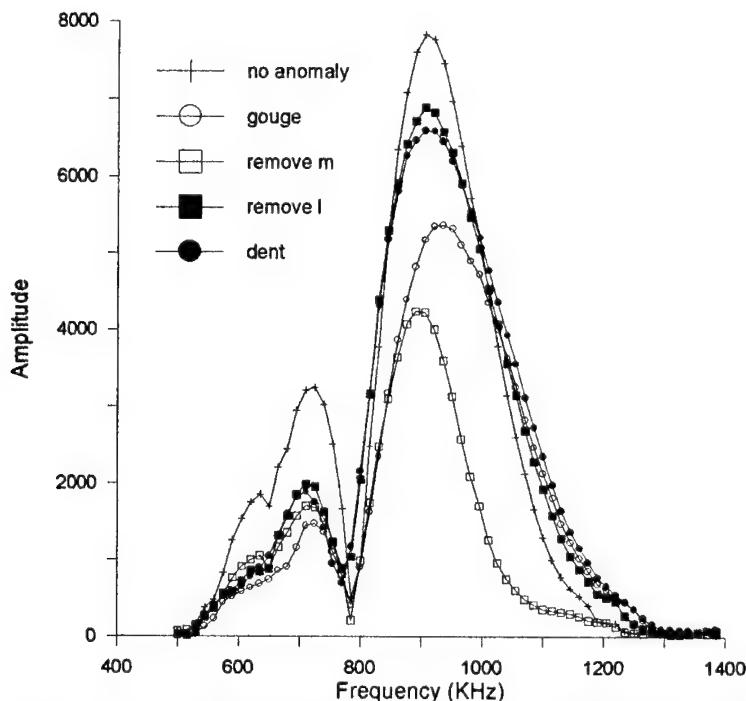


Figure 3. $V(f)$ curves for the five aluminum pipe specimens. Frequency is plotted along the horizontal axis in kHz. Received voltage amplitude is plotted along the vertical axis. Transmitter inclination angle for all curves is 18° (after Guo and Kundu, 2000).

3. Composite Plate Inspection

A number of investigators in the past have studied the Lamb wave propagation in composite plates (Karim, Mal and Bar-Cohen, 1990; Taylor and Nayfeh, 1992; Potel and de Belleval, 1993a,b; Castaings and Hosten, 1994; Nayfeh, 1995). Many investigators have also tried to use Lamb waves for damage detection in composite and metal plates (Mal, Yin, and Bar-Cohen, 1990; Karpur et.al., 1995, 1998; Maslov and Kundu, 1997; Kundu and Maslov, 1997; Yang and Kundu, 1998; Ghosh et.al., 1998; Ghosh and Kundu, 1999; Kundu et.al., 1996, 1998, 2000a,b). Kundu and associates (Kundu et.al., 1996; Maslov and Kundu, 1997; Kundu and Maslov, 1997) fabricated a multi-layered composite plate specimen and scanned it with different Lamb modes. Their experimental findings are presented below.

3.1. THE SPECIMEN

The specimen that was scanned by the Lamb wave is a five-layer metal matrix composite plate of dimension $80 \times 33 \times 1.97$ mm³. Orientations of five layers of fibers and internal defects of the specimen are shown schematically in Figure 4. Five layers or plies of SCS-6 fibers in Ti-6Al-4V matrix are oriented in 0° and 90° directions in alternate layers. SCS is a copyrighted/registered name by the fiber manufacturer, the Textron Inc. This fiber has a carbon core of about 25 μm diameter, two concentric layers of silicon carbide surround the carbon core and finally two very thin (a few microns thick) layers of carbon coating are placed on the outside. The overall fiber diameter is about 152 μm. The composite was made by foil-fiber-foil technique. The internal flaws, shown in Figure 4, were intentionally introduced in the plate during the fabrication process. The first (top) and the fifth (bottom) layers of fibers did not have any flaw. The left part of the second layer fibers (90°) was coated with boron nitride to impede the formation of good bonding between the fibers and the matrix as schematically shown in Figure 4. The fibers in the third layer (0°) were intentionally broken near the middle. The fourth layer (90°) had two areas of missing fibers, on the left side five fibers and on the right side ten fibers were removed.

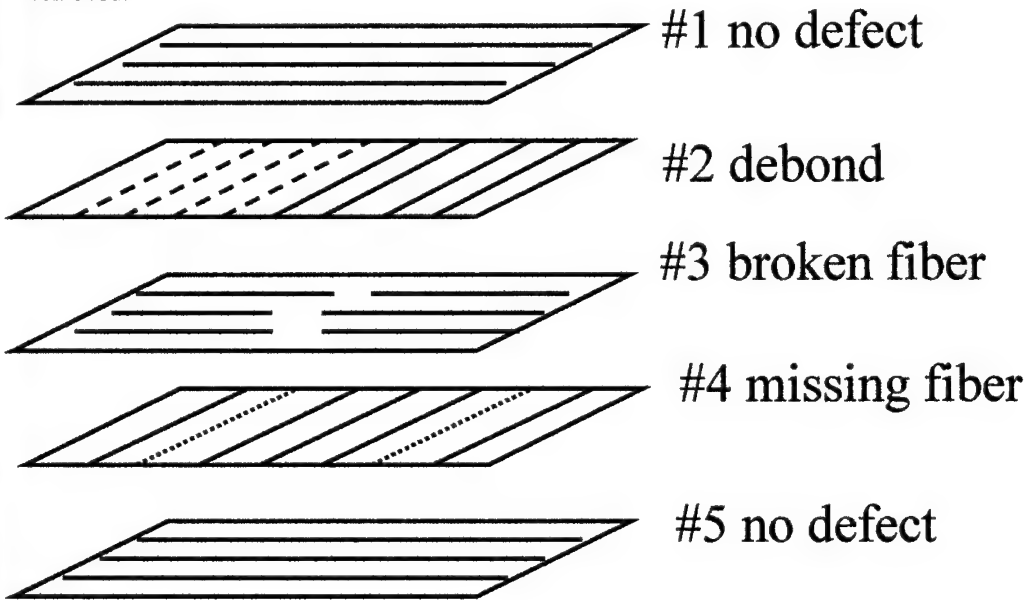


Figure 4. Schematic of the internal defects in the five layers of the composite plate specimen

3.2. EXPERIMENTAL RESULTS

Images generated by the conventional ultrasonic C-scan technique using normal incidence P-waves of different frequencies are shown in the left column of Figure 5. Images generated by different Lamb modes are shown in the right column of Figure 5. Clearly internal defects are more prominent in the Lamb wave generated images.

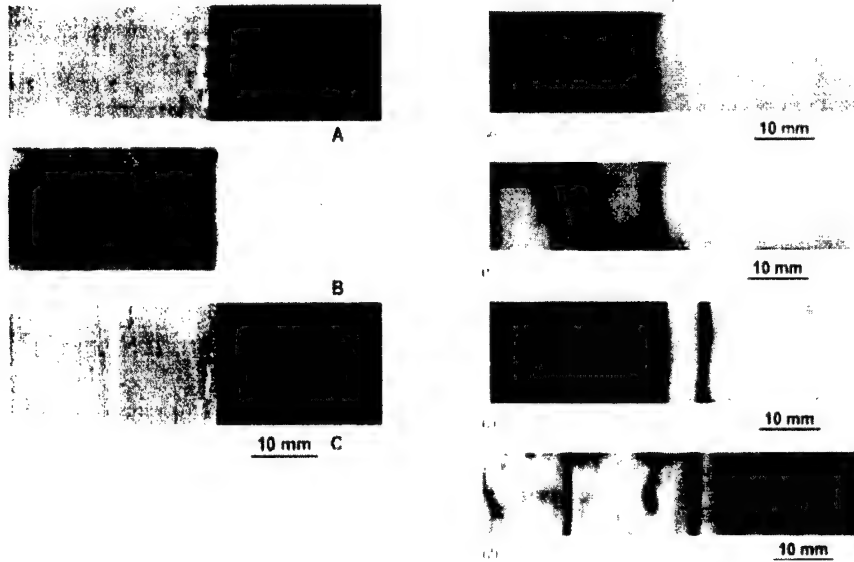


Figure 5. Left figure: Conventional C-scan images generated by 10 MHz [top (Fig.5A) and middle (Fig.5B)] and 75 MHz [bottom (Fig.5C)] focused transducers used in the pulse-echo mode. The back surface echo is omitted for constructing the top and bottom (A and C) images and it is considered for the middle image (B). Right figure: Different L-scan images of the composite plate. Fig.5a is generated with the transducer angle $\theta=16^\circ$, and the signal frequency $f=2.8$ MHz, for Fig.5b, $\theta=14^\circ$, $f=3.5$ MHz, for Fig.5c, $\theta=16^\circ$, $f=5.35$ MHz, and for Fig.5d, $\theta=20^\circ$, $f=5$ MHz. (after Kundu et.al., 1996).

3.3. NEAR LAMB MODE IMAGING

Two images shown in Figure 6 are generated by the same Lamb mode with slightly different frequencies and incident angles. The top image is generated by the 5.0 MHz signal striking the plate at 20° (corresponding phase velocity from the Snell's law is 4.36 km/s). The bottom image is produced by the 5.15 MHz signal incident at 21° (corresponding phase velocity is 4.16 km/s). In the top image the fourth layer can be clearly seen in spite of this layer being guarded by the delamination of the second layer. In this image the second layer cannot be seen at all although it is closer (compared to the fourth layer) to the transducers. However, in the bottom image both second and fourth layers can be seen.



Figure 6. For top image $\theta=20^\circ$, $f=5$ MHz, for bottom image $\theta=21^\circ$, $f=5.15$ MHz (after Kundu et.al., 2000)

Simple theoretical computations assuming isotropy and homogeneity of the plate at low frequency [Maslov and Kundu (1997)] show large stress magnitudes near the second and fourth layer positions in a defect free sample for this Lamb mode. Presence of delamination and missing fiber type defects affects these stresses and alters the reflected signal's intensity, and thus images of the defects are produced. That is why flaws of the second and fourth layers can be seen by this Lamb mode. However, when the signal frequency and the angle of incidence are changed from 5.1 MHz and 21° to 5.0 MHz and 20° respectively then the Lamb mode is not changed. For both these combinations the same Lamb mode is excited in the plate and stress, displacement fields are similar. Then why is this big difference in the Lamb wave scan or L-scan images produced by these two frequency-angle combinations? Why did one image completely ignore the second layer while the other one did not? To answer these questions one needs to carefully compute the internal stress field in this multilayered anisotropic plate not only for a specific Lamb mode but also very close to the Lamb mode as was done by Kundu et.al., 2000, and briefly described below.

3.3.1. Numerical Computation

Material constants are continuously varied until theoretical values approximately coincide with the experimental values. After some trial and error, the following stress-strain relation for individual layers was obtained.

$$\begin{Bmatrix} \sigma_{11} \\ \sigma_{22} \\ \sigma_{33} \\ \sigma_{23} \\ \sigma_{31} \\ \sigma_{12} \end{Bmatrix} = \begin{Bmatrix} 900 & 50 & 50 & 0 & 0 & 0 \\ & 150 & 96 & 0 & 0 & 0 \\ & & 150 & 0 & 0 & 0 \\ & & & 27 & 0 & 0 \\ & & & & 70 & 0 \\ & & & & & 70 \end{Bmatrix} \begin{Bmatrix} \epsilon_{11} \\ \epsilon_{22} \\ \epsilon_{33} \\ 2\epsilon_{23} \\ 2\epsilon_{31} \\ 2\epsilon_{12} \end{Bmatrix} \quad (1)$$

where x_1 is the fiber direction, elastic constants are given in GPa.

Numerically computed Lamb wave dispersion curves for the five-layer composite plate of 1.97 mm total thickness are shown in Figure 7. This is computed with the individual layer properties given in equation (1) when the Lamb wave propagates in the 90° direction or normal to the fiber direction of the top layer.

Shear stress (σ_{13}) profiles along the depth of the plate for the two frequency phase velocity combinations at which images of Figure 6 have been generated are shown in Figure 8. These two points on the dispersion plot are denoted by two squares in Figure 7. It should be noted here that for the 5 MHz signal σ_{13} is very small in the second layer and it is maximum in the fourth layer. That is why in Figure 6 we see that the image generated by the 5 MHz signal clearly shows the missing fiber defects of the fourth layer and completely ignores the delamination defect of the second layer. On the other hand for the 5.15 MHz signal (dotted line of Figure 8) the shear stress is maximum in the second layer and very small in the fourth layer. This explains why the image generated by the 5.15 MHz signal clearly shows the delamination defect of the second layer while the missing fiber defect of the fourth layer is not so clear.

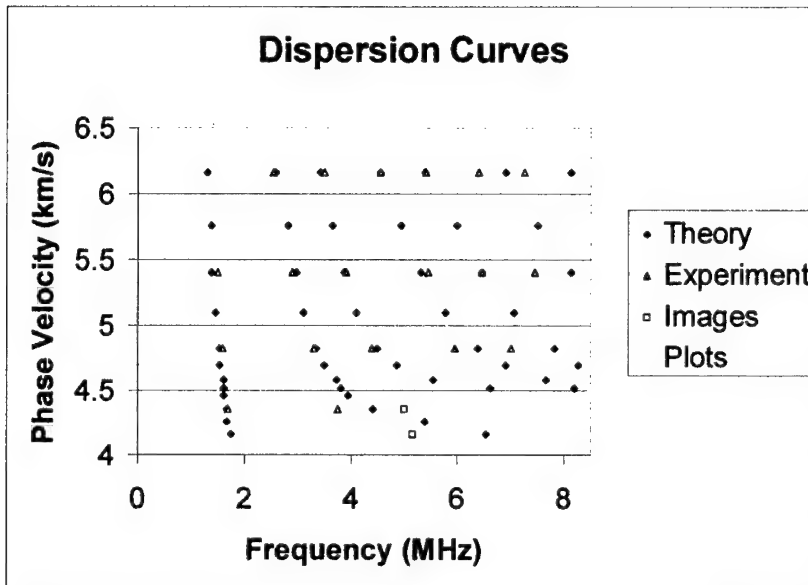


Figure 7. Numerically computed dispersion curves (diamond symbols). Twenty experimental points are shown by triangular symbols. Square markers show the frequency-phase velocity combinations used for generating the two images of Figure 6. Shear stress plots for these two points are shown in Figure 8 (after Kundu et.al.2000).

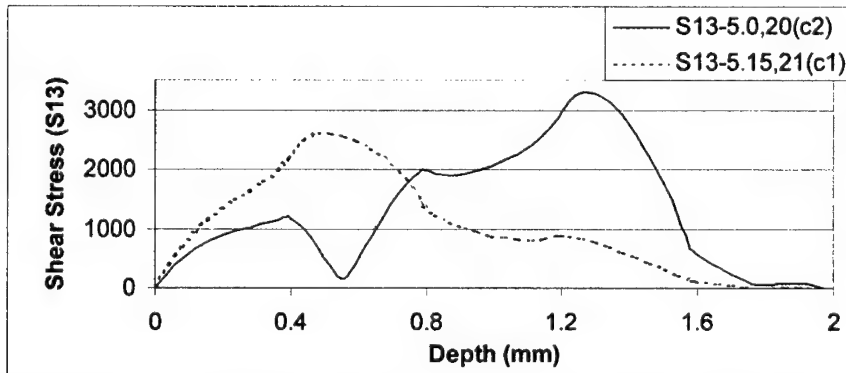


Figure 8. Shear stress variations inside the composite plate for frequency-phase velocity combinations, denoted by two square markers in figure 7. Corresponding ultrasonic images are shown in Figure 6 (Kundu et.al.2000).

4. Concrete Inspection

In spite of many developments of test techniques and equipment the use of NDE for inspecting concrete poses a number of difficulties. Compared to composite, metal and metal-based materials, ultrasonic NDE of concrete is a relatively immature discipline. The heterogeneous nature of concrete and unspecified code or standard of concrete NDE are two main areas where concrete inspection technology lags behind.

Concrete is a multi-phase material that is made of a coarse aggregate comprising particles of more than 5 mm in diameter, a fine aggregate, sand, and cement. The coarse granular structure, such as the relative concentration of the constituent particles, the degree of compaction, the moisture content, and the nature and amount of defects present, gives rise to a high degree of acoustic scattering and, therefore, attenuation. For this reason, testing is usually done at kilohertz frequency range. In addition, the presence of steel rods gives rise to more complications for inspecting reinforced concrete.

It is well known fact that there are existing codes or standards available to be used as guidelines for many construction projects that do not involve concrete. For instance, American society of Mechanical Engineers (ASME) code is commonly used for construction of boiler and pressure vessel, American Petroleum Institute (API) code for construction in petroleum industry and American Welding Society (AWS) code for construction of steel structures. In such cases, the application of NDE is well specified. However, for civil construction involving concrete, there is no specific code or standard currently available that can be used as a guideline for the selection and application of suitable NDE methods, and for the acceptance/rejection criteria. Due to these facts, the NDE community should have a wide knowledge of NDE applications, so that the NDE technique can be effectively used in a particular situation.

Concrete experts have been interested in detecting internal defects and determining properties of concrete by NDE techniques for many decades and a number of NDE techniques have been used for concrete inspection. The technique developed by Jung et.al. (1999, 2000) are briefly presented below. Their experimental setup is described first.

4.1. EXPERIMENTAL INVESTIGATION

Under this investigation a number of specimens made of plain concrete have been fabricated and inspected by different Lamb modes. The first step of Lamb wave inspection is to produce Lamb waves inside the specimen. To this aim two transducers are placed over a defect-free plate specimen. The tone-burst excitation is then used to activate the transmitting transducer and generate the stress waves. The excitation frequency is continuously varied from a minimum to a maximum value within the bandwidth of the transducer to find the peak positions that correspond to the Lamb wave modes generated in the plate. The receiving transducer receives the reflected signal after its propagation through the specimen. The received signal amplitude is then displayed on an oscilloscope screen as a function of frequency. The gate position (the "gate") represents the time window for the received signal used to generate the $V(f)$ curve) is placed near the beginning of the received signal. This is done to avoid collecting signals after those are reflected by other boundaries. Therefore, the early part of the received signal should be affected by the presence of the defect. The experimental setup is similar to the one developed by Ghosh and Kundu (1998) and Ghosh et al. (1998) and shown in Figure 9.

Kundu et.al. (1996), Maslov and Kundu (1997), Yang and Kundu (1998) generated different Lamb modes in a plate. The Lamb wave speed or the phase velocity (V_{ph}) can be obtained from the Snell's Law, similar to the previous cases,

$$V_{ph} = \frac{\alpha_w}{\sin \theta} \quad (2)$$

where V_{ph} is the Lamb wave phase velocity, α_w is the longitudinal wave speed in the coupling fluid (for water it is equal to 1.49 km/s) and θ is the angle of inclination of the transducer, i.e. the angle between the vertical axis and the transducer axis.

The signal frequency and the transducer inclination angles are set at values corresponding to a Lamb mode of interest. The specimen is then inspected with this transmitter-receiver arrangement.

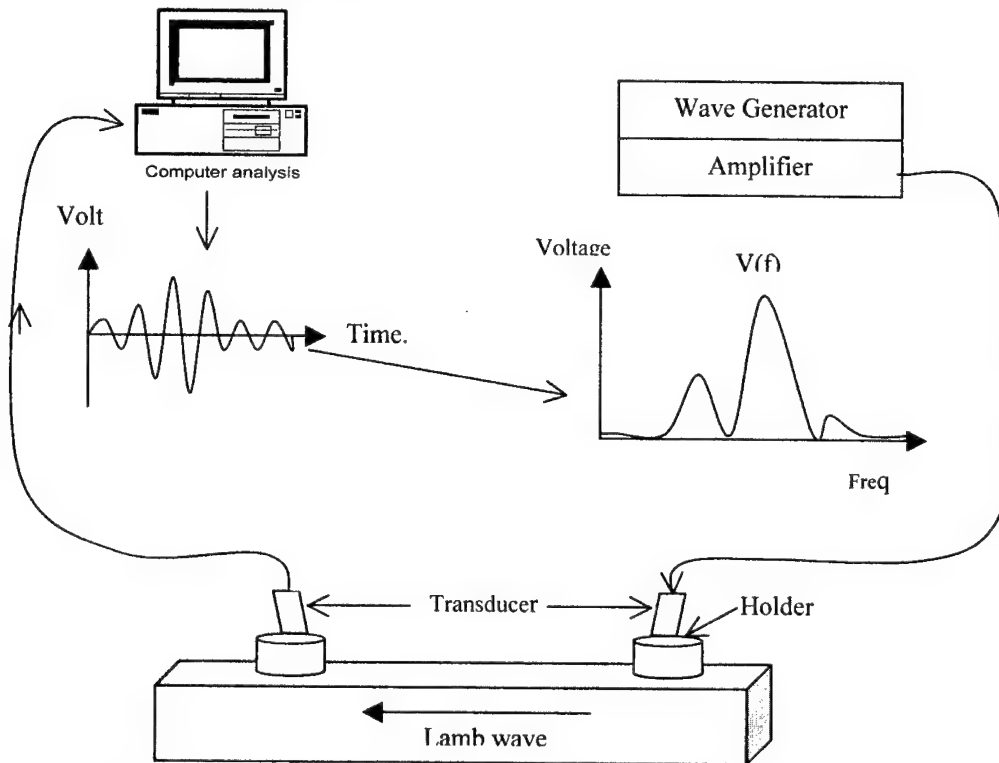


Figure 9. Experimental setup for Lamb wave inspection of concrete specimen (after Jung et.al.2000)

4.1.1. Experimental Results

The specimen is a 40 in x 12 in x 8 in (101.6 mm x 30.5 mm x 20.3 mm) plain concrete beam. The defect is a cylindrical (12.7 mm diameter and 12.7 mm long) honeycomb (aggregate without mortar) zone. The defect is located 30.5 mm from one end of the beam at a depth of 10.2 mm. The $V(f)$ curves, generated by the Lamb waves on the defective and non-defective sides of the beam are shown in Figure 10. The transducers were inclined at an angle of 16° to generate multiple strong Lamb modes in the specimen. This inclination angle corresponds to a phase velocity of 5.41 km/s (see Equation 2). The $V(f)$ curve for 16° angle of incidence were generated several times to study the

consistency of the results. All those plots are shown in Figure 10. Two strong distinguishable peaks were observed, one near 53 kHz and the second one near 116 kHz. The wavelengths corresponding to these two Lamb modes are 102 mm and 46.6 mm respectively. Clearly the maximum aggregate size (3/8 inch or 9.5 mm) is much smaller than the wavelength. More peaks near 79 kHz, 145 kHz, 160 kHz, 180 kHz, 200 kHz and 28 kHz were observed in the V(f) plot, however, these peaks are much weaker than the peaks at 53 kHz and 116 kHz.

A few in number and weaker peaks were observed over the honeycomb region. Prominent peaks were again noticed at 53 kHz and 116 kHz. Weaker peaks were observed near 80 and 160 kHz. This comparison of V(f) curves clearly shows that the amplitudes of the signal are significantly reduced because of the presence of honeycomb defect inside the specimen. However, the positions of the prominent peaks were not changed because of the presence of the honeycomb.

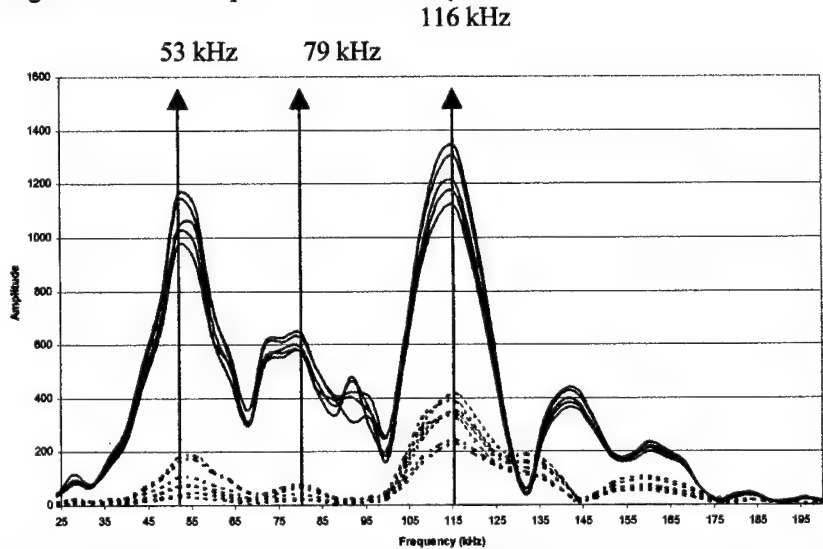


Figure 10. V(f) curves over the non-defective zone (continuous line) and the honeycomb zone (dotted line) (after Jung et.al., 2000).

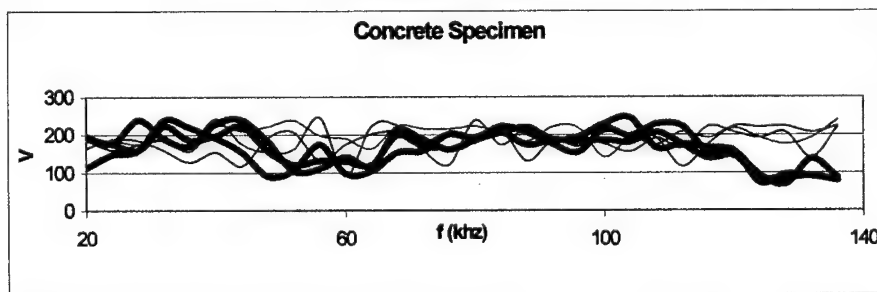


Figure 11. Voltage versus frequency curves generated by the conventional through-transmission technique for the concrete specimen. Signals from the defect free zone are shown by thin lines. Signals from the honeycomb zone are shown by thick lines (after Jung et.al., 2000).

For comparison purposes, the $V(f)$ curves for the same specimen generated by the conventional through transmission arrangement are shown in Figure 11. Clearly the Lamb wave technique detects the defect more clearly.

5. Steel-Concrete Interface Inspection

Na et.al. (2000) studied the feasibility of using Lamb waves for detecting delamination between steel rod and concrete in reinforced concrete using Lamb waves. Steel rods of 7/8 inch (22.2 mm) diameter embedded in concrete beams of square cross section (127 mm x 127 mm) were inspected. Four specimens with different degrees of delamination were inspected. One specimen had no delamination the other three specimens had 25%, 50% and 75% steel-concrete interface artificially delaminated. The rods were extended beyond the concrete beam as shown in Figure 12, so that the transducers could be mounted on the steel rod, as was done on pipe (Figure 1). However, in this case the coupling mechanism was different. Instead of water coupler, a plexiglas sphere was used as the coupler as shown in Figure 12.

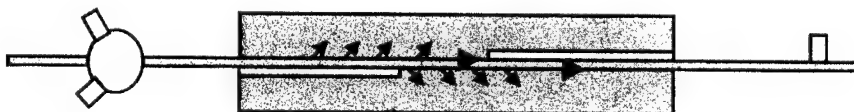


Figure 12. A steel rod embedded in a concrete beam with part of the steel-concrete interface delaminated. Transmitters are mounted on the spherical plexiglas coupler on the left side and the receiver is on the right side.

Results are shown in Figures 13 and 14. $V(f)$ curves for different extents of delamination are shown for each of the two inclination angles of transmitters, 8° (Figure 13) and 24° (Figure 14).

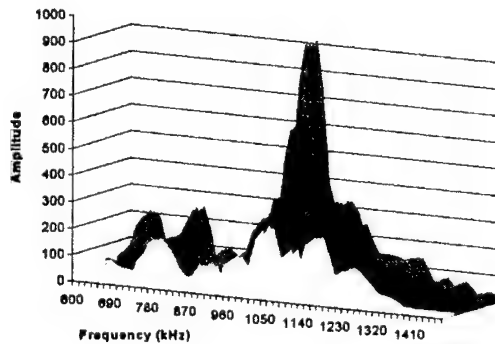


Figure 13. $V(f)$ curves for 8° angle of incidence for different degrees of delamination, denoted by different shades (after Na et al., 2000).

0% 25% 50% 75%

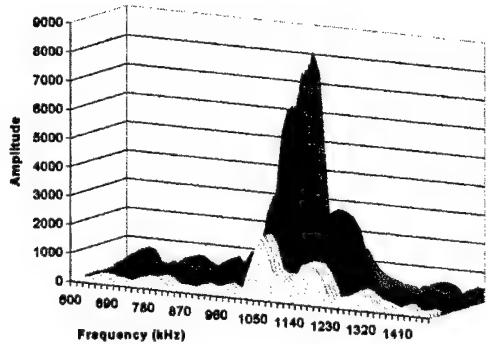


Figure 14. $V(f)$ curves for 24° angle of incidence for different degrees of delamination, denoted by different shades as indicated in Figure 13 caption (after Na et. al., 2000).

In Figures 13 and 14 one can see that $V(f)$ curves generated by both transmitter inclination angles can distinguish between different degrees of interface delamination. However, 24° inclination angle produce much stronger signal.

5. Concluding Remarks

Lamb wave inspection technique is found to be an efficient ultrasonic evaluation method for detecting damages in metal pipes, composite plates, concrete beams as well as for interface characterization. Some research findings of the author and associates are briefly reviewed in this paper.

6. Acknowledgment

Results from a number of research grants (CMS-9523349, 9896182, 9800345, MSS-9310528, W08031-14 & EP-P241/C110) funded by the National Science Foundation and Electric Power Research Institute have been presented here.

7. References

- Alleyne, D. and Cawley, P. (1995) The Long Range Detection of Corrosion in Pipes Using Lamb Waves, *Review of Progress in QNDE*, Eds. D. O. Thompson and D. E. Chimenti, Plenum Press, NY, **14B**, 2073.
- Castaings, M. and Hosten, B. (1994) Delta Operator Technique to Improve the Thomson-Haskell-Method Stability for Propagation in Multilayered Anisotropic Absorbing Plates, *Journal of the Acoustical Society of America*, **95**, 1931-1941.
- Davis, R. J. and Bubenik, T. A. (1996) The Feasibility of Magnetic Flux Leakage In-Line Inspection as a Method to Detect and Characterize Mechanical Damage, *GRI Report #GRI-95/0369*,
- Gazis, D. G. (1959) Three-Dimensional Investigation of the Propagation of Waves in Hollow Circular Cylinders, *Journal of the Acoustical Society of America*, **31**, 568.
- Ghosh, T. and Kundu, T. (1999) A New Transducer Holder Mechanism For Efficient Generation and Reception

of Lamb Modes in Large Plates, *Journal of the Acoustical Society of America*, **104**, 1498.

Ghosh, T., Kundu, T. and Karpur, P. (1998) Efficient Use of Lamb Modes for Detecting Defects in Large Plates, *Ultrasonics*, **36**, 791-801.

Guo, D. and Kundu, T. (1998) Special Sensors for Generating Lamb Waves in Pipes, *Proceedings of the Review of Progress in Quantitative Nondestructive Evaluation*, Eds. D. O. Thompson and D. E. Chimenti, Pub. Plenum Press, New York, Conf. held in Snowbird, Utah, July 19-24, 1998, **18A**, 1155-1162.

Guo, D. and Kundu, T. (2000a) A New Sensor for Pipe Inspection by Lamb Waves, *Materials Evaluation*, **58**, 991-994.

Guo, D. and Kundu, T. (2000b) Detection of Mechanical Damages in Pipes by Lamb Waves Generated by a New Sensor, *Proceedings of the 6th ASME NDE Topical Conference*, San Antonio, Texas USA, April 20-22, 1999, Pub. ASME, Ed. Corinne Darvennes, NDE-19, 137-143.

Jung, Y. C., Kundu, T. and Ehsani, M. (1999a) Detection of Internal Defects in Concrete Panels by Lamb Waves, *Proceedings of the Review of Progress in Quantitative Nondestructive Evaluation*, Eds. D. O. Thompson and D. E. Chimenti, Pub. Plenum Press, New York, Conf. held in Canada, July 1999, **19**.

Jung, Y. C., Kundu, T. and Ehsani, M. (1999b) Lamb Wave Inspection of Concrete Beams, *Recent Advances of Ultrasonic NDE and Composite Material Characterization*, IMECE 99, Nashville, Tennessee, Nov.14-19, 1999. Eds. T. Kundu and V. K. Kinra, Pub. ASME, AMD-234, NDE-17, 33-46.

Jung, Y. C., Na, W. B., Kundu, T. and Ehsani, M. R. (2000) Damage Detection in Concrete Using Lamb Waves, *Nondestructive Evaluation of Highways, Utilities, and Pipelines IV*, Ed. A. E. Aktan and S. R. Gosselin, Proceedings of SPIE NDE 2000 conf., Newport Beach, California, March 5-9, 2000, **3995**, 448-458.

Karim, M. R., Mal, A. K. and Bar-Cohen, Y. (1990) Inversion of leaky Lamb wave data by simplex algorithm, *Journal of the Acoustical Society of America*, **88**, 482-491.

Karpur, P., Benson, D. M., Matikas, T. E., Kundu, T. and Nicolaou, P. D. (1995) An Approach to Determine the Experimental Transmitter-Receiver Geometry for the Reception of Leaky Lamb Waves, *Materials Evaluation*, **53**, 1348-1352.

Karpur, P., Kundu, T. and Driti, J. (1998) Adhesive Joint Evaluation Using Lamb Wave Modes with Appropriate Displacement, Stress and Energy Distribution Profiles, *Proceedings of the Review of Progress in Quantitative Nondestructive Evaluation*, Eds. D. O. Thompson and D. E. Chimenti, Pub. Plenum Press, New York, Conf. held in Snowbird, Utah, July 19-24, 1998, **18B**, 1533-1542.

Kiefner, J. F., Hyatt, R. W. and Eiber, R. J. (1986) NDE Needs for Pipeline Integrity Assurance, *American Gas Association Catalog Number L51505*.

Kundu, T., Maslov, K. I., Karpur, P., Matikas, T. and Nicolaou, P. (1996) A Lamb Wave Scanning Approach for Mapping of Defects in [0/90]Titanium Matrix Composites, *Ultrasonics*, **34**, 43-49.

Kundu, T. and Maslov, K. I. (1997) Material Interface Inspection by Lamb Waves, *International Journal of Solids and Structures*, **34**, 3885-3901.

Kundu, T., Maji, A., Ghosh, T. and Maslov, K. I. (1998) Detection of Kissing Bonds by Lamb Waves, *Ultrasonics*, **35**, pp.573-580.

Kundu, T., Potel, C. and de Belleval, J. F. (2000a) On the Near Lamb Mode Imaging of Multilayered Composite Plates, *Ultrasonics*, in press.

Kundu, T., Potel, C., and de Belleval, J. F. (2000b) Near Lamb Mode Imaging of Multilayered Composite Plates, *Nondestructive Evaluation of Aging Aircraft, Airports, and Aerospace Hardware*, Ed. A. K. Mal, Proc. of SPIE NDE 2000, March 7-8, 2000, Newport Beach, California, **3994**, 174-183.

Mal, A. K., Yin, C. C. and Bar-Cohen, Y. (1991), Ultrasonic Nondestructive Evaluation of Cracked Composite Laminate, *Composite Engineering*, **1**, 85-101.

Maslov, K. I. and Kundu, T. (1997) Selection of Lamb Modes for Detecting Internal Defects in Laminated Composites, *Ultrasonics*, **35**, 141-150.

Na, W., Kundu, T. and Ehsani, M. R. (2000) Inspection of Concrete-Metal Rod Interface Using Guided Waves, IMECE 2000, Orlando, Florida, Nov.5-10, 2000, Eds. J. Qu and T. Kundu. Pub. ASME, NDE-18, 59-69.

Nayfeh, A. H. (1995) *Wave Propagation in Layered Anisotropic Media*, Pub. Elsevier, Amsterdam.

Potel, C. and de Belleval, J. F. (1993a) Propagation in an Anisotropic Periodically Multilayered Medium, *Journal of the Acoustical Society of America*, **93**, 2669-2677.

Potel, C. and de Belleval, J. F. (1993b) Acoustic Propagation in Anisotropic Periodically Multilayered Media: A Method to Solve Numerical Instabilities, *Journal of Applied Physics*, **74**, 2208-2214.

Taylor, T. W. and Nayfeh, A. H. (1992) Dynamic Internal Response of Fluid-Loaded Multilayered Anisotropic Media, *Journal of the Acoustical Society of America*, **91**, 519-2528.

Yang, W. and Kundu, T. (1998) Guided Waves in Multilayered Anisotropic Plates and its Use in Internal Defect Detection, *ASCE Journal of Engineering Mechanics*, **124**, 311-318.

ON THE ROLE OF MATERIAL CONSTITUTIVE RELATIONS IN LONG ROD PENETRATION MECHANICS

Z. ROSENBERG AND E. DEKEL

Rafael

P.O. Box 2250, Haifa, Israel

Abstract

Two dimensional numerical simulations were performed in order to uncover the role of constitutive properties of both penetrator and target, on the penetration process of long rods. It was found that a maximum strain to failure criterion can simulate the effects of adiabatic shearing of the penetrator nose, accounting for the DU superiority over WA rods. Moreover, recent results with extremely strong rods, can be simulated with proper strength and failure values for both penetrator and target.

1. Introduction

The complex process of long rod penetration has been studied extensively in the last 50 years by both armor and warhead designers (see [1] for a review). Various analytical and semi-empirical models have been developed, in order to account for the experimental data, by following the main mechanisms in the process. During the past decade, two- and three-dimensional simulations have taken the place of these engineering efforts, due to their improved accuracy and predictive power. The present paper summarizes some of one recent numerical work on this subject. We highlight the role of material constitutive properties, of both penetrator and target, on the penetration process, particularly, the role of elastic waves which are governed by the yield strength of these materials. The 2D simulations were performed with the Eulerian processor of the PISCES 2 DELK code described in [2]. This is a second order hydrocode, which is most suitable for large strain fields such as those encountered in deep penetrations. In order to assure convergence, we used 11 cells on the radius of the penetrator. The simulated targets were large enough to be considered semi-infinite, by the use of the FLOW boundary condition on their lateral and back surfaces (see [2]). Our main output for each simulation was the velocity-time histories of the front and back ends of the penetrator, as well as time variation of penetrator length and penetration depth. The final depth of penetration normalized to the initial penetrator length (P/L) is our main parameter for the penetration efficiency of a given penetrator-target pair.

2. The Role of Yield Strength

2.1 TARGET STRENGTH

In order to investigate the influence of target strength on the penetration process, it is best to use zero-strength penetrators. This way the effect of penetrator strength is cancelled out resulting in a non-decelerating penetrator. Our first set of simulations was for zero-strength steel penetrators, with an aspect ratio of $L/D=10$, impacting aluminum targets at velocities in the range of 0-7 km/s. Target strengths varied between 0.4-1.2 GPa, using a simple von-Mises yield criterion. Figure 1a shows the results of our simulation which exhibits the well-known shape of a very sharp rise in $P/\alpha L$ for impact velocities greater than a certain critical velocity, which depends on target strength. The high-velocity end is asymptotic reaching values of $P/\alpha L \approx 1$, where α is the square root of penetrator/target density ratio. This doubly normalized representation of the penetration depth is very convenient for comparison purposes.

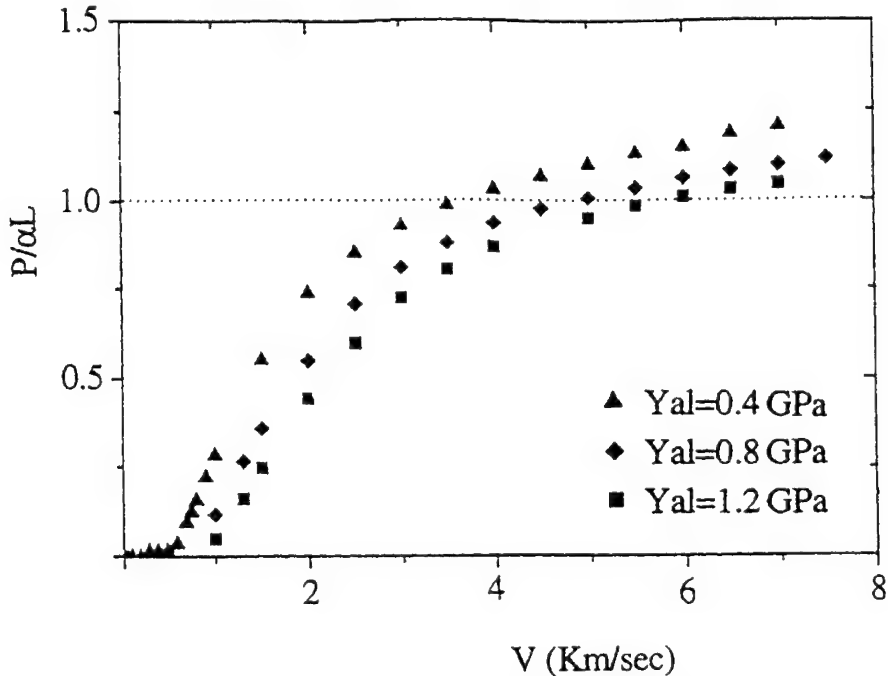


Figure 1. Our simulation results for zero-strength steel rods impacting aluminum targets with different strengths

In Figure 2, we present the results of [3] for tungsten alloy rods impacting two steel targets, with Brinell hardness in the range of 180-388 BHN. It is quite clear that the same features discussed above are also seen here, namely, the S-shaped curves for velocities above a critical value, which depends on target strength, and the asymptotic convergence at high velocities to the hydrodynamic limit α .

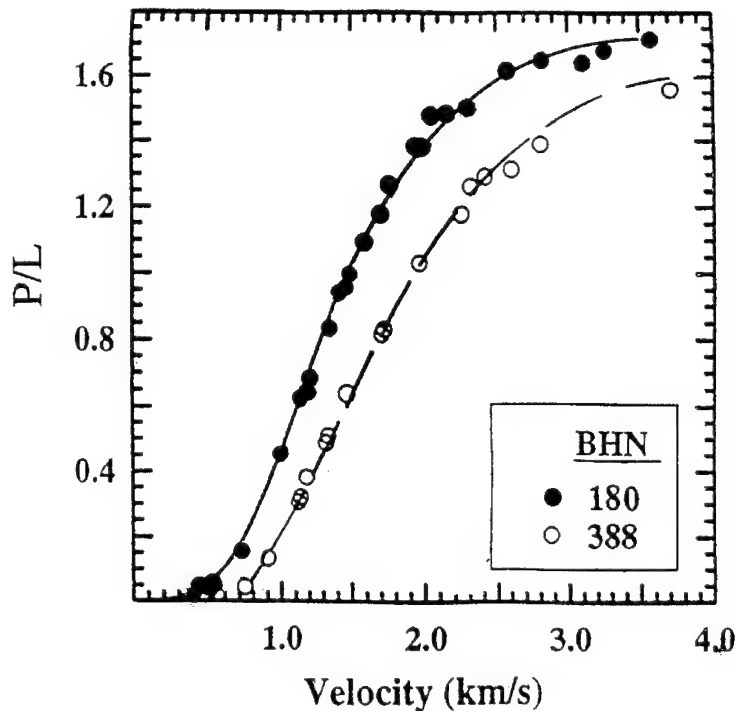


Figure 2: Experimental results [3] for WA penetrators in steel targets.

2.2 PENETRATOR STRENGTH

The influence of penetrator strength on its penetration efficiency can be seen in Figure 3. These are the simulation results for $L/D=10$ steel penetrators, with yield strengths in the range of 0-2.0 GPa, impacting an 0.4 GPa aluminum target (representing 2024-T3 Al alloy). The shape of the curve for the high strength (2 GPa) rod is quite different than that of the zero strength rod. An S-shaped curve, starting at the origin, is obtained in good agreement with experimental data. It is also interesting to note the several crossovers which occur in these curves by increasing impact velocities. These crossovers were analyzed and discussed by us in [4], and they were attributed to the effect of elastic waves, running up and down the rod length, slowing it as it penetrates the target. We also showed that these crossovers disappear when failure and softening mechanisms are added to the constitutive relations of the penetrators. Figure 4 shows experimental results from [5] for tungsten alloy penetrators ($Y_p \approx 1.4$ GPa) impacting aluminum targets in the 0-4 km/s range. Both our simulations and experiments of [5] show a leveling-off for the high strength rod at values much higher than the hydrodynamic limit of $P/L=\alpha$. These high values were attributed by Allen and Rogers [6] to a secondary penetration mechanism by which high density rods continue to penetrate the target after completion of the rod erosion process. We have shown in [7] that this suggested mechanism is probably an artifact and that high values of P/L can be obtained by high-strength penetrators, especially for large p_p/p_t values.

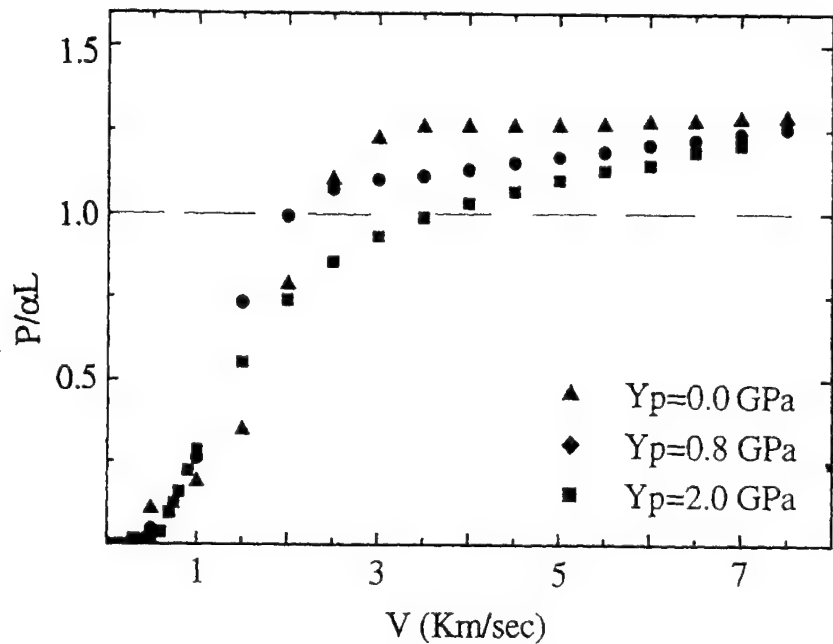


Figure 3. Our results for three different strength steel penetrators impacting an 0.4 GPa aluminum target

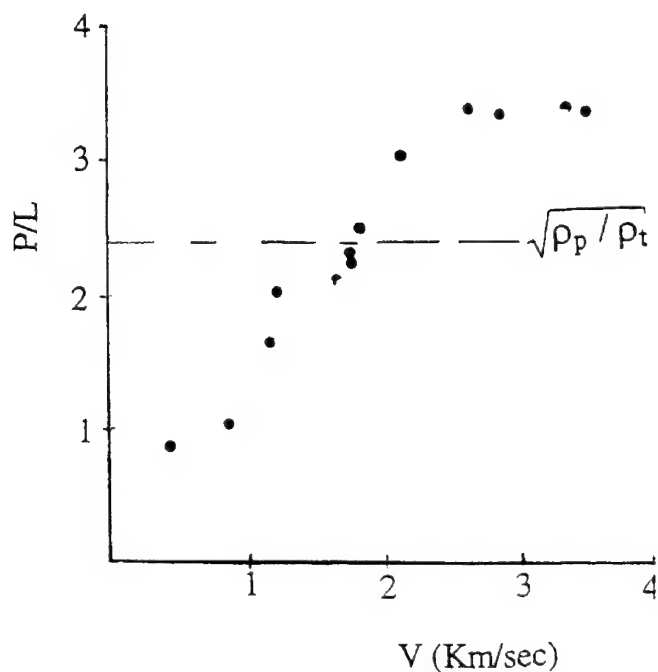


Figure 4 Experimental results [5] for WA penetrators in aluminum targets.

3. The Role of Failure

Two experimental observations were recently related to the failure characteristics of the penetrator: 1) the fact that depleted uranium (DU) penetrators are more efficient (by about 10%) than those made of tungsten alloy (WA) [8], and 2) the scaling effect, by which the ballistic efficiency of scaled WA rods (1:4) is less by about 20% than that of full-sized rods [9]. The superiority of DU over WA was attributed by Magness and Farrand [8] to the self-sharpening of penetrator nose by the adiabatic shear failure of DU. In [10] and [11], we demonstrated that with materials which undergo adiabatic failure (i.e., Ti 6Al 4V) a pointed penetration is formed, as suggested in [8], and that the nose shape of the penetrator has an important role on its ballistic efficiency. In order to emphasize this issue, we performed numerical simulations with a strain to failure criterion for the penetrator [4], by which a cell loses its strength, once it reaches a predetermined maximum strain (ϵ_F). Figure 5 shows the influence of ϵ_F on the final penetration of a WA rod (300 nm long and 15 mm in diameter), impacting an armor steel target at 1.7 km/s. It is clearly evident that for ϵ_F in the range of $\epsilon_F = 0\text{-}0.5$, the penetration depth is much higher than that for $\epsilon_F = 1\text{-}5$. This fact can be used to simulate the adiabatic shear failure with proper values of ϵ_F . In particular, values of $\epsilon_F = 0.2\text{-}0.3$ are often found in Hopkinson's bar experiments for several materials which undergo adiabatic shearing.

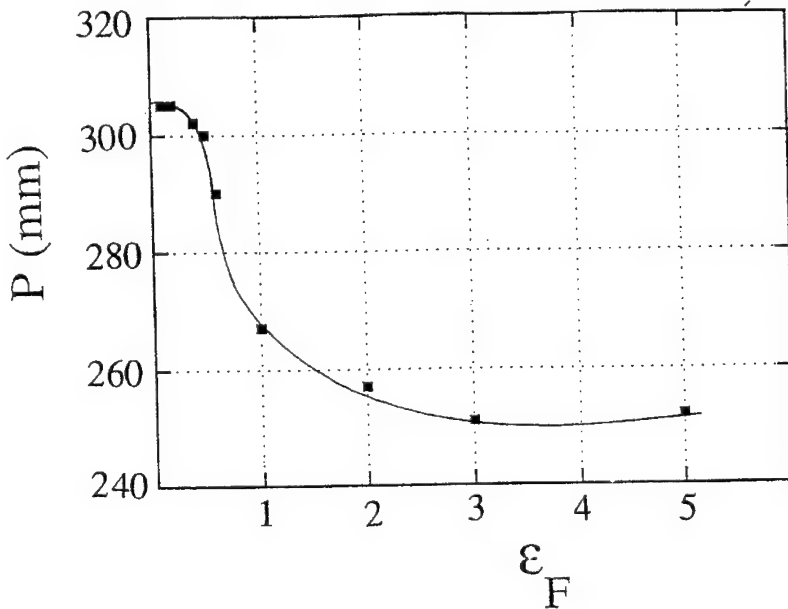


Figure 5. The dependence of penetration depth on the strain to failure for a WA penetrator impacting a steel target at 1.7 km/s.

In order to further demonstrate the ability of ϵ_F to represent the experimental data, we performed similar simulations for increasing velocities (see Figure 6). It is quite evident that the effect of ϵ_F diminishes with increasing velocity, just as the empirical data of [8] has shown for the difference between DU and WA penetrators.

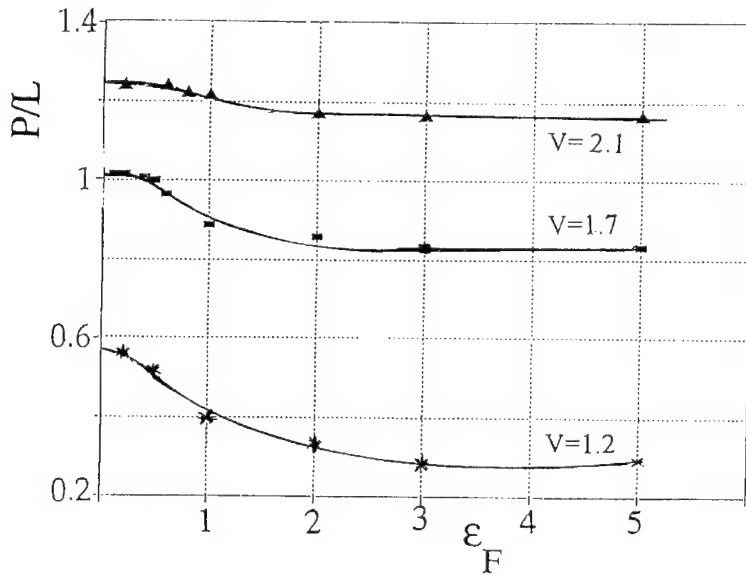


Figure 6. The influence of impact velocity on the sensitivity to ϵ_F .

As a final example for the importance of material constitutive relations on the penetration characteristics, we show in Figure 7 simulation results which were performed in order to account for the data of [12]. In these experiments, very strong, spherical-nose, steel penetrators ($L/D=10$) impacted large 6061 Al targets, at velocities in the range of 0-3 km/s. These penetrated as rigid rods for velocities of 0-1 km/s while at higher velocities deformation and erosion took place. Figure 7 shows the simulation results for the 3.0 GPa rod impacting an 0.4 GPa aluminum target, as compared with the experimental results of Ref. [12]. It is quite clear that the simulations exhibit only part of the features found in the experiments. There is a break in the penetration curve at about 1 km/s, but there is no evidence for the sharp extrema seen in the empirical data of [12]. The break at about 1 km/s is due to the transition from a rigid-rod penetration to the erosion mode.

In order to have a closer match with the data, we performed several sets of simulations with different values of ϵ_F for the target and penetrator. We found that the shape of the resulting penetration curves is very sensitive to these ϵ_F values. Figure 8 shows our results for one these sets of simulation ($\epsilon_{Al} = 0.6$, $\epsilon_{Fe} = 0.5$), from which one can distinctly see that the sharp extrema near 1 km/s is now evident in the simulations, although at the high velocity end the agreement with experiment is not as good.

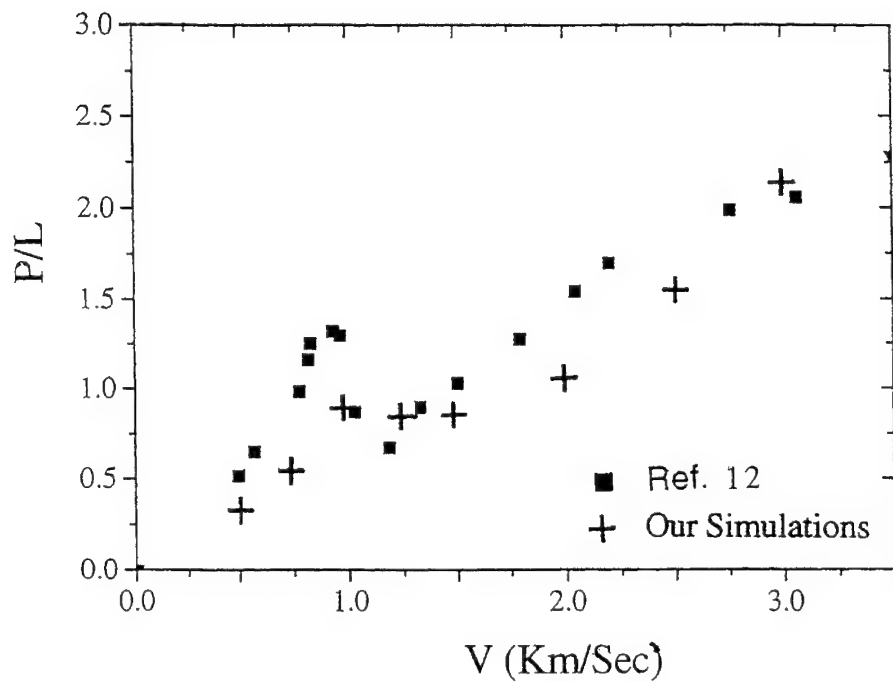


Figure 7. Comparison of our simulation results with the data of [12] for very strong steel rods impacting aluminum targets.

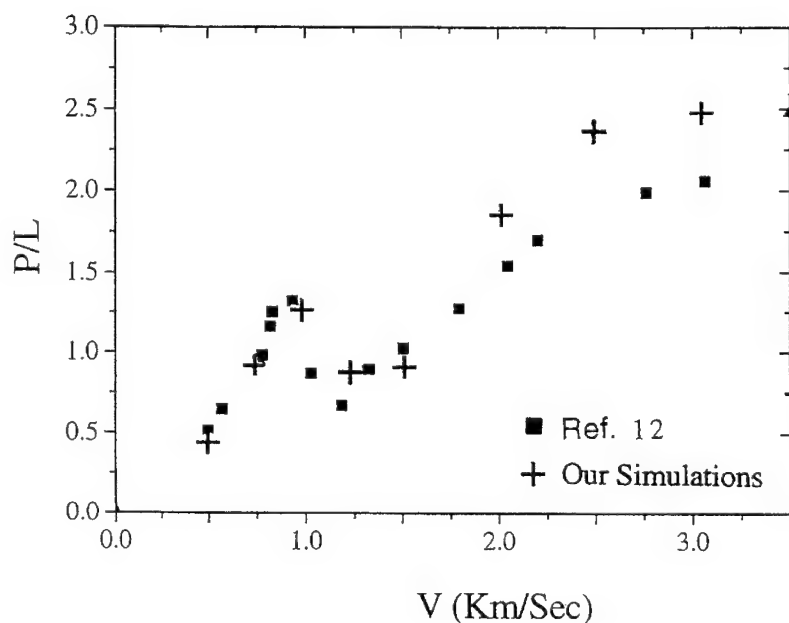


Figure 8. Comparison with experimental data [12] of simulations with the addition of ϵ_F criterion.

As far as target failure is concerned, the role of ϵ_f is most important for brittle targets (i.e., ceramics, rocks, glass, etc.), which are very difficult to simulate. An important step has been achieved by Johnson and Holmquist [13], who defined two failure surfaces, one for the intact and one for the damaged material. A simplified version of this model was suggested by us [14], where we used a single parameter to correlate the properties of the damaged material to those of the intact material. This parameter is determined by fitting an experimental result for a long rod penetration experiment. Using this value, we were able to match our simulation results with a large number of penetration experiments into ceramic tiles, as shown in [14].

4. Summary

This paper summarizes our recent work on the role of constitutive properties of the penetrator and target in long-rod penetration mechanics. We have shown that the rod strength plays an intricate role, which leads to a crossover phenomenon. The failure of rod material is an important issue in determining its ballistic efficiency, especially for materials undergoing adiabatic shear failure. The elastic waves in brittle targets can cause considerable damage and special failure criteria should be used to simulate this damage.

References

1. Anderson, C.E., and Bodner, S.R., *Int. J. Impact. Eng.*, **7**, 9 (1988).
2. Rosenberg, Z., and Dekel, E., *Int. J. Impact. Eng.*, **15**, 125 (1994).
3. Hohler, V., and Stilp, A.J., *Int. J. Impact. Eng.*, **5**, 323 (1987).
4. Rosenberg, Z., and Dekel, E., *Int. J. Impact. Eng.*, **21**, 283 (1998).
5. Hohler, V., and Stilp, A.J., *Proc. 5th Int. Symp. On Ballistics*, Toulouse, France (16-18 April, 1980).
6. Allen, W.A., and Rogers, J.W., *J. Franklin Inst.*, **272**, 275 (1961).
7. Rosenberg, Z., and Dekel, E., *Int. J. Impact. Eng.*, (2000).
8. Magness, L., and Farrand, T., in the *Proc. of Army Science Conf.*, Durham, N.C. (May 1990)
9. Magness, L., and Leonard, W., *Proc. 14th Int. Symp. On Ballistics*, Quebec, Canada (26-29 Sept., 1993).
10. Rosenberg, Z., and Dekel, E., *Int. J. Impact. Eng.*, **19**, 277 (1997).
11. Rosenberg, Z., and Dekel, E., *Int. J. Impact. Eng.*, **22**, 551 (1999).
12. Forrestal, M.J., and Piekutowski, A.J., *Int. J. Impact. Eng.*, **24**, 57 (2000)
13. Johnson, G.R., and Holmquist, T., in EXPLOMET 90, Eds. M. Meyers, L. Murr and K. Staundhammer, (Marcel Dekker Publishers, 1992), p. 1075.
14. Rosenberg, Z., Dekel, E., Hohler, V., Stilp, A., and Weber, K., *Int. J. Impact. Eng.*, **20**, 675 (1997).

WAVE PROPAGATION IN PLANARLY-STRATIFIED MULTILAYERS

A. MORRO

University of Genoa, DIBE

Via Opera Pia 11a, 16145 Genova, Italy

1. Introduction

Many applications in seismics, ocean acoustics and nondestructive evaluation are framed within wave propagation in planarly-stratified media. Planar stratification means that the material properties exhibit a one-dimensional inhomogeneity namely they vary with a Cartesian coordinate, say z . For definiteness and generality, the material parameters are taken to be piecewise smooth functions of z and suffer jump discontinuities at a finite number of surfaces $z = \text{constant}$. Geometrically, this is a multilayer configuration, namely a sequence of a finite number of layers. Each layer is allowed to be an anisotropic and dissipative solid which is pre-stressed in the equilibrium configuration.

Let $z_0 = 0, z_1, \dots, z_n = d$ be the z -coordinate of the dividers. The whole multilayer, $z \in (0, d)$, is sandwiched between two homogeneous half spaces, one of them possibly being empty. The constitutive equations are taken to be linear. Hence, by Fourier analysis, time-harmonic dependence is appropriate for any time-dependent process. Let x, y be the transverse coordinates. Owing to the homogeneity in x and y we take any pertinent function to be factorized by $\exp[i(k_x x + k_y y - \omega t)]$ where ω is the real frequency and k_x, k_y are allowed to be complex. Next we show that



Figure 1: A constitutive parameter in a multilayer.

the equations of motion and the constitutive equations can be given the form

$$\mathbf{w}'(z) = \mathbf{A}(z)\mathbf{w}(z), \quad z \in (-\infty, z_0) \cup (z_0, z_1) \cup \dots \cup (z_{n-1}, z_n) \cup (z_n, \infty), \quad (1)$$

where \mathbf{w} , the set of state variables, is a 6-tuple of unknown functions of $z \in (-\infty, \infty)$, $\mathbf{w}' := d\mathbf{w}/dz$ and \mathbf{A} is a 6×6 complex-valued matrix function of z . Starting from the system (1), the reflection-transmission process results in a boundary-value problem for \mathbf{w} . This in turn is expressed as a Cauchy problem for appropriate unknown matrices.

The purpose of this paper is to show how the solution to the reflection-transmission problem, at a planarly-stratified multilayer $z \in (0, d)$, can be determined. Given an incident wave in the homogeneous half space $z < 0$, the reflected wave in $z < 0$ is determined together with the transmitted wave in $z > d$ and the solution \mathbf{w} as $z \in (0, d)$. Both the impedance matrix and the reflectivity matrix are shown to satisfy Riccati equations in $(0, d)$. Along with appropriate boundary conditions, the pertinent matrices can be determined and the unknown field \mathbf{w} be evaluated. Alternatively, the reflection-transmission problem can be given the form of an integral equation whose solution \mathbf{w} is found to hold and is formally established.

A reference to previous approaches to the problem is in order. Continuously layered bodies are considered in [1] though in one-dimensional scalar problems. Kennett [2] and Lewicki et al [3] show that the reflectivity matrix, as a function of the space variable, satisfies a Riccati equation. The use of the impedance matrix has been less frequent, see [4] for elastic solids and [5] for electromagnetic solids. The use of the propagator matrix is described, e.g., in [6]. None of these approaches, though, allows for jump discontinuities in the slab $z \in (0, d)$. Nor do they look for the unknown field \mathbf{w} . By generalizing the procedure of [7], the approaches developed in this paper allow for any planar inhomogeneity and any number of discontinuity surfaces. Both the Riccati equations, for the reflectivity and the impedance, and the series solution for the propagator matrix, along with the pertinent boundary condition, are shown to provide the reflection and the transmission matrix of the multilayer. Meanwhile, no attention is devoted here to questions related to numerical instabilities which occur in evaluating reflection and transmission matrices of the multilayer.

An extensive literature has been developed on (time-harmonic) guided waves in multilayers, the layers being elastic or absorbing and possibly arranged in periodic structures; cf. the review article [8] and references therein. These investigations, though, involve homogeneous layers (plates) in which case the evolution equations of this paper drastically simplify.

2. Governing equations for pre-stressed, dissipative materials

The equations of motion and the constitutive equations are derived for a solid which is subject to a body force and hence experiences a pre-stress in the equilibrium configuration. The motion superposed to the equilibrium configuration is regarded as small, which motivates the linearized approximation.

It is convenient, if not imperative, to make use of three configurations, the un-stressed configuration \mathcal{R} , the pre-stressed, intermediate configuration \mathcal{R}_i and the current configuration \mathcal{R}_t [9]. We may view these configurations as the result of subsequent deformations or motions such that

$$\mathbf{X} \in \mathcal{R} \rightarrow \bar{\mathbf{x}} \in \mathcal{R}_i \rightarrow \tilde{\mathbf{x}} \in \mathcal{R}_t.$$

Denote by

$$\mathbf{u}(\mathbf{X}, t) = \tilde{\mathbf{x}}(\mathbf{X}, t) - \bar{\mathbf{x}}(\mathbf{X})$$

the displacement of the particle \mathbf{X} , at time t , due to motion. By the assumed invertibility of $\mathbf{x}(\mathbf{X})$ we can regard both \mathcal{R} and \mathcal{R}_i as reference. The superposed $-$ and \sim denote quantities pertaining to \mathcal{R}_i and \mathcal{R}_t . The symbols $\nabla_{\mathbf{X}}$ and $\nabla (= \nabla_{\tilde{\mathbf{x}}})$ denote the gradient operators relative to \mathcal{R} and \mathcal{R}_i . Sym is the set of symmetric, second-order, tensors. The superscript T means transpose.

Let $\bar{\mathbf{S}}$, $\tilde{\mathbf{S}}$ be the first Piola-Kirchhoff stress tensors, $\rho_0, \bar{\rho}$ the densities in $\mathcal{R}, \mathcal{R}_i$ and $\bar{\mathbf{F}}$ and $\tilde{\mathbf{F}}$ the deformation gradient from \mathcal{R} to \mathcal{R}_i and from \mathcal{R} to \mathcal{R}_t , i.e. $\bar{\mathbf{F}} = \nabla_{\mathbf{X}} \bar{\mathbf{x}}^T$, $\tilde{\mathbf{F}} = \nabla_{\mathbf{X}} \tilde{\mathbf{x}}^T$. It is worth remarking that, by the chain rule,

$$\tilde{\mathbf{F}} = \nabla_{\mathbf{X}} (\bar{\mathbf{x}} + \mathbf{u})^T = \bar{\mathbf{F}} + \mathbf{H}\bar{\mathbf{F}}$$

where $\mathbf{H} = \nabla \mathbf{u}^T$. Also, let $\bar{J} = \det \bar{\mathbf{F}} > 0$. The mass density ρ_0 at \mathcal{R} is related to $\bar{\rho}$ by $\rho_0 = \bar{J}\bar{\rho}$.

We now examine the equilibrium condition at \mathcal{R}_i . The equilibrium equation may be given the form

$$\nabla_{\mathbf{X}} \cdot \bar{\mathbf{S}} + \rho_0 \mathbf{b} = 0$$

where \mathbf{b} is the body force per unit mass. Since $\ddot{\tilde{\mathbf{x}}} = \ddot{\mathbf{u}}$ we can write the equation of motion as

$$\rho_0 \ddot{\mathbf{u}} = \nabla_{\mathbf{X}} \cdot \tilde{\mathbf{S}} + \rho_0 \mathbf{b}.$$

We let \mathbf{b} be a known smooth function of the position in space. Hence,

$$\mathbf{b}(\tilde{\mathbf{x}}) - \mathbf{b}(\bar{\mathbf{x}}) = (\mathbf{u} \cdot \nabla) \mathbf{b} + o(|\mathbf{u}|).$$

Subtraction and neglect of $o(|\mathbf{u}|)$ provides

$$\rho_0 \ddot{\mathbf{u}} = \nabla_{\mathbf{X}} \cdot (\tilde{\mathbf{S}} - \bar{\mathbf{S}}) + \rho_0 (\mathbf{u} \cdot \nabla) \mathbf{b}.$$

Let $\bar{\mathbf{Y}}$ and $\tilde{\mathbf{Y}} = \bar{\mathbf{Y}} + \mathbf{Y}$ be the second Piola-Kirchhoff stress tensors corresponding to $\bar{\mathbf{x}}$ and $\tilde{\mathbf{x}}$,

$$\bar{\mathbf{S}} = \bar{\mathbf{F}} \bar{\mathbf{Y}}, \quad \tilde{\mathbf{S}} = (\bar{\mathbf{F}} + \nabla_{\mathbf{X}} \mathbf{u}^T)(\bar{\mathbf{Y}} + \mathbf{Y}).$$

We regard \mathbf{Y} as small inasmuch as \mathbf{u} and $\nabla \mathbf{u}^T =: \mathbf{H}$ are small so that we neglect $\nabla_{\mathbf{X}} \mathbf{u}^T \mathbf{Y}$ as well as quadratic terms in $\mathbf{u}, \nabla_{\mathbf{X}} \mathbf{u}$ and higher. Hence we have

$$\rho_0 \ddot{\mathbf{u}} = \nabla_{\mathbf{X}} \cdot (\mathbf{H} \bar{\mathbf{F}} \bar{\mathbf{Y}} + \bar{\mathbf{F}} \mathbf{Y}) + \rho_0 (\mathbf{u} \cdot \nabla) \mathbf{b}.$$

We now determine the equation of motion with the equilibrium configuration as reference. By use of the identity $\partial(\bar{F}_{iK}/\bar{J})/\partial\bar{x}_i = 0$ we can write

$$\rho_0 \ddot{\mathbf{u}} = \nabla \cdot (\frac{1}{\bar{J}} \mathbf{H} \bar{\mathbf{F}} \bar{\mathbf{Y}} \bar{\mathbf{F}}^T + \frac{1}{\bar{J}} \bar{\mathbf{F}} \bar{\mathbf{Y}} \bar{\mathbf{F}}^T) + \rho_0 (\mathbf{u} \cdot \nabla) \mathbf{b}.$$

Observe that $\bar{\mathbf{T}} := \bar{\mathbf{F}} \bar{\mathbf{Y}} \bar{\mathbf{F}}^T / \bar{J}$ is the Cauchy stress at \mathcal{R}_i . Hence the equation of motion can be given the form

$$\rho_0 \ddot{\mathbf{u}} = \nabla \cdot (\mathbf{H} \bar{\mathbf{T}} + \frac{1}{\bar{J}} \bar{\mathbf{F}} \bar{\mathbf{Y}} \bar{\mathbf{F}}^T) + \rho_0 (\mathbf{u} \cdot \nabla) \mathbf{b}. \quad (2)$$

Incidentally, the actual Cauchy stress $\tilde{\mathbf{T}} = \hat{\mathbf{F}} \hat{\mathbf{Y}} \hat{\mathbf{F}}^T / \tilde{J}$ in the linear approximation takes the form

$$\tilde{\mathbf{T}} = \bar{\mathbf{T}} + \mathbf{H} \bar{\mathbf{T}} + \bar{\mathbf{T}} \mathbf{H}^T - \bar{\mathbf{T}} \nabla \cdot \mathbf{u} + \frac{1}{\bar{J}} \bar{\mathbf{F}} \bar{\mathbf{Y}} \bar{\mathbf{F}}^T \quad (3)$$

The result (3) traces back to Cauchy (cf. [10]).

Henceforth we let $\hat{\mathbf{Y}}$ be linear in $\hat{\mathbf{C}} = \tilde{\mathbf{C}} - \bar{\mathbf{C}}$, $\tilde{\mathbf{C}}, \bar{\mathbf{C}}$ being the right Cauchy-Green tensors. To account for dissipativity through memory effects we let

$$\mathbf{Y}(t) = \Xi \mathbf{C}(t) + \int_0^\infty \Xi'(\xi) \mathbf{C}(t - \xi) d\xi \quad (4)$$

where $\Xi, \Xi'(\xi)$ are fourth-order tensors mapping Sym into Sym.

2.1. THERMODYNAMIC RESTRICTIONS

Let $\mathbf{T}, \mathbf{L}, \rho$ be the Cauchy stress, the velocity gradient, the mass density on the pertinent space-time domain. The dependence on position is understood and not written.

The second law of thermodynamics is taken to be expressed by

$$\int_0^\tau \frac{1}{\rho(t)} \mathbf{T}(t) \cdot \mathbf{L}(t) dt > 0,$$

at any point of the body, for any non-trivial function \mathbf{L} on $[0, \tau]$ while $\mathbf{T}, \mathbf{L}, \rho$ are periodic functions with period τ .

As a consequence of the second law, the half-range sine and cosine transforms of Ξ' ,

$$\Xi'_s(\omega) = \int_0^\infty \Xi(\xi) \sin \omega \xi d\xi, \quad \Xi'_c(\omega) = \int_0^\infty \Xi(\xi) \cos \omega \xi d\xi$$

satisfy the inequality

$$\Sigma \cdot \Xi'_s \Sigma + \Theta \cdot \Xi'_s \Theta + \Sigma \cdot (\Xi'_c - \Xi'^T_c) \Theta < 0, \quad \forall \omega > 0, \quad (5)$$

for all $\Sigma, \Theta \in \text{Sym}$. In particular, Ξ'_s is required to be negative definite in Sym.

The proof follows by starting with the observation that

$$\dot{\mathbf{C}} = 2\mathbf{F}^T \mathbf{D} \mathbf{F}, \quad \mathbf{D} := (\mathbf{L} + \mathbf{L}^T)/2.$$

Hence

$$\frac{1}{\rho} \mathbf{T} \cdot \mathbf{L} = \frac{1}{2\rho_0} \mathbf{Y} \cdot \dot{\mathbf{C}}.$$

We apply these conditions to the quantities associated with the motion $\tilde{\mathbf{x}}$. We have

$$\frac{1}{\tilde{\rho}} \tilde{\mathbf{T}} \cdot \tilde{\mathbf{L}} = \frac{1}{2\rho_0} \tilde{\mathbf{Y}} \cdot \dot{\mathbf{C}} + \frac{1}{2\rho_0} \mathbf{Y} \cdot \dot{\mathbf{C}}.$$

For any periodic function \mathbf{C} , on $[0, \tau]$, the integral of $\tilde{\mathbf{Y}} \cdot \dot{\mathbf{C}}$ on $[0, \tau]$ vanishes. Hence we are left with the inequality

$$\int_0^\tau \mathbf{Y}(t) \cdot \dot{\mathbf{C}}(t) dt > 0.$$

Choose the time dependence of \mathbf{C} as $\mathbf{C}(t) = \Sigma \sin \omega t + \Theta \cos \omega t$, where Σ, Θ are symmetric second-order tensors and $\omega > 0$. The period τ equals $2\pi/\omega$. Substitution in

$$\int_0^{2\pi/\omega} \dot{\mathbf{C}}(t) \cdot [\Xi \mathbf{C}(t) + \int_0^\infty \Xi'(\xi) \mathbf{C}(t - \xi) d\xi] dt > 0$$

and integration with respect to t yield the inequality (5). The choice $\Sigma = \Theta$ provide the negative definiteness

$$\Sigma \cdot \Xi'_s(\omega) \Sigma < 0, \quad \forall \omega > 0, \quad \forall \Sigma \in \text{Sym}. \quad (6)$$

It is convenient to deal with quantities induced by the motion $\tilde{\mathbf{x}}$ with the equilibrium configuration as reference. In the linear approximation we have

$$\mathbf{C} = 2\bar{\mathbf{F}}^T \mathbf{E} \bar{\mathbf{F}}, \quad \mathbf{E} := (\mathbf{H} + \mathbf{H}^T)/2.$$

Hence we can write

$$\frac{1}{J} (\bar{\mathbf{F}} \mathbf{Y} \bar{\mathbf{F}}^T)_{lm} = K_{lmnp} E_{np}(t) + \int_0^\infty K'_{lmnp}(\xi) E_{np}(t - \xi) d\xi$$

where

$$K_{lmnp} = \frac{2}{J} \bar{F}_{lL} \bar{F}_{mM} \bar{F}_{nN} \bar{F}_{pP} \Xi_{LMNP}, \quad K'_{lmnp} = \frac{2}{J} \bar{F}_{lL} \bar{F}_{mM} \bar{F}_{nN} \bar{F}_{pP} \Xi'_{LMNP}.$$

Moreover, by (6) we find that

$$\mathbf{B} \cdot \mathbf{K}'_s(\omega) \mathbf{B} < 0, \quad \forall \omega > 0, \quad \forall \mathbf{B} \in \text{Sym}.$$

Letting

$$\mathcal{T}(t) = \mathbf{H}(t) \bar{\mathbf{T}} + \mathbf{K} \mathbf{H}(t) + \int_0^\infty \mathbf{K}'(\xi) \mathbf{H}(t - \xi) d\xi,$$

we can write the equation of motion in the form

$$\rho_0 \ddot{\mathbf{u}} = \nabla \cdot \mathcal{T}. \quad (7)$$

2.2. DEFINITENESS PROPERTIES

For a time-harmonic dependence, $\mathbf{u}(\mathbf{x}, t) \propto \exp(-i\omega t)$, we let \mathcal{T} be given by

$$\mathcal{T} = \mathbf{G} \partial \mathbf{u} / \partial \mathbf{x} \quad (T_{jh} = G_{jhl} \partial u_l / \partial x_h), \quad (8)$$

where \mathbf{G} is a complex-valued fourth-order tensor given by

$$G_{jhl} = \delta_{jk} \bar{T}_{lh} + K_{jhl} + \int_0^\infty K'_{jhl}(\xi) \exp(i\omega\xi) d\xi.$$

For any fourth-order tensor Γ and vectors \mathbf{a}, \mathbf{b} we let $\mathbf{a}\Gamma\mathbf{b}$ be the second-order tensor defined by

$$(\mathbf{a}\Gamma\mathbf{b})_{jk} = \Gamma_{jhl} a_h b_l.$$

If Γ is (negative) definite in Sym then $\mathbf{b}\Gamma\mathbf{b}$ is definite in the underlying vector space V . For,

$$0 > (\mathbf{a} \otimes \mathbf{b} + \mathbf{b} \otimes \mathbf{a}) \cdot \Gamma(\mathbf{a} \otimes \mathbf{b} + \mathbf{b} \otimes \mathbf{a}) = 4\mathbf{a} \cdot (\mathbf{b}\Gamma\mathbf{b})\mathbf{a}$$

for all non-zero \mathbf{a}, \mathbf{b} gives the result. As a consequence, since the imaginary part \mathbf{G}_I of \mathbf{G} is negative definite in Sym then also the imaginary part \mathcal{G}_I of $\mathcal{G} = \mathbf{e}_3 \mathbf{G} \mathbf{e}_3$ is negative definite in V . Let $\mathcal{G} = \mathcal{G}_R + i\mathcal{G}_I$ and observe that

$$\mathcal{G}_R = \mathbf{e}_3 \cdot \bar{\mathbf{T}} \mathbf{e}_3 \mathbf{1} + \mathbf{e}_3 \mathbf{K} \mathbf{e}_3 + \mathbf{e}_3 \mathbf{K}'_c \mathbf{e}_3, \quad \mathcal{G}_I = \mathbf{e}_3 \mathbf{K}'_s \mathbf{e}_3$$

whence $\mathcal{G}_R, \mathcal{G}_I \in \text{Sym}$.

We now show that \mathcal{G} is invertible. Let $\mathbf{w} \in \mathbb{C}^3$ and observe that $\mathcal{G}\mathbf{w} = \mathbf{0}$ is equivalent to

$$\mathcal{G}_R \mathbf{w}_R - \mathcal{G}_I \mathbf{w}_I = \mathbf{0}, \quad \mathcal{G}_I \mathbf{w}_R + \mathcal{G}_R \mathbf{w}_I = \mathbf{0}.$$

Inner multiply by \mathbf{w}_I and \mathbf{w}_R , respectively, and apply the symmetry of \mathcal{G}_R and \mathcal{G}_I . Subtraction yields

$$\mathbf{w}_R \cdot \mathcal{G}_I \mathbf{w}_R + \mathbf{w}_I \cdot \mathcal{G}_I \mathbf{w}_I = \mathbf{0}.$$

The negative definiteness of \mathcal{G}_I implies that $\mathbf{w}_R, \mathbf{w}_I = \mathbf{0}$ and hence $\mathbf{w} = \mathbf{0}$ whence we have the invertibility of \mathcal{G} .

In elasticity, $\mathcal{G} = \mathbf{e}_3 \cdot \bar{\mathbf{T}} \mathbf{e}_3 \mathbf{1} + \mathbf{e}_3 \mathbf{K} \mathbf{e}_3$ is real-valued. It is reasonable to assume the ellipticity condition, $\mathbf{K} > 0$ in Sym . This implies that \mathcal{G} is positive definite if $\mathbf{e}_3 \cdot \bar{\mathbf{T}} \mathbf{e}_3$ is positive or slightly negative. Now $\mathcal{G}\mathbf{w} = \mathbf{0}$ amounts to

$$\mathcal{G}\mathbf{w}_R = \mathbf{0}, \quad \mathcal{G}\mathbf{w}_I = \mathbf{0}.$$

Inner multiplication by \mathbf{w}_R and \mathbf{w}_I and summation gives

$$\mathbf{w}_R \cdot \mathcal{G}\mathbf{w}_R + \mathbf{w}_I \cdot \mathcal{G}\mathbf{w}_I = \mathbf{0}.$$

Hence we have $\mathbf{w}_R, \mathbf{w}_I = \mathbf{0}$, namely $\mathbf{w} = \mathbf{0}$, and \mathcal{G} is invertible.

3. State-variable equations

We now look for time-harmonic waves of the form

$$\mathbf{u}(\mathbf{x}, t) = \hat{\mathbf{u}}(z) \exp[i(\mathbf{k}_{\parallel} \cdot \mathbf{x} - \omega t)]$$

where ω is the real frequency and \mathbf{k}_{\parallel} is a given complex-valued wave vector, perpendicular to \mathbf{e}_3 . Hence $\hat{\mathbf{u}}$ is a unknown vector function of z . To obtain the governing equations in the form of a first-order system it is convenient to consider

$$\boldsymbol{\tau} := \mathcal{T}\mathbf{e}_3 = \hat{\boldsymbol{\tau}}(z) \exp[i(\mathbf{k}_{\parallel} \cdot \mathbf{x} - \omega t)].$$

In un-stressed bodies $\mathcal{T}\mathbf{e}_3$ is the traction at planes perpendicular to the z -axis. Upon the observation that

$$\nabla = \frac{\partial}{\partial \mathbf{x}_{\parallel}} + \mathbf{e}_3 \frac{\partial}{\partial z} \quad (9)$$

where \mathbf{x}_{\parallel} is the part of \mathbf{x} perpendicular to \mathbf{e}_3 , eqs (7) and (8) give

$$-\rho\omega^2 \mathbf{u} = i\mathcal{T}\mathbf{k}_{\parallel} + \boldsymbol{\tau}',$$

$$\mathcal{T} = i\mathbf{G}(\mathbf{u} \otimes \mathbf{k}_{\parallel}) + \mathbf{G}(\mathbf{u}' \otimes \mathbf{e}_3).$$

Evaluation of $\mathcal{T}\mathbf{e}_3$ and application of \mathcal{G}^{-1} gives

$$\hat{\mathbf{u}}' = \mathbf{A}^I \hat{\mathbf{u}} + \mathbf{A}^{II} \hat{\boldsymbol{\tau}} \quad (10)$$

where

$$\mathbf{A}^I = -i\mathcal{G}^{-1}(\mathbf{e}_3 \mathbf{G} \mathbf{k}_{\parallel}), \quad \mathbf{A}^{II} = \mathcal{G}^{-1}.$$

Meanwhile, evaluation of $\mathcal{T}\mathbf{k}_{\parallel}$ and substitution gives

$$\hat{\boldsymbol{\tau}}' = \mathbf{A}^{III} \hat{\mathbf{u}} + \mathbf{A}^{IV} \hat{\boldsymbol{\tau}} \quad (11)$$

where

$$\mathbf{A}^{III} = -\rho\omega^2 \mathbf{1} + \mathbf{k}_{\parallel} \mathbf{G} \mathbf{k}_{\parallel} - (\mathbf{k}_{\parallel} \mathbf{G} \mathbf{e}_3) \mathcal{G}^{-1}(\mathbf{e}_3 \mathbf{G} \mathbf{k}_{\parallel}), \quad \mathbf{A}^{IV} = (\mathbf{A}^I)^T.$$

Letting $\mathbf{w} = [\hat{\mathbf{u}}, \hat{\boldsymbol{\tau}}]^T$ and defining the matrix \mathbf{A} in the block form

$$\mathbf{A} = \begin{bmatrix} \mathbf{A}^I & \mathbf{A}^{II} \\ \mathbf{A}^{III} & \mathbf{A}^{IV} \end{bmatrix}$$

we can write the governing equations in the form (1). Hereafter we keep representing 6×6 matrices through four 3×3 blocks as for \mathbf{A} . This in turn shows that the 6-tuple $\mathbf{w} = [\hat{\mathbf{u}}, \hat{\boldsymbol{\tau}}]^T$ is the set of state variables.

3.1. JUMP CONDITIONS

In multilayers, the matrix \mathbf{A} may suffer jump discontinuities across the dividers. To solve (1) in multilayers we then need the jump conditions of the unknown field

w. The displacement \mathbf{u} and the traction $\mathbf{t} = \tilde{\mathbf{T}}\mathbf{e}_3$ are taken to be continuous. Hence we need the jump condition for τ .

Observe that

$$\hat{\mathbf{T}} = \bar{\mathbf{T}} + \bar{\mathbf{T}}\mathbf{H}^T - \bar{\mathbf{T}}\nabla \cdot \mathbf{u} + \boldsymbol{\tau}.$$

Application to \mathbf{e}_3 gives

$$\mathbf{t} = \bar{\mathbf{T}}\mathbf{e}_3 + \bar{\mathbf{T}}\mathbf{H}^T\mathbf{e}_3 - \bar{\mathbf{T}}\mathbf{e}_3 \nabla \cdot \mathbf{u} + \boldsymbol{\tau}.$$

By means of the representation (9) we find that

$$\bar{\mathbf{T}}\mathbf{H}^T\mathbf{e}_3 - \bar{\mathbf{T}}\mathbf{e}_3 \nabla \cdot \mathbf{u} = i(\bar{\mathbf{T}}\mathbf{k}_{\parallel} \otimes \mathbf{e}_3 - \bar{\mathbf{T}}\mathbf{e}_3 \otimes \mathbf{k}_{\parallel})\mathbf{u}.$$

Substitution gives

$$\mathbf{t} = \bar{\mathbf{T}}\mathbf{e}_3 + i(\bar{\mathbf{T}}\mathbf{k}_{\parallel} \otimes \mathbf{e}_3 - \bar{\mathbf{T}}\mathbf{e}_3 \otimes \mathbf{k}_{\parallel})\mathbf{u} + \boldsymbol{\tau}.$$

The traction \mathbf{t} comprises an additive time-independent term $\bar{\mathbf{T}}\mathbf{e}_3$. Hence, letting

$$\mathbf{t} - \bar{\mathbf{T}}\mathbf{e}_3 = \hat{\mathbf{t}}(z) \exp[i(\mathbf{k}_{\parallel} \cdot \mathbf{x} - \omega t)],$$

we can write the (invertible) relation

$$\begin{bmatrix} \hat{\mathbf{u}} \\ \hat{\boldsymbol{\tau}} \end{bmatrix} = \begin{bmatrix} 1 & 0 \\ \mathbf{M} & 1 \end{bmatrix} \begin{bmatrix} \hat{\mathbf{u}} \\ \hat{\boldsymbol{\tau}} \end{bmatrix}, \quad \mathbf{M} := -i[\bar{\mathbf{T}}\mathbf{k}_{\parallel} \otimes \mathbf{e}_3 - \bar{\mathbf{T}}\mathbf{e}_3 \otimes \mathbf{k}_{\parallel}].$$

Boundary conditions are usually given in terms of displacement and traction. The value of $\boldsymbol{\tau}$ is determined through

$$\hat{\boldsymbol{\tau}} = -\mathbf{M}\hat{\mathbf{u}} + \hat{\mathbf{t}}.$$

Denote by $[\![\cdot]\!]$ the jump of a quantity across a surface, namely

$$[\![f(z)]\!] = f(z_+) - f(z_-).$$

Hence the continuity of \mathbf{t} , $\bar{\mathbf{T}}\mathbf{e}_3$ and \mathbf{k}_{\parallel} yields

$$\mathbf{0} = [\![\hat{\mathbf{t}}]\!] = i[\![\bar{\mathbf{T}}\mathbf{k}_{\parallel}]\!](\mathbf{e}_3 \cdot \hat{\mathbf{u}}) + [\![\hat{\boldsymbol{\tau}}]\!]$$

whence we have the jump of $\boldsymbol{\tau}$ as

$$[\![\hat{\boldsymbol{\tau}}]\!] = -i[\![\bar{\mathbf{T}}\mathbf{k}_{\parallel}]\!](\mathbf{e}_3 \cdot \hat{\mathbf{u}}). \quad (12)$$

Accordingly,

$$\mathbf{w}(z_+) = \mathbf{\Pi}(z)\mathbf{w}(z_-), \quad \mathbf{\Pi} := \begin{bmatrix} 1 & 0 \\ -i[\![\bar{\mathbf{T}}\mathbf{k}_{\parallel}]\!] \otimes \mathbf{e}_3 & 1 \end{bmatrix}.$$

4. Impedance matrix

Let $\mathbf{Z}(z)$ be the $\mathbb{C}^{3 \times 3}$ -matrix function such that

$$\hat{\tau} = \mathbf{Z}\hat{\mathbf{u}}.$$

Differentiation with respect to z and comparison with (1) yields

$$(\mathbf{Z}' + \mathbf{ZA}^I + \mathbf{ZA}^{II}\mathbf{Z} - \mathbf{A}^{III} - \mathbf{A}^{IV}\mathbf{Z})\hat{\mathbf{u}} = 0.$$

This relation holds for every vector $\hat{\mathbf{u}}$ only if \mathbf{Z} satisfies the Riccati differential equation

$$\mathbf{Z}' = \mathbf{A}^{III} + \mathbf{A}^{IV}\mathbf{Z} - \mathbf{ZA}^I - \mathbf{ZA}^{II}\mathbf{Z}. \quad (13)$$

If $\mathbf{Z}(\bar{z})$ is known at some \bar{z} then the integration, in the existence domain $I \ni \bar{z}$, provides $\mathbf{Z}(z)$, $z \in I$. Once \mathbf{Z} is determined, the function $\hat{\mathbf{u}}$ is found by solving the linear differential equation

$$\hat{\mathbf{u}}' = (\mathbf{A}^I + \mathbf{A}^{II}\mathbf{Z})\hat{\mathbf{u}}$$

with a suitable value $\hat{\mathbf{u}}(\bar{z})$. The vector $\hat{\tau}$ is then determined by applying \mathbf{Z} to $\hat{\mathbf{u}}$.

The matrix $\mathbf{W} = \mathbf{Z}^{-1}$, such that $\hat{\mathbf{u}} = \mathbf{W}\hat{\mathbf{t}}$, is found to satisfy the Riccati differential equation

$$\mathbf{W}' = \mathbf{A}^I + \mathbf{A}^{II} - \mathbf{WA}^{IV} - \mathbf{WA}^{III}\mathbf{W}.$$

The matrix \mathbf{Z} differs from the standard impedance matrix [7] in that τ is different from \mathbf{t} . Indeed, since

$$\hat{\mathbf{t}} = (\mathbf{Z} - \mathbf{M})\hat{\mathbf{u}}$$

then $\mathbf{Z} - \mathbf{M}$ is the impedance matrix. Hence, across any surface $z = \text{constant}$, we have

$$[\mathbf{Z}] = [\mathbf{M}] = -i[\bar{\mathbf{T}}\mathbf{k}] \otimes \mathbf{e}_3.$$

To fix \mathbf{Z} at some value of z we naturally have recourse to the boundary condition. Here we look at the divider $z = d$ and consider three possibilities.

Free boundary. At $z = d$ we have $\bar{\mathbf{T}}\mathbf{e}_3 = \mathbf{0}$ and $\hat{\mathbf{t}} = \mathbf{0}$ while \mathbf{u} is undetermined. Hence we let $\mathbf{Z}(d) - \mathbf{M}(d) = \mathbf{0}$ whence $\mathbf{Z}(d_-) = -i(\bar{\mathbf{T}}\mathbf{k}_{||}) \otimes \mathbf{e}_3$. Integration of (13) yields $\mathbf{Z}(0)$.

Fixed boundary. At $z = d$ we have $\mathbf{u} = \mathbf{0}$ while \mathbf{t} is undetermined. We then consider \mathbf{W} and set $\mathbf{W}(d) = \mathbf{0}$. By integration we obtain $\mathbf{W}(0)$.

Homogeneous half-space as $z > d$. The value of $\mathbf{Z}(0)$ is connected with the wave modes occurring in the half-space $z > d$. The connection is made operative in the next section.

5. Reflectivity matrix

We restrict attention to the homogeneous half-spaces $z < 0$, $z > d$. Let the matrix \mathbf{A} be simple. Denote by λ_α the (not necessarily distinct) eigenvalues of \mathbf{A} and by \mathbf{p}_α the associated independent eigenvectors, $\alpha = 1, 2, \dots, 6$. Let \mathbf{P} be the matrix whose ordered columns are $\mathbf{p}_1, \mathbf{p}_2, \dots, \mathbf{p}_6$ and $\mathbf{\Lambda} = \text{diag}[\lambda_1, \dots, \lambda_6]$. It is a well known result that

$$\mathbf{P}^{-1} \mathbf{A} \mathbf{P} = \mathbf{\Lambda}. \quad (14)$$

Let

$$\mathbf{E}(z) = \exp \left[\int_0^z \mathbf{\Lambda}(\xi) d\xi \right]$$

and

$$\mathbf{v} = \mathbf{E}^{-1} \mathbf{P}^{-1} \mathbf{w}.$$

Owing to (1) we obtain

$$\mathbf{v}' = -\mathbf{E}^{-1} \mathbf{Q} \mathbf{E} \mathbf{v} \quad (15)$$

where $\mathbf{Q} = \mathbf{P}^{-1} \mathbf{P}'$. Hence \mathbf{v} is constant, as $z < 0$ and $z > d$. The meaning of \mathbf{v} follows by considering $\mathbf{w} = \mathbf{P} \mathbf{E} \mathbf{v}$, namely

$$\mathbf{w} \exp[i(\mathbf{k}_\parallel \cdot \mathbf{x} - \omega t)] = \sum_{\alpha=1}^6 v_\alpha(z) \exp \left[\int_0^z \lambda_\alpha(\tau) d\tau \right] \mathbf{p}_\alpha(z) \exp[i(\mathbf{k}_\parallel \cdot \mathbf{x} - \omega t)]$$

whence $\{v_\alpha\}$ are the amplitudes of the propagation modes. It is reasonable to assume that they partition in three forward propagating modes, ($\mathbf{v}^f = [v_1, v_2, v_3]^T$), and three backward, ($\mathbf{v}^b = [v_4, v_5, v_6]^T$). Hence $\mathbf{v} = [\mathbf{v}^f, \mathbf{v}^b]^T$ and we define the reflectivity matrix \mathbf{R} through

$$\mathbf{v}^b = \mathbf{R} \mathbf{v}^f.$$

To establish the connection between \mathbf{Z} and \mathbf{R} observe that

$$\begin{bmatrix} \hat{\mathbf{u}} \\ \mathbf{Z} \hat{\mathbf{u}} \end{bmatrix} = \begin{bmatrix} \mathbf{P}' \mathbf{E}' & \mathbf{P}^{II} \mathbf{E}^{IV} \\ \mathbf{P}^{III} \mathbf{E}' & \mathbf{P}^{IV} \mathbf{E}^{IV} \end{bmatrix} \begin{bmatrix} \mathbf{v}^f \\ \mathbf{R} \mathbf{v}^f \end{bmatrix}.$$

Evaluation of $\hat{\mathbf{u}}$ - first row - and substitution in the second row gives

$$\mathbf{Z} \mathbf{P}' \mathbf{E}' \mathbf{v}^f + \mathbf{Z} \mathbf{P}^{III} \mathbf{E}^{IV} \mathbf{R} \mathbf{v}^f = \mathbf{P}^{III} \mathbf{E}' \mathbf{v}^f + \mathbf{P}^{IV} \mathbf{E}^{IV} \mathbf{R} \mathbf{v}^f$$

whence

$$\mathbf{Z} = (\mathbf{P}^{III} \mathbf{E}' + \mathbf{P}^{IV} \mathbf{E}^{IV} \mathbf{R})(\mathbf{P}' \mathbf{E}' + \mathbf{P}^{II} \mathbf{E}^{IV} \mathbf{R})^{-1}$$

with inverse

$$\mathbf{R} = (\mathbf{Z} \mathbf{P}^{II} - \mathbf{P}^{IV} \mathbf{E}^{IV})^{-1} (\mathbf{P}^{III} - \mathbf{Z} \mathbf{P}' \mathbf{E}').$$

As shown in [7], the matrix function $\mathbf{R}(z)$ satisfies the Riccati differential equation

$$\mathbf{R}' = \mathbf{N}^{III} + \mathbf{N}^{IV} \mathbf{R} - \mathbf{R} \mathbf{N}' - \mathbf{R} \mathbf{N}^{II} \mathbf{R}$$

where

$$\mathbf{N} = -\mathbf{E}^{-1}\mathbf{P}^{-1}\mathbf{P}'\mathbf{E}.$$

Also, if the transmissivity matrix \mathbf{T} is defined such that

$$\mathbf{T}(z)\mathbf{v}^f(z) = \mathbf{v}^f(d), \quad \mathbf{T}(d) = \mathbf{1},$$

then $\mathbf{T}(z)$ is determined through \mathbf{R} by the differential equation [7]

$$\mathbf{T}' = -\mathbf{T}\mathbf{N}^I - \mathbf{T}\mathbf{N}^{II}\mathbf{R}.$$

When the half-space $z > d$ is homogeneous we set, at $z = d_+$,

$$\mathbf{R} = \mathbf{0}$$

to mean that only transmitted waves occur. Hence we have

$$\mathbf{Z}(d) = \mathbf{P}^{III}(\mathbf{P}^I)^{-1}.$$

As for the reflection matrix, the transmission matrix is the value (of \mathbf{T}) at the beginning of the layer, $\mathbf{T}(0_-)$, such that

$$\mathbf{T}(0_-)\mathbf{v}^f(0_-) = \mathbf{v}^f(d_+).$$

5.1. JUMP CONDITION

At any jump discontinuity of \mathbf{A} the matrix \mathbf{R} suffers a jump discontinuity. It is then convenient to determine $\mathbf{R}_-(z) := \mathbf{R}(z_-)$ in terms of $\mathbf{R}_+(z) := \mathbf{R}(z_+)$ at any value of z . First we write $\hat{\mathbf{u}}$ and $\hat{\mathbf{t}}$ in terms of \mathbf{v} , namely

$$\begin{bmatrix} \hat{\mathbf{u}} \\ \hat{\mathbf{t}} \end{bmatrix} = \begin{bmatrix} \mathbf{1} & \mathbf{0} \\ \mathbf{M} & \mathbf{1} \end{bmatrix} \mathbf{P}\mathbf{E} \begin{bmatrix} \mathbf{v}^f \\ \mathbf{R}\mathbf{v}^f \end{bmatrix}.$$

The continuity of $\hat{\mathbf{u}}$ and $\hat{\mathbf{t}}$ results in

$$\begin{bmatrix} \mathbf{v}_-^f \\ \mathbf{R}_-\mathbf{v}_-^f \end{bmatrix} = \mathbf{J} \begin{bmatrix} \mathbf{v}_+^f \\ \mathbf{R}_+\mathbf{v}_+^f \end{bmatrix}$$

where

$$\mathbf{J} = \mathbf{E}^{-1}\mathbf{P}_-^{-1} \begin{bmatrix} \mathbf{1} & \mathbf{0} \\ [\mathbf{M}] & \mathbf{1} \end{bmatrix} \mathbf{P}_+ \mathbf{E}. \quad (16)$$

Evaluation of \mathbf{v}_-^f , substitution and the identical validity with respect to \mathbf{v}_+^f yields

$$\mathbf{R}_-(\mathbf{J}^I + \mathbf{J}^{II}\mathbf{R}_+) = \mathbf{J}^{III} + \mathbf{J}^{IV}\mathbf{R}_+.$$

Hence we obtain the sought relation in the form

$$\mathbf{R}_- = (\mathbf{J}^{III} + \mathbf{J}^{IV}\mathbf{R}_+)(\mathbf{J}^I + \mathbf{J}^{II}\mathbf{R}_+)^{-1}. \quad (17)$$

6. Propagator matrix

Let $\Omega_k(z, z_{k-1})$, $z \in [z_{k-1}, z_k]$, be defined by

$$\mathbf{w}(z) = \Omega_k(z, z_{k-1})\mathbf{w}(z_{k-1}), \quad z \in (z_{k-1}, z_k) \quad \Omega_k(z_{k-1}, z_{k-1}) = \mathbf{1}.$$

Hence Ω_k is the propagator matrix in the layer (z_{k-1}, z_k) . Substitution in (1) gives

$$\Omega'_k(z, z_{k-1}) = \mathbf{A}(z)\Omega_k(z, z_{k-1}), \quad z \in (z_{k-1}, z_k),$$

whence we have the integral equation

$$\Omega_k(z, z_{k-1}) = \int_{z_{k-1}}^z \mathbf{A}(\xi)\Omega_k(\xi, z_{k-1})d\xi, \quad z \in (z_{k-1}, z_k). \quad (18)$$

For simplicity, it is understood and not written that \mathbf{A} is the restriction to the pertinent interval (z_{k-1}, z_k) . Define the sequence of matrix functions $\{\mathbf{A}_m(z, \eta)\}$, $z_{k-1} \leq \eta \leq z \leq z_k$, to be given by

$$\mathbf{A}_1(z, \xi) = \mathbf{A}(\xi),$$

$$\mathbf{A}_{m+1}(z, \eta) = \int_{\eta}^z \mathbf{A}_m(z, \nu)\mathbf{A}_1(\nu, \eta)d\nu, \quad m = 1, 2, \dots$$

If \mathbf{A} is bounded on (z_{k-1}, z_k) then the solution $\Omega_k(z, z_{k-1})$ to (18) exists and is unique in $L^2(z_{k-1}, z_k)$ and is represented by the Neumann series

$$\Omega_k(z, z_{k-1}) = \mathbf{1} + \sum_{m=1}^{\infty} \int_{z_{k-1}}^z \mathbf{A}_m(z, \xi)d\xi, \quad z \in (z_{k-1}, z_k). \quad (19)$$

Since $\Omega_k(z, z_{k-1})$ is given by the series in (19), it is of interest to evaluate the error associated with the approximation of $\Omega_k(z, z_{k-1})$ as given by a finite number of terms, $m = 1, \dots, n$, for a selected n , namely

$$\Omega_k^{(n)}(z, z_{k-1}) = \mathbf{1} + \sum_{m=1}^n \int_{z_{k-1}}^z \mathbf{A}_m(z, \xi)d\xi, \quad z \in [z_{k-1}, z_k].$$

The estimate is given as follows for any matrix norm $\|\cdot\|$.

Proposition. If $M = \sup\{\|\mathbf{A}(\eta)\| : z_{k-1} \leq \eta \leq z_k\}$ then, as $z \in (z_{k-1}, z_k)$,

$$\|\Omega_k(z, z_{k-1}) - \Omega_k^{(n)}(z, z_{k-1})\| < \frac{\exp[M(z - z_{k-1})]}{(n+1)!}(z - z_{k-1})^{n+1}. \quad (20)$$

Proof. Application of the norm $\|\cdot\|$ to $\Omega_k - \Omega_k^{(n)}$ allows us to write

$$\|\Omega_k(z, z_{k-1}) - \Omega_k^{(n)}(z, z_{k-1})\| \leq \sum_{m=n+1}^{\infty} \int_{z_{k-1}}^z \|\mathbf{A}_m(z, \xi)\|d\xi, \quad z \in [z_{k-1}, z_k].$$

Now

$$\|\mathbf{A}_{m+1}(z, \eta)\| \leq \int_{\eta}^z \|\mathbf{A}_m(z, \xi)\| M d\xi$$

whence

$$\|\mathbf{A}_2(z, \eta)\| \leq M^2(z - \eta), \quad \|\mathbf{A}_n(z, \eta)\| \leq \frac{M^n(z - \eta)^{n-1}}{(n-1)!}.$$

Accordingly,

$$\int_{z_{k-1}}^z \|\mathbf{A}_m(z, \xi)\| d\xi \leq \frac{M^m}{(m-1)!} \int_{z_{k-1}}^z (z - \xi)^{m-1} d\xi = \frac{[M(z - z_0)]^m}{m!}.$$

Hence we obtain

$$\|\boldsymbol{\Omega}_k(z, z_{k-1}) - \boldsymbol{\Omega}_k^{(n)}(z, z_{k-1})\| \leq \sum_{m=n+1}^{\infty} \frac{[M(z - z_0)]^m}{m!}.$$

The right-hand side is the remainder of $\exp[M(z - z_0)]$ relative to the polynomial $\sum_{m=0}^n [M(z - z_0)]^m / m!$. By means of the Lagrange's form of the remainder we have the estimate

$$\sum_{m=n+1}^{\infty} \frac{[M(z - z_0)]^m}{m!} = \frac{\exp[M(\xi - z_{k-1})]}{(n+1)!} (z - z_{k-1})^{n+1}, \quad \xi \in (z_{k-1}, z).$$

Since $\xi < z$, the estimate (20) follows. \square

Once we know the (exact or approximate) matrices $\boldsymbol{\Omega}_k$, $k = 1, \dots, n$, we can determine $\mathbf{w}(z_n)$ in terms of $\mathbf{w}(0)$. Now, at any layer k ,

$$\mathbf{w}((z_k)_-) = \boldsymbol{\Omega}_k(z_k, z_{k-1}) \mathbf{w}((z_{k-1})_+).$$

Also, let $\boldsymbol{\Pi}_k = \boldsymbol{\Pi}(z_k)$. Start from $\mathbf{w}(0_-)$ and observe that $\mathbf{w}(0_+) = \boldsymbol{\Pi}_0 \mathbf{w}(0_-)$. Hence apply $\boldsymbol{\Omega}_1$ and then $\boldsymbol{\Pi}_1$ and so on to get

$$\mathbf{w}(d_+) = \boldsymbol{\Pi}_n \boldsymbol{\Omega}_n \boldsymbol{\Pi}_{n-1} \dots \boldsymbol{\Omega}_1 \boldsymbol{\Pi}_0 \mathbf{w}(0_-).$$

If, rather, $[\hat{\mathbf{u}}, \hat{\mathbf{t}}]^T(z_n)$ is required in terms of $[\hat{\mathbf{u}}, \hat{\mathbf{t}}]^T(0)$ we apply the matrix \mathbf{M} to obtain

$$[\hat{\mathbf{u}}, \hat{\mathbf{t}}]^T(d_+) = \boldsymbol{\Omega}(d, 0) [\hat{\mathbf{u}}, \hat{\mathbf{t}}]^T(0_-)$$

where

$$\boldsymbol{\Omega}(d, 0) = \mathbf{M}(d_+) \boldsymbol{\Pi}_n \boldsymbol{\Omega}_n \boldsymbol{\Pi}_{n-1} \dots \boldsymbol{\Omega}_1 \boldsymbol{\Pi}_0 \mathbf{M}^{-1}(0_-).$$

The matrix $\boldsymbol{\Omega}(d, 0)$ is the propagator of the whole multilayer; it incorporates the effects of the single layers through $\boldsymbol{\Omega}_1, \dots, \boldsymbol{\Omega}_n$, the jump of \mathbf{w} at the dividers through $\boldsymbol{\Pi}_0, \boldsymbol{\Pi}_1, \dots, \boldsymbol{\Pi}_n$ and the passage from $[\hat{\mathbf{u}}, \hat{\mathbf{t}}]$ to \mathbf{w} (and viceversa) through \mathbf{M} . If \mathbf{w} is continuous at the dividers and no change of variable is performed then $\boldsymbol{\Omega}(d, 0)$ is just the composition of the matrices of the single layers.

7. Reflection and transmission of a multilayer

An incident wave is allowed to arrive from $-\infty$ and to hit the layer at $z = 0$. Reflected and transmitted waves originate at $z = 0$ and $z = d$ and propagate away to $-\infty$ and $+\infty$, respectively. Our purpose is to derive the reflected and transmitted waves in terms of the incident one and of the properties of the layer.

In the (homogeneous) half-spaces $z < 0$ and $z > d$ the matrix \mathbf{A} is taken to have 6 linearly-independent eigenvectors $\mathbf{p}_1, \dots, \mathbf{p}_6$, associated with the eigenvalues $\lambda_1, \dots, \lambda_6$. The matrix \mathbf{P} is invertible and hence we define the 6-tuple \mathbf{s} as

$$\mathbf{s} = \mathbf{P}^{-1} \mathbf{w}.$$

Accordingly \mathbf{w} and $[\mathbf{u}, \mathbf{t}]^T$ take the form

$$\mathbf{w} = \sum_{\alpha=1}^6 s_\alpha(z) \mathbf{p}_\alpha(z), \quad [\mathbf{u}, \mathbf{t}]^T = \sum_{\alpha=1}^6 s_\alpha(z) \mathbf{p}_\alpha(z) \exp[i(\mathbf{k}_\parallel \cdot \mathbf{x} - \omega t)].$$

To find the dependence of \mathbf{s} on z we observe that, upon substitution, the vector \mathbf{s} is found to satisfy the first-order system of equations

$$\mathbf{s}' = \mathbf{\Lambda} \mathbf{s} - \mathbf{Q}^{-1} \mathbf{Q}' \mathbf{s}.$$

In homogeneous regions,

$$\mathbf{s}' = \mathbf{\Lambda} \mathbf{s}$$

and hence $\mathbf{s}(z) = \exp[\mathbf{\Lambda}(z - z_0)] \mathbf{v}$, where $\mathbf{v} \in \mathbb{C}^6$. Accordingly we have

$$[\mathbf{u}, \mathbf{t}]^T = \sum_{\alpha=1}^6 v_\alpha \mathbf{p}_\alpha(z) \exp[i(\mathbf{k}_\parallel \cdot \mathbf{x} + \sigma_\alpha z - \omega t)]$$

where $\sigma_\alpha = -i\lambda_\alpha$. We assume that, depending on the values of σ_α , three of them correspond to forward-propagating waves, say $\alpha = 1, 2, 3$, and three to backward-propagating waves, $\alpha = 4, 5, 6$. Accordingly, let $\mathbf{v}^f = [v_1, v_2, v_3]^T$, $\mathbf{v}^b = [v_4, v_5, v_6]^T$. Any \mathbf{v} can then be represented as

$$\mathbf{v} = \begin{bmatrix} \mathbf{v}^f \\ \mathbf{v}^b \end{bmatrix}.$$

In general we can write \mathbf{w} as

$$\mathbf{w} = \mathbf{P} \mathbf{E} \mathbf{v}$$

where $\mathbf{E}(z) = \exp(\int_{z_0}^z \mathbf{\Lambda}(\xi) d\xi)$. However, for the sake of simplicity, it is convenient to consider separately the half spaces $z \leq 0$ and $z \geq d$. Hence we let $z_0 = 0$ or $z_0 = d$ according as we consider $z \leq 0$ or $z \geq d$. To be precise, if the incident wave

is coming from $-\infty$ then as $z > d$ we have $\mathbf{v} = [\mathbf{v}^f, \mathbf{0}]^T$, which means that only transmitted waves occur as $z > d$. Hence we have

$$\begin{aligned}\mathbf{w}(z) &= \mathbf{P}_- \exp(\Lambda_- z) \begin{bmatrix} \mathbf{v}^f \\ \mathbf{v}^b \end{bmatrix}, \quad z < 0, \\ \mathbf{w}(z) &= \mathbf{P}_+ \mathbf{E}(d) \exp(\Lambda_+(z - d)) \begin{bmatrix} \mathbf{v}^f \\ \mathbf{0} \end{bmatrix}, \quad z > d\end{aligned}$$

where Λ_- , Λ_+ and \mathbf{P}_- , \mathbf{P}_+ are the constant values of Λ and \mathbf{P} as $z < 0$ and $z > d$. Denote by \mathbf{v}^i the incident value of \mathbf{v} , namely $\mathbf{v}^i = \mathbf{v}^f(0_-)$. At $z = 0_-$ or $z = d_+$ we have

$$\mathbf{w}(0_-) = \mathbf{P}_- \begin{bmatrix} \mathbf{v}^i \\ \mathbf{R}_0 \mathbf{v}^i \end{bmatrix}, \quad \mathbf{w}(d_+) = \mathbf{P}_+ \mathbf{E}(d) \begin{bmatrix} \mathbf{T}_0 \mathbf{v}^i \\ \mathbf{0} \end{bmatrix}, \quad (21)$$

where $\mathbf{R}_0 = \mathbf{R}(0_-)$ is the reflection matrix and $\mathbf{T}_0 = \mathbf{T}(0_-)$ is the transmission matrix, namely

$$\mathbf{v}^b(0_-) = \mathbf{R}_0 \mathbf{v}^i, \quad \mathbf{v}^f(d_+) = \mathbf{T}_0 \mathbf{v}^i.$$

Since $\mathbf{w}(d) = \Omega(d, 0)\mathbf{w}(0)$, we have

$$\mathbf{P}_+ \mathbf{E}(d) \begin{bmatrix} \mathbf{T}_0 \mathbf{v}^i \\ \mathbf{0} \end{bmatrix} = \Omega(d, 0) \mathbf{P}_- \begin{bmatrix} \mathbf{v}^i \\ \mathbf{R}_0 \mathbf{v}^i \end{bmatrix}.$$

Letting

$$\Phi = \mathbf{E}(d) \mathbf{P}_+^{-1} \Omega(d, 0) \mathbf{P}_-$$

we can write

$$\begin{bmatrix} \mathbf{T}_0 \mathbf{v}^i \\ \mathbf{0} \end{bmatrix} = \begin{bmatrix} \Phi^I & \Phi^{II} \\ \Phi^{III} & \Phi^{IV} \end{bmatrix} \begin{bmatrix} \mathbf{v}^i \\ \mathbf{R}_0 \mathbf{v}^i \end{bmatrix}.$$

Hence by the arbitrariness of \mathbf{v}^i we obtain

$$\mathbf{R}_0 = -(\Phi^{IV})^{-1} \Phi^{III}, \quad \mathbf{T}_0 = \Phi^I - \Phi^{II} (\Phi^{IV})^{-1} \Phi^{III}. \quad (22)$$

If, instead, the layer ends with a fixed boundary or a free boundary then only the reflection matrix is meaningful and the conditions are given as follows.

1) *Fixed boundary.* The displacement \mathbf{u} is zero while the traction \mathbf{t} is undetermined, at the boundary $z = d$. Accordingly,

$$\begin{bmatrix} \mathbf{0} \\ \hat{\mathbf{t}}(d) \end{bmatrix} = \mathbf{w}(d) = \Omega(d, 0) \mathbf{P}_- \begin{bmatrix} \mathbf{v}^i \\ \mathbf{R}_0 \mathbf{v}^i \end{bmatrix}.$$

Let

$$\Psi = \Omega(d, 0) \mathbf{P}_-.$$

Hence we have

$$\mathbf{0} = (\Psi^I + \Psi^{II} \mathbf{R}_0) \mathbf{v}^i$$

for every vector \mathbf{v}^i . This implies that

$$\mathbf{R}_0 = -(\Psi^{II})^{-1}\Psi^I.$$

2) *Free boundary.* At the boundary, $z = d$, the traction \mathbf{t} is zero while the displacement \mathbf{u} is undetermined. Accordingly we write

$$\begin{bmatrix} \hat{\mathbf{u}}(d) \\ \mathbf{0} \end{bmatrix} = \mathbf{w}(d) = \Psi \begin{bmatrix} \mathbf{v}^i \\ \mathbf{R}_0 \mathbf{v}^i \end{bmatrix}$$

whence we have

$$\mathbf{0} = (\Psi^{III} + \Psi^{IV}\mathbf{R}_0)\mathbf{v}^i$$

Again we make use of the arbitrariness of \mathbf{v}^i to obtain

$$\mathbf{R}_0 = -(\Psi^{IV})^{-1}\Psi^{III}.$$

7.1. REFLECTION AND TRANSMISSION RELATIVE TO \mathbf{w} .

The matrices \mathbf{R}_0 and \mathbf{T}_0 express reflection and transmission in terms of the wave modes. It is more customary to evaluate the reflection and transmission in terms of the state variables \mathbf{w} . First, consider the displacement \mathbf{u} . By (21), the reflected and transmitted displacements, $\mathbf{u}^r, \mathbf{u}^t$, are given by

$$\hat{\mathbf{u}}^r(0_-) = \mathbf{P}_-^{II}\mathbf{R}_0\mathbf{v}^i, \quad \hat{\mathbf{u}}^t(d_+) = \mathbf{P}_+^I\mathbf{E}^I(d)\mathbf{T}_0\mathbf{v}^i.$$

Since the incident displacement is related to \mathbf{v}^i by $\hat{\mathbf{u}}^i = \mathbf{P}_-^I\mathbf{v}^i$ then the invertibility of \mathbf{P}_-^I gives

$$\mathbf{v}^i = (\mathbf{P}_-^I)^{-1}\hat{\mathbf{u}}^i(0_-).$$

We define the reflection and transmission matrices $\mathbf{R}_u, \mathbf{T}_u$ through

$$\hat{\mathbf{u}}^r(0_-) = \mathbf{R}_u \hat{\mathbf{u}}^i(0_-), \quad \hat{\mathbf{u}}^t(d_+) = \mathbf{T}_u \hat{\mathbf{u}}^i(0_-).$$

Hence we have

$$\mathbf{R}_u = \mathbf{P}_-^{II}\mathbf{R}_0(\mathbf{P}_-^I)^{-1}, \quad \mathbf{T}_u = \mathbf{P}_+^I\mathbf{E}^I(d)\mathbf{T}_0(\mathbf{P}_-^I)^{-1}. \quad (23)$$

By arguing in the same way, the matrices \mathbf{R}_τ and \mathbf{T}_τ such that

$$\hat{\boldsymbol{\tau}}^r(0_-) = \mathbf{R}_\tau \hat{\boldsymbol{\tau}}^i(0_-), \quad \hat{\boldsymbol{\tau}}^t(d_+) = \mathbf{T}_\tau \hat{\boldsymbol{\tau}}^i(0_-)$$

turn out to be given by

$$\mathbf{R}_\tau = \mathbf{P}_-^{IV}\mathbf{R}_0(\mathbf{P}_-^{III})^{-1}, \quad \mathbf{T}_\tau = \mathbf{P}_+^{III}\mathbf{E}^I(d)\mathbf{T}_0(\mathbf{P}_-^{III})^{-1}. \quad (24)$$

8. Comments and applications

The methods described above are all applicable to reflection-transmission problems in multilayers. The impedance \mathbf{Z} is convenient when \mathbf{w} is continuous, so that \mathbf{Z} is continuous too, at discontinuities of \mathbf{A} .

The reflectivity \mathbf{R} provides a more direct connection to the problem at hand but is usually discontinuous. The use of \mathbf{R} is decisively efficient when the multilayer consists of homogeneous layers. In such a case $\mathbf{P}' = \mathbf{0}, \mathbf{N} = \mathbf{0}$ and the Riccati equation provides the constancy of \mathbf{R} within each layer. The value of the reflection matrix \mathbf{R}_0 is then determined by the boundary condition, and hence $\mathbf{R}(d)$, and the jump of \mathbf{R} at the dividers.

The propagator matrix Ω has the advantage that a close form, though in a series form, is known for the solution. It is certainly of interest when \mathbf{A} is varying with z .

By way of application we now consider the propagation of transverse waves in isotropic, un-stressed homogeneous layers. The reflectivity matrix \mathbf{R} is then more convenient. The layer is sandwiched between two homogeneous half-spaces and then jump discontinuities of \mathbf{A} are allowed to occur at the boundaries of the layer.

8.1. TRANSVERSE WAVES IN A SINGLE HOMOGENEOUS LAYER

If \mathbf{k}_{\parallel} is in the \mathbf{e}_1 direction then the system (1) decouples and it follows that $[\hat{u}_2, \hat{t}_2]^T$ satisfies the system

$$\frac{d}{dz} \begin{bmatrix} \hat{u}_2 \\ \hat{t}_2 \end{bmatrix} = \begin{bmatrix} 0 & 1/\mu \\ -\mu\sigma_T^2 & 0 \end{bmatrix} \begin{bmatrix} \hat{u}_2 \\ \hat{t}_2 \end{bmatrix}$$

where μ is the coefficient of shear viscoelasticity and

$$\sigma_T = \sqrt{(\rho\omega^2/\mu) - \mathbf{k}_{\parallel}^2},$$

the root being that with minimal argument. Moreover, \mathbf{P} is taken in the form

$$\mathbf{P} = \begin{bmatrix} 1/\mu & 1/\mu \\ i\sigma_T & -i\sigma_T \end{bmatrix}.$$

Denote by $\mu_-, \bar{\mu}, \mu_+$ and $\sigma_-, \bar{\sigma}, \sigma_+$ the values of μ and σ_T as $z < 0, z \in (0, d), z > d$.

The matrix \mathbf{R} is 1×1 ; denote it as R . Let $R(d_+) = 0$. This means that no wave is reflected within the homogeneous half-space $z > d$. Since $[\mathbf{M}] = \mathbf{0}$, by (16) we find that

$$\begin{aligned} \mathbf{J}(d) &= \mathbf{E}^{-1}(d)\mathbf{P}^{-1}(d_-)\mathbf{P}(d_+)\mathbf{E}(d) \\ &= \frac{1}{2} \begin{bmatrix} \bar{\mu}/\mu_+ + \sigma_+/\bar{\sigma} & (\bar{\mu}/\mu_+ - \sigma_+/\bar{\sigma}) \exp(-2i\bar{\sigma}d) \\ (\bar{\mu}/\mu_+ - \sigma_+/\bar{\sigma}) \exp(2i\bar{\sigma}d) & \bar{\mu}/\mu_+ + \sigma_+/\bar{\sigma} \end{bmatrix}. \end{aligned}$$

Hence, by (17) we have

$$R(d_-) = \exp(2i\bar{\sigma}d) \frac{\bar{\mu}\bar{\sigma} - \mu_+\sigma_+}{\bar{\mu}\bar{\sigma} + \mu_+\sigma_+}.$$

Since $R' = 0$ as $z \in (0, d)$ then $R(0_+) = R(d_-)$. Now,

$$\mathbf{J}(0) = \frac{1}{2} \begin{bmatrix} \mu_-/\bar{\mu} + \bar{\sigma}/\sigma_- & \mu_-/\bar{\mu} - \bar{\sigma}/\sigma_- \\ \mu_-/\bar{\mu} - \bar{\sigma}/\sigma_- & \mu_-/\bar{\mu} + \bar{\sigma}/\sigma_- \end{bmatrix}.$$

Hence we find that

$$\begin{aligned} R_0 = R(0_-) &= \frac{J^{III}(0) + J^{IV}(0)R(0_+)}{J^I(0) + J^{II}(0)R(0_+)} \\ &= \frac{(\mu_- \sigma_- - \bar{\mu} \bar{\sigma})(\bar{\mu} \bar{\sigma} + \mu_+ \sigma_+) + (\mu_- \sigma_- + \bar{\mu} \bar{\sigma})(\bar{\mu} \bar{\sigma} - \mu_+ \sigma_+) \exp(2i\bar{\sigma}d)}{(\mu_- \sigma_- + \bar{\mu} \bar{\sigma})(\bar{\mu} \bar{\sigma} + \mu_+ \sigma_+) + (\mu_- \sigma_- - \bar{\mu} \bar{\sigma})(\bar{\mu} \bar{\sigma} - \mu_+ \sigma_+) \exp(2i\bar{\sigma}d)}. \end{aligned}$$

Also, we find that

$$R_u = R_0, \quad R_t = -R_0.$$

As a check, consider the limit case of a single discontinuity. Let $d = 0$, $\bar{\sigma} = \sigma_+$, $\bar{\mu} = \mu_+$. It follows the standard result

$$R_0 = \frac{\mu_- \sigma_- - \mu_+ \sigma_+}{\mu_- \sigma_- + \mu_+ \sigma_+}.$$

Acknowledgment

The author is grateful to Prof. A. Mal for bringing reference [8] to his attention.

References

1. Brekhovskikh L.M.: *Waves in Layered Media*, Academic Press, New York, 1980, ch. 3.
2. Kennett B.L.N.: Guided wave propagation in laterally varying media - I. Theoretical development, *Geophys. J. R. astr. Soc.*, **79** (1984), 235-255.
3. Lewicki P., Burridge R., and De Hoop M. V.: Beyond effective medium theory: pulse stabilization for multimode wave propagation in high-contrast layered media, *SIAM J. Appl. Math.*, **56** (1996), 256-276.
4. Hager W.W. and Rostamian R.: Reflection and refraction of elastic waves for stratified materials, *Wave Motion*, **10** (1988), 333-348.
5. Titchener J.B. and Willis J.R.: The reflection of electromagnetic waves from stratified anisotropic media, *IEEE Trans. Antennas Propagat.*, **39** (1991), 35-39.
6. Kennett B.L.N.: *Seismic Wave Propagation in Stratified Media*, Cambridge University Press (1985), ch. 2.
7. Caviglia G. and Morro A.: Riccati equations for wave propagation in planarly-stratified solids, *Eur. J. Mechanics A/Solids*, to appear.
8. Chimenti D. E.: Guided waves in plates and their use in materials characterization, *Appl. Mech. Rev.*, **50** (1997), 247-284.
9. Caviglia G. and Morro A.: *Inhomogeneous Waves in Solids and Fluids*, World Scientific, Singapore (1992), §2.2.
10. Iesan D.: *Prestressed Bodies*, Longman, Harlow (1989), §1.2.

ULTRASONIC LAMB WAVES IN LAYERED PIEZOELECTRIC PLATES

J. M. ORELLANA AND B. COLLET

*Laboratoire de Modélisation en Mécanique (U.M.R.) 7607,
Université Pierre et Marie Curie / C.N.R.S
Case 162 - 4 place Jussieu, 75252 Paris Cedex 05, France.*

1. Introduction

The propagation of *guided ultrasonic waves* (GUW) in deformable solid media has been an active research subject for the last thirty years due to its applications in *non-destructive evaluation* (NDE) of homogeneous and advanced composite materials used in mechanical, aerospace and civil engineering [1-4]. Stratified and fibrous *piezoelectric composite* materials have also lately given rise to increasingly active researches because of its numerous possible applications in sensors, actuators, active control and adaptive structures for their electromechanical conversion abilities [5]. Recently, the microelectronic technology has outstandingly progressed, particularly in the domain of multilayered piezoelectric semiconductors structures: heterostructures, multiple quantum well structures and the monolithic integration of surface acoustic waves (SAW) devices [6]. The high-performance *electro-acoustic* and *acousto-optic* devices utilizing GUW in multilayered structures are currently developed for a variety of applications in the field of communications, signal processing, optical computing, . . . Thus, a detailed *knowledge* of the GUW *propagation characteristics* in piezoelectric multilayered structures, crucial for the accurate design of GUW devices, is urgently required. However, the task complexity due to great variety of structure geometries and related type of wave delay advances. Modeling wave propagation in piezoelectric layered media must take into account electromechanical material properties of layers, number and thickness of layers, electromechanical nature of interfacial and boundary conditions, and direction of propagation as well. Limited available analytical treatments make them fully dependent on computational capabilities. Also attempts in modeling ultrasonic waves propagation reported in literature can hardly cope with the demands of results in a large range of frequency along with a simple fast method.

The purpose of the present work is to study *harmonic plane wave propagation* in *infinite piezoelectric laminated structures* perfectly coated with thin metallic electrodes. We focus our attention on free stiffened Lamb-like waves in multilay-

ered plates. Layers are made of high symmetry materials (hexagonal or cubic). Open-circuit and short-circuit surfaces boundary conditions are considered. The outline of the paper is as follows: In Sec. 2, the basic coupled equations which govern the dynamics of the layered piezoelectric structure are briefly reviewed. The solutions for sagittal plane modes by means of the state variables formalism are given in Sec. 3. In Sec. 4, the treatment of interface and boundary conditions by three methods is analyzed : (i) the transfer matrix approach; (ii) the local surface impedance concept; and (iii) the global matrix method. Finally in Sec. 5, some illustrative numerical results obtained by the previous three methods, for selected configurations (bilayer, sandwich and mirror seven layers) are presented and discussed in order to locate the birth of numerical instabilities and to show the influences of material properties of layers and electromechanical boundary conditions on the dispersive behavior.

2. Problem statement

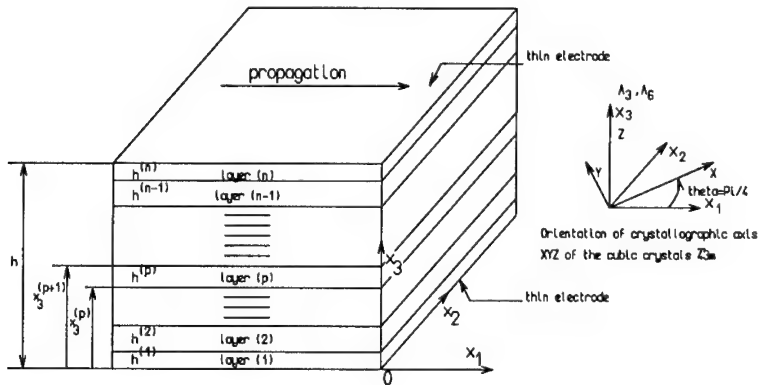


Figure 1. The geometry and coordinate system.

Let us consider a *multilayered plate* with infinite lateral extent consisting of n *piezoelectric layers* rigidly bonded at their interfaces and stacked perpendicularly to x_3 -direction, where (x_1, x_2, x_3) is the reference Cartesian coordinate system as shown in Fig. 1. The origin of the coordinate system is chosen to be located in the bottom of the composite structure. The plane of each layer is parallel to $x_1 - x_2$ plane, which is also chosen to coincide with the bottom surface of the multilayered plate. The stratified structure thus considered allows *the propagation of piezoelectric Lamb waves*. Each layer (p) is a *rotated cubic* ($\bar{4}3m$) or an *hexagonal* ($6mm$) piezoelectric crystal. The three-fold (A_3) or six-fold (A_6) crystallographic axis are directed along the x_3 -axis. The layer (p) of thickness $h^{(p)}$ takes up the region $x_3^{(p)} < x_3 < x_3^{(p+1)}$ where $x_3^{(p)}$ is the position of the lower surface of the layer (p). Thus the total thickness of the layered plate is equal to $h = \sum_{p=1}^n h^{(p)}$. Moreover, the bottom and top surfaces of the laminated piezoelectric structure are

covered by *very thin metal electrodes*. In the subsequent analysis, the mass effects of electrodes are neglected.

The components of mechanical displacement, the electric potential, the elastic stiffness moduli measured at constant or zero electric field, the piezoelectric coupling coefficients, dielectric permittivities measured at constant or zero strain field, the stress, the components of electric displacement and the density of the p th layers are denoted using Voigt's convention, by $u_i^{(p)}$, $\phi^{(p)}$, $c_{\alpha\beta}^{E(p)}$, $e_{i\alpha}^{(p)}$, $\varepsilon_{ij}^{S(p)}$, $T_\alpha^{(p)}$, $D_i^{(p)}$ and $\rho^{(p)}$ respectively, where $i, j = 1, 2, 3$ and $\alpha, \beta = 1, 2, \dots, 6$.

In the present investigation, we are concerned for each ply (p) with *plane strain* wave motion

$$\begin{aligned} u_i^{(p)} &= u_i^{(p)}(x_j, t), \quad u_2^{(p)}(x_j, t) = 0, \\ \phi^{(p)} &= \phi^{(p)}(x_j, t), \quad i, j = 1, 3. \end{aligned} \quad (1)$$

From this generalized displacement field and with respect to the selected crystallographic class and the geometrical arrangement, the relevant local field equations for the ply (p), in the *quasi-electrostatic approximation*, reduce to the three coupled equations [7]

$$\begin{aligned} c_{11}^{E(p)} u_{1,11}^{(p)} + c_{44}^{E(p)} u_{1,33}^{(p)} + (c_{13}^{E(p)} + c_{44}^{E(p)}) u_{3,13}^{(p)} + (e_{15}^{(p)} + e_{31}^{(p)}) \phi_{,13}^{(p)} &= \rho^{(p)} \ddot{u}_1^{(p)}, \\ (c_{13}^{E(p)} + c_{44}^{E(p)}) u_{1,13}^{(p)} + c_{44}^{E(p)} u_{3,11}^{(p)} + c_{33}^{E(p)} u_{3,33}^{(p)} + e_{15}^{(p)} \phi_{,11}^{(p)} + e_{33}^{(p)} \phi_{,33}^{(p)} &= \rho^{(p)} \ddot{u}_3^{(p)}, \\ (e_{15}^{(p)} + e_{31}^{(p)}) u_{1,13}^{(p)} + e_{15}^{(p)} u_{3,11}^{(p)} + e_{33}^{(p)} u_{3,33}^{(p)} - \varepsilon_{11}^{S(p)} \phi_{,11}^{(p)} - \varepsilon_{33}^{S(p)} \phi_{,33}^{(p)} &= 0, \end{aligned} \quad (2)$$

where the constraints $e_{33}^{(p)} = 0$, $e_{31}^{(p)} = e_{15}^{(p)}$, $\varepsilon_{11}^{S(p)} = \varepsilon_{33}^{S(p)}$ are imposed on materials coefficients for rotated cubic crystals. The two first equations (2)_{1,2} consist of the momentum equations and the last is the charge conservation equation or Gauss's law.

The components of stress and electric displacement associated with the interface continuity and boundary conditions are given by the *constitutive relations*

$$\begin{aligned} T_3^{(p)} &= c_{13}^{E(p)} u_{1,1}^{(p)} + c_{33}^{E(p)} u_{3,3}^{(p)} + e_{33}^{(p)} \phi_{,3}^{(p)}, \\ T_5^{(p)} &= c_{44}^{E(p)} (u_{1,3}^{(p)} + u_{3,1}^{(p)}) + e_{15}^{(p)} \phi_{,1}^{(p)}, \\ D_3^{(p)} &= e_{31}^{(p)} u_{1,1}^{(p)} + e_{33}^{(p)} u_{3,3}^{(p)} - \varepsilon_{33}^{S(p)} \phi_{,3}^{(p)}. \end{aligned} \quad (3)$$

The relevant $3n$ field equations (2) are supplemented with $6(n-1) + 6$ *electromechanical interface continuity* and *boundary conditions*

$$\begin{aligned} u_1^{(p+1)} &= u_1^{(p)}, \quad u_3^{(p+1)} = u_3^{(p)}, \quad T_3^{(p+1)} = T_3^{(p)}, \quad T_5^{(p+1)} = T_5^{(p)}, \\ \phi^{(p+1)} &= \phi^{(p)}, \quad D_3^{(p+1)} = D_3^{(p)} \quad \text{at} \quad x_3 = x_3^{(p+1)}, \quad p = 1, 2, \dots, (n-1), \end{aligned} \quad (4)$$

(i) for the stress-free piezoelectric layered plate in electrically open-circuit

$$\begin{aligned} T_3^{(1)} &= 0, \quad T_5^{(1)} = 0, \quad D_3^{(1)} = 0, \quad \text{at} \quad x_3 = 0, \\ T_3^{(n)} &= 0, \quad T_5^{(n)} = 0, \quad D_3^{(n)} = 0, \quad \text{at} \quad x_3 = h, \end{aligned} \quad (5)$$

(ii) for the stress-free piezoelectric layered plate in electrically short-circuit

$$\begin{aligned} T_3^{(1)} &= 0, & T_5^{(1)} &= 0, & \phi^{(1)} &= 0, & \text{at } x_3 = 0, \\ T_3^{(n)} &= 0, & T_5^{(n)} &= 0, & \phi^{(n)} &= 0, & \text{at } x_3 = h. \end{aligned} \quad (6)$$

3. State space formulation

There are essentially two means to deal with governing field equations in acoustic guided waves propagation problems : partial waves method and state space formulation. The direct approach or the *partial waves method* remains the favorite among the engineering community [2]. The newer *state space formulation* or *Stroh's formalism* [8] is well-known in the materials sciences, applied mathematics and physics community. The state space formulation is mathematically elegant and technically powerful. A distinctive feature of this method is that the general solution is provided in terms of the *eigenvalues* and *eigenvectors* of the *Stroh's matrix*. However, unlike in control theory, derivation of the state space equation from the relevant field equations is not always straightforward in the case of anisotropic elasticity or piezoelectricity [9-10]. In the particular studied case of the *piezoelectric Lamb waves*, the field equations of linear piezoelectricity involve a system of second order differential equation with respect to the x_3 variable. By introducing additional continuous fields $T_3^{(p)}$, $T_5^{(p)}$ and $D_3^{(p)}$ across interfaces $x_3^{(p)}$ and $x_3^{(p+1)}$, the field equations and constitutive relations can be reformulated as a first order system of differential equations. The methodology used here reduces the order of original equation system, the state space approach converts a boundary value problem into an equivalent initial value problem in terms of state variables.

When specialized to *plane harmonic waves*, the above formulation leads to an homogeneous first-order system with piecewise constant coefficients whose the solution is merely the product of the solution for each layer. As pointed above, we are concerned with the harmonic plane waves propagating along the x_1 -direction, therefore the state variables for the layer (p) can be written as

$$\begin{aligned} u_j^{(p)} &= \bar{u}_j^{(p)}(x_3)e^{i(k_1 x_1 - \omega t)}, & j &= 1, 3, & \phi^{(p)} &= \bar{\phi}^{(p)}(x_3)e^{i(k_1 x_1 - \omega t)}, \\ T_\alpha^{(p)} &= \bar{T}_\alpha^{(p)}(x_3)e^{i(k_1 x_1 - \omega t)}, & \alpha &= 3, 5, & D_3^{(p)} &= \bar{D}_3^{(p)}(x_3)e^{i(k_1 x_1 - \omega t)}, \end{aligned} \quad (7)$$

where k_1 and ω are the x_1 -component of the wave vector and the circular frequency. We set the 6-state vector as

$$\bar{S}^{(p)} = [i\bar{T}_3^{(p)}, \bar{u}_1^{(p)}, i\bar{D}_3^{(p)}, \bar{u}_3^{(p)}, i\bar{T}_5^{(p)}, \bar{\phi}^{(p)}]^T. \quad (8)$$

It can be shown that, for such motion, the *governing field equations* can be recast into the form of a matrix differential equation

$$\frac{d\bar{S}^{(p)}}{dx_3} = iN^{(p)}\bar{S}^{(p)}, \quad \text{with} \quad N^{(p)} = \begin{bmatrix} 0 & P^{(p)} \\ Q^{(p)} & 0 \end{bmatrix}, \quad (9)$$

where $N^{(p)}$ is the 6×6 real block Stroh's matrix. The 3×3 symmetric submatrices $P^{(p)}$ and $Q^{(p)}$ are defined by

$$\begin{aligned}
P_{11}^{(p)} &= -\rho^{(p)} \omega^2, & P_{12}^{(p)} &= -k_1, & P_{13}^{(p)} &= 0, & P_{22}^{(p)} &= -1/c_{44}^{E(p)}, \\
P_{23}^{(p)} &= -k_1 e_{15}^{(p)} / c_{44}^{E(p)}, & P_{33}^{(p)} &= -k_1^2 \kappa^{(p)} / c_{44}^{E(p)}, & Q_{11}^{(p)} &= -\varepsilon_{33}^{(p)} / \gamma^{(p)}, \\
Q_{12}^{(p)} &= -k_1 \nu^{(p)} / \gamma^{(p)}, & Q_{13}^{(p)} &= -e_{33}^{(p)} / \gamma^{(p)}, \\
Q_{22}^{(p)} &= (-\nu c_{13}^{(p)} - \mu^{(p)} e_{31}^{(p)}) k_1^2 / \gamma^{(p)} - \rho^{(p)} \omega^2, & Q_{23}^{(p)} &= -k_1 \mu^{(p)} / \gamma^{(p)}, \\
Q_{33}^{(p)} &= c_{33}^{(p)} / \gamma^{(p)}, & \kappa^{(p)} &= e_{15}^{(p)2} + \varepsilon_{11}^{(p)} c_{44}^{E(p)}, & \gamma^{(p)} &= \varepsilon_{33}^{(p)} c_{33}^{(p)} + e_{33}^{(p)2}, \\
\mu^{(p)} &= c_{13}^{(p)} e_{33}^{(p)} - e_{31}^{(p)} c_{33}^{(p)}, & \nu^{(p)} &= c_{13}^{(p)} \varepsilon_{33}^{(p)} + e_{31}^{(p)} e_{33}^{(p)}.
\end{aligned}$$

It should be noted that the *block structure* of the matrix $N^{(p)}$ is not a coincidence but, in fact, the result of judiciously ordering of the state variables in order to minimize the calculus and computational efforts. It should also be mentioned that the state space equation for the piezoelectricity is structurally the same as the state space equation for anisotropic elasticity except for the two additional quantities $\phi^{(p)}$ and $D_3^{(p)}$ due to the electric field contribution. The state space equation for pure elastic dielectric can be recovered by setting the piezoelectric constants, $e_{i\alpha}^{(p)}$, to zero. The solution to (9) can be written as

$$\bar{S}^{(p)} = \begin{bmatrix} R_1^{(p)} & R_3^{(p)} \\ R_2^{(p)} & R_4^{(p)} \end{bmatrix} \begin{bmatrix} D^{(p)}(x_3 - x_3^{(p)}) & 0 \\ 0 & D^{(p)-1}(x_3 - x_3^{(p)}) \end{bmatrix} \begin{pmatrix} c_1^{(p)} \\ c_2^{(p)} \end{pmatrix}, \quad (10)$$

where $D^{(p)}(x_3) = \text{diag}(e^{i\lambda_{(1)}^{(p)} x_3}, e^{i\lambda_{(2)}^{(p)} x_3}, e^{i\lambda_{(3)}^{(p)} x_3})$ is a 3x3 exponential diagonal matrix, $\lambda_{(\alpha)}^{(p)}$ are the complex eigenvalues of 6x6 non-symmetric matrix $N^{(p)}$ with the following properties $\lambda_{(4)}^{(p)} = -\lambda_{(1)}^{(p)}$, $\lambda_{(5)}^{(p)} = -\lambda_{(2)}^{(p)}$, $\lambda_{(6)}^{(p)} = -\lambda_{(3)}^{(p)}$, $R_{1,2,3,4}$ are 3x3 right eigenvectors submatrices and $c_1^{(p)}$, $c_2^{(p)}$ two constant 3-vectors.

According to the values of $\text{Im}(\lambda_{(\alpha)}^{(p)})$ and $\text{Re}(P_{\text{oy}n_3}^{(p)}(x_3^{(p)}))$, partial waves can be split into two subsets [11] :

(i) if $\text{Im}(\lambda_{(\alpha)}^{(p)}) > 0$ or $\text{Im}(\lambda_{(\alpha)}^{(p)}) = 0$ and $\text{Re}(P_{\text{oy}n_3}^{(p)}(x_3^{(p)})) > 0$, where $\alpha = 1, 2, 3$, which corresponds to *upgoing partial waves* in x_3 -positive direction, obtained by setting $c_2^{(p)} = 0$,

(ii) if $\text{Im}(\lambda_{(\alpha)}^{(p)}) < 0$ or $\text{Im}(\lambda_{(\alpha)}^{(p)}) = 0$ and $\text{Re}(P_{\text{oy}n_3}^{(p)}(x_3^{(p)})) < 0$, where $\alpha = 1, 2, 3$, which corresponds to *downgoing partial waves* in x_3 -negative direction, obtained by setting $c_1^{(p)} = 0$, where the x_3 component of the complex Poynting vector, for the layer (p) , is defined by

$$P_{\text{oy}n_3}^{(p)} = \frac{1}{2} i \omega (-\bar{T}_5^{(p)} \bar{u}_1^{(p)*} - \bar{T}_3^{(p)} \bar{u}_3^{(p)*} + \bar{\phi}^{(p)} \bar{D}_3^{(p)*}), \quad (11)$$

where the asterisk * indicates the complex conjugate quantity.

4. Treatment of interface and boundary conditions

Once formal solutions are obtained in each layer (p), it remains to enforce interfacial and boundary conditions of the multilayered structure. Various methods have been proposed to carry out this main task which must take into account different parameters for instance : number and thickness of ply, frequency range,... . Usually, two principal approaches emerge from literature : transfer techniques and direct approaches.

Matrix transfer methods are commonly used in transmission lines, electromagnetic and acoustic guided waves in stratified media. These techniques are based on *local transfers* of informations regarding the state variables characterizing the input and the output of the unit cells or layers. The *global transfer* is based on *local transfers* and fields continuity conditions at junctions or interfaces. The *Thomson-Haskell transfer matrix formalism* [2,12] is advantageous since the *order* of the transfer global matrix is *independent of the number of layers*. The maximum dimension necessary for a matrix transfer is eight, for piezoelectric media. Unfortunately, at *high frequency-thickness product*, the method suffers from a *loss of precision* leading to inaccurate results. This difficulty can be discarded successfully with local surface impedance concept. The *Local surface impedance approach* [13-14] is based on local surface impedance transfer of each interface. It keeps the transfer method advantages, by the rank of matrices independent of the number of layers, but without numerical instabilities. It also allows more flexibility in boundary conditions treatment.

Direct methods rely on simultaneous enforcement of all the conditions. In the *Global matrix method* [15-16], once we know the *general solution* for each material layer and boundary conditions, we are ready to combine the layers equations to describe the entire system. A *single 6n matrix* for n layered structure with only bounded terms, represents the complete equation system. Compared to the transfer matrix technique, this method has the *advantage* to be *numerically stable* at high frequency-thickness products. The *drawback* is that the global matrix may be large and the solution therefore may require of *high computer processing unity (CPU) times* and *important RAM memory* when the systems involve many layers. However, the speed of treatment of some actual computers with high frequency processors along with available optimized softwares reduce the effects of this limitation.

4.1. THOMSON-HASKELL APPROACH AND INSTABILITIES

Initially introduced to compute seismic surface waves dispersion functions, the Thomson-Haskell method or transfer matrix technique is easily extended to guided waves problems in anisotropic elastic and piezoelectric media [2,14,17]. The local transfer matrix method allows us to relate the state vectors specialized to the lower and upper surfaces of the layer (p). The transfer of information of each layer is given by the linear application

$$\bar{S}^{(p)}(x_3^{(p+1)}) = A^{(p)} \bar{S}^{(p)}(x_3^{(p)}), \quad (12)$$

where the 6×6 square matrix $A^{(p)}$ is the *local transfer matrix* for layer (p) . By applying the above procedure for each layer and using the continuity of state vector at the layer interfaces. We finally relate the state vector at the bottom surface of the stratified piezoelectric structure, $x_3 = 0$, to that at its top surface $x_3 = h$, via the local transfer matrix multiplication

$$\begin{aligned} \bar{S}^t &= A \bar{S}^b, \quad A = A^{(n)} A^{(n-1)} \dots A^{(2)} A^{(1)}, \\ \bar{S}^b &= \bar{S}^{(1)} \Big|_{x_3=0} \quad \bar{S}^t = \bar{S}^{(n)} \Big|_{x_3=h}, \end{aligned} \quad (13)$$

where A is the *global transfer matrix* of the total structure. The state vectors $\bar{S}_{o,s}^{b,t}$ for a layered plate *free of traction* in *open* or *short-circuit condition* at $x_3 = 0, h$ are respectively defined by

$$\bar{S}_o^{b,t} = \bar{S}^{b,t} \Big|_{\bar{T}_3=\bar{D}_3=\bar{T}_5=0}, \quad \bar{S}_s^{b,t} = \bar{S}^{b,t} \Big|_{\bar{T}_3=\bar{T}_5=\bar{\phi}=0}. \quad (14)$$

For nontrivial solutions for the wave amplitudes we get the *dispersion relations* for an *open* and *short-circuit*, by setting the sub-determinants of the global matrix transfer equal to zero

$$D_o(\omega, k_1) = \begin{vmatrix} A_{12} & A_{14} & A_{16} \\ A_{32} & A_{34} & A_{36} \\ A_{52} & A_{54} & A_{56} \end{vmatrix} = 0, \quad D_s(\omega, k_1) = \begin{vmatrix} A_{12} & A_{13} & A_{14} \\ A_{52} & A_{53} & A_{54} \\ A_{62} & A_{63} & A_{64} \end{vmatrix} = 0. \quad (15)$$

The local transfer matrices are made of exponentially growing or decaying terms associated with partial waves in each layer. When we consider a multi-ply structure made of a *large number of layers* or of layers with *very different thickness* as in the case of some guided wave devices, the magnitude order of different terms in the transfer matrices becomes important. Accordingly, the global matrix transfer is *ill-conditioned or singular*. The Thomson-Haskell matrix method is *not numerically stable* in the cases where the depth of propagating *evanescent waves* is small with respect to the thickness of layers. This gives rise to results (dispersion curves, reflection and transmission factors, spatial distributions of the electroacoustic fields,...) with large errors, due to numerical overflow.

4.2. LOCAL SURFACE IMPEDANCE MATRICES

To overcome these numerical difficulties, well known in numerical analysis referred to as the exponential dichotomy, and to treat various geometries with prescribed boundary conditions, it is more convenient to use the concept of *interface* or *local surface impedance matrix*. This concept has been initially developed to study the SAW in half-infinite homogeneous anisotropic elastic media and piezoelectric crystals. This method has been recently extended to SAW and guided acoustic waves (GAW) in piezoelectric multi-ply structures [13,14,18]. This approach consists of using the expression of general solution (10) to establish a relation between two partial state vectors $U_{o,s}^{(p)}$ and $V_{o,s}^{(p)}$ defined respectively by

(i) for a layered plate in open-circuit

$$U_o^{(p)} = \left[\bar{u}_1^{(p)}, \bar{u}_3^{(p)}, \bar{\phi}^{(p)} \right]^T, V_o^{(p)} = \left[\bar{T}_5^{(p)}, \bar{T}_3^{(p)}, \bar{D}_3^{(p)} \right]^T, \quad (16)$$

(ii) for a layered plate in short-circuit

$$U_s^{(p)} = \left[\bar{u}_1^{(p)}, \bar{u}_3^{(p)}, \bar{D}_3^{(p)} \right]^T, V_s^{(p)} = \left[\bar{T}_5^{(p)}, \bar{T}_3^{(p)}, \bar{\phi}^{(p)} \right]^T. \quad (17)$$

Then the solutions (10) can be now written for a layered plate in open or short-circuit as :

$$\begin{pmatrix} U_{o,s}^{(p)} \\ V_{o,s}^{(p)} \end{pmatrix} = \begin{bmatrix} R_{o1,s1}^{(p)} & R_{o3,s3}^{(p)} \\ R_{o2,s2}^{(p)} & R_{o4,s4}^{(p)} \end{bmatrix} \begin{bmatrix} D^{(p)}(x_3 - x_3^{(p)}) & 0 \\ 0 & D^{(p)-1}(x_3 - x_3^{(p)}) \end{bmatrix} \begin{pmatrix} c_{o1,s1}^{(p)} \\ c_{o2,s2}^{(p)} \end{pmatrix}, \quad (18)$$

where

$$\begin{aligned} R_{o1,s1}^{(p)} &= I_{o,s}^+ R_1^{(p)} + I_{o,s}^- R_2^{(p)}, & R_{o2,s2}^{(p)} &= -i(I_{o,s}^- R_1^{(p)} + I_{o,s}^+ R_2^{(p)}), \\ R_{o3,s3}^{(p)} &= I_{o,s}^+ R_3^{(p)} + I_{o,s}^- R_4^{(p)}, & R_{o4,s4}^{(p)} &= -i(I_{o,s}^- R_3^{(p)} + I_{o,s}^+ R_4^{(p)}), \end{aligned} \quad (19)$$

$$\begin{aligned} I_o^+ &= (I_{oij}^+ = 0, i, j = 1, 2, 3, \text{ except } I_{o12}^+ = 1), \\ I_o^- &= (I_{oij}^- = 0, i, j = 1, 2, 3, \text{ except } I_{o21}^- = I_{o33}^- = 1), \\ I_s^+ &= (I_{sij}^+ = 0, i, j = 1, 2, 3, \text{ except } I_{s12}^- = 1, I_{s33}^- = -i), \\ I_s^- &= (I_{sij}^- = 0, i, j = 1, 2, 3, \text{ except } I_{s21}^- = 1). \end{aligned} \quad (20)$$

The partial or local impedance matrices $Z_{o,s}^{(p)}$ are defined by linear applications $V_{o,s}^{(p)} = Z_{o,s}^{(p)} U_{o,s}^{(p)}$, where

$$Z_{o,s}^{(p)} = \begin{bmatrix} Z_{om,sm}^{(p)} & Z_{oe,se}^{(p)} \\ \hat{Z}_{oe,se}^{(p)} & \hat{Z}_{oe,se}^{(p)} \end{bmatrix}. \quad (21)$$

The 3×3 mixed impedance matrices $Z_{o,s}^{(p)}$ are made of 2×2 mechanical impedance matrices $Z_{om,sm}^{(p)}$ (N/m^3), $Z_{oe,se}^{(p)}$ and $\hat{Z}_{oe,se}^{(p)}$ are $2D$ -vectors whose components are physically homogeneous to (C/m^3) and $\hat{Z}_{oe,se}^{(p)}$ are scalars quantities homogeneous to (F/m^2) . It is possible to show that the surface impedance matrices for upgoing and downgoing waves marked $+$, $-$ are given respectively by

$$Z_{o,s}^{(p)+} = R_{o2,s2}^{(p)} R_{o1,s1}^{(p)-1}, \quad Z_{o,s}^{(p)-} = R_{o4,s4}^{(p)} R_{o3,s3}^{(p)-1}. \quad (22)$$

Now, we consider the layer (p) . Let us set $Z_{ol,sl}^{(p)}$ the local surface impedance at the lower face $x_3 = x_3^{(p)}$. By using the previous results it can be shown that the local surface impedance at the upper face $x_3 = x_3^{(p+1)}$ is given by

$$Z_{ou,su}^{(p)}(x_3^{(p+1)}) = (Z_{o,s}^{(p)+} H_{o,s}^{(p)} + Z_{o,s}^{(p)-})(I + H_{o,s}^{(p)})^{-1}, \quad (23)$$

in which

$$\begin{aligned} H_{o,s}^{(p)} &= M_{o1,s1}^{(p)} R_{o,s}^{(p)} M_{o2,s2}^{(p)}, \\ R_{o,s}^{(p)} &= (Z_{o,s}^{(p)+} - Z_{ol,sl}^{(p)}(x_3^{(p)}))^{-1} (Z_{ol,sl}^{(p)}(x_3^{(p)}) - Z_{o,s}^{(p)-}), \end{aligned} \quad (24)$$

$$M_{o1,s1}^{(p)} = R_{o1,s1}^{(p)} D^{(p)}(h^{(p)}) R_{o1,s1}^{(p)-1} \quad M_{o2,s2}^{(p)} = R_{o3,s3}^{(p)} D^{(p)}(h^{(p)}) R_{o3,s3}^{(p)-1}. \quad (25)$$

At this step it is worthwhile noting that all terms of 3×3 exponential diagonal matrix $D^{(p)}$ are bounded by unity

$$\left| D_{\alpha\alpha}^{(p)}(h^{(p)}) \right| \leq 1, \alpha = 1, 2, 3, \text{ without summation on } \alpha.$$

$M_{o1,s1}^{(p)}$ are the partial propagating matrices associated with the upgoing waves, with similar results for downgoing waves. $R_{o,s}^{(p)}$ are the reflection matrices relating the upgoing waves to the downgoing waves across the surface $x_3^{(p)}$. By using the same arguments, the impedance matrices can be written for any number of ply. The interlamellar continuity conditions (4) are rewritten as

$$Z_{ol,sl}^{(p+1)}(x_3^{(p+1)}) = Z_{ou,su}^{(p)}(x_3^{(p+1)}), \quad \text{for } p = 1, 2, \dots, (n-1). \quad (26)$$

The above results can now be applied in the evaluation of the top surface impedance of total laminate plate. In order to satisfy the boundary conditions (5-6) at the bottom surface of the total laminated structure, we set the surface impedance matrices $Z_{ol,sl}^{(1)}(0) = 0$. On using an *efficient recursive algorithm*, easily implemented in computer program, based on the equations (22-26), we evaluate the surface impedance matrices $Z_{ou,su}^{(n)}(h)$ at the top surface

$$V_{o,s}^{(n)}(h) = Z_{ou,su}^{(n)}(h) U_{o,s}^{(n)}(h). \quad (27)$$

Applying boundary conditions to the top of the structure, makes finally to dispersion equation,

$$\det(Z_{ou,su}^{(n)}(h)) = 0. \quad (28)$$

As shown in next section, one of the advantages of this recursive algorithm is its *stability* in presence of *evanescent waves*, which makes its use particularly suitable for applications in a *wide range of frequencies*.

One also note that we can examine *mixed boundary conditions* using previous results. For a multi-ply plate in open-circuit condition at its bottom and short-circuit conditions at its top and conversely, it can be shown that dispersion equations take on the form

$$\det(Z_{omu,smu}^{(n)}(h)) = 0. \quad (29)$$

4.3. GLOBAL MATRIX METHOD

The *global matrix* technique is based on the importance of choice of *spatial origins* for upgoing and downgoing bulk waves [15-16,19]. The efficiently *simple process* consists of assembling directly a *single matrix* deduced from the $6n$ continuity conditions at each interface and boundary conditions at external surfaces of the

structure. Unlike a transfer method the difficulty of the problem depends on the number of layers n because, as in direct method, amplitudes of all layers must appear. The original point of this method, to *solve instability problem*, is to introduce different spatial references of bulk waves according to their behavior in each layer. Accordingly, this method is still numerically robust, for any range of *product frequency \times total thickness ($f \times h$)* value, because it does not rely, in particular at *very high frequency*, on coupling of inhomogeneous waves from one interface from another. No assumption is made about interdependence between state vector at each interface. However, for structures with numerous layers, as the number of matrix component increases, this technique involves roots extraction from *large order determinant*.

The expression of the general solution (10) for the layer (p) can be rewrittten by using the previous notations, as

$$\bar{S}^{(p)} = \begin{bmatrix} R_1^{(p)} & R_3^{(p)} \\ R_2^{(p)} & R_4^{(p)} \end{bmatrix} \begin{bmatrix} D^{(p)}(x_3 - x_3^{(p)}) & 0 \\ 0 & D^{(p)^{-1}}(x_3 - x_3^{(p+1)}) \end{bmatrix} \begin{pmatrix} \tilde{c}_1^{(p)} \\ \tilde{c}_2^{(p)} \end{pmatrix}. \quad (30)$$

The *interface continuity and boundary conditions* (4-6) can be expressed in a modified form involving only bounded terms. These equations are finally collected together to form an homogeneous linear *system of 6n dimension*

$$R_{o,s} \tilde{c}_{o,s} = 0, \quad (31)$$

where

$$R_{o,s} = \begin{bmatrix} R_{o2,s2}^{(n)} D^{(n)}(h^{(n)}) & R_{o4,s4}^{(n)} & 0 & 0 & \dots & \dots \\ \ddots & \ddots & \ddots & \ddots & \ddots & \ddots \\ \dots & R_{o1,s1}^{(p)} & R_{o3,s3}^{(p)} D^{(p)}(h^{(p)}) & -R_{o1,s1}^{(p-1)} D^{(p-1)}(h^{(p-1)}) & -R_{o3,s3}^{(p-1)} & \dots \\ \dots & R_{o2,s2}^{(p)} & R_{o4,s4}^{(p)} D^{(p)}(h^{(p)}) & -R_{o2,s2}^{(p-1)} D^{(p-1)}(h^{(p-1)}) & -R_{o4,s4}^{(p-1)} & \dots \\ \ddots & \ddots & \ddots & \ddots & \ddots & \ddots \\ \dots & 0 & 0 & R_{o2,s2}^{(1)} & R_{o4,s4}^{(1)} D^{(1)}(h^{(1)}) & \end{bmatrix},$$

$$\tilde{c}_{o,s} = \left[\tilde{c}_{o1,s1}^{(n)}, \tilde{c}_{o2,s2}^{(n)}, \tilde{c}_{o1,s1}^{(n-1)}, \tilde{c}_{o2,s2}^{(n-1)}, \dots, \tilde{c}_{o1,s1}^{(2)}, \tilde{c}_{o2,s2}^{(2)}, \tilde{c}_{o1,s1}^{(1)}, \tilde{c}_{o2,s2}^{(1)} \right].$$

The solutions to the wave problems corresponding to nontrivial solutions for $\tilde{c}_{o,s}$ require that the determinant of $R_{o,s}$, is zero :

$$\det R_{o,s} = 0. \quad (32)$$

5. Numerical examples and discussions

In this section, some numerical results for *specific layered configurations* are presented and discussed. In the numerical simulations we choose crystals of class *6mm Cadmium Sulfide* (CdS), *Zinc Oxide* (ZnO), and rotated *43m Gallium Arsenide*

(GaAs), Aluminium Arsenide (AlAs), as the constituent layers of the structures. In Figures 2-5 the dispersion curves for *Lamb-like plate modes* for four examples of layered structures with the identical layer thickness in open or short surfaces boundary conditions are presented : (i) a bilayer AlAs/GaAs in open-circuit where AlAs extends from $x_3 = 0$ to $h/2$ and GaAs occupies the remainder; (ii) a bilayer ZnO/CdS in short-circuit where ZnO extends from $x_3 = 0$ to $h/2$ and CdS occupies the remainder; (iii) a sandwich ZnO/GaAs/ZnO in short-circuit; and (iv) a seven-layered plate in open-circuit where the lowest layer is AlAs followed by three GaAs/AlAs bilayers. The material constants used in the calculations are collected in Table I.

Table I

| Material parameters | CdS | ZnO | GaAs | AlAs |
|--|-------|-------|--------|--------|
| $c_{11}^E (10^{10} \text{ N/m}^2)$ | 8.56 | 20.97 | 14.57 | 14.75 |
| $c_{13}^E (10^{10} \text{ N/m}^2)$ | 4.62 | 10.51 | 5.38 | 5.70 |
| $c_{33}^E (10^{10} \text{ N/m}^2)$ | 9.36 | 21.09 | 11.88 | 12.02 |
| $c_{44}^E (10^{10} \text{ N/m}^2)$ | 1.49 | 4.24 | 5.94 | 5.89 |
| $\rho (\text{kg/m}^3)$ | 4824 | 5676 | 5307 | 3760 |
| $e_{15} (\text{C/m}^2)$ | -0.21 | -0.59 | -0.154 | -0.225 |
| $e_{31} (\text{C/m}^2)$ | -0.24 | -0.61 | -0.154 | -0.225 |
| $e_{33} (\text{C/m}^2)$ | 0.44 | 1.14 | 0 | 0 |
| $\epsilon_{11}^S (10^{-11} \text{ F/m})$ | 7.99 | 7.38 | 11.061 | 8.907 |
| $\epsilon_{33}^S (10^{-11} \text{ F/m})$ | 8.44 | 7.83 | 11.061 | 8.907 |

In what follows $V_{P.R.O}$ and $V_{P.R.S}$ denote, the *piezoelectric Rayleigh velocities* in open and short surfaces boundary conditions respectively. Specifically, Fig. 2. shows phase velocity dispersion curves versus the frequency-thickness product $f \times h$ for the "Lamb-like" waves in the bilayer AlAs/GaAs in open-circuit. In the opposite, in the case of homogeneous plate, the *breaking* of geometrical and material *symmetries* do not permit to obtain pure antisymmetric and symmetric modes. As in case of homogeneous plates, we observe that only the first two fundamental modes do not exhibit cut-off frequency. A significant feature observed in Fig. 2. is the distinct *flattening* of the modes around the value $V_{P.R.O \text{ AlAs}} = 3391 \text{ ms}^{-1}$. As the dispersion curves approach this hidden line from the left they exhibit the well-known *plateau* and *step phenomenon*. This phenomenon is similar to that observed in purely elastic bilayers, the energy is *trapped* in the layer whose the velocities are the *slowest*. Along the plateau the curves are almost parallel to the hidden line with phase speed almost constant. We also notice that the phase velocity of the *first fundamental mode* for large frequency-thickness product tends asymptotically toward $V_{P.R.O \text{ GaAs}} = 2864 \text{ ms}^{-1}$, while all other modes at the high frequency limit, after crossing the hidden line, seem to approach the previous piezoelectric Rayleigh velocity $V_{P.R.O \text{ GaAs}}$ or piezoelectric Stoneley wave if it exists. This particular point it is not analytically obvious and will need further development to conclude. Finally, we note that the dispersion spectra obtained

for this configuration are in good agreement with results presented in recent work [20].

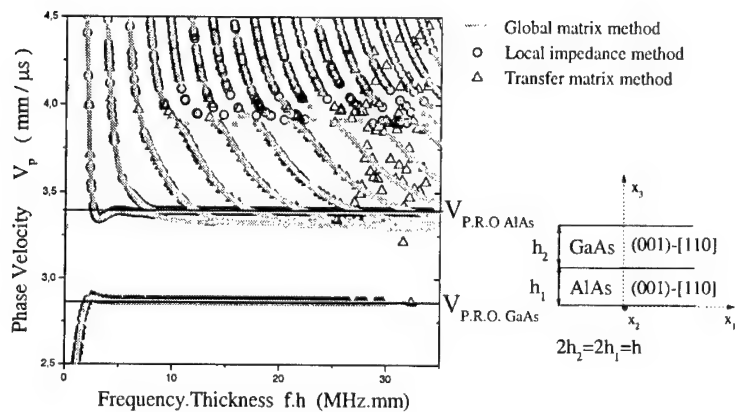


Figure 2. Dispersion curves of Lamb waves in bilayer AlAs/GaAs in open-circuit.

In Fig. 3. the corresponding phase velocity dispersion curves versus the frequency-thickness product for the "Lamb-like" waves in the bilayer ZnO/CdS in short-circuit are presented. The observations and conclusions from this graph are similar to those of the previous configuration. However, quantitative differences occur and it is first noted that the plateau phenomenon takes place in proximity of the phase velocity equal to $V_{P.R.S} \text{ ZnO} = 2696 \text{ ms}^{-1}$. We also observe that the phase velocity of the first mode for high values of the frequency-thickness product tends asymptotically toward $V_{P.R.S} \text{ CdS} = 1723 \text{ ms}^{-1}$, while for all other modes, after the *terracing phenomenon* and when the frequency-thickness product becomes large, the phase velocities seem to tend asymptotically toward the vertically polarized shear wave $V_{S.V} \text{ CdS} = 1790 \text{ ms}^{-1}$ or piezoelectric Stoneley wave if it exists.

In Fig. 4. we have plotted the phase velocity dispersion curves versus the frequency-thickness product of the lower order modes of Lamb waves in sandwich ZnO/GaAs/ZnO plate in short-circuit. In this *symmetric* layered structure the modes are, as in homogeneous plate, *antisymmetric* or *symmetric*. As previously observed, only the first two modes do not present cut-off frequencies. All higher-order modes end in a cut-off frequency and exhibit a complex behavior where symmetric and antisymmetric modes cross each other several times. It is also noted that at high values of the frequency-thickness product, the energy is *trapped* in the skin formed of the *slower material*. The linear dispersion spectrum displays a mode *clustering behavior* close to that observed in finite periodically layered media. Finally, we now turn to the mirror seven-layered plate AlAs/GaAs/.../GaAs/AlAs. This structure is symmetric, the outer layers are two identical AlAs layers. Accordingly, the

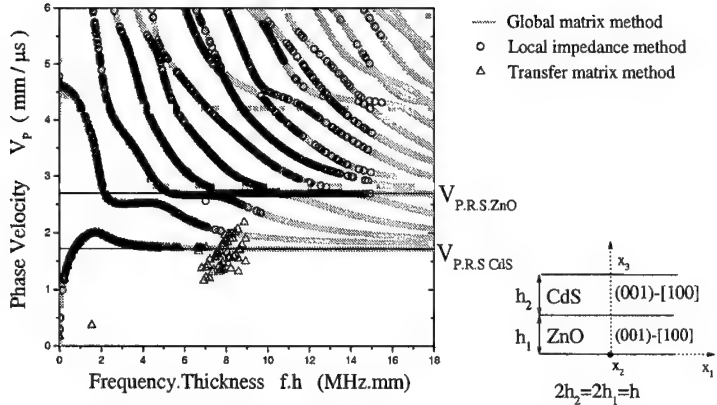


Figure 3. Dispersion curves of Lamb waves in bilayer ZnO/CdS in short-circuit.

wave motions occur with either antisymmetric or symmetric field distribution. Figure 5. shows the variations of the phase velocity for the Lamb-like modes as function of the product frequency-thickness. We find again two first fundamental antisymmetric and symmetric modes without cut-off frequency, while all other modes present a complex behavior (crossing and repulsion). We notice in Fig. 5., that all modes seem to tend toward asymptotic value $V_{P.R.O AlAs}$ for large $f \times h$. In this region of dispersion spectrum the energy is totally trapped in AlAs. Here also the mode *clustering behavior* appears clearly. The number of modes in observed clusters seems correlated to the number of different material used.

A further point of interest is, in Fig. 2-5, the *comparison* of numerical solutions obtained by the *three approaches* detailed in previous section : (i) Stroh formalism associated with matrix transfer method; (ii) Stroh formalism associated with local surface impedance method; and (iii) Stroh formalism associated with global matrix method. These comparative studies show in particular the great influence of piezoelectric materials and their assembly on the *birth* of *numerical instabilities*. When the product frequency-thickness is lower than a critical value $(f \times h)_c$, the three methods produce identical dispersion curves. For instance, in the cases of bilayers ZnO/CdS in short-circuit and AlAs/GaAs in open circuit (Fig. 2-3), the values are respectively $(f \times h)_c ZnO/CdS \approx 6.5 MHz.mm$ and $(f \times h)_c AlAs/GaAs \approx 27 MHz.mm$. For more complex configurations such as like sandwich ZnO/GaAs/ZnO and seven layers AlAs/GaAs/.../GaAs/AlAs in open-circuit, the critical values are respectively $(f \times h)_c ZnO/GaAs/ZnO \approx 12.5 MHz.mm$ and $(f \times h)_c AlAs/GaAs/.../GaAs/AlAs \approx 27.5 MHz.mm$. Beyond these critical values, the *transfer matrix approach* suffers from *numerical instabilities* illustrated by clouds or clusters of dots. In the four cases considered, the two other methods

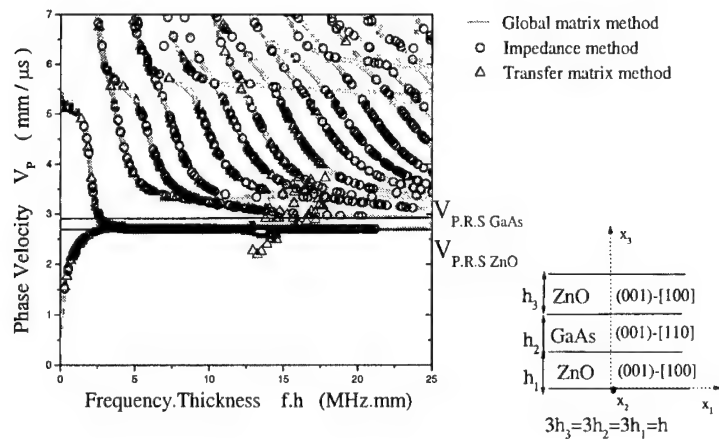


Figure 4. Phase velocity dispersion curves of Lamb waves for a sandwich plate ZnO/GaAs/ZnO in short-circuit case.

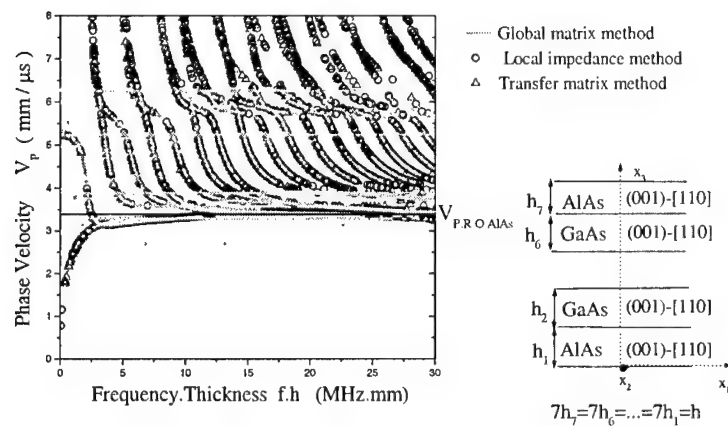


Figure 5. Phase velocity dispersion curves of Lamb waves for a seven layered plate AlAs/GaAs.../GaAs/AlAs in open-circuit case.

work well in large range of product $f \times h$ and extend the dispersion curves already obtained by the usual technique. However, we have a minor reservation as regard to the local surface impedance method. It converges slowly in the range of phase

velocities limited by two piezoelectric Rayleigh velocities of two materials. It is in this range of phase velocities and after at the end of the plateau, where the exchange of energy are strongest, that the dispersion curves show localized important curvature variations. Only the global matrix method is completely satisfying, which can serve as a *benchmark method*, but the price of this success is the drastic increase of computation time which limits actually its use. This technical difficulty is due in part, to the order of global matrix which depends on the number of layers, for e.g. : the global matrix for a seven layered plate is a 42×42 matrix.

6. Concluding remarks

In this paper, we have examined the propagation of *ultrasonic Lamb waves* in *multilayered piezoelectric* structures in open-circuit and short-circuit boundary conditions. The *state variable* formalism associated with the transfer matrix method, the local surface impedance concept and the global matrix approach are successively presented. Numerical simulations have been performed for a limited number of *specific configurations* (bilayer, sandwich plates and seven plies mirror structure). The results show the *influence* of the materials properties of layers and electromechanical boundary conditions on the linear dispersion spectra. Comparative tests allow us to specify quantitatively the *validity range* of the classical transfer matrix method. This study collects some basic *reference elements* that are essential for the selection process of treatment methods of interface and boundary conditions and for the building of new exact or approximate models. In particular, it has been clearly established that the efficient recursive algorithm based on the *local surface impedance* is the best compromise between, numerical precision, computer processing unit time and stability on large range of frequency.

In addition, the analysis presented may be also considered as a preliminary work to others studies concerning the propagation of Lamb waves in finite or semi-infinite *periodic piezoelectric* structures. The extension to Lamb waves, to *acousto-optic* interactions in multilayered plates, and to other materials and symmetries will be treated in future papers.

References

1. Brekhovskikh, L. M. and Godin, O. A. (1990) *Acoustic of Layered Media I - Plane and Quasi-Planes Waves*, Springer-Verlag, Berlin.
2. Nayfeh, A. H. (1995) *Wave propagation in layered anisotropic media with applications to composites*, Elsevier, Amsterdam.
3. Chimenti, D. E. (1997) Guided waves in plates and their use in materials characterisation, *Appl. Mech. Rev.* **50**, 247-284.
4. Rose, J. L. (2000) Guided waves nuances for ultrasonic non destructive evaluation, *IEEE Trans. Ultrason., Ferroelect., Freq., Contr.* **47**, 575-583.
5. Sumar, M. and Rao, S. S. (1999) Recent advances in sensing and control of flexible structures via piezoelectric materials technology, *Appl. Mech. Rev.* **52**, 1-16.

6. Smith, D. L., Kogan, Sh. M., Ruden, P. P. and Mailhot, C. (1996) Acousto-optic modulation of III-V semiconductor multiple quantum wells, *Phys. Rev. B.* **53**, 1421-1428.
7. Tiersten, H. F. (1969) *Linear piezoelectric plate vibrations*, Plenum, New York.
8. Ting, T. C. (1996) *Anisotropic Elasticity Theory and Applications*, Oxford University Press, New York.
9. Lothe, J. and Barnett, D. M. (1976) Integral formalism for surface waves in piezoelectric crystals. Existence considerations, *J. Appl. Phys.* **47**, 1799-1807.
10. Sosa, H. A. (1992) On the modelling of piezoelectric laminated structures, *Mech. Res. Comm.* **19**, 541-546.
11. Laprus, W. and Danicki, E. (1997) Piezoelectric interfacial waves in lithium niobate and other crystals, *J. Appl. Phys.* **81**, 855-861.
12. Lowe, M.J.S. (1995) Matrix techniques for modeling ultrasonic waves in multilayered media, *IEEE Trans. Ultrason., Ferroelect., Freq., Contr.* **42**, 525-542.
13. Honein, B., Braga, A. M. B., Barbone, P. and Herrmann, G. (1991) Wave propagation in piezoelectric layered media with some applications, *J. of Intell. Mater. Syst. and Struct.* **2**, 542-557.
14. Adler, E. L. (1994) SAW and pseudo-SAW properties using matrix methods , *IEEE Trans. Ultrason., Ferroelect., Freq., Contr.* **41**, 876-882.
15. Mal, A. K. (1988) Wave propagation in layered composite laminates under periodic surface loads, *Wave motion* **10**, 257-266.
16. Mal, A. K. , Xu, P. C. and Bar-Cohen, Y. (1989) Analysis of leaky Lamb waves in bonded, *Int. J. Engng Sci.* **27**, 779-791.
17. Stewart, J. T. and Yong, Y. K. (1996) Exact analysis of the propagation of acoustic waves in multilayered Anisotropic Piezoelectric Plates, *IEEE Trans. Ultrason., Ferroelect., Freq., Contr.* **41**, 375-389.
18. Orellana, J. M and Collet. B. (2000) Propagation of guided waves in stratified piezoelectric structures, in *Mechanics of electromagnetic materials and structures* eds. Yang, J. Y. and Maugin, G. A., 125-131, IOS press, Amsterdam.
19. Pavlakovic, B., Lowe. M., Alleyne, D. and Cawley, P. (1997) Dispersive: A general purpose program for creating dispersion curves, *in Reviews of Progress in QNDE* eds. Thompson, D. O and Chimenti, D. E. **16**, 185-192, Plenum Press, New-York.
20. Lefebvre, J. E., Zhang, V., Gazalet, J. and Gryba, T. (1999) Legendre polynomial approach for modeling free-ultrasonic waves in multilayered plates, *J. Appl. Phys.* **85**, 3419-3427.

RADIATION MODE MODEL FOR MULTILAYERED STRUCTURES.

J. VANDEPUTTE⁽¹⁾, G. SHKERDIN⁽²⁾, O. LEROY⁽¹⁾

(1) I.R.C.; Katholieke Universiteit Leuven Campus Kortrijk

E. Sabbelaan 53, 8500 Kortrijk, Belgium

(2) Institute of Radioengineering and electronics, Russian Academy of Sciences, Moscow, Russia

Introduction.

Interaction of bounded acoustic beams with multilayered structures has been investigated extensively by several researchers in the last half of this century. It was W. T. Thompson⁹ who treated the problem the first time and introduced the "transfer matrix". This matrix describes the relation between the displacements and stresses at the top of a layer and those at the bottom of the layer. It was the initial impetus for further research.^{6-8,10-13}

In this paper, a multilayered solid embedded in a liquid is considered. The aim of this paper is to present the modelling of the interaction of bounded acoustic beams with a multilayer by means of the Mode Method^{1,2,3,4,5}.

The study of the reflected profile of an incident Gaussian beam enables us to characterize material parameters or to estimate the elastic properties of the reflector. It is known^{8,13} that computational difficulties occur for high frequencies, thick layers and large angles of incidence. We dealt with this problem in our model by restricting the spectrum of radiation modes to the most substantial ones.

In the first section, the general decomposition formula in radiation modes for a multilayered structure is derived. In the second section, an illustrative application is given. Determination of the residual stress in a plastically deformed plate is developed. In a first subsection, the modelling of the plastically deformed plate is worked out. A parabolic distributed residual stress is chosen in subsection two. In the final subsection, computations are done. It is shown that the residual stress can be measured by means of the reflected amplitude and phase profile of a Gaussian beam incident at a Lamb angle.

1. Construction of the orthogonal set of radiation modes for a multilayered structure.

Consider a multilayered structure of total thickness d embedded in an elastic liquid. We assume n viscoelastic solid layers with infinite extent in the z -direction. Layer j has thickness d_j and lower interface at y_{j-1} and upper interface at y_j , see fig. 1.

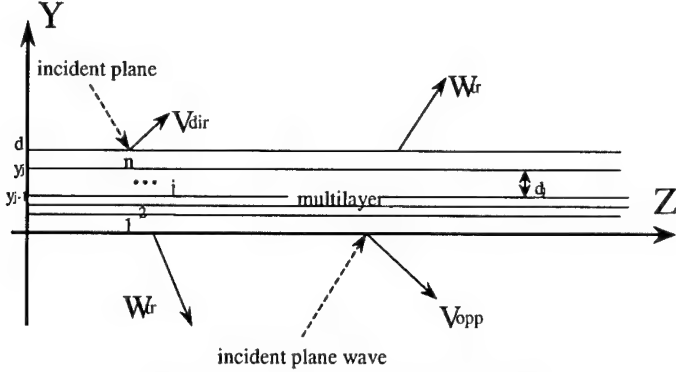


Fig. 1 Multilayered structure embedded in a liquid.

Firstly, we consider the radiation modes generated by plane waves incident from the upper liquid (called type 1). It can be remembered that a radiation mode represents the resulting total field, i.e. the incident, reflected and transmitted field, and the waves in the medium¹⁻⁴. The displacement field of this first type of radiation modes can be written as :

$$\begin{aligned}\bar{u}^1 &= \nabla(\Phi^i + \Phi^r) && \text{for } y > d \\ \bar{u}^1 &= \nabla(\Phi^t) && \text{for } y < 0.\end{aligned}\quad (1)$$

The displacement field in the medium has been omitted because we are only interested in the field in the liquid. The potential functions are represented by :

$$\begin{aligned}\Phi^i &= A \exp[i(-k_y y + k_z z) - \omega t] \\ \Phi^r &= A V_{dir} \exp[i(k_y y + k_z z) - \omega t] \\ \Phi^t &= A W_{tr} \exp[i(-k_y y + k_z z) - \omega t]\end{aligned}\quad (2)$$

with k_y and k_z the y- and z-component of the wavenumber k in the surrounding liquid ; ω the angular frequency. A denotes an arbitrary amplitude, V_{dir} the reflection coefficient, and W_{tr} the transmission coefficient.

Secondly, the radiation modes can be generated by plane waves incident from the other side of the multilayer ($y < 0$) (called type 2). The displacement field of this second type of radiation modes can be written as :

$$\begin{aligned}\bar{u}^2 &= \nabla(\tilde{\Phi}^i + \tilde{\Phi}^r) && \text{for } y < 0 \\ \bar{u}^2 &= \nabla(\tilde{\Phi}^t) && \text{for } y > d.\end{aligned}\quad (3)$$

The potential functions are represented by :

$$\begin{aligned}\tilde{\Phi}^i &= A \exp[i(k_y y + k_z z) - \omega t] \\ \tilde{\Phi}^r &= A V_{opp} \exp[i(-k_y y + k_z z) - \omega t] \\ \tilde{\Phi}^t &= A W_{tr} \exp[i(k_y y + k_z z) - \omega t]\end{aligned}\quad (4)$$

Here, V_{opp} denote the reflection coefficient at the beneath side of the multilayer.

For each layer, indexed by k , we define the propagator matrix $b_{ij}^{(k)}$, which links the displacement and stress tensor components at an arbitrary point in one layer to the components at the bottom of the considered layer. Requiring continuity of the normal and tangential displacements and stresses at each interface, leads to the transfermatrix of the multilayer :

$$\begin{pmatrix} u_z(d) \\ u_y(d) \\ T_{yy}(d) \\ T_{yz}(d) \end{pmatrix} = \begin{pmatrix} a_{ij} \end{pmatrix} \begin{pmatrix} u_z(0) \\ u_y(0) \\ T_{yy}(0) \\ T_{yz}(0) \end{pmatrix}, \quad i = 1, \dots, 4; \quad j = 1, \dots, 4. \quad (5)$$

$$\text{with } a_{ij} = \sum_{k_1, k_2, \dots, k_{n-1}} b_{ik_{n-1}}^{(n)}(d) b_{k_{n-1}k_{n-2}}^{(n-1)}(y_{k_{n-1}}) \dots b_{k_2k_1}^{(2)}(y_2) b_{k_1j}^{(1)}(y_1) \quad (6)$$

The reflection and transmission coefficients can now be calculated by continuity requirements at $y = d$ and $y = 0$.

Two radiation modes of type 1 and type 2, incident at the same angle of incidence, are not orthogonal although they have a completely different nature. Performing an analogous procedure as in ref. 1, 2 leads to two new types of radiation modes :

$$\vec{u}^r = \vec{u}^1 + \vec{u}^2 \quad (7)$$

$$\vec{u}^{r''} = \vec{u}^1 + b\vec{u}^2$$

The parameter b can be determined by requiring that the orthogonality condition (see eq. (8) in ref. 5) should be fulfilled for radiation modes of type 1 and 2 with the same angle of incidence. It is easily seen that for symmetrical multilayers or a plate, this parameter b is equal to -1, which corresponds to the symmetrical ($r''=s$) and anti-symmetrical ($r''=a$) radiation modes^{1,2}. Written more exhaustively, the displacement components of the first new type radiation modes become :

if $y > d$:

$$u_z^{r'} = Aik_z \left\{ \exp[-ik_y(y-d)] + \alpha_1 \exp[ik_y(y-d)] \right\} \exp[ik_z z] \quad (8)$$

$$u_y^{r'} = Aik_y \left\{ -\exp[-ik_y(y-d)] + \alpha_1 \exp[ik_y(y-d)] \right\} \exp[ik_z z];$$

if $y < 0$:

$$u_z^{r'} = Aik_z \left\{ \exp[ik_y y] + \delta_1 \exp[-ik_y y] \right\} \exp[ik_z z] \quad (9)$$

$$u_y^{r'} = Aik_y \left\{ \exp[ik_y y] - \delta_1 \exp[-ik_y y] \right\} \exp[ik_z z];$$

$$\text{with } \alpha_1 = V_{dir} + W_{tr} \quad (10)$$

$$\delta_1 = V_{opp} + W_{tr}$$

Radiation modes of the second new type are described by :

if $y > d$:

$$u_z^{r''} = Aik_z \left\{ \exp[-ik_y(y-d)] + \alpha_2 \exp[ik_y(y-d)] \right\} \exp[ik_z z] \quad (11)$$

$$u_y^{r''} = Aik_y \left\{ -\exp[-ik_y(y-d)] + \alpha_2 \exp[ik_y(y-d)] \right\} \exp[ik_z z];$$

if $y < 0$:

$$u_z^{r''} = Aik_z \left\{ b \exp[ik_y y] + \delta_2 \exp[-ik_y y] \right\} \exp[ik_z z] \quad (12)$$

$$u_y^{r''} = Aik_y \left\{ b \exp[ik_y y] - \delta_2 \exp[-ik_y y] \right\} \exp[ik_z z];$$

with $\alpha_2 = V_{dir} + bW_{tr}$

$$\delta_2 = bV_{opp} + W_{tr}$$

Rigorous formulas for V_{dir} , W_{tr} , V_{opp} and b are given in the appendix.

As a consequence we have a complete set of radiation modes for the multilayered structure. An arbitrary acoustic field can be decomposed into the radiation modes :

$$\vec{u}(y, z) = \sum_{r=r', r''} \int_0^{+\infty} C^{(r)}(k_y) \vec{u}^{(r)}(y, z; k_y) dk_y \quad (14)$$

where summation is taken over the two new types of radiation modes, integration is taken over the continuous spectrum of radiation modes. $C^{(r)}(k_y)$ denotes the expansion coefficient. The Stoneley modes are omitted, because they are not excited. Only Gaussian beams, incident at angles $\ll 90^\circ$, are considered here and as a consequence they have expansion coefficients equal to zero. The expansion for the stress tensor component is analogous^{1,5} to (14). The expansion coefficient can be calculated by means of the z-component of the incident displacement field along the $z = z_0$ - axis :

$$C^{(r)}(k_y) = - \frac{\int u_z^{inc}(y, z_0) T_{zz}^{(r)}(y, z_0; k_y) dy}{\tilde{Q}^{(r)}(k_y)} \quad (15)$$

An expression for the normalization constant $\tilde{Q}^{(r)}(k_y)$ is given in the appendix.

Generally, computational difficulties can occur for high frequencies, thick layers or great angles of incidence. We avoided these kind of problems by restricting the spectrum of radiation modes to the most substantial ones in (14). We let k_y vary in the neighbourhood of k_y^{inc} , the y-component of the wavevector of the incident Gaussian beam.

2. Application : determination of residual stresses in a plate.

2.1 MODELLING A PLASTICALLY DEFORMED PLATE.

We assume a plastically deformed plate. Consider the non-linear stress-strain relation (Hooke) :

$$T_{ij} = C_{ijkl} e_{kl} + D_{ijklmn} e_{kl} e_{mn} \quad (16)$$

with T_{ij} and e_{kl} , respectively the stress and strain components; C_{ijkl} and D_{ijklmn} , the linear and non-linear stiffness coefficients. This prestressed plate will now be impinged by a finite acoustic beam. The total acoustic strain is then given by

$$e_{kl} = e_{kl}^{st} + e_{kl}^{ac} \quad (17)$$

with e_{kl}^{st} and e_{kl}^{ac} , respectively the static and acoustic strain. Inserting (17) into (16), neglecting the product term with two acoustic strains (we assume the static strain to be much larger than the acoustic strain) and omitting the terms purely related to the static strain, we become :

$$T_{ij}^{ac} = C_{ijkl} e_{kl}^{ac} + D_{ijklmn} e_{kl}^{ac} e_{mn}^{st}, \quad (18)$$

denoting the total acoustic stress.

2.2 PARABOLIC DISTRIBUTED RESIDUAL STRESS IN AN ISOTROPIC PLATE.

We will consider a parabolic prestressed plate. This structure will be discretized by dividing the plate into $2n+1$ substructures or layers. For each layer ($i=1, \dots, 2n+1$) a uniform stress is assumed :

$$e_{xx} = e_{yy} = e_{zz} = S_i, \quad (19)$$

with S_i a real number ; the shear stresses are supposed to be equal to zero.

The parabolic initial stress distribution is defined as follows :

$$\begin{aligned} S_{n+1} &= \gamma && \text{(central layer)} \\ S_{n+1 \pm m} &= \gamma - \gamma \frac{4m^2}{(2n+1)^2}, && m < n \end{aligned} \quad (20)$$

with γ the maximal strain, at the center of the plate.

For convenience, we will consider a fixed layer with strain S in order to derive the stress-strain relation.

Putting (20) in (18), we get :

$$T_{ij}^{ac} = C_{ijkl} e_{kl}^{ac} + D_{ijklmn} S e_{kl}^{ac} \quad (21)$$

As a result, considering isotropic structures, (21) reduces to :

$$T_{ij}^{ac} = 2\mu e_{ij}^{ac} + \lambda e_{kk} \delta_{ij} \quad (22)$$

$$\lambda = \lambda_0 \left(1 + \frac{2D_{1122ii}}{C_{1122}} S\right) \quad (23)$$

with

$$\mu = \mu_0 \left(1 + \frac{2D_{1122ii}}{C_{1212}} S\right)$$

and λ_0, μ_0 denoting the Lamé constants of the unstressed plate.

It is easy to show that the density is decreased due to the plastic deformation, and is approximately equal to

$$\rho \approx \rho_0 (1 - 3S) \quad (24)$$

with ρ_0 the density in the unstressed case.

We summarize by stating that modelling a parabolic prestressed isotropic plate amounts to adapting ρ_0 , λ_0 and μ_0 in each layer by means of the relations given by (23) and (24). It can be shown that the coefficients of S in (23) are approximately equal to 1.

2.3 NUMERICAL COMPUTATIONS.

Calculations were done in order to measure the residual stress characterized by different values of the parameter γ by means of amplitude and phase curves. We consider a transducer placed at $y_0 = 10\text{cm}$ and $z_0 = 0\text{cm}$, emitting a Gaussian acoustic beam with initial halfwidth 1 cm. The beam is incident at $22^{\circ}31'$, the S2-Lamb angle, on a brass plate of thickness 2 mm. The surrounding liquid is water with phase velocity of sound equal to 1480 m/s; the parameters of the brass plate are : $v_l = 4410 \text{ m/s}$, $v_t = 2150 \text{ m/s}$ and $\rho = 8600 \text{ kg/m}^3$, denoting the longitudinal and shear velocity, and density respectively. The frequency is 3 Mhz. Fig. 3, 4 and 5 show the amplitude and phase curves of the reflected profile in a plane perpendicular to the wavevector after 8 cm propagation ($\ell = 8 \text{ cm}$, see fig. 2). Four values of γ are considered and compared : $\gamma = 0$ (there is no residual stress), $\gamma = 10^{-2}$, $\gamma = 10^{-3}$ and $\gamma = 10^{-4}$. 11 layers were assumed to model these parabolic residual stresses.

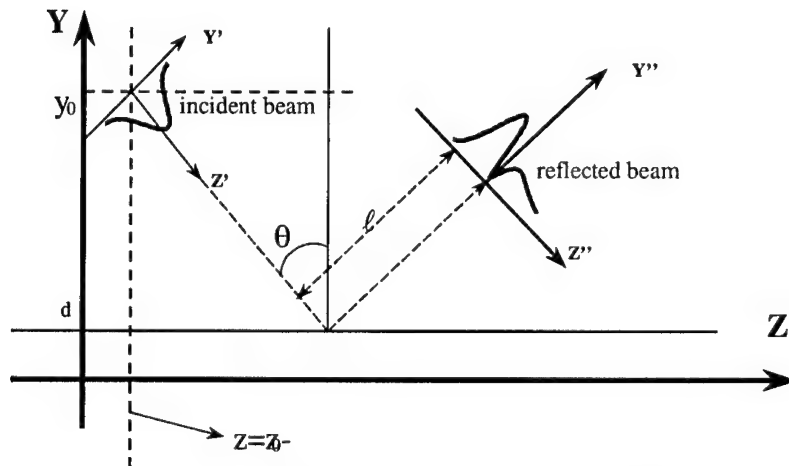


Fig. 2 Reflection on a multilayer, coordinate system.

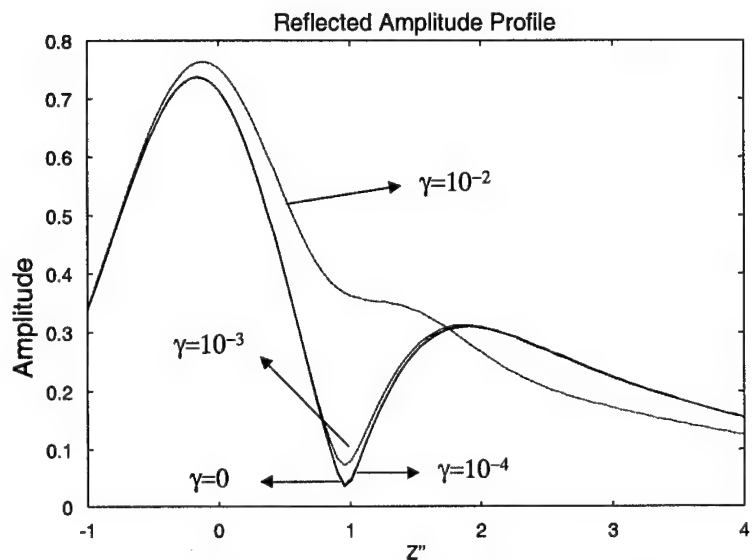


Fig. 3 Amplitude of the reflected profile at plane $\ell = 8$ cm.

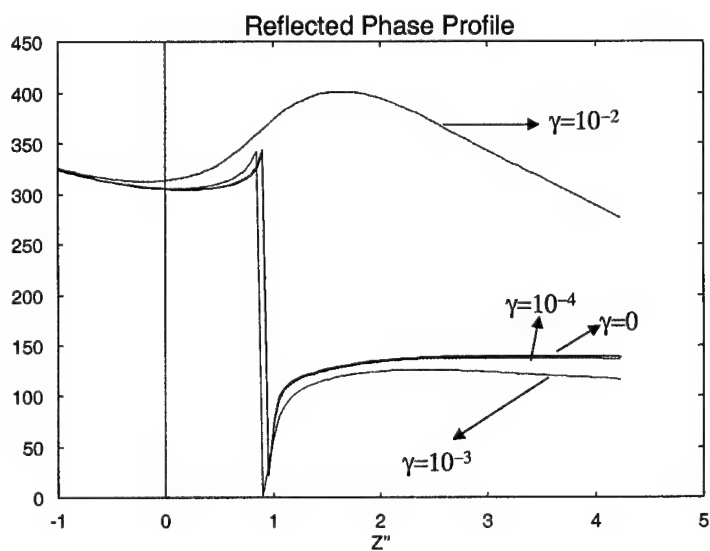


Fig. 4 Phase curves of the reflected profile at plane $\ell = 8$ cm.

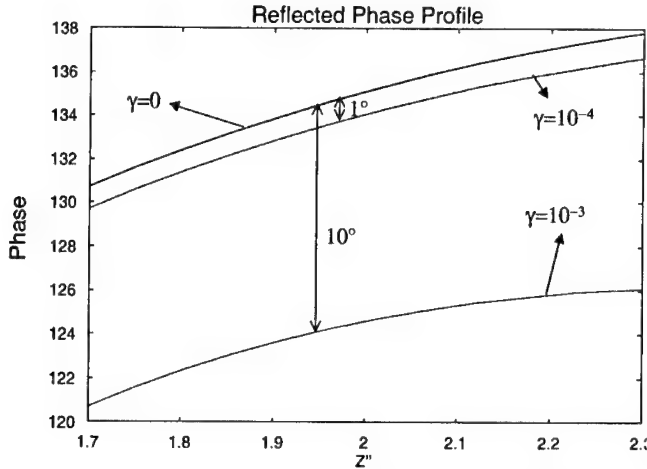


Fig. 5 Phase curves of the reflected profile at plane $\ell = 8$ cm.

Analyzing the amplitude profiles, there is only an observable effect in case of $\gamma = 10^{-2}$ and $\gamma = 10^{-3}$. On the other hand, fig. 4 and 5 shows that residual stresses up to $\gamma = 10^{-4}$ are measurable by considering the phase difference in the point where the shifted component of the reflected amplitude profile reaches its maximum. Phase differences of 1° ($\gamma = 10^{-4}$) and 10° ($\gamma = 10^{-3}$) are found.

3. Conclusion

The Radiation Mode Model was presented and extended for multilayered structures. A general Radiation Mode decomposition formula was derived and enables us to study the reflected, refracted and transmitted profiles of an incident acoustic beam. One particular application was worked out : measuring residual stresses by means of phase effects in the reflected profile. A parabolic prestressed plate is chosen and it is shown that the residual stress is measurable with a high accuracy.

APPENDIX

$$V_{dir} = \frac{\beta_0 - \beta_{01} + i(\frac{\lambda k^2}{k_y} \beta_1 + \frac{k_y}{\lambda k^2} \beta_2)}{\Delta} \quad (A1)$$

$$V_{opp} = \frac{\beta_{01} - \beta_0 + i(\frac{\lambda k^2}{k_y} \beta_1 + \frac{k_y}{\lambda k^2} \beta_2)}{\Delta} \quad (A2)$$

$$W_{tr} = \frac{2}{\Delta} \quad (A3)$$

$$\text{with } \Delta = \beta_0 + \beta_{01} + i\left(-\frac{\lambda k^2}{k_y}\beta_1 + \frac{k_y}{\lambda k^2}\beta_2\right), \quad (\text{A4})$$

$$\beta_0 = a_{33} - \frac{a_{43}a_{31}}{a_{41}} \quad \beta_{01} = a_{22} - \frac{a_{21}a_{42}}{a_{41}} \quad (\text{A5}) \quad (\text{A6})$$

$$\beta_1 = a_{23} - \frac{a_{43}a_{21}}{a_{41}} \quad \beta_2 = a_{32} - \frac{a_{42}a_{31}}{a_{41}} \quad (\text{A7}) \quad (\text{A8})$$

$$b = -\frac{\beta_0 - \beta_{01} + i\left(\frac{\lambda k^2}{k_y}\beta_1 + \frac{k_y}{\lambda k^2}\beta_2\right) + 2}{\beta_{01} - \beta_0 + i\left(\frac{\lambda k^2}{k_y}\beta_1 + \frac{k_y}{\lambda k^2}\beta_2\right) + 2} \quad (\text{A9})$$

$$\tilde{Q}^{(r)}(k_y) = 2A^2 ik_z \lambda k^2 e^{2ik_z z} \pi(\alpha_1 + \delta_1) \quad (\text{A10})$$

$$\tilde{Q}^{(r)}(k_y) = 2A^2 ik_z \lambda k^2 e^{2ik_z z} \pi(\alpha_2 + b\delta_2)$$

REFERENCES

- ¹R.Briers, O. Leroy, and G. N. Shkerdin, "Mode theory as a framework for the investigation of the generation of a Stoneley wave at a liquid/solid interface", J. Acoust. Soc. Am. **95**, (1994).
- ²R. Briers, O. Leroy, and G. N. Shkerdin, "Conversion of a Stoneley wave at the extremity of a fluid loaded plate," J. Acoust. Soc. Am. **101**, 1347-1357 (1997).
- ³R. Briers, O. Leroy, and G. N. Shkerdin, "A liquid wedge as generating technique for Lamb and Rayleigh waves," J. Acoust. Soc. Am. **102** (4), 2117-2124 (1997).
- ⁴R. Briers, O. Leroy, and G. N. Shkerdin, "Stoneley wave excitation by a bounded beam at the down-step of a thin layer on a substrate," J. Acoust. Soc. Am. **102** (4), 2108-2112 (1997).
- ⁵J. Vandepitte, O. Leroy, R. Briers and G. N. Shkerdin, "Extension of the mode method for viscoelastic media and focused ultrasonic beams", Submitted to JASA.
- ⁶B. A. Auld, *Acoustic fields and waves in solids*, 1973.
- ⁷L. M. Brekhovskikh, *Waves in Layered Media*. New York : Academic, 1960.
- ⁸Michael J. S. Lowe, "Matrix Techniques for Modeling Ultrasonic Waves in Multilayered Media", IEEE Transactions on Ultrasonics, Ferroelectrics and frequency control. Vol. 42, No. 4, July 1995.
- ⁹W.T. Thomson, "Transmission of Elastic Waves through a Stratified Solid Medium", Journal of Applied Physics, Vol. (21), February, 1950.
- ¹⁰P. Shaw and P. Bugl, "Transmission of Plane Waves through Layered Linear Viscoelastic Media", J. Acoust. Soc. Am. **46**, 1969.
- ¹¹D. B. Bogy and S. M. Gracewski, "On the plane-wave reflection coefficient and nonspecular reflection of bounded beams for layered half-spaces underwater", J. Acoust. Soc. Am. **74** (2), 1983.
- ¹²P. Cervenka and Pascal Challande, "A new efficient algorithm to compute the exact reflection and transmission factors for plane waves in layered absorbing media (liquids and solids)", J. Acoust. Soc. Am. **89** (4), 1991.
- ¹³T. Kundu, "On the nonspecular reflection of bounded acoustic beams", J. Acoust. Soc. Am. **83** (1), 1988.
- ¹⁴L. M. Brekhovskikh, O. A. Godin, "*Acoustics of layered media*", Moscow Science, 1989.

ELASTIC WAVE SCATTERING FROM A PERTURBED FLAT INTERFACE

S. NAIR

Illinois Institute of Technology, Chicago, Illinois

D. A. SOTIROPOULOS

Southern Polytechnic State University, Marietta, Georgia

1. Introduction

Reflection and refraction of ultrasonic waves form fundamental techniques in the non-destructive evaluation of structural components. When these techniques are applied to composite structures the interface between different layers plays a crucial role. A part of the non-destructive evaluation deals with the monitoring of the health of interfaces. Delaminations along the interface and local buckling of the layer are common defects in layered composites. In this paper the effect of a geometrically perturbed flat interface on the reflection and refraction of elastic waves is considered. Specifically, the perturbation is assumed to be in the form of a sinusoid with small amplitude compared to the wave length of the incident beam. Any periodic imperfections of the interface caused by local buckling or by machining prior to fabrication, can be represented as a Fourier series. A basic solution of the reflection problem with a single sine wave imperfection can be of use in analyzing these more complicated periodic perturbation of interfaces. The method used here is the regular perturbation expansion of the equations of dynamic elasticity with the amplitude of the interfacial curve forming the small parameter.

Perturbative methods have a long history in their applications in elastic wave problems. The dispersion of Love waves due to a small amplitude curvature of the surface was studied by Mal (1962). Markenscoff and Lekoudis (1976) have considered Love waves when the elastic layer has a slowly varying thickness. Recently, the effect of interface roughness as a random variable has been the subject of a number of studies—Nagy and Rose (1993), Pecorari, et al. (1995), etc. Further citations can be found in the

above papers. The scattering problem has received considerably more extensive treatment in the context of electromagnetic waves. The paper by Chandler-Wilde et al. (1999) gives a large number of references on this topic.

In this paper two types of linear elastic materials are considered—isotropic and orthotropic incompressible. Although, the results for isotropic materials are implied in the second order perturbation calculations given by Pecorari, et al. (1995), they are explicitly given here. They provide a unified view of the general problem. Incident longitudinal and shear waves are treated here simultaneously in a vector formulation in the case of isotropy. A perturbed interface separating two orthotropic incompressible materials is studied here for the first time. Elastic wave reflections from flat interfaces in incompressible orthotropic and monoclinic materials are treated by the present authors (1997, 1999a, 1999b).

2. Formulation

Two distinct linear elastic media, one occupying the space $-\infty < x_1, x_3 < \infty$, $-\infty < x_2 < f(x_1)$ and the other occupying the space $-\infty < x_1, x_3 < \infty$, $f(x_1) < x_2 < \infty$ are considered (see Fig. 1). Along the interface $x_2 = f(x_1)$ the two are assumed to be perfectly bonded. With reference to the interface the media will be referred as the upper and lower medium. In the first part of this paper it is assumed that the media are isotropic and in plane strain in the x_3 -direction. The boundary, $x_2 = f(x_1)$, is specified by

$$f(x_1) = 2a \cos mx_1, \quad (1)$$

where $2a$ is the amplitude of the sinusoidal curve and $2\pi/m$ is the wave length.

The stress-strain relations for the lower medium are given by

$$\begin{aligned} \sigma_{11} &= (\lambda + 2\mu)\partial_1 u_1 + \lambda\partial_2 u_2, \\ \sigma_{22} &= (\lambda + 2\mu)\partial_2 u_2 + \lambda\partial_1 u_1, \\ \sigma_{12} &= \mu(\partial_2 u_1 + \partial_1 u_2), \end{aligned} \quad (2)$$

where u_i and σ_{ij} represent the displacement and the stress components and ∂_i the partial differentiation with respect to x_i .

The equations of motion are

$$\begin{aligned} \partial_1 \sigma_{11} + \partial_2 \sigma_{12} &= \rho \ddot{u}_1, \\ \partial_1 \sigma_{12} + \partial_2 \sigma_{22} &= \rho \ddot{u}_2, \end{aligned} \quad (3)$$

Eliminating the stresses in the above equations using the equations (2) and assuming time-harmonic waves with

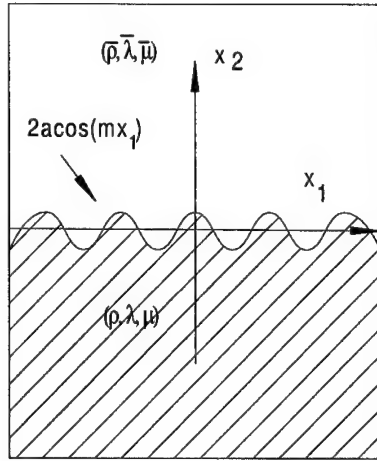


Figure 1. The sinusoidal interface separating two elastic media.

$$u_i(x_1, x_2, t) = U_i(x_1, x_2) e^{-i\Omega t} \quad (4)$$

the equations of motion can be expressed as

$$\begin{aligned} [\omega_T^2 \partial_1^2 + \omega_L^2 (\partial_2^2 + \omega_T^2)] U_1 + (\omega_T^2 - \omega_L^2) \partial_1 \partial_2 U_2 &= 0, \\ [\omega_T^2 \partial_2^2 + \omega_L^2 (\partial_1^2 + \omega_T^2)] U_2 + (\omega_T^2 - \omega_L^2) \partial_1 \partial_2 U_1 &= 0, \end{aligned} \quad (5)$$

where

$$\omega_L^2 = \frac{\rho \Omega^2}{\lambda + 2\mu}, \quad \omega_T^2 = \frac{\rho \Omega^2}{\mu}. \quad (6)$$

The two equations in (5) reduce to the single equation

$$(\omega_L^2 + \Delta)(\omega_T^2 + \Delta) U_i = 0, \quad i = 1, 2 \quad (7)$$

where \$\Delta\$ is the Laplace operator.

The solutions of equation (7) are sought in the form

$$U_i = A_i e^{i\mathbf{k}\cdot\mathbf{x}}, \quad (8)$$

where \$\mathbf{k} = (k_1, k_2) = k\nu\$ with \$\mathbf{k}\$ being the wave vector, \$k\$ its magnitude and \$\nu\$ the unit vector in the direction of propagation.

Substitution of equation (8) in (7) yields two solutions for \$k\$, the longitudinal wave number, \$k_L\$, and the transverse wave number, \$k_T\$, having the following expressions:

$$k_L^2 = \omega_L^2, \quad k_T^2 = \omega_T^2 \quad (9)$$

From equation (5), it is seen that for longitudinal waves (L-waves)

$$A_1 = k_{L1} A_L, \quad A_2 = k_{L2} A_L \quad (10)$$

and for transverse waves (T-waves)

$$A_1 = k_{T2} A_T, \quad A_2 = -k_{T1} A_T \quad (11)$$

where the quantities A_L and A_T are potential amplitudes. Specifically,

$$A_L^2 = U^2 / \omega_L^2, \quad A_T^2 = U^2 / \omega_T^2. \quad (12)$$

In the following the subscripts L and T will be omitted whenever the context clarifies the situation. Omitting the factor $i\exp[i(\mathbf{k} \cdot \mathbf{x} - \Omega t)]$ the stresses in the material can be expressed as:

For L-waves:

$$\sigma_{12} = 2\mu k_1 k_2 A, \quad \sigma_{11} = (\lambda k^2 + 2\mu k_1^2) A, \quad \sigma_{22} = (\lambda k^2 + 2\mu k_2^2) A, \quad (13)$$

For T-waves:

$$\sigma_{12} = \mu(k_2^2 - k_1^2) A, \quad \sigma_{11} = 2\mu k_1 k_2 A, \quad \sigma_{22} = -2\mu k_1 k_2 A, \quad (14)$$

Except for the material constants, the equations for the displacements and stresses for the upper medium are the same as those in (2) to (14). To distinguish the quantities pertaining to the upper medium, they will be denoted by an over-bar. Thus, the density and Lamé constants for the upper medium are $\bar{\rho}$, $\bar{\lambda}$, and $\bar{\mu}$, respectively.

With \mathbf{n} being the outward normal to the interface from the lower medium, the continuity of displacements and stresses require

$$U_1 - \bar{U}_1 = 0, \quad U_2 - \bar{U}_2 = 0, \quad (15)$$

$$(\sigma_{11} - \bar{\sigma}_{11})n_1 + (\sigma_{12} - \bar{\sigma}_{12})n_2 = 0, \quad (\sigma_{12} - \bar{\sigma}_{12})n_1 + (\sigma_{22} - \bar{\sigma}_{22})n_2 = 0 \quad (16)$$

If $\psi(x_1, x_2)$ is any field variable, on $x_2 = f(x_1) \ll 1$,

$$\psi(x_1, f(x_1)) \approx \psi(x_1, 0) + f(x_1) \partial_2 \psi(x_1, 0) \quad (17)$$

and the components of the normal are approximated as

$$n_1 \approx -f', \quad n_2 \approx 1 \quad (18)$$

where the prime denotes differentiation with respect to x_1 .

These approximations allow one to expand all field variables in regular perturbation series as

$$U_i = U_i^{(0)} + U_i^{(1)} + \dots, \quad \sigma_{ij} = \sigma_{ij}^{(0)} + \sigma_{ij}^{(1)} + \dots, \quad (19)$$

and similar quantities for the upper medium. Using the above forms and the approximations (18) in equations (15) and (16), the continuity for the zeroth and first order quantities can be separated as

$$\begin{aligned} U_1^{(0)} &= \bar{U}_1^{(0)}, & U_2^{(0)} &= \bar{U}_2^{(0)}, \\ \sigma_{12}^{(0)} - \bar{\sigma}_{12}^{(0)} &= 0, & \sigma_{22}^{(0)} - \bar{\sigma}_{22}^{(0)} &= 0 \end{aligned} \quad (20)$$

$$\begin{aligned} U_1^{(1)} - \bar{U}_1^{(1)} &= -f\partial_2(U_1^{(0)} - \bar{U}_1^{(0)}), & U_2^{(1)} - \bar{U}_2^{(1)} &= -f\partial_2(U_2^{(0)} - \bar{U}_2^{(0)}), \\ \sigma_{12}^{(1)} - \bar{\sigma}_{12}^{(1)} &= f'(\sigma_{11}^{(0)} - \bar{\sigma}_{11}^{(0)}) - f\partial_2(\sigma_{12}^{(0)} - \bar{\sigma}_{12}^{(0)}), & \sigma_{22}^{(1)} - \bar{\sigma}_{22}^{(1)} &= -f\partial_2(\sigma_{22}^{(0)} - \bar{\sigma}_{22}^{(0)}) \end{aligned} \quad (21)$$

The zeroth order problem is the classical reflection-refraction problem in which an incident L or T-wave in the lower medium produces reflected L and T-waves in it and refracted L and T-waves in the upper medium. Assuming the amplitudes of the incident waves to be I_L and I_T , the amplitudes of the reflected waves to be R_L and R_T , and those of the refracted waves to be \bar{R}_L and \bar{R}_T , the reflection-refraction problem can be treated in a unified way if it is assumed that the incident L and T-waves have the same component of the wave vector in the direction of x_1 , i. e., k_1 is common. In order to satisfy the continuity of stresses and displacements, the reflected waves and the refracted waves must also have wave vectors with the same x_1 -component, k_1 . These six wave vectors are shown in Fig. 2. The x_2 -components of the wave vectors may be expressed using the notation,

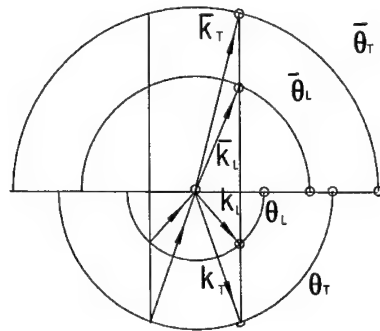


Figure 2. The wave vectors in the upper and lower media with a common k_1 -component (incident L-waves and T-waves are considered simultaneously).

$$\begin{aligned} t_L &= \tan \theta_L, & t_T &= \tan \theta_T, & \bar{t}_L &= \tan \bar{\theta}_L, & \bar{t}_T &= \tan \bar{\theta}_T, \\ k_{L2} &= k_1 t_L, & k_{T2} &= k_1 t_T, & \bar{k}_{L2} &= k_1 \bar{t}_L, & \bar{k}_{T2} &= k_1 \bar{t}_T. \end{aligned} \quad (22)$$

Using the vectors

$$\mathbf{I} = \begin{Bmatrix} I_L \\ I_T \end{Bmatrix}, \quad \mathbf{R} = \begin{Bmatrix} R_L \\ R_T \end{Bmatrix}, \quad \bar{\mathbf{R}} = \begin{Bmatrix} \bar{R}_L \\ \bar{R}_T \end{Bmatrix}, \quad (23)$$

the continuity of displacements gives

$$\mathbf{A}_{\bar{R}}(t) \bar{\mathbf{R}} - \mathbf{A}_R(t) \mathbf{R} = \mathbf{A}_I(t) \mathbf{I}, \quad (24)$$

and the continuity of tractions gives

$$\kappa \mathbf{B}_{\bar{R}}(t) \bar{\mathbf{R}} - \mathbf{B}_R(t) \mathbf{R} = \mathbf{B}_I(t) \mathbf{I}, \quad (25)$$

where

$$\kappa = \bar{\mu}/\mu, \quad (26)$$

$$\begin{aligned} \mathbf{A}_{\bar{R}}(t) &= \begin{bmatrix} 1 & \bar{t}_T \\ \bar{t}_L & -1 \end{bmatrix}, \\ \mathbf{A}_R(t) &= \begin{bmatrix} 1 & -t_T \\ -t_L & -1 \end{bmatrix}, \\ \mathbf{A}_I(t) &= \begin{bmatrix} 1 & t_T \\ t_L & -1 \end{bmatrix}, \end{aligned} \quad (27)$$

and

$$\begin{aligned} \mathbf{B}_{\bar{R}}(t) &= \begin{bmatrix} 2\bar{t}_L & \bar{t}_T^2 - 1 \\ (\bar{k}_T^2/\bar{k}_L^2)(1 + \bar{t}_L^2) - 2 & -2\bar{t}_T \end{bmatrix}, \\ \mathbf{B}_R(t) &= \begin{bmatrix} -2t_L & t_T^2 - 1 \\ (k_T^2/k_L^2)(1 + t_L^2) - 2 & 2t_T \end{bmatrix}, \\ \mathbf{B}_I(t) &= \begin{bmatrix} 2t_L & t_T^2 - 1 \\ (k_T^2/k_L^2)(1 + t_L^2) - 2 & -2t_T \end{bmatrix}. \end{aligned} \quad (28)$$

The above four equations give the required amplitudes \mathbf{R} and $\bar{\mathbf{R}}$ of the zeroth order solutions.

From equation (1) the boundary shape f can be written as

$$f(x_1) = a[e^{imx_1} + e^{-imx_1}] \quad (29)$$

As the boundary conditions (21) are linear in f , the first order perturbation solutions can be divided into two sets—one due to the first term in (29) and the other due to the second term. The second set can be generated by changing (m) to $(-m)$ after obtaining the first set. Equation (21) also shows that the component of wave vector along x_1 , for the first order solutions, is $(k_1 \pm m)$. The two first order wave vectors (one advanced and the other retarded) are shown in Fig. 3. With this, the displacement components can be written as

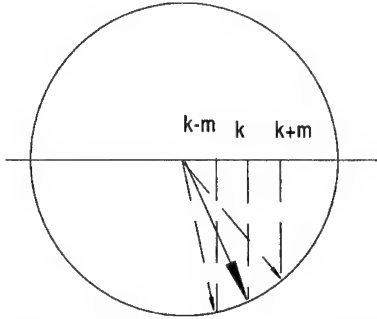


Figure 3. Two first order waves produced by the interface for a primary wave with horizontal component k .

$$U_j^{(1)} = i a_j e^{i(\mathbf{p} \cdot \mathbf{x} - \Omega t)} \quad j = 1, 2, \quad (30)$$

where the imaginary number i has been inserted to have the amplitudes a_j real when substituted in the non-homogeneous boundary conditions (21), and

$$p_1 = k_1 + m, \quad p_{L2} = \sqrt{k_L^2 - p_1^2}, \quad p_{T2} = \sqrt{k_T^2 - p_1^2}. \quad (31)$$

The angles of the forward scattered (first order) waves can be defined as

$$\begin{aligned} \tau_L &= \tan \phi_L, \quad \tau_T = \tan \phi_T, \quad \bar{\tau}_L = \tan \bar{\phi}_L, \quad \bar{\tau}_T = \tan \bar{\phi}_T, \\ p_{L2} &= p_1 \tau_L, \quad p_{T2} = p_1 \tau_T, \quad \bar{p}_{L2} = p_1 \bar{\tau}_L, \quad \bar{p}_{T2} = p_1 \bar{\tau}_T. \end{aligned} \quad (32)$$

The potential amplitude vectors for the scattered waves can be written as

$$\mathbf{r} = \epsilon \begin{Bmatrix} r_L \\ r_T \end{Bmatrix}, \quad \bar{\mathbf{r}} = \epsilon \begin{Bmatrix} \bar{r}_L \\ \bar{r}_T \end{Bmatrix}, \quad (33)$$

where $\epsilon = a\omega_L$ is a nondimensional measure of the height of the perturbed interface.

The continuity conditions (21) for the displacements give

$$\mathbf{A}_{\bar{R}}(\tau)\bar{\mathbf{r}} - \mathbf{A}_R(\tau)\mathbf{r} = \frac{k_1/\omega_L}{p_1/k_1}[\mathbf{C}_I\mathbf{I} + \mathbf{C}_R\mathbf{R} - \mathbf{C}_{\bar{R}}\bar{\mathbf{R}}], \quad (34)$$

and the continuity of tractions gives

$$\kappa\mathbf{B}_{\bar{R}}(\tau)\bar{\mathbf{r}} - \mathbf{B}_R(\tau)\mathbf{r} = \frac{k_1/\omega_L}{(p_1/k_1)^2}[\mathbf{D}_I\mathbf{I} + \mathbf{D}_R\mathbf{R} - \kappa\mathbf{D}_{\bar{R}}\bar{\mathbf{R}}], \quad (35)$$

where the matrices \mathbf{A} 's and \mathbf{B} 's are the same as those given in equations (26) and (27), except that all symbols t have to be replaced by τ . The newly introduced matrices \mathbf{C} 's and \mathbf{D} 's are given by

$$\begin{aligned} \mathbf{C}_I &= \begin{bmatrix} t_L & t_T^2 \\ t_L^2 & -t_T \end{bmatrix} \\ \mathbf{C}_R &= \begin{bmatrix} -t_L & t_T^2 \\ t_L^2 & t_T \end{bmatrix} \\ \mathbf{C}_{\bar{R}} &= \begin{bmatrix} \bar{t}_L & \bar{t}_T^2 \\ \bar{t}_L^2 & -\bar{t}_T \end{bmatrix} \end{aligned} \quad (36)$$

$$\begin{aligned} \mathbf{D}_I &= \begin{bmatrix} 2t_L^2 - \gamma[(k_T^2/k_L^2)(1+t_L^2) - t_L^2] & t_T(t_T^2 - 1) - 2\gamma t_T \\ t_L[(k_T^2/k_L^2)(1+t_L^2) - 2] & -2t_T^2 \end{bmatrix} \\ \mathbf{D}_R &= \begin{bmatrix} 2t_L^2 - \gamma[(k_T^2/k_L^2)(1+t_L^2) - t_L^2] & -t_T(t_T^2 - 1) + 2\gamma t_T \\ -t_L[(k_T^2/k_L^2)(1+t_L^2) - 2] & -2t_T^2 \end{bmatrix} \\ \mathbf{D}_{\bar{R}} &= \begin{bmatrix} 2\bar{t}_L^2 - \gamma[(\bar{k}_T^2/\bar{k}_L^2)(1+\bar{t}_L^2) - \bar{t}_L^2] & \bar{t}_T(\bar{t}_T^2 - 1) - 2\gamma\bar{t}_T \\ \bar{t}_L[(\bar{k}_T^2/\bar{k}_L^2)(1+\bar{t}_L^2) - 2] & -2\bar{t}_T^2 \end{bmatrix} \end{aligned} \quad (37)$$

where $\gamma = m/k_1 = \delta/\cos\theta_L$, with $\delta = m/\omega_L$. Here δ is a nondimensional measure of interface perturbation wave length.

The effect of the sinusoidal interface is contained in the above matrices. It is to be noted that in addition to the usual parameters: $k_L, k_T, \bar{k}_L, \bar{k}_T$, and κ , two new parameters: $\epsilon = a\omega_L$ and $\delta = m/\omega_L$ characterizing the interface asperity height and wave length appear in these relations. The first order amplitudes \mathbf{r} measure the quantity ϵ , while the scattering angle ϕ_L or ϕ_T measures the quantity δ .

3. Reflection from a Free Surface

The solution to the problem of reflection from a sinusoidal free surface is a special case of the above formulation. If it is assumed that the upper medium is absent. The continuity requirement for displacements, equation

(24), has to be omitted and the refracted wave amplitudes have to be set to zero. Equation (25) becomes

$$\mathbf{B}_R(t)\mathbf{R} = -\mathbf{B}_I(t)\mathbf{I}, \quad (38)$$

which yields the classical reflection amplitudes.

For the first order solutions, again, the displacement condition (34) has to be omitted and the stress condition (35) becomes

$$\mathbf{B}_R(\tau)\mathbf{r} = -\frac{k_1^2}{p_1^2}[\mathbf{D}_I\mathbf{I} + \mathbf{D}_R\mathbf{R}], \quad (39)$$

4. Normal Incidence

As the above formulation utilizes the common component k_1 of all wave vectors for normalization, the case of normal incidence, where $k_1 = 0$, needs special consideration. When $k_1 = 0$ equations (24) and (25) give uncoupled relations for the longitudinal and transverse components. The solutions are

$$\bar{R}_L = \frac{2}{\xi(\kappa\xi + 1)}I_L, \quad R_L = \frac{\kappa\xi - 1}{\kappa\xi + 1}I_L \quad (40)$$

$$\bar{R}_T = \frac{2}{\eta(\kappa\eta + 1)}I_T, \quad R_T = \frac{\kappa\eta - 1}{\kappa\eta + 1}I_T \quad (41)$$

where $\xi = \bar{k}_L/k_L$ and $\eta = \bar{k}_T/k_T$.

Assuming $\delta \ll 1$, the terms on the left side of equations (34) and (35) uncouple. Solutions of these equations can be obtained as

$$\begin{aligned} r_L &= \frac{2\xi}{\kappa\xi + 1} \frac{\kappa\eta^2 - 1}{\kappa\eta^2 + \xi} I_L \\ \bar{r}_L &= 2\left[\frac{1}{\kappa\eta^2 + \xi} - \frac{1}{\kappa\xi + 1}\right]I_L \end{aligned} \quad (42)$$

$$\begin{aligned} r_T &= 2\frac{k_T}{k_L} \frac{\kappa\eta - 1}{\kappa\eta + 1} I_T \\ \bar{r}_T &= 2\frac{k_T}{k_L} \frac{1 - \eta}{\eta(\kappa\eta + 1)} I_T \end{aligned} \quad (43)$$

Further, for the reflection from a free surface, setting $\kappa = 0$,

$$r_L = -2I_L, \quad r_T = -2\frac{k_T}{k_L}I_T \quad (44)$$

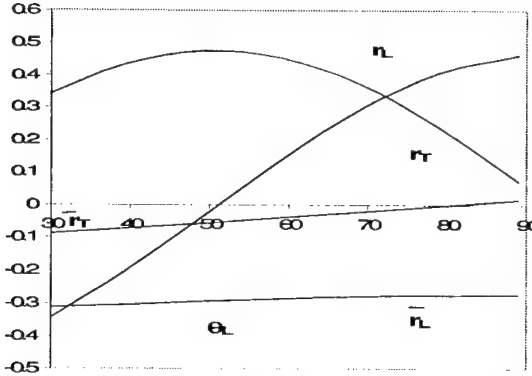


Figure 4. Dependence of first order amplitudes on the angle of incidence, θ_L , of an L-wave with $I = 1$ for $k_T/k_L = \bar{k}_T/\bar{k}_L = 2$, $\kappa = \bar{\mu}/\mu = 2$, and $\delta = 0.1$.

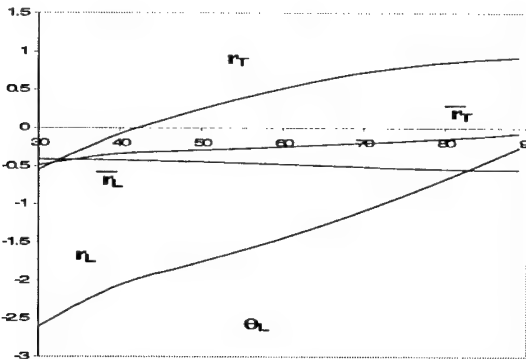


Figure 5. Dependence of first order amplitudes on the angle of incidence, θ_L , of an T-wave with $I = 1$ for $k_T/k_L = \bar{k}_T/\bar{k}_L = 2$, $\kappa = \bar{\mu}/\mu = 2$, and $\delta = 0.1$.

5. Examples for Isotropic Media

Fig. 4 shows the amplitudes of the first order waves, r_L , \bar{r}_L , r_T , \bar{r}_T , as functions of the incident angle θ_L for an L-wave of amplitude, $I = 1$. The material parameters used are: $k_T/k_L = \bar{k}_T/\bar{k}_L = 2$, $\kappa = \bar{\mu}/\mu = 2$, $\delta = 0.1$. It can be seen that r_L has a maximum at about $\theta_L = 50^\circ$.

Fig. 5 shows the first order amplitudes for the same material combination when the incident wave is a T-wave. The incidence angle θ_T is related to θ_L as $\cos \theta_T = 0.5 \cos \theta_L$ for this case.

6. Orthotropic Incompressible Media

For incompressible materials in plane strain, $\partial_1 u_1 + \partial_2 u_2 = 0$ and $\partial_3 u_3 = 0$. Assuming one of the axes of symmetry is parallel to the x_1 -axis, the stress strain relations are given by

$$\begin{aligned}\sigma_{11} &= -p + C_{11}\partial_1 u_1 + C_{12}\partial_2 u_2 \\ \sigma_{22} &= -p + C_{12}\partial_1 u_1 + C_{22}\partial_2 u_2 \\ \sigma_{12} &= C_{66}(\partial_2 u_1 + \partial_1 u_2)\end{aligned}\quad (45)$$

where p is the hydrostatic pressure (not to be confused with wave vector components p_1 and p_2) and C_{11}, C_{12}, C_{22} and C_{66} are elastic constants.

The incompressibility condition can be satisfied by expressing the displacement components in terms of a potential, ψ , as

$$u_1 = \partial_2 \psi \quad u_2 = -\partial_1 \psi \quad (46)$$

Eliminating p between the two equations of motion, (3), the potential ψ satisfies

$$\Delta^2 \psi + 4\beta \partial_1^2 \partial_2^2 \psi = \rho \Delta \ddot{\psi} / \mu \quad (47)$$

where

$$\mu = C_{66}, \quad \beta = (C_{11} + C_{22} - 2C_{12} - C_{66})/C_{66} \quad (48)$$

where, for positive definite energy density, $\mu > 0$ and $\beta > -1$.

Assuming plane harmonic solutions of the form

$$\psi = \frac{1}{i} A e^{i(\mathbf{k} \cdot \mathbf{x} - \Omega t)} \quad (49)$$

where i has been inserted to have the displacement components similar in form to those in (11), the components of the wave vector \mathbf{k} satisfies the quartic

$$k^4 + 4\beta k_1^2 k_2^2 - \omega^2 k^2 = 0, \quad (50)$$

where $\omega^2 = \rho \Omega^2 / \mu$.

Generic plots of k_1/ω versus k_2/ω (slowness curves) are shown in Fig. 6 for the case of $\beta < 0$ and for the case of $\beta > 0$.

It is known that the energy flux corresponding to any wave vector \mathbf{k} terminating on the slowness curve, is directed normal to the curve (Fedorov, 1968).

In the presence of a sinusoidal interface, as is done for the isotropic case, it is assumed that the upper medium has the parameters, $\bar{\rho}$, $\bar{\mu}$, and $\bar{\beta}$ and the lower medium, where the incident wave is traveling, has the

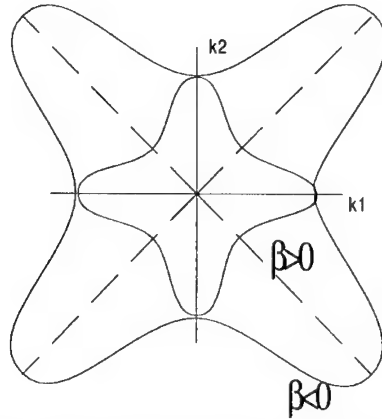


Figure 6. Generic shapes of slowness curves for the parameter $\beta < 0$ and $\beta > 0$.

parameters, ρ , μ , and β . The k_1 -components of the incident, reflected, and refracted waves are identical. For a given value of k_1 , by defining

$$k_2/k_1 = t \quad (51)$$

the quartic (50) can be written as

$$t^4 + 2(2\beta + 1)t^2 + 1 - \omega^2(t^2 + 1)/k_1^2 = 0 \quad (52)$$

From the slowness curve shown in Fig. 6 it is clear that, when $\beta > 0$ two real solutions of (52) correspond to the incident wave with the tangent of the incident angle t and the reflected primary wave with tangent $-t$. There are also two complex solutions representing surface waves. Only one of these, the one with negative imaginary part, t_2 , is admissible, in order to have the amplitude of the surface wave decaying along the negative x_2 -direction.

As shown in Fig. 7, when $\beta < 0$, there are values of k_1 for which four real solutions exist. The criteria that the energy flux must be directed towards the interface for an incident wave and away from the interface for a reflected wave rule out two of these four solutions. This has been discussed by Nair and Sotiropoulos (1997). In Fig. 7 the energy flux is directed towards the interface for incident wave vectors with their origin on the sector AB of the inner curve and also for those on CD. Interestingly, when the incident wave vectors originate from the CD-sector, the phase velocity is directed away from the interface but the energy flux is directed towards the interface. Setting $dk_1/dk_2 = 0$, the points (A and C) where the tangent is vertical can be found. This gives an allowable disjointed range for the incident angle as

$$-\cos^{-1}[(-4\beta)^{-1/4}] \leq \theta_I \leq 0 \quad \text{and} \quad \cos^{-1}[(-4\beta)^{-1/4}] \leq \theta_I \leq \pi/2 \quad (53)$$

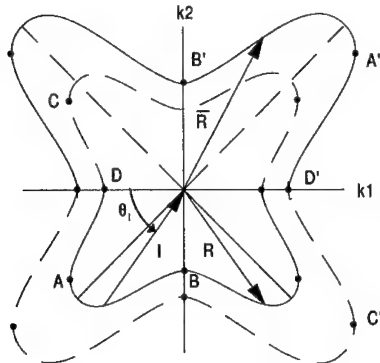


Figure 7. Generic shapes of slowness curves for the upper medium with $\bar{\beta} < 0$ (outer curve) and the lower medium with $\beta < 0$ (inner curve).

with the phase velocity having an x_1 -component directed from left to right.

In the schematic shown in Fig. 7, as the slowness curve for the upper medium encloses that for the lower medium, for each k_1 there is a real solution for \bar{k} . This establishes a unique refracted body wave. On the other hand if the slowness curve for the upper medium is inside that of the lower medium, there are values of k_1 for which real solutions for \bar{k} do not exist. This results in surface waves in the upper medium. This solution for (52)(with “barred” parameters) will be denoted by \bar{t}_1 . The second solution of (52), \bar{t}_2 for the upper medium is complex with its imaginary part positive for surface waves decaying along positive x_2 .

As before, omitting a factor of $iA\exp[i(k_1x_1 - \Omega t)]$, the stresses at the surface can be written as

$$\begin{aligned}\sigma_{11} &= 2\alpha k_1 k_2 (1 + 2\beta k_2^2/k^2) \\ \sigma_{22} &= -2\alpha k_1 k_2 (1 + 2\beta k_1^2/k^2) \\ \sigma_{12} &= \alpha (k_2^2 - k_1^2) \\ p &= \frac{k_1 k_2}{k^2} [2C_{66}(k_2^2 - k_1^2) + (C_{11} - C_{12})k_1^2 + (C_{12} - C_{22})k_1^2]\end{aligned}\quad (54)$$

Similar to what has been done in the case of isotropic media, the potential amplitude of the incident wave is denoted by \mathbf{I} , the two reflected waves by R_1 (body wave) and R_2 (surface wave), and the two refracted waves by \bar{R}_1 (body or surface wave) and \bar{R}_2 (surface wave).

The boundary conditions (20) can be written in the same form as (24) and (25) with \mathbf{I} being a scalar and the defining relations

$$\kappa = \bar{\mu}/\mu \quad (55)$$

$$\begin{aligned}\mathbf{A}_{\bar{R}}(t) &= \begin{bmatrix} 1 & 1 \\ \bar{t}_1 & \bar{t}_2 \end{bmatrix}, \\ \mathbf{A}_R(\theta) &= \begin{bmatrix} 1 & 1 \\ t_1 & t_2 \end{bmatrix}, \\ \mathbf{A}_I(\theta) &= \left\{ \begin{array}{l} 1 \\ t \end{array} \right\},\end{aligned}\tag{56}$$

and

$$\begin{aligned}\mathbf{B}_{\bar{R}}(t) &= \begin{bmatrix} \bar{t}_1^2 - 1 & \bar{t}_2^2 - 1 \\ \bar{t}_1(1 + \frac{2\bar{\beta}}{1+\bar{t}_1^2}) & \bar{t}_2(1 + \frac{2\bar{\beta}}{1+\bar{t}_2^2}) \end{bmatrix}, \\ \mathbf{B}_R(t) &= \begin{bmatrix} t_1^2 - 1 & t_2^2 - 1 \\ t_1(1 + \frac{2\beta}{1+t_1^2}) & t_2(1 + \frac{2\beta}{1+t_2^2}) \end{bmatrix}, \\ \mathbf{B}_I(\theta) &= \left\{ \begin{array}{l} t^2 - 1 \\ t(1 + \frac{2\beta}{1+t^2}) \end{array} \right\}.\end{aligned}\tag{57}$$

where $t_1 = -t$.

Having the amplitudes \mathbf{R} and $\bar{\mathbf{R}}$, the first order amplitudes are obtained from equation (21) as equations (34) and (35) with a new interpretation for ω_L as ω and

$$\begin{aligned}\mathbf{C}_I &= \left\{ \begin{array}{l} t \\ t^2 \end{array} \right\} \\ \mathbf{C}_R &= \begin{bmatrix} t_1 & t_2 \\ t_1^2 & t_2^2 \end{bmatrix} \\ \mathbf{C}_{\bar{R}} &= \begin{bmatrix} \bar{t}_1 & \bar{t}_2 \\ \bar{t}_1^2 & \bar{t}_2^2 \end{bmatrix}\end{aligned}\tag{58}$$

$$\begin{aligned}\mathbf{D}_I &= \left\{ \begin{array}{l} t(t^2 - 1) - \gamma t(1 + \frac{2\beta t^2}{1+t^2}) \\ t^2(1 + \frac{2\beta t^2}{1+t^2}) \end{array} \right\} \\ \mathbf{D}_R &= \begin{bmatrix} t_1(t_1^2 - 1) - \gamma t_1(1 + \frac{2\beta t_1^2}{1+t_1^2}) & t_2(t_2^2 - 1) - \gamma t_2(1 + \frac{2\beta t_2^2}{1+t_2^2}) \\ t_1^2(1 + \frac{2\beta t_1^2}{1+t_1^2}) & t_2^2(1 + \frac{2\beta t_2^2}{1+t_2^2}) \end{bmatrix} \\ \mathbf{D}_{\bar{R}} &= \begin{bmatrix} \bar{t}_1(\bar{t}_1^2 - 1) - \gamma \bar{t}_1(1 + \frac{2\beta \bar{t}_1^2}{1+\bar{t}_1^2}) & \bar{t}_2(\bar{t}_2^2 - 1) - \gamma \bar{t}_2(1 + \frac{2\beta \bar{t}_2^2}{1+\bar{t}_2^2}) \\ \bar{t}_1^2(1 + \frac{2\beta \bar{t}_1^2}{1+\bar{t}_1^2}) & \bar{t}_2^2(1 + \frac{2\beta \bar{t}_2^2}{1+\bar{t}_2^2}) \end{bmatrix}\end{aligned}\tag{59}$$

Solving equations (34) and (35) with the above matrices, $\bar{\mathbf{r}}$ and \mathbf{r} can be found for any combination of parameters.

As has been done for the isotropic case, reflection from a perturbed interface can be treated using the equations (38) and (39).

7. Normal Incidence for Orthotropic Incompressible Case

When $k_1 = 0$, using the notation $\kappa = \bar{\mu}/\mu$ and $\eta = \bar{\omega}/\omega$, it is seen that there is a unique reflected body wave and a unique refracted body wave with amplitudes

$$R_1 = \frac{\kappa\eta - 1}{\kappa\eta + 1} \mathbf{I}, \quad \bar{R}_1 = \frac{2}{\eta(\kappa\eta + 1)} \mathbf{I}. \quad (60)$$

For the forward scattered wave $p_1 = m$ and from the quartic (50) for the two first order reflected waves,

$$p_{21} = -\omega \left[1 - \frac{4\beta + 1}{2} \frac{m^2}{\omega^2} \right], \quad p_{22} = -im \quad (61)$$

where the second imaginary wave number indicates a surface wave (if the amplitude is nonzero). For the refracted waves,

$$\bar{p}_{21} = \bar{\omega} \left[1 - \frac{4\bar{\beta} + 1}{2} \frac{m^2}{\bar{\omega}^2} \right], \quad \bar{p}_{22} = im. \quad (62)$$

Using these in equations (56) and (57) and assuming $m/\omega \ll 1$, it is seen that the non-vanishing components are,

$$r_1 = 2 \frac{\kappa\eta - 1}{\kappa\eta + 1} \mathbf{I}, \quad \bar{r}_1 = \frac{2}{\eta} \frac{1 - \eta}{\kappa\eta + 1} \mathbf{I}, \quad (63)$$

which are identical to those given in equation (43).

8. Numerical Example for Orthotropic Case

An upper orthotropic incompressible medium with $\bar{\beta} = 1/8$ and a lower medium with $\beta = -1/2$ are considered to illustrate the reflection-refraction problem. The other parameters are: $\eta = \bar{\omega}/\omega = 2$ and $\kappa = \bar{\mu}/\mu = 2$. The slowness curve for the upper medium is convex and that for the lower medium is non-convex. With reference to Fig. 7, the wave vector for the incident wave can have an angle in the range, $CD = [-32.8^\circ, 0]$ or $AB = [32.8^\circ, 90^\circ]$. As mentioned earlier, the energy flux of the incident wave has to be directed towards the interface, that of the reflected wave towards $x_2 \rightarrow -\infty$, and that of the refracted wave towards $x_2 \rightarrow \infty$. Also, when surface

TABLE I. Zeroth and first order reflection and refraction coefficients when the incident angle is negative (parameters: $\beta = -0.5$, $\bar{\beta} = 0.125$, $\bar{\mu}/\mu = 2$, $m = 0.1$.)

| θ_I | -32.765 | -26.212 | -19.659 | -13.106 | -6.553 | 0.000 |
|---------------|---------|---------|---------|---------|--------|-------|
| $ R_1 $ | 0.00 | 0.119 | 0.249 | 0.419 | 0.656 | 1.000 |
| $ R_2 $ | 1.00 | 0.779 | 0.606 | 0.441 | 0.252 | 0.000 |
| $ \bar{R}_1 $ | 0.00 | 0.072 | 0.100 | 0.095 | 0.062 | 0.000 |
| $ \bar{R}_2 $ | 0.00 | 0.057 | 0.083 | 0.082 | 0.055 | 0.000 |
| $ r_1 $ | 0.529 | 0.353 | 0.200 | 0.146 | 0.288 | 0.580 |
| $ r_2 $ | 1.056 | 0.820 | 0.608 | 0.487 | 0.489 | 0.585 |
| $ \bar{r}_1 $ | 0.198 | 0.154 | 0.112 | 0.074 | 0.039 | 0.014 |
| $ \bar{r}_2 $ | 0.130 | 0.084 | 0.069 | 0.066 | 0.048 | 0.010 |

TABLE II. Zeroth and first order reflection and refraction coefficients when the incident angle is positive (parameters: $\beta = -0.5$, $\bar{\beta} = 0.125$, $\bar{\mu}/\mu = 2$, $m = 0.1$.)

| θ_I | 32.765 | 44.212 | 55.659 | 67.106 | 78.553 | 90.000 |
|---------------|--------|--------|--------|--------|--------|--------|
| $ R_1 $ | 1.000 | 0.340 | 0.831 | 0.665 | 0.3466 | 0.000 |
| $ R_2 $ | 0.000 | 0.542 | 0.838 | 0.945 | 1.158 | 1.000 |
| $ \bar{R}_1 $ | 0.00 | 0.070 | 0.596 | 1.397 | 2.056 | 0.000 |
| $ \bar{R}_2 $ | 0.00 | 0.080 | 0.374 | 0.247 | 0.068 | 0.000 |
| $ r_1 $ | 1.056 | 0.474 | 0.447 | 0.124 | 10.68 | 0.000 |
| $ r_2 $ | 0.529 | 0.205 | 0.492 | 0.713 | 2.761 | 0.000 |
| $ \bar{r}_1 $ | 0.130 | 0.059 | 0.528 | 0.424 | 10.85 | 0.000 |
| $ \bar{r}_2 $ | 0.200 | 0.055 | 0.053 | 0.130 | 2.971 | 0.000 |

waves are present, they must decay along the direction perpendicular to the interface.

The results of the computation are presented in Table I and II. In computing the matrix elements, it is important to select the correct roots of the quartics for k_2, \bar{k}_2, p_2 and \bar{p}_2 so that the reflected and refracted waves satisfy the energy flux criterion, namely, they are directed away from the interface and, in case of surface waves, their amplitudes decay.

9. Conclusions

The effect of a perturbed flat interface on the reflection and refraction coefficients associated with an incident plane harmonic wave is considered. The perturbation is in the form of a sinusoid with a small amplitude relative to the wave length of the incident wave. Two different classes of linear elastic materials are studied. The first class consists of two different isotropic materials on the upper and lower sides of the interface and the second class consists of two different orthotropic incompressible materials. From an inspection of the reflected or refracted amplitudes and the corresponding wave vector directions the amplitude and the wave length of the sinusoidal perturbation can be inferred. Conversely, for a well defined interface the anisotropy of the elastic medium may be inferred. Numerical examples are provided to illustrate the effect of the perturbed interface on the first order corrections to the flat interface problem.

References

Chandler-Wilde, S. N., Ross, C. R., and Zhang, B., 1999, "Scattering by Infinite One-dimensional Rough Surfaces," Proc. R. Soc. Lond. A, 455, pp. 3767-3787.

Fedorov, F.I., 1968, Theory of Elastic Waves in Crystals, Plenum Press, New York.

Mal, A. K., 1962, "Dispersion of Love Waves in Spherical Earth with Corrugated Surface," Pure and Applied Geophysics, 53, No. 3, pp. 25-44.

Markenscoff, X. and Lekoudis, S. G., 1976, "Love Waves in Slowly Varying Layered Media," Pure and Applied Geophysics, 114, No. 5, pp. 805-810.

Nagy, P. B. and Rose, J. H., 1993, "Surface Roughness and the Ultrasonic Detection of Subsurface Scatterers," Journal of Applied Physics, 73, No. 2, pp. 566-580.

Nair, S. and Sotiropoulos, D., 1997, "Elastic Waves in Orthotropic Incompressible Materials and Reflection from an Interface," J. Acoustic Society of America, 102, No. 1, pp. 102-107.

Nair, S. and Sotiropoulos, D., 1999a, "Interfacial Waves in Incompressible Monoclinic Materials with an Interlayer," Mechanics of Materials, 31, pp. 225-233.

Pecorari, C., Mendelsohn, D. A., and Adler, L., 1995, "Ultrasonic Wave Scattering from Rough Imperfect Interfaces, Part II. Incoherent and Coherent Scattered Fields," Journal of Nondestructive Evaluation, 14, No. 1, pp. 117-126.

Sotiropoulos, D. and Nair, S., 1999b, "Elastic Waves in Monoclinic Incompressible Materials and Reflection from an Interface," J. Acoustic Society of America, 105, No. 5, pp. 2981-2983.

THE EFFECT OF STRESS ON INTERFACIAL WAVES IN ELASTIC COMPRESSIBLE INTERLAYERS

D. A. SOTIROPOULOS
*Southern Polytechnic State University
Marietta, GA 30060, USA*

C. G. SIFNIOTOPoulos
*Northwestern University
Evanston, IL 60208, USA*

Abstract. The characteristics of elastic interfacial waves in pre-stressed compressible interlayers are examined. The interlayer is separated from an infinite surrounding solid of a generally different non-linear elastic compressible material by planar parallel boundaries. The underlying stress conditions in the two solids are homogeneous with their underlying finite strain having common principal axes, one axis being normal to the planar interfaces. For arbitrary materials and otherwise arbitrary stress, the dispersion equation of superposed small amplitude waves is derived in explicit form for propagation along a principal pre-strain axis lying on an interfacial plane. Analysis of the dispersion equation reveals the characteristics of propagating waves. In respect of the solids' material and pre-stress parameters, single or multiple mode propagation occurs or no propagation at all. The propagation characteristics are classified into categories defined by the material and pre-stress parameters. For wavelengths large as compared to the interlayer thickness, the interfacial wave speed is derived in explicit form yielding parameter conditions for the non-existence of interfacial waves. The bifurcation equation, a limiting case of the dispersion equation, is also examined yielding standing waves as solutions which define the boundaries of stability for the propagating waves. Graphical illustrations are also presented based on numerical computations for Blatz-Ko materials.

1. Introduction

Understanding of the propagating and standing interfacial wave characteristics of layered stressed solids is of significance in several areas of applications such as the ultrasonic non-destructive evaluation and characterization of materials, their interfaces and stress conditions, the design of vibration isolators, and the processing of electronic signals. Of particular attention, here, is the study of non-linear elastic layered materials as are, for example, rubber-like materials and biological tissues.

The layered structure considered is composed of a layer imbedded in an infinite solid, each under finite strain, and subsequently superposed by a small dynamic stress state resulting to the generation of interfacial waves propagating parallel to the planar boundaries separating the two solids. The goal of the present study is to understand the propagation characteristics and the dependence of wave speed on frequency, material parameters and pre-stress conditions. To make the mathematics tractable, the case considered is such that the principal axes of pre-strain are common in the two solids,

with one of them being perpendicular to the planar interfaces. Moreover, propagation is considered along one of the principal pre-strain axes. For such a case, a detailed analysis is performed that reveals the propagation and standing wave characteristics.

The analogous to the case of the present study but with incompressible materials was considered by the present authors, Sotiropoulos and Sifniotopoulos (1995). When the materials are compressible, as is the case here, several cases dealt with previously in the literature are obtained as limiting cases of the present study. When the interlayer material becomes vacuum, Rayleigh-type waves result in a pre-stressed half-space, a problem first examined by Hayes and Rivlin (1961) and for more general pre-stress conditions by Dowaikh and Ogden (1991). When the surrounding infinite material becomes vacuum, the structure under consideration here reduces to a plate of arbitrary thickness in one direction and of infinite extent in the other direction. For waves propagating along the infinite plate dimension, the dependence of the wave speed on pre-stress parameters was investigated by Roxburgh and Ogden (1994). When the thickness of the interlayer is large as compared with the wavelengths, the problem under consideration here reduces to one of Stoneley-type waves in two semi-infinite pre-stressed solids. This will be dealt with in the present paper as the limit of high frequency waves. The simple case of equibiaxial in-plane deformations was examined by one of the present authors, Sotiropoulos (2000).

2. Mathematical Formulation

An interlayer of arbitrary uniform thickness embedded in an infinite solid is considered. The two solids are of pre-stressed compressible non-linear elastic and isotropic materials and they are subjected to pure homogeneous finite strains. The principal strain directions in the two solids are aligned, one direction being normal to the two planar interfaces. The interlayer lies between $x_2=0$ and $x_2=-h$, with h denoting its thickness, in a rectangular Cartesian coordinate system (x_1, x_2, x_3) the axes of which coincide with the principal strain directions. The principal stretches are denoted by $\lambda_1, \lambda_2, \lambda_3$ and $\lambda_1^*, \lambda_2^*, \lambda_3^*$ for the surrounding solid and interlayer respectively. Herewith, all quantities referring to the interlayer will be superscripted by a star (*). The compressibility of the two materials gives

$$\lambda_1\lambda_2\lambda_3=J, \quad \lambda_1^*\lambda_2^*\lambda_3^*=J^* \quad (1)$$

where $J=\rho_r/\rho$ with ρ_r and ρ the densities before and after the strain is applied.

On the underlying deformations is superposed a time harmonic interfacial wave of small amplitude propagating along the positive x_1 -axis on the upper interfacial boundary. Motion is considered in the (x_1, x_2) -plane with velocity components v_1, v_2 independent of x_3 . The interfacial wave below, inside and above the interlayer is represented respectively by the velocities

$$\left. \begin{aligned} v_1 &= A \exp(s k x_2 - i k x_1 + i \omega t) \\ v_2 &= B \exp(s k x_2 - i k x_1 + i \omega t) \end{aligned} \right\} \quad x_2 \leq -h \quad (2)$$

$$\left. \begin{array}{l} v_1^* = A^* \exp(s^* kx_2 - ikx_1 + i\omega t) \\ v_2^* = B^* \exp(s^* kx_2 - ikx_1 + i\omega t) \end{array} \right\} \begin{array}{l} -h \leq x_2 \leq 0 \\ \end{array} \quad (3)$$

$$\left. \begin{array}{l} v'_1 = A' \exp(-skx_2 - ikx_1 + i\omega t) \\ v'_2 = B' \exp(-skx_2 - ikx_1 + i\omega t) \end{array} \right\} \begin{array}{l} x_2 \geq 0 \\ \end{array} \quad (4)$$

where $k = \omega/c$ is the wavenumber, ω being the circular frequency, and c the phase speed to be determined together with s and s^* . A, B, A^*, B^*, A', B' are arbitrary constants within the context of incremental infinitesimal motion. By definition, the interfacial wave must decay, that is, v_1, v_2 must vanish as $x_2 \rightarrow \infty$ and v'_1, v'_2 must also vanish as $x_2 \rightarrow -\infty$. Therefore, s must have positive real part. No requirement is placed *ab initio* on s^* unless $kh \rightarrow \infty$ in which case s^* must also have positive real part. For the underlying solid, the component equations of motion are:

$$\alpha_{11}v_{1,11} + \gamma_2 v_{1,22} + \delta v_{2,12} = \rho_r v_{1,tt} \quad (5)$$

$$\delta v_{1,12} + \gamma_1 v_{2,11} + \alpha_{22} v_{2,22} = \rho_r v_{2,tt}$$

where, i symbolizes $\partial/\partial x_i$ and

$$\alpha_{ij} = JA_{0ijij}, \quad \gamma_1 = JA_{01212}, \quad \gamma_2 = JA_{02121} \quad (6)$$

$$\delta = \alpha_{12} + \gamma_2 - J\sigma_2 \quad 2\beta = \alpha_{11}\alpha_{22} + \gamma_1\gamma_2 - \delta^2$$

$$JA_{0ijij} = \gamma_i \gamma_j [\partial^2 W / (\partial \lambda_i \partial \lambda_j)] \quad (7)$$

$$JA_{0ijij} = \begin{cases} \left[\lambda_i (\partial W / \partial \lambda_i) - \lambda_j (\partial W / \partial \lambda_i) \right] \lambda_i^2 / (\lambda_i^2 - \lambda_j^2) & i \neq j, \quad \lambda_i \neq \lambda_j \\ 1/2 \left[JA_{0iiii} - JA_{0ijij} + \lambda_i (\partial W / \partial \lambda_i) \right] & i \neq j, \quad \lambda_i = \lambda_j \end{cases} \quad (8)$$

$$A_{0ijji} = A_{0jiji} = A_{0jjij} - \sigma_i \quad (9)$$

in which σ_i are the principal Cauchy stresses and are given as

$$J\sigma_i = \lambda_i (\partial W / \partial \lambda_i) \quad (10)$$

with $W(\lambda_1, \lambda_2, \lambda_3)$ being the strain energy density function after deformation. Necessary and sufficient conditions for the material constants of equation (5) to be strongly elliptic are (Dowaikh and Ogden, 1991)

$$\alpha_{11} > 0, \quad \alpha_{22} > 0, \quad \gamma_1 > 0, \quad \gamma_2 > 0 \quad (11)$$

$$[(\alpha_{11}\alpha_{22})^{1/2} + (\gamma_1\gamma_2)^{1/2}]^2 - \delta^2 > 0 \quad (12)$$

Eliminating one of the velocities in (5) gives

$$\begin{aligned} \alpha_{11}\gamma_1 v_{m,1111} + 2\beta v_{m,1122} + \alpha_{22}\gamma_2 v_{m,2222} = \\ \rho_r (\alpha_{11} + \gamma_1) v_{m,11tt} + \rho_r (\alpha_{22} + \gamma_2) v_{m,22tt} - \rho_r^2 v_{m,tttt} \end{aligned} \quad (13)$$

for $m = 1$ or 2 . Substitution of one of (2) in (13) results in

$$\alpha_{22}\gamma_2 s^4 - [2\beta - \rho_r c^2 (\alpha_{22} + \gamma_2)] s^2 + (\alpha_{11} - \rho_r c^2)(\gamma_1 - \rho_r c^2) = 0 \quad (14)$$

Equation (14) gives two solutions s_1^2 and s_2^2 as

$$\begin{aligned} s_1^2 + s_2^2 &= [2\beta - \rho_r c^2 (\alpha_{22} + \gamma_2)] / (\alpha_{22}\gamma_2) \\ s_1 s_2 &= [(\alpha_{11} - \rho_r c^2)(\gamma_1 - \rho_r c^2)] / (\alpha_{22}\gamma_2) \end{aligned} \quad (15)$$

from which we see that s_1^2, s_2^2 are either real or complex conjugates. This is equivalent to the product and the sum of s_1, s_2 being positive. This yields, that in order to have a diminishing wave as $|x_2| \rightarrow \infty$,

$$\alpha_{11} > \gamma_1, \quad 0 \leq c^2 \leq \begin{cases} \gamma_1 / \rho_r, & \bar{\delta}^2 \leq \bar{\alpha}_{22} (\bar{\alpha}_{11} - 1) \\ (\gamma_1 - \alpha_{11} \eta_L^2) / [\rho_r (1 - \eta_L^2)], & \bar{\delta}^2 > \bar{\alpha}_{22} (\bar{\alpha}_{11} - 1) \end{cases} \quad (16)$$

$$\alpha_{11} < \gamma_1, \quad 0 \leq c^2 \leq \begin{cases} \alpha_{11}/\rho_r, \quad \bar{\delta}^2 \leq 1 - \bar{\alpha}_{11} \\ (\gamma_1 - \alpha_{11}\eta_L^2)/[\rho_r(1 - \eta_L^2)], \quad \bar{\delta}^2 > 1 - \bar{\alpha}_{11} \end{cases} \quad (17)$$

where

$$\eta = [(\gamma_1 - \rho_r c^2) / (\alpha_{11} - \rho_r c^2)]^{1/2}, \quad \eta^* = [(\gamma_1^* - \rho_r^* c^2) / (\alpha_{11}^* - \rho_r^* c^2)]^{1/2} \quad (18)$$

and $\eta_L = \eta$ at $s_1 + s_2 = 0$. Equations (16), (17) define the upper bounds of the interfacial phase speed. Moreover, these upper bounds correspond to phase speeds of body waves in a pre-stressed infinite material and whose energy flux vector is along the x_1 -axis (parallel to the interfacial boundary for the problem under consideration). In addition, the upper equations of (16), (17) define phase speeds of body waves whose wave vector is also along the x_1 -axis, whereas the lower equation of (16), (17) correspond to body waves with a wave vector at an angle to the x_1 -axis. For the properties of body waves in a pre-stressed infinite material the reader is referred to the recent work of Ogden and Sotiropoulos (1998).

Substitution of (2) in (5) yields

$$\begin{aligned} v_1 &= [A_1 \exp(s_1 kx_2) + A_2 \exp(s_2 kx_2)] \exp[i(\omega t - kx_1)] \\ v_2 &= [B_1 \exp(s_1 kx_2) + B_2 \exp(s_2 kx_2)] \exp[i(\omega t - kx_1)] \end{aligned} \quad (19)$$

with

$$is_m \delta B_m = (\rho_r c^2 + \gamma_2 s_m^2 - \alpha_{11}) A_m, \quad m = 1, 2 \quad (20)$$

The same hold for the overlying solid but with primed quantities and also s replaced by $-s$. For the interlayer we have

$$\begin{aligned} v_1^* &= [A_1^* \exp(s_1^* kx_2) + A_2^* \exp(s_2^* kx_2) \\ &\quad + A_3^* \exp(s_3^* kx_2) + A_4^* \exp(s_4^* kx_2)] \exp[i(\omega t - kx_1)] \\ v_2^* &= [B_1^* \exp(s_1^* kx_2) + B_2^* \exp(s_2^* kx_2) \\ &\quad + B_3^* \exp(s_3^* kx_2) + B_4^* \exp(s_4^* kx_2)] \exp[i(\omega t - kx_1)] \end{aligned} \quad (21)$$

with

$$\begin{aligned} i s_m^* \delta^* B_m^* &= (\rho_r^* c^2 + \gamma_2^* s_m^{*2} - \alpha_{11}^*) A_m^*, & m = 1, 2, 3, 4 \\ s_3^* &= -s_1^*, \quad s_4^* = -s_2^* \end{aligned} \quad (22)$$

3. The Dispersion Equation

The dispersion equation will be obtained on use of the boundary conditions on the two interfacial planes, $x_2 = 0$ and $x_2 = -h$. The interlayer is assumed to be welded to the infinite solid, and thus the velocity and traction rate are continuous across the two interfaces. The relevant components of the traction rate in the underlying solid are given by

$$\begin{aligned} S_{021} &= [(\gamma_2 / J) - \sigma_2] v_{2,1} + (\gamma_2 / J) v_{1,2} \\ S_{022} &= (\alpha_{12} / J) v_{1,1} + (\alpha_{22} / J) v_{2,2} \end{aligned} \quad (23)$$

Substitution of (19)-(22) and of the corresponding ones for the overlying solid in the boundary conditions results in a set of eight linear algebraic homogeneous equations for the eight independent unknown constants (coefficients) $A_1, A_2, A_1', A_2', A_1^*, A_2^*, A_3^*, A_4^*$. For a nontrivial solution the determinant of the coefficients must vanish yielding the dispersion equation. However, it is the purpose of the present paper to analyze the propagation characteristics. Therefore, in order to analyze the dispersion equation, it is necessary to have it in explicit form. Carrying out the operations in the determinant and simplifying, we obtain the dispersion equation in the following form

$$\begin{aligned} N &= [C^2(\eta, \eta^*, \sigma, r) + D^2(\eta, \eta^*, r)(s_1^* + s_2^*)^2] \\ &\quad [\sinh^2(\frac{1}{2}kh(s_1^* + s_2^*)) / (s_1^* + s_2^*)^2] \\ &- [C^2(\eta, -\eta^*, \sigma, r) + D^2(\eta, -\eta^*, r)(s_1^* - s_2^*)^2] \\ &\quad [\sinh^2(\frac{1}{2}kh(s_1^* - s_2^*)) / (s_1^* - s_2^*)^2] \\ &+ C(\eta, \eta^*, \sigma, r) D(\eta, \eta^*, r) \sinh[kh(s_1^* + s_2^*)] / (s_1^* + s_2^*) \\ &- C(\eta, -\eta^*, \sigma, r) D(\eta, -\eta^*, r) \sinh[kh(s_1^* - s_2^*)] / (s_1^* - s_2^*) \\ &+ E(\eta, -\eta^*, r) = 0 \end{aligned} \quad (24)$$

where the coefficients of (24) are defined by

$$\begin{aligned}
C(\eta, \eta^*, \sigma, r) = & \bar{\gamma}_1 [(\eta / \bar{a}_{22}^{1/2}) + 1] f^*(\eta^*, \sigma^*) / (1 - \eta^{*2}) \\
& + r^2 \bar{\gamma}_1 [(\eta^* / \bar{a}_{22}^{*1/2}) + 1] f(\eta, \sigma) / (1 - \eta^2) \\
& + 2r \bar{\gamma}_1^{1/2} \bar{\gamma}_1^{*1/2} [(1 - \sigma) / \bar{\gamma}_1^{1/2} - (\bar{a}_{12} / \bar{a}_{22}^{1/2}) \eta] \cdot \\
& [(1 - \sigma^*) / \bar{\gamma}_1^{*1/2} - (\bar{a}_{12}^* / \bar{a}_{22}^{*1/2}) \eta^*]
\end{aligned} \quad (25)$$

$$D(\eta, \eta^*, r) = r (\bar{a}_{22}^{1/2} \eta + \bar{a}_{22}^{*1/2} \eta^*) (s_1 + s_2) \quad (26)$$

$$E(\eta, \eta^*, r) = 4r^2 \bar{a}_{22}^{1/2} \eta \bar{a}_{22}^{*1/2} (s_1 + s_2)^2 \quad (27)$$

in which

$$\begin{aligned}
f(\eta, \sigma) = & (\bar{a}_{12}^2 / \bar{a}_{22}^{1/2}) \eta^3 + [\bar{a}_{11} - 1 + (1 - \sigma)^2 / \bar{\gamma}_1] \eta^2 \\
& + [[\bar{a}_{22} (\bar{a}_{11} - 1) - \bar{a}_{12}^2] / \bar{a}_{22}^{1/2}] \eta - (1 - \sigma)^2 / \bar{\gamma}_1
\end{aligned} \quad (28)$$

$$\begin{aligned}
(s_1 + s_2)^2 = & (\bar{\gamma}_1 / \bar{a}_{22}) \cdot [(\bar{a}_{11} - 1 + \bar{\delta}^2) \eta^2 \\
& + 2 \bar{a}_{22}^{1/2} (\bar{a}_{11} - 1) \eta + \bar{a}_{22} (\bar{a}_{11} - 1) - \bar{\delta}^2] / (1 - \eta^2)
\end{aligned} \quad (29)$$

with

$$\begin{aligned}
\bar{a}_{11} = & \bar{a}_{11} / \bar{\gamma}_1, \quad \bar{a}_{22} = \bar{a}_{22} / \bar{\gamma}_2, \quad \bar{\delta} = \delta / (\bar{\gamma}_1 \bar{\gamma}_2)^{1/2}, \\
\bar{\gamma}_1 = & \gamma_1 / \bar{\gamma}_2, \quad \bar{a}_{12} = a_{12} / (\gamma_1 \bar{\gamma}_2)^{1/2}, \quad \sigma = J \sigma_2 / \bar{\gamma}_2
\end{aligned} \quad (30)$$

and

$$r = \gamma_2 J^*/(\gamma_2^* J) \quad (31)$$

η^* can be written in terms of η as

$$\begin{aligned}
\eta^{*2} = & [(R \bar{a}_{11} - 1) \eta^2 + 1 - R] / [(R \bar{a}_{11} - \bar{a}_{11}^*) \eta^2 + \bar{a}_{11}^* - R], \\
R = & \gamma_1 \rho_r^* / (\gamma_1^* \rho_r)
\end{aligned} \quad (32)$$

When the interlayer material becomes vacuum ($\gamma_2^* \rightarrow 0$) the dispersion equation (24) becomes a secular equation independent of frequency, kh, and it is

$$f(\eta, \sigma) = 0 \quad (33)$$

This is identical to the equation obtained by Dowaikh and Ogden (1991) governing the propagation of surface waves in a pre-stressed compressible half-space.

When the surrounding material becomes vacuum then equation (24) yields

$$\begin{aligned} f^*(\eta^*, \sigma^*) \sinh [\frac{1}{2} kh (s_1^* + s_2^*)] / (s_1^* + s_2^*) = \\ \pm f^*(-\eta^*, \sigma^*) \sinh [\frac{1}{2} kh (s_1^* - s_2^*)] / (s_1^* - s_2^*) \end{aligned} \quad (34)$$

which is identical to the equation obtained by Roxburgh and Ogden (1994) for the frequency equation in a plate.

For high frequency interfacial waves, $kh \rightarrow \infty$, the dispersion equation (24) yields

$$\begin{aligned} \varphi(c) = & [(\eta / \bar{\alpha}_{11}^{1/2}) + 1] [f(\eta^*, \sigma^*) / (1 - \eta^{*2})] \bar{\gamma}_1^* \\ & + r(s_1 + s_2)(s_1^* + s_2^*) (\bar{\alpha}_{22}^{1/2} \eta + \bar{\alpha}_{22}^{*1/2} \eta^*) \\ & + 2r(\bar{\gamma}_1 \bar{\gamma}_1^*)^{1/2} [(1 - \sigma) / \bar{\gamma}_1^{1/2} - (\bar{\alpha}_{12} / \bar{\alpha}_{22}^{1/2}) \eta^*] \cdot \\ & [(1 - \sigma^*) / \bar{\gamma}_1^{*1/2}] - (\bar{\alpha}_{12}^* / \bar{\alpha}_{22}^{*1/2}) \eta^* \\ & + r^2 \bar{\gamma}_1 [\eta^* / \bar{\alpha}_{22}^{*1/2} + 1] f(\eta, \sigma) / (1 - \eta^2) = 0 \end{aligned} \quad (35)$$

which is the secular equation governing the propagation of Stoneley-type waves in two pre-stressed half-spaces. One of the half-spaces is of the same material as that of the original surrounding solid and the other half-space is of the same material as that of the original interlayer. In fact, equation (35) determines the asymptotic solutions for high frequency interfacial waves. It can be shown that the necessary and sufficient condition for the existence of a high frequency solution and, in fact, unique is $\varphi(0)\varphi(c_{\max}) < 0$, with c_{\max} defined in (16)-(19). Particular attention will now be focused on equibiaxial in-plane deformations, $\lambda_1 = \lambda_2$, $\lambda_1^* = \lambda_2^*$. It can be shown that if the densities of the two materials are the same after deformation, $\rho = \rho^*$, and $\bar{\alpha} < 1$ or/and $\bar{\alpha}^* < 1$, then interfacial waves may exist depending on the material and pre-stress parameters. It can also be shown that if $\rho = \rho^*$ and $\bar{\alpha} > 1$, $\bar{\alpha}^* > 1$ then interfacial waves cannot exist; this includes Stoneley's result for stress-free materials. Furthermore, if $\rho \neq \rho^*$, $R=1$ and $\bar{\alpha} > 1$, $\bar{\alpha}^* > 1$ interfacial waves exist; this includes Stoneley's result where the two materials

are stress-free and have equal shear wave speeds. In addition, if $\rho \neq \rho^*$, $\bar{\alpha} < 1$, $\bar{\alpha}^* < 1$ then interfacial waves exist only if r satisfies $(1 - \bar{\alpha}^*)/(1 + \bar{\alpha}^*) < r < (1 + \bar{\omega})/(1 - \bar{\alpha})$.

4. Interlayer of Small Thickness

When the interlayer thickness is small compared to the wavelength, $kh \ll 1$, the dispersion equation (24), to the first power in kh , gives

$$2 \bar{a}_{22}^{1/2} \eta (s_1 + s_2) + g(\eta, \sigma, r, R) \kappa = 0 \quad (36)$$

where

$$\begin{aligned} g(\eta, \sigma, r, R) = & r^2 \bar{\gamma}_1 [(\bar{a}_{22}^{1/2} \eta / \bar{a}_{22}^*) + 1] f(\eta, \sigma) / (1 - \eta^2) \\ & + 2r \bar{\gamma}_1^{*1/2} \bar{\gamma}_1^{1/2} [(1 - \sigma) / \bar{\gamma}_1^{1/2} - (\bar{a}_{12} / \bar{a}_{22}^{1/2}) \eta] \cdot \\ & [(1 - \sigma^*) \bar{\gamma}_1^{*1/2} - \bar{a}_{22}^{1/2} \bar{a}_{12}^* / \bar{a}_{22}^*] \end{aligned} \quad (37)$$

with $\kappa = kh / r$. It is revealing to consider further the case $\bar{\alpha}_{11} > 1$ and $\bar{\delta}^2 \leq \bar{\alpha}_{22} (\bar{\alpha}_{11} - 1)$. Then, at $\kappa = 0$ the only solution of (36) is $\eta = 0$. Thus, the η that satisfies the dispersion equation can be written to the first power in κ as $\eta = \eta_1 \kappa$. This, upon substitution in (36) yields

$$\eta_1 = \frac{1}{2} \bar{\gamma}_1^{-1/2} [\bar{a}_{22} (\bar{\alpha}_{11} - 1) - \bar{\delta}^2]^{-1/2} [\bar{\gamma}_1^* (R - 1) + (1 - r)^2] \quad (38)$$

The phase speed is subsequently derived from (18) as

$$c = c_L [1 - \eta_1^2 \kappa^2 (\bar{\alpha}_{11} - 1) / 2] \quad (39)$$

However, to satisfy the decay conditions η must be positive. Therefore, interfacial waves cannot propagate when

$$\bar{\gamma}_1^* (R - 1) + (1 - r)^2 \leq 0 \quad (40)$$

or, equivalently, when

$$R \leq 1 \text{ and } \max \{0, 1 - [\bar{\gamma}_1^* (1 - R)]^{1/2}\} \leq r \leq 1 + [\bar{\gamma}_1^* (1 - R)]^{1/2} \quad (41)$$

Necessary conditions to satisfy (40) or (41) are

$$R \leq 1 \text{ and } r \leq 1 + \bar{\gamma}_1^{*1/2} \quad (42)$$

The above simple but important conditions define material and pre-stress parameters to be used for design criteria as well as for non-destructive evaluation and characterization. For equibiaxial in-plane deformations as well as for materials that are not pre-stressed ($\gamma_1^* = 1$), it is concluded from (42) that $R > 1$ or $r > 2$ guarantees the propagation of low-frequency interfacial waves. From the opposite point of view, in order not to allow propagating interfacial waves, it is necessary that $R < 1$ and $r < 2$.

If, however, $\bar{\alpha}_{11} > 1$ and $\bar{\delta}^2 > \bar{\alpha}_{22}(\bar{\alpha}_{11} - 1)$ or $\bar{\alpha}_{11} < 1$ and $\bar{\delta}^2 > 1 - \bar{\alpha}_{11}$ then at $\kappa = 0$ the only solution of (36) is $\eta = \eta_L$, where η_L is the solution $s_1 + s_2 = 0$ and is given by

$$\eta_L = [-\bar{\alpha}_{22}^{1/2} (\bar{\alpha}_{11} - 1) + \sqrt{|\bar{\delta}| [\bar{\delta}^2 - (\bar{\alpha}_{11} - 1)(\bar{\alpha}_{22} - 1)]^{1/2}}] / (\bar{\delta}^2 + \bar{\alpha}_{11} - 1) \quad (43)$$

In this cases, and for small kh , η may be expressed as $\eta = \eta_L + \eta_2 \kappa^2$. Then, to obtain η_2 the dispersion equation must be considered up to the second power in kh resulting to a second degree algebraic equation for η_2 . The phase speed is subsequently given as

$$c = c_0 [1 - \eta_L \eta_2 \kappa^2 (\bar{\alpha}_{11} - 1) \gamma_1 / \rho_r c_0^2 (1 - \eta_L^2)^2] \quad (44)$$

where c_0 is the phase speed that satisfies $s_1 + s_2 = 0$ and is given by

$$c_0^2 = c_L^2 (1 - \bar{\alpha}_{11} \eta_L^2) / (1 - \eta_L^2) \quad (45)$$

Finally, if $\bar{\alpha}_{11} < 1$ and $\bar{\delta} \leq 1 - \bar{\alpha}_{11}$ then at $\kappa = 0$, equation (36) has no solution that satisfies the decay condition.

5. Standing Waves

Standing waves represent quasi-static interfacial deformations and are given as solutions of the bifurcation equation, which is a limiting case of the dispersion equation when $\omega \rightarrow 0$, $c \rightarrow 0$ and kh arbitrary. The bifurcation equation not only provides conditions on material and pre-stress parameters for the existence of standing waves but also has a strong influence on interfacial wave motion. For given material and pre-stress parameters satisfaction of the bifurcation equation gives those values of kh for which stopping bands of propagating interfacial waves either begin or end. Numerical results on this will be presented in the next section.

6. Numerical Results and Discussion

The numerical examples deal with Blatz-Ko materials whose strain energy function is

$$W = \frac{1}{2} \mu (\lambda_1^{-2} + \lambda_2^{-2} + \lambda_3^{-2} + 2J - 5) \quad (46)$$

from which we obtain

$$\alpha_{11} = 3\mu/\lambda_1^2, \quad \alpha_{22} = 3\mu/\lambda_2^2, \quad \gamma_1 = \mu/\lambda_2^2, \quad \gamma_2 = \mu/\lambda_1^2, \quad \alpha_{12} = \mu J \quad (47)$$

and

$$J\sigma_i = \mu(J\lambda_i^2 - 1)/\lambda_i^2, \quad i = 1, 2, 3 \quad (48)$$

In Fig. 1, the surrounding solid is stress-free whereas the interlayer is deformed in the same plane as that of the superimposed interfacial wave motion, that is, $\lambda_3^* = 1$. This results in $\lambda_2^* = \lambda_1^{*-1/3}$. The strong ellipticity condition is always satisfied for the surrounding solid whereas for the interlayer it requires that $0.3724 < \lambda_1^* < 2.6851$. In Fig. 1(a), for $\lambda_1^* = 0.8$, the interfacial wave characteristics are classified into three regimes depending on the values of r and R . In regime (0) propagating interfacial waves cannot exist at small frequencies in accordance with the inequality (40). In fact, they do not exist at any frequency. In regime (I), there is propagation at small frequencies but no propagation at high frequencies, that is, Stoneley-type waves do not exist. In regime (II), there is a high frequency asymptote and since this regime does not intersect with regime (0), there is propagation for all frequencies. Figures 1(b), 1(c), 1(d), 1(e) show the dependence of η on the non-dimensional wavenumber, kh , in the different regimes of Fig. 1(a). Note that in regime (I), there is a single or multiple mode propagation depending on whether R is smaller or larger than unity.

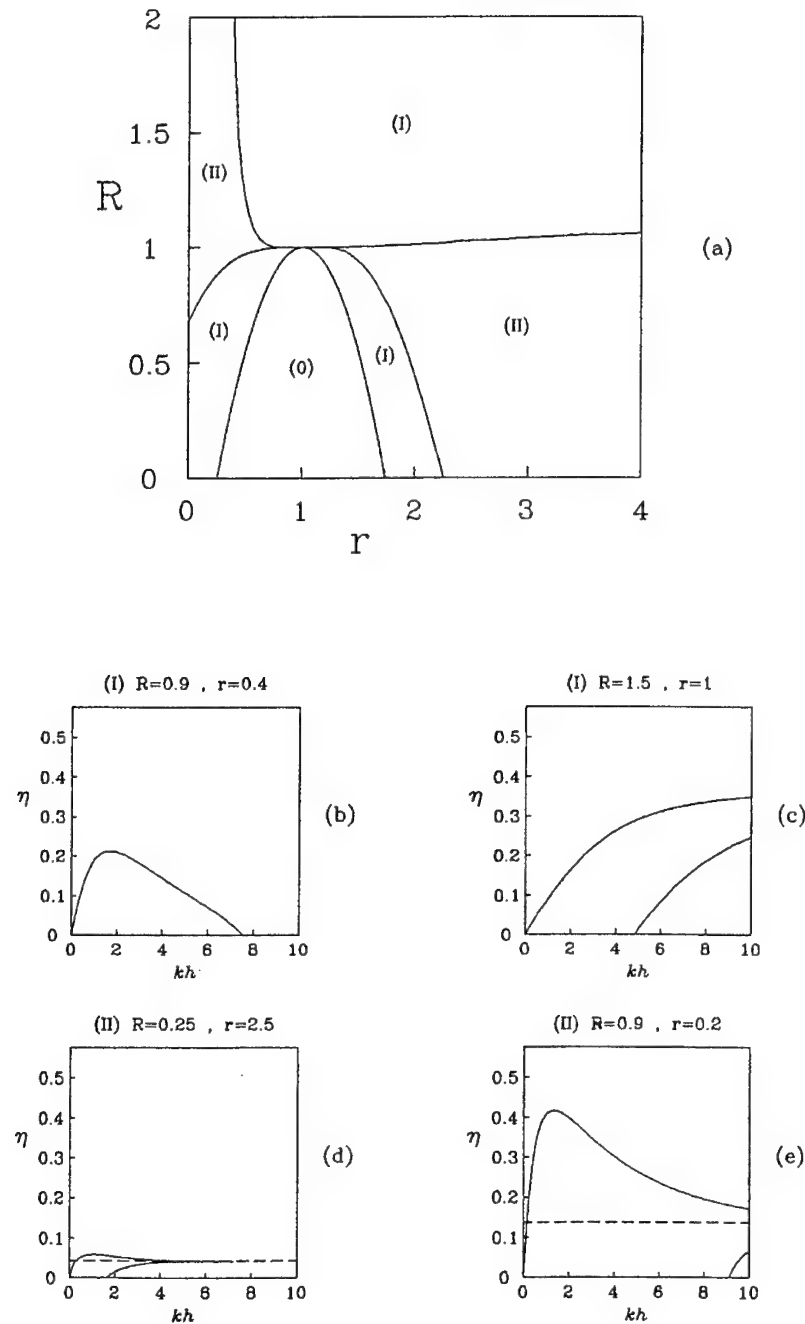


Figure 1. Blatz-Ko materials with a stress-free surrounding solid and an interlayer with in-plane underlying deformations and with $\lambda_1 = 0.8$. (a) Regions of existence of propagating interfacial waves for different r , R values: (0) no propagation, (I) no high frequency propagation, (II) one high frequency asymptote. (b), (c), (d), (e) Dependence of the non-dimensional phase speed parameter, η , on the non-dimensional wavenumber, kh .

For comparison, Fig. 2 is presented in which both the interlayer and the surrounding solid are stress-free resulting to Poisson materials (equal Lame' constants). The absence of stress is demonstrated quantitatively to have a significant effect on the frequency regions of existence of interfacial propagating waves as well as on the dependence of phase speed on frequency.

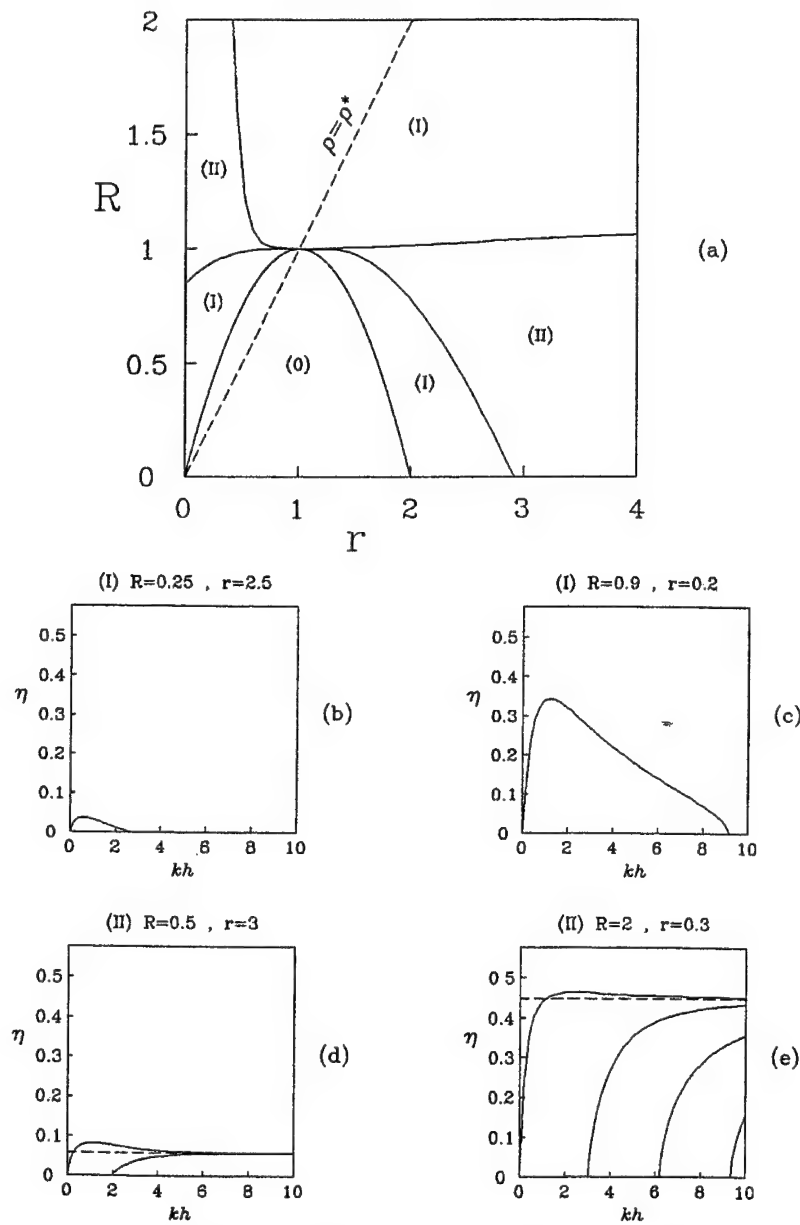


Figure 2. Same as the caption of Fig. 1 but with a stress-free interlayer as well.

In Fig. 3, both materials are stressed but only along the x_2 -axis which is perpendicular to the interfaces. This implies that $\lambda_1=\lambda_3$, $\lambda_2=\lambda_1^{-1}$. The same holds true for the interlayer stretches as well. Figure 3 represents the case $\lambda_1=0.9$, which together with the strong ellipticity condition requires that $r<1.4251$. In Fig. 3(a) the shaded area violates this condition. Figures 3(b), 3(c), 3(d), 3(e) show the η dependence on kh in the different regimes of Fig. 3(a).

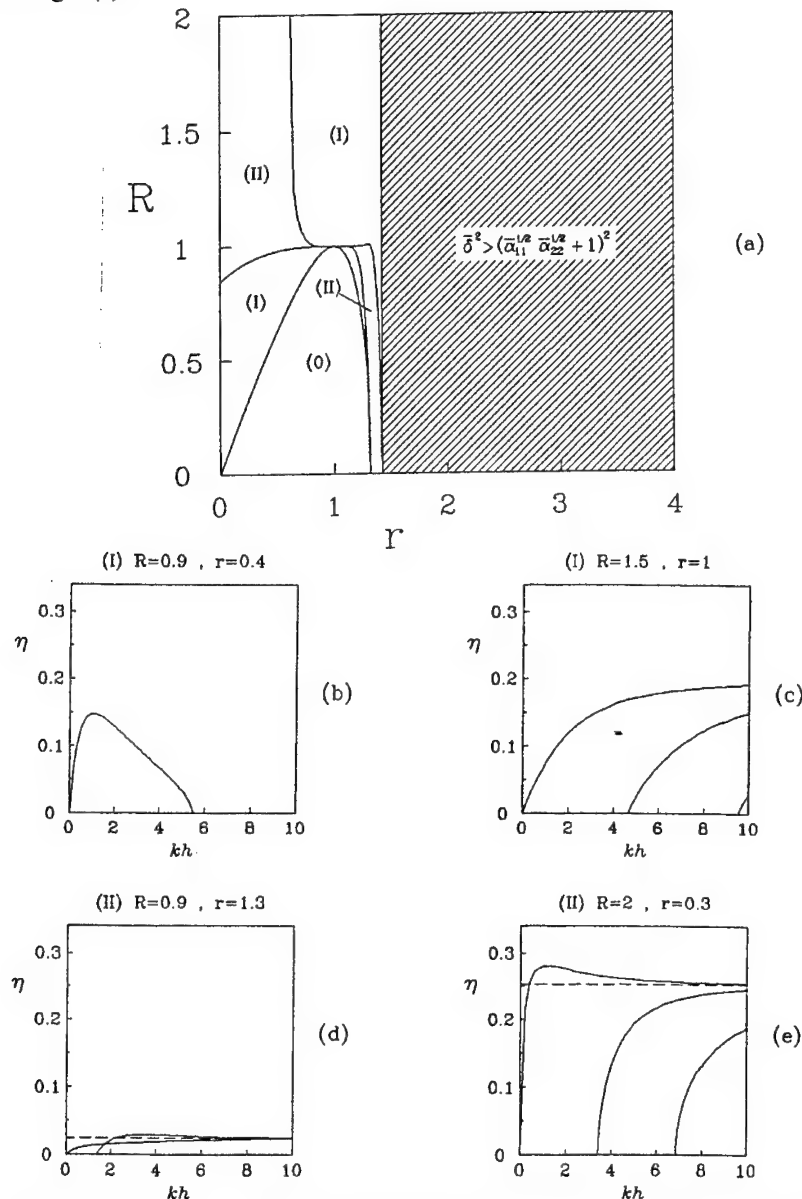


Figure 3. Same as the caption of Fig. 1 but with stressing perpendicular to the interfaces and with $\lambda_1=0.9$.

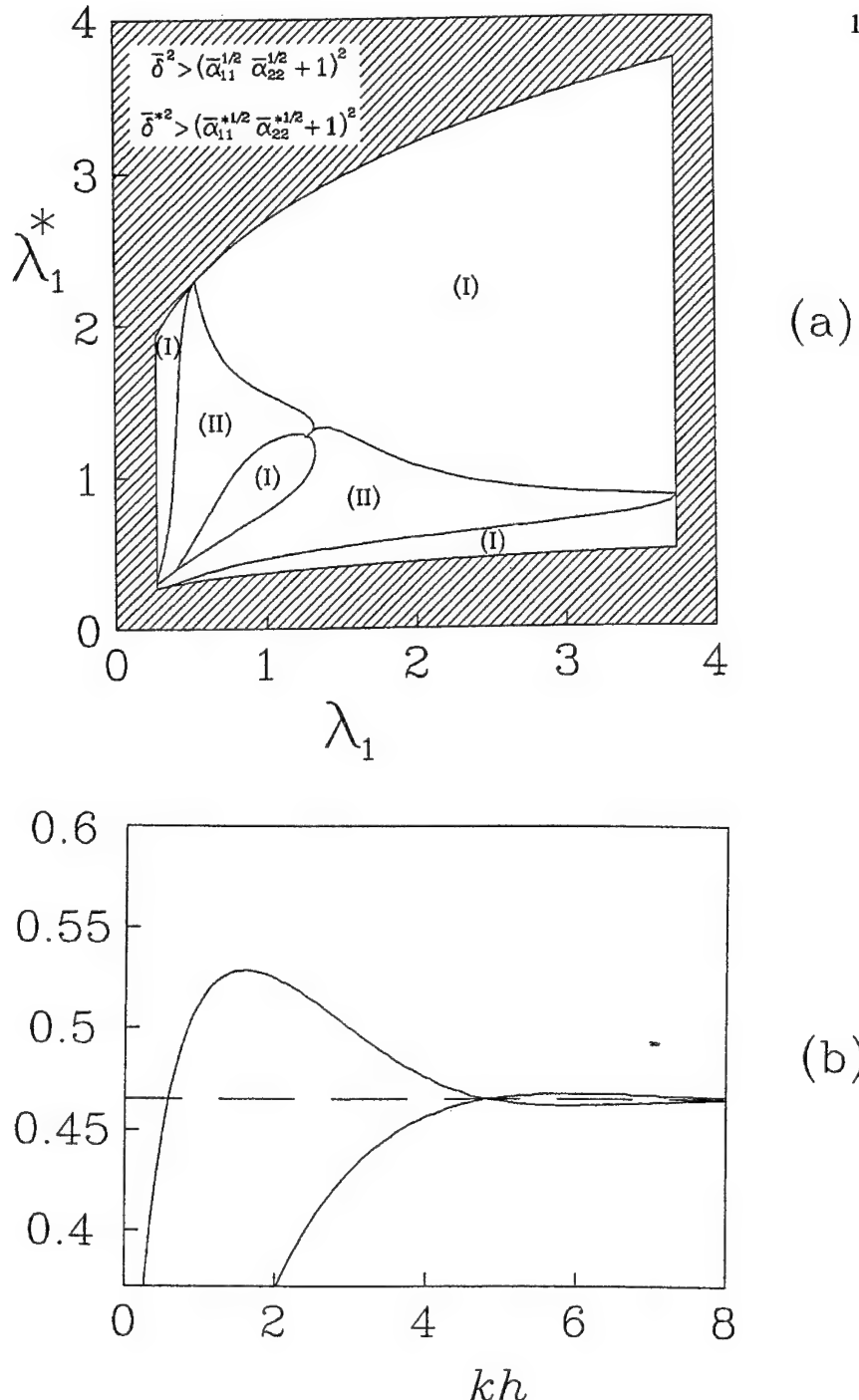


Figure 4. Blatz-Ko materials with $\lambda_2=\lambda_3=\lambda_3^*=1$, $\mu/\mu^*=\rho_r/\rho_r^*=1$. (a) The existence of high frequency propagation as it depends on λ_1 and λ_1^* ; regions (I) and (II) are defined as in the caption of Fig. 1. (b) Standing wave existence as it depends on λ_1^* and kh for a stress-free surrounding solid.

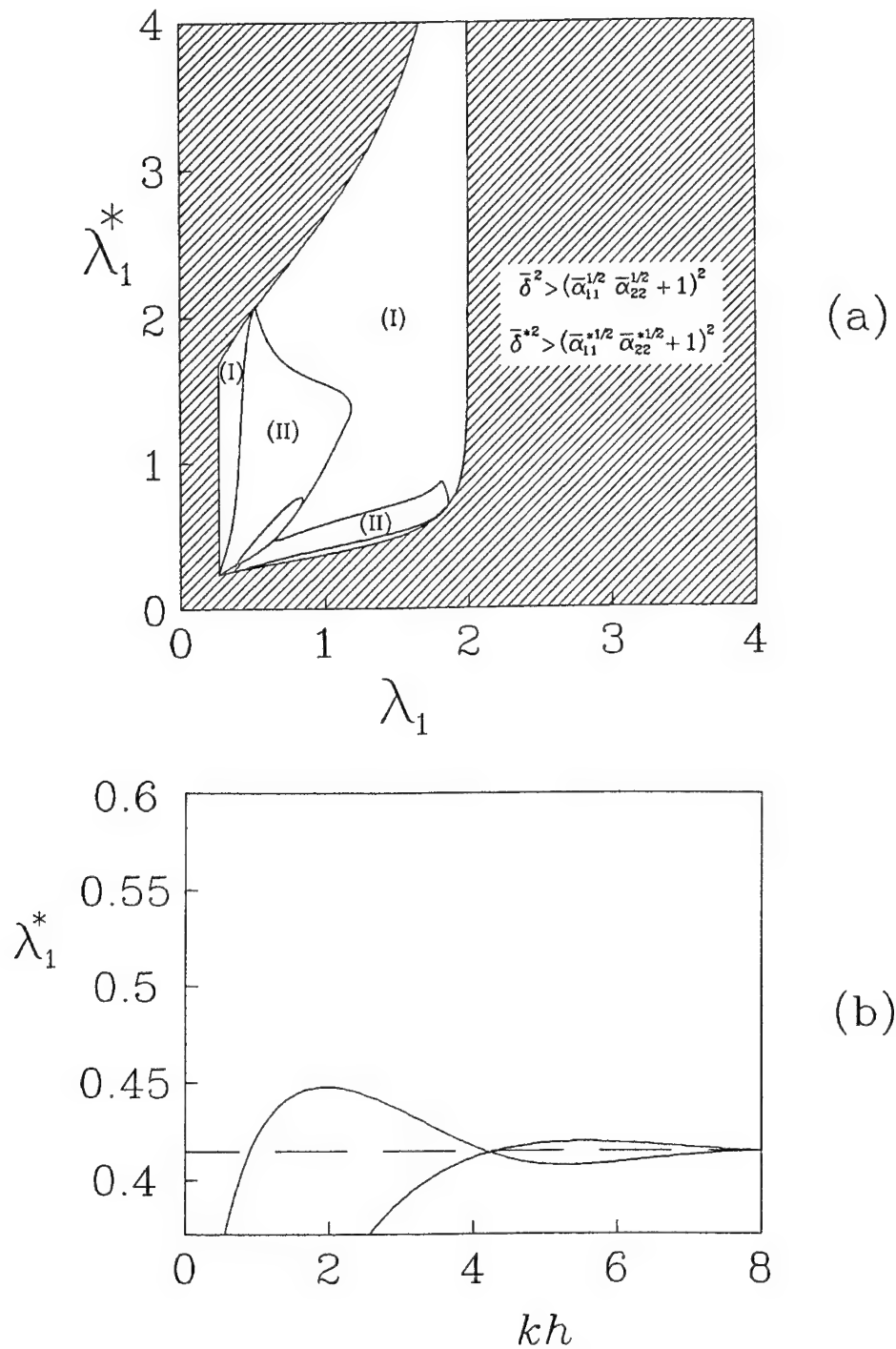


Figure 5. Same as the caption of Fig. 4 but with $\mu/\mu^* = \rho_r/\rho_r^* = 2$.

A different and, from the practical point of view, useful way of presenting the effect of stress on the existence or not of high frequency asymptotes is shown in Fig. 4(a). The two regimes (I) and (II) are drawn in the (λ_1, λ_1^*) -plane for Blatz-Ko materials with $\lambda_2 = \lambda_3 = \lambda_3^* = 1$, $\mu/\mu^* = \rho_r/\rho_r^* = 1$. In the shaded area, the strong ellipticity condition is violated. It is noted that, $\lambda_1 = \lambda_1^*$ (which results in $\lambda_2^* = 1$) falls in region (I) as no Stoneley wave can exist in stress-free materials of equal density. The existence of standing waves is demonstrated in Fig. 4(b) for the same case as that considered in Fig. 4(a) and, moreover, with the surrounding solid being stress-free, $\lambda_1 = 1$. For a given stretch, λ_1^* , in the interlayer Fig. 4(b) defines the ratio of the interlayer thickness, h , to the standing wavelength, $\Lambda = 2\pi/k$, for which standing waves exist.

The effect of different materials on high frequency asymptotes and on the existence of standing waves is demonstrated on Fig. 5(a), 5(b) in which $\mu/\mu^* = \rho_r/\rho_r^* = 2$. Fig. 5(a) is analogous to Fig. 4(a) and Fig. 5(b) to Fig. 4(b). The effect of material deviation with the same underlying stress is very pronounced. It is noted here that the stress-free case, $\lambda_1 = \lambda_1^*$, falls in region (II) as Stoneley waves exist in materials of equal shear wave speed.

Acknowledgment: We would like to express our thanks to Carolyn Magee of the Mathematics Department for typing the manuscript that includes all the cumbersome equations.

References

- M. A. Dowaikh and R. W. Ogden, On surface waves and deformations in a compressible elastic half-space, *Stability, Appl. Cont. Mech.* 1 (1991) 27
- M. A. Hayes and R. S. Rivlin, Surface waves in deformed elastic materials, *Arch. Ration. Mech. Anal.* 8 (1961) 358
- R. W. Ogden and D. A. Sotiropoulos, Reflection of plane waves from the boundary of a pre-stressed compressible elastic half-space, *IMA Journal of Applied Mathematics* 61 (1998), 61
- D. G. Roxburgh and R. W. Ogden, Stability and vibration of pre-stressed compressible elastic plates, *Int. J. Eng. Sci.* 32 (1994) 427
- D. A. Sotiropoulos and C. G. Sifniotopoulos, Interfacial waves in pre-stressed incompressible elastic interlayer, *J. Mech. Phys. Solids* 43 (1995) 365
- D. A. Sotiropoulos, Guided elastic waves in a pre-stressed compressible interlayer, *Ultrasonics* 38 (2000) 821

Author Index

Collet, B. p. 125
Dai, H. H. p. 55
Dekel, E. p. 99
Fu, Y. p. 55
Georgiadis, H. G. p. 63
Kundu, T. p. 83
Leroy, O. p. 141
Mal, A. p. 1
Markenscoff, X. p. 37
Mei-Chiang, L. p. 71
Morro, A. p. 107
Nair, S. p. 151
Orellana, J. M. p. 125
Pan, K. p. 55
Pecorari, C. p. 45
Rosenberg, Z. p. 99
Shkerdin, G. p. 141
Sifniotopoulos, C. G. p. 169
Sotiropoulos, D. A. p. 151, 169
Vandeputte, J. p. 141
Velgaki, E. G. p. 63
Wijeyewickrema, A. C. p. 71
Ziegler, F. p. 25

Mechanics

SOLID MECHANICS AND ITS APPLICATIONS

Series Editor: G.M.L. Gladwell

24. G. Prathap: *The Finite Element Method in Structural Mechanics*. 1993 ISBN 0-7923-2492-7
25. J. Herskovits (ed.): *Advances in Structural Optimization*. 1995 ISBN 0-7923-2510-9
26. M.A. González-Palacios and J. Angeles: *Cam Synthesis*. 1993 ISBN 0-7923-2536-2
27. W.S. Hall: *The Boundary Element Method*. 1993 ISBN 0-7923-2580-X
28. J. Angeles, G. Hommel and P. Kovács (eds.): *Computational Kinematics*. 1993 ISBN 0-7923-2585-0
29. A. Curnier: *Computational Methods in Solid Mechanics*. 1994 ISBN 0-7923-2761-6
30. D.A. Hills and D. Nowell: *Mechanics of Fretting Fatigue*. 1994 ISBN 0-7923-2866-3
31. B. Tabarrok and F.P.J. Rimrott: *Variational Methods and Complementary Formulations in Dynamics*. 1994 ISBN 0-7923-2923-6
32. E.H. Dowell (ed.), E.F. Crawley, H.C. Curtiss Jr., D.A. Peters, R. H. Scanlan and F. Sisto: *A Modern Course in Aeroelasticity*. Third Revised and Enlarged Edition. 1995 ISBN 0-7923-2788-8; Pb: 0-7923-2789-6
33. A. Preumont: *Random Vibration and Spectral Analysis*. 1994 ISBN 0-7923-3036-6
34. J.N. Reddy (ed.): *Mechanics of Composite Materials*. Selected works of Nicholas J. Pagano. 1994 ISBN 0-7923-3041-2
35. A.P.S. Selvadurai (ed.): *Mechanics of Poroelastic Media*. 1996 ISBN 0-7923-3329-2
36. Z. Mróz, D. Weichert, S. Dorosz (eds.): *Inelastic Behaviour of Structures under Variable Loads*. 1995 ISBN 0-7923-3397-7
37. R. Pyrz (ed.): *IUTAM Symposium on Microstructure-Property Interactions in Composite Materials*. Proceedings of the IUTAM Symposium held in Aalborg, Denmark. 1995 ISBN 0-7923-3427-2
38. M.I. Friswell and J.E. Mottershead: *Finite Element Model Updating in Structural Dynamics*. 1995 ISBN 0-7923-3431-0
39. D.F. Parker and A.H. England (eds.): *IUTAM Symposium on Anisotropy, Inhomogeneity and Nonlinearity in Solid Mechanics*. Proceedings of the IUTAM Symposium held in Nottingham, U.K. 1995 ISBN 0-7923-3594-5
40. J.-P. Merlet and B. Ravani (eds.): *Computational Kinematics '95*. 1995 ISBN 0-7923-3673-9
41. L.P. Lebedev, I.I. Vorovich and G.M.L. Gladwell: *Functional Analysis. Applications in Mechanics and Inverse Problems*. 1996 ISBN 0-7923-3849-9
42. J. Menčík: *Mechanics of Components with Treated or Coated Surfaces*. 1996 ISBN 0-7923-3700-X
43. D. Bestle and W. Schiehlen (eds.): *IUTAM Symposium on Optimization of Mechanical Systems*. Proceedings of the IUTAM Symposium held in Stuttgart, Germany. 1996 ISBN 0-7923-3830-8
44. D.A. Hills, P.A. Kelly, D.N. Dai and A.M. Korsunsky: *Solution of Crack Problems. The Distributed Dislocation Technique*. 1996 ISBN 0-7923-3848-0
45. V.A. Squire, R.J. Hosking, A.D. Kerr and P.J. Langhorne: *Moving Loads on Ice Plates*. 1996 ISBN 0-7923-3953-3
46. A. Pineau and A. Zaoui (eds.): *IUTAM Symposium on Micromechanics of Plasticity and Damage of Multiphase Materials*. Proceedings of the IUTAM Symposium held in Sèvres, Paris, France. 1996 ISBN 0-7923-4188-0
47. A. Naess and S. Krenk (eds.): *IUTAM Symposium on Advances in Nonlinear Stochastic Mechanics*. Proceedings of the IUTAM Symposium held in Trondheim, Norway. 1996 ISBN 0-7923-4193-7
48. D. Ieşan and A. Scalia: *Thermoelastic Deformations*. 1996 ISBN 0-7923-4230-5

Mechanics

SOLID MECHANICS AND ITS APPLICATIONS

Series Editor: G.M.L. Gladwell

49. J.R. Willis (ed.): *IUTAM Symposium on Nonlinear Analysis of Fracture*. Proceedings of the IUTAM Symposium held in Cambridge, U.K. 1997 ISBN 0-7923-4378-6
50. A. Preumont: *Vibration Control of Active Structures*. An Introduction. 1997 ISBN 0-7923-4392-1
51. G.P. Cherepanov: *Methods of Fracture Mechanics: Solid Matter Physics*. 1997 ISBN 0-7923-4408-1
52. D.H. van Campen (ed.): *IUTAM Symposium on Interaction between Dynamics and Control in Advanced Mechanical Systems*. Proceedings of the IUTAM Symposium held in Eindhoven, The Netherlands. 1997 ISBN 0-7923-4429-4
53. N.A. Fleck and A.C.F. Cocks (eds.): *IUTAM Symposium on Mechanics of Granular and Porous Materials*. Proceedings of the IUTAM Symposium held in Cambridge, U.K. 1997 ISBN 0-7923-4553-3
54. J. Roorda and N.K. Srivastava (eds.): *Trends in Structural Mechanics*. Theory, Practice, Education. 1997 ISBN 0-7923-4603-3
55. Yu.A. Mitropolskii and N. Van Dao: *Applied Asymptotic Methods in Nonlinear Oscillations*. 1997 ISBN 0-7923-4605-X
56. C. Guedes Soares (ed.): *Probabilistic Methods for Structural Design*. 1997 ISBN 0-7923-4670-X
57. D. François, A. Pineau and A. Zaoui: *Mechanical Behaviour of Materials*. Volume I: Elasticity and Plasticity. 1998 ISBN 0-7923-4894-X
58. D. François, A. Pineau and A. Zaoui: *Mechanical Behaviour of Materials*. Volume II: Visco-plasticity, Damage, Fracture and Contact Mechanics. 1998 ISBN 0-7923-4895-8
59. L.T. Tenek and J. Argyris: *Finite Element Analysis for Composite Structures*. 1998 ISBN 0-7923-4899-0
60. Y.A. Bahei-El-Din and G.J. Dvorak (eds.): *IUTAM Symposium on Transformation Problems in Composite and Active Materials*. Proceedings of the IUTAM Symposium held in Cairo, Egypt. 1998 ISBN 0-7923-5122-3
61. I.G. Goryacheva: *Contact Mechanics in Tribology*. 1998 ISBN 0-7923-5257-2
62. O.T. Bruhns and E. Stein (eds.): *IUTAM Symposium on Micro- and Macrostructural Aspects of Thermoplasticity*. Proceedings of the IUTAM Symposium held in Bochum, Germany. 1999 ISBN 0-7923-5265-3
63. F.C. Moon: *IUTAM Symposium on New Applications of Nonlinear and Chaotic Dynamics in Mechanics*. Proceedings of the IUTAM Symposium held in Ithaca, NY, USA. 1998 ISBN 0-7923-5276-9
64. R. Wang: *IUTAM Symposium on Rheology of Bodies with Defects*. Proceedings of the IUTAM Symposium held in Beijing, China. 1999 ISBN 0-7923-5297-1
65. Yu.I. Dimitrienko: *Thermomechanics of Composites under High Temperatures*. 1999 ISBN 0-7923-4899-0
66. P. Argoul, M. Frémond and Q.S. Nguyen (eds.): *IUTAM Symposium on Variations of Domains and Free-Boundary Problems in Solid Mechanics*. Proceedings of the IUTAM Symposium held in Paris, France. 1999 ISBN 0-7923-5450-8
67. F.J. Fahy and W.G. Price (eds.): *IUTAM Symposium on Statistical Energy Analysis*. Proceedings of the IUTAM Symposium held in Southampton, U.K. 1999 ISBN 0-7923-5457-5
68. H.A. Mang and F.G. Rammerstorfer (eds.): *IUTAM Symposium on Discretization Methods in Structural Mechanics*. Proceedings of the IUTAM Symposium held in Vienna, Austria. 1999 ISBN 0-7923-5591-1

Mechanics

SOLID MECHANICS AND ITS APPLICATIONS

Series Editor: G.M.L. Gladwell

69. P. Pedersen and M.P. Bendsøe (eds.): *IUTAM Symposium on Synthesis in Bio Solid Mechanics*. Proceedings of the IUTAM Symposium held in Copenhagen, Denmark. 1999 ISBN 0-7923-5615-2

70. S.K. Agrawal and B.C. Fabien: *Optimization of Dynamic Systems*. 1999 ISBN 0-7923-5681-0

71. A. Carpinteri: *Nonlinear Crack Models for Nonmetallic Materials*. 1999 ISBN 0-7923-5750-7

72. F. Pfeifer (ed.): *IUTAM Symposium on Unilateral Multibody Contacts*. Proceedings of the IUTAM Symposium held in Munich, Germany. 1999 ISBN 0-7923-6030-3

73. E. Lavendelis and M. Zakhzhevsky (eds.): *IUTAM/IFToMM Symposium on Synthesis of Non-linear Dynamical Systems*. Proceedings of the IUTAM/IFToMM Symposium held in Riga, Latvia. 2000 ISBN 0-7923-6106-7

74. J.-P. Merlet: *Parallel Robots*. 2000 ISBN 0-7923-6308-6

75. J.T. Pindera: *Techniques of Tomographic Isodyne Stress Analysis*. 2000 ISBN 0-7923-6388-4

76. G.A. Maugin, R. Drouot and F. Sidoroff (eds.): *Continuum Thermomechanics. The Art and Science of Modelling Material Behaviour*. 2000 ISBN 0-7923-6407-4

77. N. Van Dao and E.J. Kreuzer (eds.): *IUTAM Symposium on Recent Developments in Non-linear Oscillations of Mechanical Systems*. 2000 ISBN 0-7923-6470-8

78. S.D. Akbarov and A.N. Guz: *Mechanics of Curved Composites*. 2000 ISBN 0-7923-6477-5

79. M.B. Rubin: *Cosserat Theories: Shells, Rods and Points*. 2000 ISBN 0-7923-6489-9

80. S. Pellegrino and S.D. Guest (eds.): *IUTAM-IASS Symposium on Deployable Structures: Theory and Applications*. Proceedings of the IUTAM-IASS Symposium held in Cambridge, U.K., 6–9 September 1998. 2000 ISBN 0-7923-6516-X

81. A.D. Rosato and D.L. Blackmore (eds.): *IUTAM Symposium on Segregation in Granular Flows*. Proceedings of the IUTAM Symposium held in Cape May, NJ, U.S.A., June 5–10, 1999. 2000 ISBN 0-7923-6547-X

82. A. Lagarde (ed.): *IUTAM Symposium on Advanced Optical Methods and Applications in Solid Mechanics*. Proceedings of the IUTAM Symposium held in Futuroscope, Poitiers, France, August 31–September 4, 1998. 2000 ISBN 0-7923-6604-2

83. D. Weichert and G. Maier (eds.): *Inelastic Analysis of Structures under Variable Loads. Theory and Engineering Applications*. 2000 ISBN 0-7923-6645-X

84. T.-J. Chuang and J.W. Rudnicki (eds.): *Multiscale Deformation and Fracture in Materials and Structures*. The James R. Rice 60th Anniversary Volume. 2001 ISBN 0-7923-6718-9

85. S. Narayanan and R.N. Iyengar (eds.): *IUTAM Symposium on Nonlinearity and Stochastic Structural Dynamics*. Proceedings of the IUTAM Symposium held in Madras, Chennai, India, 4–8 January 1999 ISBN 0-7923-6733-2

86. S. Murakami and N. Ohno (eds.): *IUTAM Symposium on Creep in Structures*. Proceedings of the IUTAM Symposium held in Nagoya, Japan, 3–7 April 2000. 2001 ISBN 0-7923-6737-5

87. W. Ehlers (ed.): *IUTAM Symposium on Theoretical and Numerical Methods in Continuum Mechanics of Porous Materials*. Proceedings of the IUTAM Symposium held at the University of Stuttgart, Germany, September 5–10, 1999. 2001 ISBN 0-7923-6766-9

88. D. Durban, D. Givoli and J.G. Simmonds (eds.): *Advances in the Mechanics of Plates and Shells. The Avinoam Libai Anniversary Volume*. 2001 ISBN 0-7923-6785-5

89. U. Gabbert and H.-S. Tzou (eds.): *IUTAM Symposium on Smart Structures and Strutonic Systems*. Proceedings of the IUTAM Symposium held in Magdeburg, Germany, 26–29 September 2000. 2001 ISBN 0-7923-6968-8

Mechanics

SOLID MECHANICS AND ITS APPLICATIONS

Series Editor: G.M.L. Gladwell

90. Y. Ivanov, V. Cheshkov and M. Natova: *Polymer Composite Materials – Interface Phenomena & Processes*. 2001 ISBN 0-7923-7008-2
91. R.C. McPhedran, L.C. Botten and N.A. Nicorovici (eds.): *IUTAM Symposium on Mechanical and Electromagnetic Waves in Structured Media* held in Sydney, NSW, Australia, 18-22 Januari 1999. 2001 ISBN 0-7923-7038-4
92. D.A. Sotiropoulos (ed.): *IUTAM Symposium on Mechanical Waves for Composite Structures Characterization*. Proceedings of the IUTAM Symposium held in Chania, Crete, Greece, June 14-17, 2000. 2001 ISBN 0-7923-7164-X
93. V.M. Alexandrov and D.A. Pozharskii: *Three-Dimensional Contact Problems*. 2001 ISBN 0-7923-7165-8